HIGH-ORDER COMPUTER-ASSISTED ESTIMATES OF TOPOLOGICAL ENTROPY

By

Johannes Grote

A DISSERTATION

Submitted to
Michigan State University
in partial fulfillment of the requirements
for the degree of

DOCTOR OF PHILOSOPHY

Physics and Astronomy
and
Mathematics

2009

ABSTRACT

HIGH-ORDER COMPUTER-ASSISTED ESTIMATES OF TOPOLOGICAL ENTROPY

By

Johannes Grote

The concept of Taylor Models is introduced, which offers highly accurate C^0-estimates for the enclosures of functional dependencies, combining high-order Taylor polynomial approximation of functions and rigorous estimates of the truncation error, performed using verified interval arithmetic. The focus of this work is on the application of Taylor Models in algorithms for strongly nonlinear dynamical systems. A method to obtain sharp rigorous enclosures of Poincaré maps for certain types of flows and surfaces is developed and numerical examples are presented.

Differential algebraic techniques allow the efficient and accurate computation of polynomial approximations for invariant curves of certain planar maps around hyperbolic fixed points. Subsequently we introduce a procedure to extend these polynomial curves to verified Taylor Model enclosures of local invariant manifolds with C^0-errors of size $10^{-10} - 10^{-14}$, and proceed to generate the global invariant manifold tangle up to comparable accuracy through iteration in Taylor Model arithmetic.

Knowledge of the global manifold structure up to finite iterations of the local manifold pieces enables us to find all homoclinic and heteroclinic intersections in the generated manifold tangle. Combined with the mapping properties of the homoclinic points and their ordering we are able to construct a subshift of finite type as a topological factor of the original planar system to obtain rigorous lower bounds for its topological entropy. This construction is fully automatic and yields homoclinic tangles with several hundred homoclinic points.

As an example rigorous lower bounds for the topological entropy of the Hénon map are computed, which to the best knowledge of the authors yield the largest such estimates published so far.

To my parents

ACKNOWLEDGMENTS

Exceptional people to work with can be found everywhere, if one takes the time to look closely enough, and East Lansing is no exception.

I would like to thank my academic advisor Professor Martin Berz for his continued support, inexhaustible patience and spirited guidance during my studies at MSU, and I must include Professors Kyoko Makino and Sheldon Newhouse in the same breath. Working with these people, who are as great scientists as they are individuals, has been a privilege and a blessing for me.

I truly appreciate Professors Philip Duxbury and Moxun Tang kindly serving on my guidance committee, and Professor Bhanu Mahanti for being the Graduate Director who cares.

To the U.S. Department of Energy, the Studienstiftung des Deutschen Volkes and the MSU Graduate School I am indebted for financial support throughout my stay at MSU.

I would like to acknowledge my fellow students Shashikant Manikonda, Youn-Kyung Kim, Pavel Snopok, Alexey Poklonskiy, Alexander Wittig, Ravi Jagasia, He Zhang, Roberto Armellin and Pierluigi DiLizia for many deep thoughts and even more laughs. Too many people have been part of my life here in the States to name them individually without forgetting someone who deserves to be mentioned, so I shall not, and you know who you are. I value your friendships above all.

Markus Neher of Technical University of Karlsruhe deserves recognition for support in more ways than one, and I hope to have the opportunity to repay him adequately.

Lastly and most importantly, I would like to thank my ever supportive family, and my dear Ina for sharing my path all this time. I could not have done it without you.

TABLE OF CONTENTS

LIST OF FIGURES

CHAPTER 1

Introduction

Ever since the first computers were used to simulate mathematical models and develop an intuitive understanding of their behavior, numerical mathematics has been concerned with the question of the accuracy of these computational results,

Interval methods, first conceptualized by Moore [49, 50], offer a way to implement self-contained numerical algorithms that compute interval range bounds of the solution of a computation, thus automatically obtaining C^0 error estimates. While interval arithmetic works fine for specific problems in e.g. linear algebra, global optimization or verified integration of ODEs, in general this approach has only limited practicality as interval arithmetic has to cope with fundamental problems that limit the accuracy of the interval range enclosure of solutions, among which are the dependency problem and the wrapping effect (explained in more detail in Appendix A), and a particularly unfavorable scaling of the computational effort with the dimensionality.

Taylor Models have been conceived in the 1990s [5, 41] as an approach to verified computing that would alleviate the problems of interval arithmetic while still yielding valid C^0 error estimates in an automated fashion. In spirit, they originated in the map methods which had been successfully applied in particle accelerator simulations for decades. Transfer maps, i.e. the action on the beam of a particular particle

optical element like magnets, drifts or absorbers, were computed as polynomial Taylor expansions to high order, and the suitable composition of transfer maps allowed accurate predictions about the stability of the beam for very long times.

Frameworks were developed that made these complex polynomial manipulations fast and efficient, like the differential algebraic picture of Taylor polynomial arithmetic presented in Appendix B. But the question about the convergence of these high-order Taylor expansions was of secondary interest. The reason for this was that in the high-energy beam physics field, the equations of motion were typically only weakly nonlinear and Taylor expansions of the associated transfer maps had a very beneficial convergence behavior.

The picture changes dramatically if one wants to use Taylor approximations in a strongly nonlinear setting. Here, the question of bounding the truncation errors and, after algorithm implementation, also round-off errors in floating point arithmetic becomes paramount. Taylor Models are based on efficient polynomial manipulation techniques to obtain highly acurate polynomial approximations and combine them with rigorous interval arithemetic to bound the Taylor remainder errors. Since the truncation error scales favorably in displacement from the expansion point with the polynomial expansion order plus one, the fundamental drawbacks of interval arithmetic can be mitigated by bounding the truncation error over small, but still sufficiently large, domains.

Chapter 2 presents and reviews important mathematical concepts to the extent to which they are relevant for this present work. Introductions to Poincaré maps, invariant manifolds, topological entropy and symbolic dynamics are covered by citing the key concepts and results, while the treatment of Taylor Models is more in-depth and their definitions and properties are presented in a more detailed and exhaustive manner.

In chapter 3 we present a technique to obtain Taylor Model enclosures of Poincaré

maps of flows for quite general types of Poincaré sections. The technique rests on the availability of high-order inversion of polynomial functional dependencies, and the ability to Taylor expand solutions of implicit equations. This yields quite accurate Taylor polynomial approximations of Poincaré maps which can be outfitted with rigorous remainder bounds *a posteriori* with derivative information given by the underlying ODE of the system. Examples for both nonverified polynomial approximations and verified Taylor Model enclosures of the Poincaré maps are provided.

Chapter 4 introduces us to invariant manifolds of discrete dynamical systems, or to be more precise of planar diffeomorphisms, and the problem of accurately representing them numerically. Since invariant manifolds are of high significance in the determination of long-term behavior of a multitude of dynamical systems, from forced oscillations to the Lorenz system to mission design in astrophysics, and in particular in strongly nonlinear settings, obtaining accurate approximations of the global manifold tangle structure is desirable. We present an approach in which Taylor Model enclosures of invariant manifolds can be found with C^0 error sizes of 10^{-12} and smaller.

In chapter 5 we develop a novel automated approach to finding rigorous lower bounds of the topological entropy for certain planar systems. This is achieved by determining symbolic dynamics in a constructive manner. The technique combines many results and algorithms from the previous sections, using homoclinic points and invariant manifold segments to define topological rectangles and rigorously determining their mapping properties, thus constructing a subshift of finite type as a topological factor of the original system.

A short overview of the fundamentals of interval arithmetic and differential algebraic structures for the manipulation of Taylor polynomials is given in the appendices A and B.

CHAPTER 2

Fundamental Concepts

In this chapter we introduce fundamental mathematical concepts from dynamical systems theory to the extent that they are featured in the Taylor Model based verified algorithms in later chapters. Most of the material is canonical and presented without proof, more in-depth treatment of the topics is provided by the cited references. Sections 2.2, 2.3 and 2.4 in particular draw on [55].

In the last section, we introduce the notion of Taylor Models in a somewhat more exhaustive manner, as Taylor Models are still a relatively novel concept.

2.1 Poincaré maps

Poincaré maps, first conceived by Henri Poincaré [58] in the 1880s, are a classical tool for the analysis of the stability of certain periodic or near-periodic orbits that a continuous dynamical system might exhibit. Instead of analyzing the orbit structure of the corresponding flow in the entire phase space, using Poincaré maps one only looks on the action of the system on suitably chosen surfaces (typically planes, or hyperplanes, but also more general classes of differentiable manifolds) that are transverse to the flow. The fundamental advantage which the Poincaré map offers is that the dynamics can now be analyzed in a space that has a dimension which has

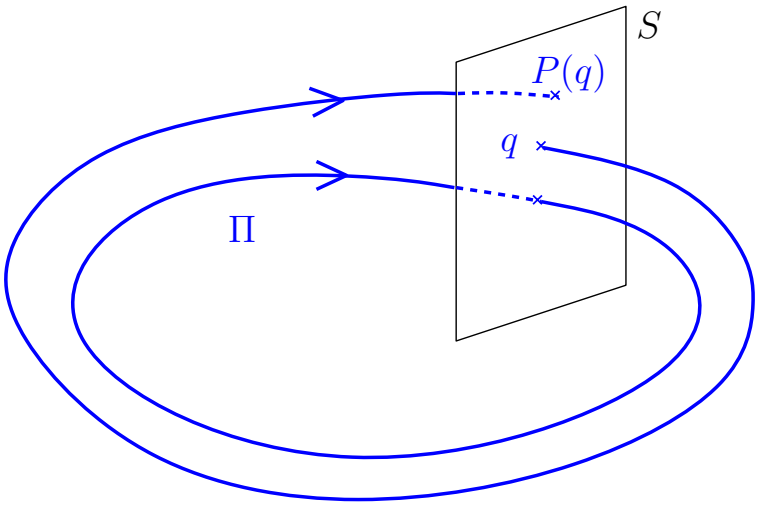

Figure 2.1. The Poincaré map P describes the first return of an orbit in the neighborhood of a periodic orbit Π to a surface S which is transversed by both.

been reduced by one compared to the original phase space, while still preserving all the 'interesting' qualities of the orbit structure. In low-dimensional dynamics, this dimension-reduction is a significant simplification and Poincaré maps have become a successfully applied tool both in a more purely mathematical context (like forced oscillations) as well as in physics and astrophysics problems, like the three body problem or particle accelerators.

The underlying idea of Poincaré maps is a simple one. Consider the autonomous system

$$\dot{x} = f(x), \tag{2.1}$$

where $f : \mathbb{R}^n \longrightarrow \mathbb{R}^n$ is C^1, and we assume for simplicity that the flow $\varphi : \mathbb{R}^n \times \mathbb{R} \longrightarrow \mathbb{R}^n$ of (2.1) exists globally, and assume now that there is a periodic orbit $\Pi \subset \mathbb{R}^n$ of period $T > 0$. Consider a hyperplane S of dimension $n-1$ that is transverse to Π, i.e. $\Pi \cap S = \{p\}$ and $f(p)$ is not tangent to S at p. Then naturally $\varphi(p, T) = p \in S$ again, because of the periodicity. However, one can show that in this situation also the orbits starting at points q sufficiently close to p, which are then typically not

periodic anymore, will also intersect S transversely, say at a point $P(q)$, as shown in Figure 2.1. The mapping $q \longrightarrow P(q)$ is called the Poincaré map.

2.1 Theorem. *Let $E \subset \mathbb{R}^n$ be open, let $f \in C^1(E)$ and let $\varphi : E \times \mathbb{R} \longrightarrow E$ be the flow of (2.1). Assume that for some $p \in E$ the orbit $\Pi := \{\varphi(p,t) : 0 \leq t \leq T\}$ is periodic with period T such that $\Pi \subset E$. Consider now a C^1-manifold S which is transverse to Π at p, i.e. $f(p)$ does not lie in the tangent space T_pS.*

Then there exists $\varepsilon > 0$ and a C^1- function $\tau : B_\varepsilon(p) \longrightarrow \mathbb{R}$ such that

$$\varphi(q, \tau(q)) \in S \ \forall\, q \in B_\varepsilon(p)$$

and $\tau(p) = T$.

This function τ denotes the crossing time for the choice of initial condition q until the orbit first intersects S.

2.2 Definition. *In the situation of the preceding theorem, we define the Poincaré map $P : B_\varepsilon(p) \cap S \longrightarrow S$ as*

$$P(q) := \varphi(q, \tau(q)) \ \ \forall\, q \in B_\varepsilon(p) \cap S \ .$$

Evidently this definition could be generalized to allow nonperiodic reference orbits $\varphi(p,t)$, as long as the return to S is again transverse.

Intuitively, statements about the qualitative properties of the reference orbit Π, e.g. whether it is attracting or repelling or has a saddle point in $p \in S$, can now be derived from looking at the derivative of the Poincaré map at p: the orbit $\Pi \subset E$ is hyperbolic (attracting, repelling, saddle) if and only if p is a hyperbolic fixed point (sink, source, or saddle, respectively) of the Poincaré map P.

2.2 Invariant manifolds, hyperbolicity and homoclinic points

2.3 Definition. *(Topological and C^r-manifolds) A topological n-manifold X is a second-countable Hausdorff topological space with a collection $\{(U_i, \varphi_i)\}_{i\in\mathcal{I}}$ such that*

1. *U_i is open $\forall\, i \in \mathcal{I}$ and $X \subset \bigcup_{i\in\mathcal{I}} U_i$.*
2. *$\varphi_i : U_i \longrightarrow \varphi_i(U_i) \subset \mathbb{R}^n$ is a homeomorphism $\forall\, i \in \mathcal{I}$ such that $\varphi_i(U_i)$ is open.*
3. *if $U_i \cap U_j \neq \emptyset$ for some $i, j \in \mathcal{I}$, the transition map $\left(\varphi_i \circ \varphi_j^{-1}\right) : \varphi_j\left(U_i \cap U_j\right) \longrightarrow \varphi_i\left(U_i \cap U_j\right)$ is a homeomorphism.*

In this case we call $\{(U_i, \varphi_i)\}_{i\in\mathcal{I}}$ an atlas and the φ_i charts.

A C^r n-manifold is a topological n-manifold where the transition maps in 3. are C^r.

Of particular interest to us are, of course, differentiable submanifolds (curves, surfaces, hypersurfaces etc.) of $\mathbb{R}^n$.

2.4 Definition. *(Immersed and embedded manifold) Let X and Y be two C^r n_X- and n_Y-manifolds, respectively, and let $f : X \longrightarrow Y$ be a C^r-map such that the linearization $L_x : T_xX \longrightarrow T_{f(x)}Y$ of f at x is injective on the tangent spaces $\forall\, x \in X$. In this case we call f an immersion, and the image $f(X) \subset Y$ is called an immersed C^r submanifold of Y.*

$f(X)$ is called an embedded submanifold if additionally f is injective and the relative topology on $f(X)$ inherited from Y equals the topology induced by f on $f(X)$.

Note that in the definition of an immersed manifold, the immersion f itself need not be injective (see Figure 2.2), just its derivative acting on a tangent space.

In the following let X be a smooth n-manifold and let $f : X \longrightarrow X$ be a C^r-diffeomorphism from X into itself.

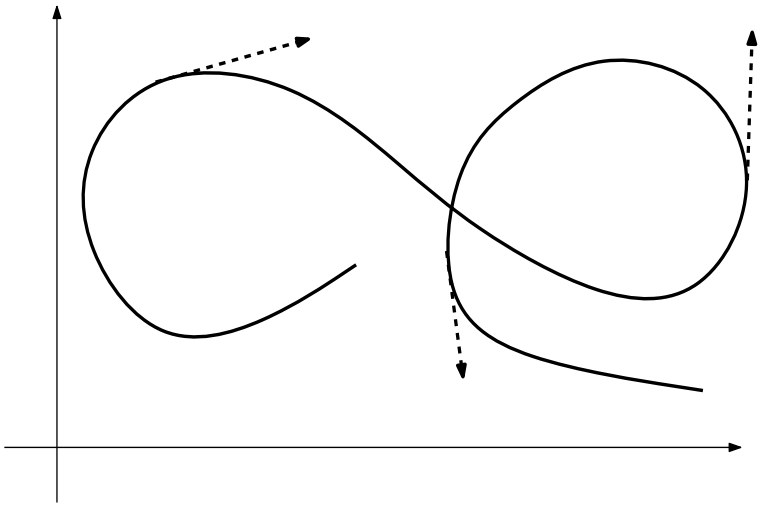

Figure 2.2. A non-injectively immersed curve in the plane, together with examples for its tangent vectors (dashed).

2.5 Definition. *(Hyperbolic fixed and periodic points)*

A fixed point $p \in X$ of f is called hyperbolic iff the Jacobian $Df(p)$ has no eigenvalues of norm one. We also say that p is

1. *a sink if all eigenvalues have norm less than 1,*

2. *a source if all eigenvalues have norm greater than 1,*

3. *a saddle if there exist eigenvalues of both types.*

A periodic point q of f with period N is accordingly called a hyperbolic sink (source, saddle) if it is a hyperbolic sink (source, saddle) fixed point of f^N.

The significance of hyperbolic fixed and periodic points is that in their neighborhoods the tangent spaces (and the dynamics) can be classified according to certain invariant subspaces:

2.6 Theorem. *(Hyperbolic splitting) Let $p \in X$ be a hyperbolic fixed point of f, then there exists a direct sum decomposition $T_pX = E_p^u \oplus E_p^s$ such that*

1. *E_p^u and E_p^s are invariant under $Df(p)$.*

2. *$Df(p)|_{E_p^s}$ has eigenvalues of norm less than 1.*

3. *$Df(p)|_{E_p^u}$ has eigenvalues of norm greater than 1.*

In the situation of the theorem we also call E_p^u and E_p^s the unstable and stable eigenspaces at p. One can now ask if there are generalizations to the concept of eigenspaces that stay invariant under the map f itself and not just the linearization. To this end we define the stable and unstable sets

$$W^s(p) := \left\{ x \in X : f^n(x) \underset{n\to\infty}{\longrightarrow} p \right\}$$

and

$$W^u(p) := \left\{ x \in X : f^{-n}(x) \underset{n\to\infty}{\longrightarrow} p \right\}$$

of points diverging from or converging to p. The next theorem, also known as the Invariant Manifold Theorem, asserts that these sets in fact have a nice differentiable structure, as depicted in Figure 2.3:

2.7 Theorem. *(Hadamard-Perron) Let $p \in X$ be a hyperbolic fixed point of f and let $T_pX = E_p^u \oplus E_p^s$ as per the previous theorem. Then $W^\sigma(p)$ is a C^r injectively immersed copy of E_p^σ tangent to E_p^σ at p for $\sigma = u, s$.*

In light of the last theorem we call the sets $W^u(p)$ and $W^s(p)$ the unstable and stable manifold of p, respectively. Intuitively, one might think that $W^u(p)$ and $W^s(p)$ are not only injectively immersed manifolds, but even embedded with a nice topology. The counterexamples to this conjecture are precisely the complicated manifold structures connected to hyperbolic and horseshoe dynamics which we will be concerned with in the later chapters of this work.

2.8 Definition. *(Homoclinic and heteroclinic points) Let $p_1, p_2 \in X$ be hyperbolic fixed points of f.*

1. *If $W^u(p_1) \cap W^s(p_1) \neq \emptyset$, then any point in $W^u(p_1) \cap W^s(p_1)$ is called a homoclinic point (of p_1).*

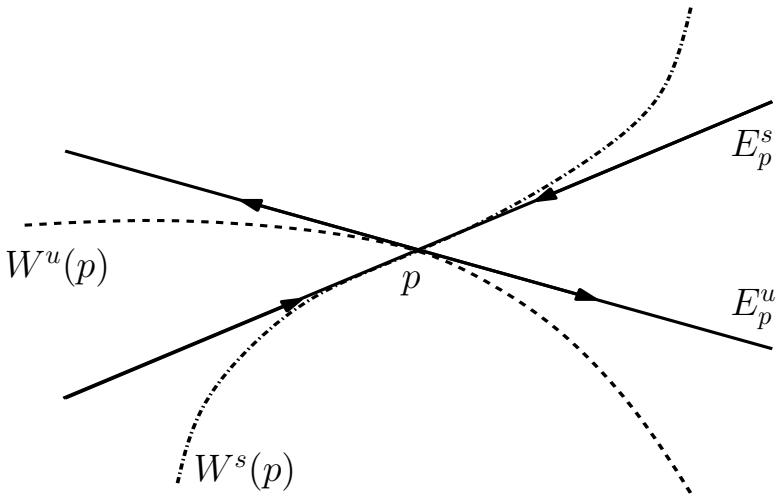

Figure 2.3. Unstable and stable manifolds $W^u(p)$ (dashed) and $W^s(p)$ (dash-dotted), tangential to the respective eigenspaces E_p^u and E_p^s at the hyperbolic fixed point p.

2. *If* $W^u(p_1) \cap W^s(p_2) \neq \emptyset$ *(or* $W^u(p_2) \cap W^s(p_1) \neq \emptyset$*), then any point in* $W^u(p_1) \cap W^s(p_2)$ *(or* $W^u(p_2) \cap W^s(p_1)$*) is called a heteroclinic point (of* p_1 *and* p_2*).*

A homo-/heteroclinic point q is called transverse if the tangent spaces of the invariant manifolds intersecting at q are transverse.

For ease of expression we will mosly restrict ourselves to homoclinic points, even though corresponding statements usually apply to heteroclinic points. Homoclinic points are of great interest, since they can be viewed, depending on the angle, as a cause or symptom of chaotic motion. Let $q \in (W^u(p) \cap W^s(p))$ be a homoclinic point for f of the fixed point p. Then it is obvious that also every image or preimage of q is going to be such a homoclinic point, i.e.

$$f^k(q) \in \left(W^u(p) \cap W^s(p)\right) \; \forall\, k \in \mathbb{Z}.$$

So the existence of one homoclinic point implies a countably infinite number of homoclinic points. Since by definition images and preimages of q converge to p, we

thus have an ever finer accumulation of manifold intersections near p and accordingly a very complicated bunching up of the corresponding manifold branches. This in essence is the sign of chaos, since any two points arbitrarily close to p will have rapidly diverging orbits under f.

2.3 Topological entropy

2.9 Definition. *(Topological entropy) Let (X, d) be a compact metric space and let $\Phi : X \longrightarrow X$ be a topological endomorphism, i.e. a continuous self-map of X. Let $x, y \in X$ and $n \in \mathbb{N}_0$. Then an n-orbit $O(n, x)$ of x is the sequence $\left\{\Phi^k(x)\right\}_{k=0}^{n-1}$. For $\varepsilon > 0$, we say that two n-orbits $O(n, x)$ and $O(n, y)$ are ε-separated if $\exists\, k \in \{0, ..., n-1\}$ such that*

$$d\left(\Phi^k(x), \Phi^k(y)\right) > \varepsilon \ .$$

Let now $r(n, \varepsilon, \Phi) \in \mathbb{N}_0$ denote the maximal number of ε-separated n-orbits of Φ in X (note that this number is well-defined due to the compactness of X). Then we define the topological entropy $h(\Phi)$ of Φ as

$$h(\Phi) := \lim_{\varepsilon \to 0} \limsup_{n \to \infty} \frac{1}{n} \max\{0, \log(r(n, \varepsilon, \Phi))\}.$$

This definition appears cumbersome at first, in particular it does not seem to lend itself to a straightforward implementation in a computer environment due to the double limit in the definition. However, one can develop an intuitive understanding of the meaning of the entropy as a measure of the chaoticity of the underlying map Φ. For example, for small ε there are approximately $e^{h(\Phi)n}$ different ε-separated n-orbits in X, i.e. the number of separated orbits grows exponentially with the map iterate.

The topological entropy has numerous interesting properties, of which we will state some of the most useful :

2.10 Remark. *In the following $(X, d_X), (Y, d_Y)$ are compact metric spaces.*

1. *Let $\Phi : X \longrightarrow Y$ be a homeomorphism, then for its inverse Φ^{-1} we have*

$$h\left(\Phi^{-1}\right) = h\left(\Phi\right) \ .$$

2. *For an isometric endomorphism $\Phi : X \longrightarrow X$, i.e. $d_X\left(\Phi\left(x_1\right), \Phi\left(x_2\right)\right) = d_X\left(x_1, x_2\right)$ holds $\forall\, x_1, x_2 \in X$, it follows*

$$h\left(\Phi\right) = 0 \ .$$

3. *If for an endomrphism $\Phi : X \longrightarrow X$ and a subset $\Sigma \subset X$ we have that $\Phi\left(\Sigma\right) \subset \Sigma$, then*

$$h\left(\Phi|_\Sigma\right) \leq h\left(\Phi\right) \ .$$

4. *For an endomorphism $\Phi : X \longrightarrow X$ and $n \in \mathbb{N}_0$, we have*

$$h\left(\Phi^n\right) = n\, h\left(\Phi\right) \ .$$

5. *For any continuous flow $\varphi_t : X \longrightarrow X$, $t \in \mathbb{R}$, likewise*

$$h\left(\varphi_t\right) = |t|\ h\left(\varphi_1\right) \ .$$

6. *If $\Phi : X \longrightarrow X$ and $\Psi : Y \longrightarrow Y$ are topological endomorphisms, then $\Phi \times \Psi : X \times Y \longrightarrow X \times Y$ is a topological endomorphism and*

$$h\left(\Phi \times \Psi\right) = h\left(\Phi\right) + h\left(\Psi\right) \ .$$

We are interested in how the topological entropy changes if we project the action of a map onto a simpler space:

2.11 Definition. *Let X, Y be compact metric spaces and let $\Phi : X \longrightarrow X$, $\Psi : Y \longrightarrow Y$ be topological endomorphisms,, respectively. If there is a continuous surjection*

$\pi : X \longrightarrow Y$ *such that* $\Psi \circ \pi = \pi \circ \Phi$*, then we say that* Ψ *is a (topological) factor of* Φ*.*

If Φ *and* Ψ *are mutually factors of each other, we say that they are topologically conjugate.*

In the setting of the last definition, if Ψ is a factor of Φ, then the dynamics of Ψ mimic the dynamics of Φ, albeit they are simplified by the projection onto the domain of Ψ. This results in immediate estimates for the entropy:

2.12 Theorem. *In the setting of Definition 2.11, if* Ψ *is a topological factor of* Φ*, then*

$$h(\Psi) \leq h(\Phi) \ .$$

It follows that if Ψ and Φ are conjugate, then

$$h(\Psi) = h(\Phi) \ .$$

The last theorem means that we can find lower bounds for the topological entropy of complicated maps if we manage to find topological factors for which the entropy can be computed more easily. This will constitute the main idea for rigorous entropy estimates in the later chapters of this work. Furthermore, the topological entropy is a dynamical invariant, an intrinsic quantity that remains constant under coordinate transformations, and as such is particularly interesting.

In the case of planar dynamics on a 2-dimensional manifold we can get a good intuition for the topological entropy by seeing its similarity to the concept of Lyapunov exponents. Let X be a two-dimensional C^1-manifold and let $\gamma : [a,b] \longrightarrow X$ be a smooth curve defined on the real interval $[a,b]$. Let $|\gamma|$ denote the arclength of γ. For a C^∞-endomorphism $\Phi : X \longrightarrow X$ we define the growth factor of γ under Φ as

$$G(\gamma, \Phi) := \limsup_{n \longrightarrow \infty} \frac{1}{n} \max\left\{0, \log\left(\left|\Phi^n(\gamma)\right|\right)\right\} \ ,$$

i.e. asymptotically, the iterates of γ grow by a factor of $e^{G(\gamma,\Phi)}$ in length with every iteration of Φ. Then the following theorem can be shown [53, 54, 65, 66]:

2.13 Theorem. *Let X be a two-dimensional C^1-manifold and $\Phi : X \longrightarrow X$ be a C^∞-endomorphism. Then*

$$h(\Phi) = \sup_{C^\infty\text{-}curves\ \gamma \subset X} G(\gamma, \Phi) \ .$$

If X is additionally compact with piecewise smooth boundary, and Φ is area-decreasing, then

$$h(\Phi) = \max_{\gamma \subset \partial X} G(\gamma, \Phi) \ .$$

2.4 Shift maps, subshifts of finite type and symbolic dynamics

In this section we introduce the notion of symbolic dynamics, which denotes the concept of imitating the qualitative behavior of a dynamical system defined on a general metric space with a derived system defined on a much simpler phase space with a finite number of possible system states.

2.14 Definition. *(Shift map) Let $N > 0$, and let $\alpha := \{1, 2, ..., N\}$. We call the set α an alphabet of length N. Consider now the space of right-infinite sequences consisting of elements in N*

$$\Sigma_N^+ := \left\{ \mathbf{a} = (a_n)_{n \in \mathbb{N}_0} : a_n \in \alpha \, \forall \, n \in \mathbb{N}_0 \right\} \ .$$

Note that Σ_N^+ can be made into a compact metric space with the introduction of the metric d given by

$$d(\mathbf{a}, \mathbf{b}) := \sum_{n \in \mathbb{N}_0} \frac{|a_n - b_n|}{2^n} \ .$$

We now define the left shift map $\sigma : \Sigma_N^+ \longrightarrow \Sigma_N^+$ as

$$(\sigma(\mathbf{a}))_n := a_{n+1} \ \forall \, \mathbf{a} = (a_n)_{n \in \mathbb{N}_0} \in \Sigma_N^+ \ .$$

It is easy to see that σ is surjective and continuous and thus a topological endomorphism. Also one can generalize Σ_N^+ to the set $\Sigma_N = \left\{\mathbf{a} = (a_n)_{n\in\mathbb{Z}} : a_n \in \alpha \,\forall\, n \in \mathbb{Z}\right\}$ of doubly infinite sequences over the alphabet α with the corresponding metric, in which case we can also consider the right shift map, but we shall only be concerned with the left shift.

While the study of the dynamics of shift maps on general sequence spaces is interesting in of itself, we are interested in particular invariant subsets of Σ_N^+ :

2.15 Definition. *(Subshift of finite type) Assume that α, Σ_N^+ and σ are given as in the previous definition, and let $A \in \{0,1\}^{N\times N}$ be an $N \times N$-matrix with $A_{ij} \in \{0,1\}$ $\forall\, i,j \in \alpha$. Consider the subset $\Sigma_A^+ \subset \Sigma_N^+$ given by*

$$\Sigma_A^+ := \left\{\mathbf{a} \in \Sigma_N^+ : A_{a_n a_{n+1}} \neq 0 \,\forall\, n \in \mathbb{N}_0\right\} \ .$$

Clearly Σ_A^+ is invariant under σ and we call the pair $\left(\sigma, \Sigma_A^+\right)$ a subshift of finite type or topological Markov chain of Σ_N^+, and we call the matrix A the incidence matrix of $\left(\sigma, \Sigma_A^+\right)$.

The motivation to introduce such subshifts is that, unlike general maps, the computation of their topological entropy is straightforward, as we will see. An $N \times N$-matrix A is called irreducible if for every index $(i,j) \in \alpha \times \alpha$ there exists a power $k\,(i,j) \in N$ such that $\left(A^{k(i,j)}\right)_{ij} > 0$.

2.16 Theorem. *(Perron-Frobenius) Let A be an irreducible nonnegative real matrix. Then there is a unique simple, real, positive eigenvalue $\lambda_A \in R^+$ that has maximal absolute value. This λ_A is also called Perron-number and equals the spectral radius of A.*

For an irreducible incidence matrix A and the corresponding subshift $\left(\sigma, \Sigma_A^+\right)$ according to Definitions 2.14 and 2.15, we also call $\left(\sigma, \Sigma_A^+\right)$ an irreducible subshift. Now for the statement about the topological entropy of subshifts:

2.17 Theorem. *Let* $\left(\sigma, \Sigma_A^+\right)$ *be an irreducible subshift. Let* λ_A *be the Perron number of* A*. Then for the topological entropy of* σ *we have*

$$h(\sigma) = \log \lambda_A \ .$$

So for subshifts the entropy can be obtained easily by doing an eigenvalue analysis of the incidence matrix. We also get another intuitive idea of thinking about the entropy of a subshift of finite type: A fixed point $\mathbf{a}^*$ of $\left(\sigma, \Sigma_A^+\right)$ is a sequence where $a_n^* = a_{n+1}^* \, \forall \, n$. Correspondingly, a fixed point $\mathbf{a}^{**}$ of order $m > 1$ of $\left(\sigma, \Sigma_A^+\right)$ is a sequence where $a_n^{**} = a_{n+m}^{**} \forall \, n$.

2.18 Theorem. *Let* $N(\sigma, k)$ *denote the cardinality of the set of all fixed points of order* k *of the subshift* $\left(\sigma, \Sigma_A^+\right)$*. Then*

$$h(\sigma) = \limsup_{k \longrightarrow \infty} \frac{1}{k} \log N(\sigma, k) \ .$$

To put it differently, for a subshift $\left(\sigma, \Sigma_A^+\right)$ with positive topological entropy there exist fixed points of any order and their number grows exponentially with the order.

In light of Theorems 2.12 and 2.17 it is now clear how to find entropy estimates for complicated general maps: If possible, determine a subshift of finite type as a topological factor of the original map, and a lower bound of the original map's entropy can be obtained from the spectral radius analysis of the SFT's incidence matrix.

2.19 Definition. *(Symbolic dynamics) Let* X *be a compact metric space and let* $\Phi : X \longrightarrow X$ *be a topological endomorphism . We say that* Φ *exhibits symbolic dynamics if there are subsets* $\Lambda \subseteq X$ *such that* $\Phi|_\Lambda$ *has a subshift of finite type* $\left(\sigma, \Sigma_A^+\right)$ *as a topological factor.*

The question remains whether a given map exhibits symbolic dynamics, and how close the lower entropy bounds stemming from the SFT analysis are. The following surprising result due to Katok [26,33] confirms that this approach is indeed viable for typical maps of interest to us:

2.20 Theorem. *Let f be a C^r-diffeomorphism, $r \geq 2$, on a compact surface M. f has nonzero topological entropy if and only if it exhibits symbolic dynamics. Furthermore, $\forall\, \varepsilon > 0$ exists a subshift σ_ε such that*

$$h(\sigma_\varepsilon) > h(f) - \varepsilon.$$

2.5 Taylor Models

In this section we present the concept of Taylor Models (TM), which have first been introduced in the 1990s by Berz and Makino [44]. Taylor Model techniques were motivated from particle beam research, which has long successfully applied high-order multivariate polynomial manipulation to model transfer maps of particle optical elements in accelerators. This technique works exceptionally well because the equations of motion governing the dynamics of high-energy particle beams are usually only weakly nonlinear, and in practice the question of convergence of the power series expansions of the transfer maps is rarely a main focus.

Taylor's Theorem asserts that any sufficiently smooth real-valued function on $\mathbb{R}^v$ can be approximated by a Taylor polynomial of finite order n, where the truncation error term scales with the $(n+1)$st power in the displacement from the expansion point. If we wish to apply polynomial approximations of functional dependencies in a strongly nonlinear setting, of course the size of the error term becomes a central problem that one wishes to estimate. Taylor Models offer a framework in which self-contained bounds of the truncation error can be found in an automated fashion, thus yielding rigorous C^0-estimates and allowing Taylor Models to be used in verified algorithms and computer-assisted theorem proving.

2.21 Definition. *(Taylor Model) Let $D \subset \mathbb{R}^v$ be compact, let $G \subset \mathbb{R}^v$ be open such that $D \subset G$, and let $f : G \longrightarrow \mathbb{R}$ be a real-valued C^{n+1}-function. Assume a point $x_0 \in D$, and let $P : \mathbb{R}^v \longrightarrow \mathbb{R}$ be the Taylor polynomial of order n of f around the*

expansion point x_0. If there is a closed real interval $I \subset \mathbb{R}$ such that

$$f(x) - P(x - x_0) \in I \; \forall \, x \in D,$$

then the pair $T = (P, I)$ is called a Taylor Model (of order n) of f around x_0. For intuitive reasons we also write $T = (P, I) = P + I$.

In the situation of the previous definition, we also say that f is contained in T, or that T encloses f, or that T is an enclosure for f. The interval I is simply an interval bound of the truncation error $f - P$ over D. Naturally, in practice we wish I to be as narrow as possible, and we will see results about the scaling propety of I later on.

2.22 Remark. *Another way to think about Taylor Models is as a quotient space of $C^{n+1}(G, \mathbb{R})$. We call two functions $f, g \in C^{n+1}(G, \mathbb{R})$ equivalent if they both are contained in the same Taylor Model $T = (P, I)$. It is clear that this constitutes an equivalence relation between f and g and T is the equivalence class for all functions contained in it.*

Now that Taylor Models have been defined, the question is whether operations can be defined on these objects that are compatible with the arithmetic on the functions which are contained in the Taylor Models. For example, can we define an addition in such a way that the sum $T_1 + T_2$ of two TMs T_1 and T_2 is again a Taylor Model for the sum of any two functions contained in the original T_1 and T_2, respectively. In the following we assume the conventions

$$A + B := \{a + b : a \in A \wedge b \in B\},$$

$$A \cdot B := \{a \cdot b : a \in A \wedge b \in B\},$$

$$x + A := \{x + a : a \in A\},$$

$$x \cdot A := \{x \cdot a : a \in A\},$$

for two sets $A, B \subset \mathbb{R}$ and $x \in \mathbb{R}$:

2.23 Definition. *(TM-Addition and Multiplication) Let D, G and x_0 as in the previous definition. Consider two C^{n+1}-functions $f, g : G \longrightarrow \mathbb{R}$ and their respective n-th order Taylor Models $T_f = \left(P_f, I_f\right)$ and $T_g = \left(P_g, I_g\right)$ around x_0. We define*

1. *the addition*

$$T_f + T_g := \left(P_f + P_g, I_f + I_g\right),$$

2. *the scalar multiplication by $c \in \mathbb{R}$*

$$c \cdot T_f := \left(c \cdot P_f, c \cdot I_f\right),$$

3. *the multiplication*

$$T_f \cdot T_g := \left(\left(P_f \cdot P_g\right)_{\leq n}, I_{f \cdot g}\right),$$

where $\left(P_f \cdot P_g\right)_{\leq n}$ are all terms of the polynomial $P_f \cdot P_g = \left(P_f \cdot P_g\right)_{\leq n} + \left(P_f \cdot P_g\right)_{>n}$ of order at most n, and $\left(P_f \cdot P_g\right)_{>n}$ is the part of the polynomial $P_f \cdot P_g$ containing all terms of order $n+1$ through $2n$. The remainder interval is defined as

$$I_{f \cdot g} := B\left(\left(P_f \cdot P_g\right)_{>n}\right) + B\left(P_f\right) \cdot I_g + B\left(P_g\right) \cdot I_f + I_f \cdot I_g \ .$$

Here $B(P)$ denotes any interval range bound of a polynomial P over D, i.e. $B(P)$ is a closed real interval such that

$$P(x) \in B(P) \ \forall\, x \in D.$$

The generalization of Taylor Models and their arithmetic to higher dimensions is straightfoward by performing the function enclosure and operations from Definitions 2.21 and 2.23 componentwise.

Indeed, the definition of Taylor Model operations 2.23 is compatible with the corresponding operations on the contained functions:

2.24 Theorem. *Let D, G and x_0 as before, let $f, g : G \longrightarrow \mathbb{R}$ be C^{n+1}-functions contained in the n-th order TMs T_f and T_g. Then the functions $f + g$ and $f \cdot g$ are contained in the Taylor Models $T_f + T_g$ and $T_f \cdot T_g$ as defined in Def. 2.23.*

Proof. We show the statement for the multiplication, the proofs for the addition and scalar multiplication work analogously. Let $x \in D$, then $f(x) = P_f(x) + \delta_f(x)$ and $g(x) = P_g(x) + \delta_g(x)$, where $\delta_f(x) \in I_f$ and $\delta_g(x) \in I_g$.

Then

$$\begin{aligned}(f \cdot g)(x) = f(x) \cdot g(x) &= \Big(P_f(x) + \delta_f(x)\Big) \cdot \big(P_g(x) + \delta_g(x)\big) \\ &= P_f(x) \cdot P_g(x) + P_g(x) \cdot \delta_f(x) + P_f(x) \cdot \delta_g(x)\end{aligned}$$

where $\Big(P_f \cdot P_g\Big)$ is a polynomial which is the sum of two polynomials $\Big(P_f \cdot P_g\Big)_{\leq n}$ and $\Big(P_f \cdot P_g\Big)_{>n}$ that contain all terms of order up to and including n and terms of order $n+1$ to $2n$, respectively. Hence

$$\begin{aligned}(f \cdot g)(x) &= \Big(P_f \cdot P_g\Big)_{\leq n}(x) + \Big(P_f \cdot P_g\Big)_{>n}(x) + P_g(x) \cdot \delta_f(x) + P_f(x) \cdot \delta_g(x) \\ &= \Big(P_f \cdot P_g\Big)_{\leq n}(x) + \delta_{f \cdot g}(x)\end{aligned}$$

where

$$\delta_{f \cdot g}(x) \in B\left(\Big(P_f \cdot P_g\Big)_{>n}\right) + B\Big(P_f\Big) \cdot I_g + B\big(P_g\big) \cdot I_f + I_f \cdot I_g = I_{f \cdot g} \; \forall\, x \in D,$$

where again $B(P)$ denotes any interval range bound of a polynomial P over D. It follows that

$$(f \cdot g)(x) \in \Big(P_f \cdot P_g\Big)_{\leq n}(x) + I_{f \cdot g}.$$

□

Now that addition and multiplication of TMs have been introduced, the next question is if we can define elementary functions for TMs and their composition.

2.25 Remark. *(Elementary functions for TMs) We do not want to go into detail here regarding the definition of intrinsic functions for Taylor Models and refer to [41] for details. Instead, we will demonstrate the procedure using the exponential function as an example, and the definition of TM-analogs of other elementary functions follows in much the same spirit. The idea is to Taylor expand the elementary function (note that elementary functions are, on suitable domains, smooth) in the same way as the TM at which you want to evaluate the elementary function, and take care of the truncation error term again.*

Let $T = P_T + I_T$ be an n-th order real TM over the domain $D \subset \mathbb{R}^v$, and write $T = C_T + T_{\geq 1} = C_T + \left(P_{\geq 1} + I_T\right)$. Here C_T denotes the constant part of the TM, and $T_{\geq 1} := T - C_T$. Let $k \geq n$. Then

$$\begin{aligned}
\exp(T) &= \exp\left(C_T + T_{\geq 1}\right) = \exp(C_T) \cdot \exp\left(T_{\geq 1}\right) \\
&= \exp(C_T) \cdot \left(\sum_{m=0}^{n} \frac{\left(T_{\geq 1}\right)^m}{m!} + \sum_{m=n+1}^{k} \frac{\left(T_{\geq 1}\right)^m}{m!} + \frac{\left(T_{\geq 1}\right)^{k+1}}{(k+1)!} \exp\left(\theta \cdot T_{\geq 1}\right) \right), \qquad (2.2) \\
&\qquad \text{with } \theta \in [0,1], \\
&\subset P_{\exp(T)} + I_{\exp(T)}
\end{aligned}$$

We define $P_{\exp(T)}$ to be the polynomial part of order n of the right hand side of (2.2). For the interval remainder $I_{\exp(T)}$ observe the following:

All expressions in (2.2) can be evaluated with TM-operations as in (2.23) with the exception of the last summand in the parantheses, which can be estimated using interval arithmetic:

$$\frac{\left(T_{\geq 1}\right)^{k+1}}{(k+1)!} \exp\left(\theta \cdot T_{\geq 1}\right) \subset \frac{\left(B\left(P_{\geq 1}\right) + I_T\right)^{k+1}}{(k+1)!} \exp\left([0,1] \cdot \left(B\left(P_{\geq 1}\right) + I_T\right)\right),$$

where the last exponential can be bounded using the interval methods. The first sum in the parantheses in Def.2.2 produces both the polynomial part $P_{\exp(T)}$ of $\exp(T)$ as

well as contributions to the interval bound $I_{\exp(T)}$*, the second sum and error term only contribute to* $I_{\exp(T)}$*.*

2.26 Remark. *(Antiderivation) If a Taylor Model* $\left(P_f, I_f\right)$ *contains a function* f*, we want to be able to find the Taylor Model which contains the integral of* f*. This very useful operation on* $\left(P_f, I_f\right)$ *is called the antiderivation* ∂_i^{-1}*.*

Let $G \subset \mathbb{R}^v$ *open, let* $f : G \longrightarrow \mathbb{R}$ *be* C^{n+1}*, and let* $T_f = \left(P_f, I_f\right)$ *be an* n*-th order Taylor Model for* f *around the origin over the interval box* $[a_1, b_1] \times ... \times [a_v, b_v] \subset G \subset \mathbb{R}^v$*. Write* P_f *as the sum of two polynomials* $P_{f,n}$ *of exact order* n *and* $P_{f,<n} := P_f - P_{f,n}$ *of order up to and including* $n-1$*. Then define*

$$\partial_i^{-1}\left(T_f\right) := \left(P_{\partial_i^{-1}\left(T_f\right)}, I_{\partial_i^{-1}\left(T_f\right)}\right)$$

where

$$P_{\partial_i^{-1}\left(T_f\right)} := \int_0^{x_i^i} P_{<n}\left(x\prime\right) dx\prime_i$$

and

$$I_{\partial_i^{-1}\left(T_f\right)} := \left(B\left(P_{f,n}\right) + I_f\right) \cdot \left(b_i - a_i\right) \ .$$

It is easy to show that with these definitions

$$f \subset \left(P_f, I_f\right) \Longrightarrow \int f\, dx_i \subset \partial_i^{-1}\left(\left(P_f, I_f\right)\right) \ .$$

The great success of Taylor polynomial approximation has always been based on the high-order scaling of the error term with the, usually small, displacement from the expansion point. It is important to see that the Taylor Model operations introduced above maintain that beneficial scaling property for the TM remainder bounds:

2.27 Theorem. *(Taylor Model Scaling Theorem) Let* $G \subset \mathbb{R}^v$ *open,* $x_0 \in G$*, and* $h > 0$ *such that* $x_0 + [-h, h]^v \subset G$*. Let* $f, g : G \longrightarrow \mathbb{R}$ *be* C^{n+1}*-functions contained in the* n*-th order TMs* $T_f = P_f + I_f$ *and* $T_g = P_g + I_g$ *around* x_0 *over the domain* $x_0 + [-h, h]^v$ *with scaling properties* $I_f = \mathcal{O}\left(h^{n+1}\right)$ *and* $I_g = \mathcal{O}\left(h^{n+1}\right)$*. Let*

$\left(P_{f+g}, I_{f+g}\right)$ *and* $\left(P_{f\cdot g}, I_{f\cdot g}\right)$ *be the addition and multiplication TMs of* T_f *and* T_g *according to Definition 2.23, and let* $\left(P_{s(f)}, I_{s(f)}\right)$ *be a TM for any intrinsic function* s *defined for Taylor Models in the fashion of remark (2.25). Then*

$$I_{f+g} = \mathcal{O}\left(h^{n+1}\right),$$
$$I_{f\cdot g} = \mathcal{O}\left(h^{n+1}\right),$$
$$I_{s(f)} = \mathcal{O}\left(h^{n+1}\right).$$

The essential property of all Taylor Model operations is of course that they are compatible with the corresponding operations on the functions contained.

2.28 Theorem. *(Fundamental Theorem of Taylor Model Arithmetic) Let* $G_f \subset \mathbb{R}^v$ *open and let the* C^{n+1}*-function* $f : \mathbb{R}^v \longrightarrow \mathbb{R}^v$ *be contained in the* v*-dimensional* n*-th order TM* $T_f = \left(P_f, I_f\right)$ *over the compact domain* $D_f \subset G_f$ *. Likewise, let* $G_g \subset \mathbb{R}^v$ *open, let* $D_g \subset \mathbb{R}^v$ *be compact such that the range bound* $B\left(\left(P_f, I_f\right)\right) \subset D_g$*, and let the* C^{n+1}*-function* $g : \mathbb{R}^v \longrightarrow \mathbb{R}$ *be given as a finite code list of binary operations and elementary functions. Now let* $T_{g\circ f} = \left(P_{g\circ f}, I_{g\circ f}\right)$ *be the* n*-th order TM obtained by executing the code list of* g *in TM arithmetic starting with the TM* T_f*.*

Then we have that

$$g \circ f \subset T_{g\circ f}$$

and if I_f *has the* $n+1$*st order scaling property as in Theorem 2.27, then so does* $I_{g\circ f}$*.*

Proof. The proof follows immediately by induction over the finite code list of g using Theorems 2.24 and 2.27. □

2.5.1 Applications of Taylor Models

In the introduction to this section it has already been hinted at that Taylor Models are suitable objects to construct a self-verified computing framework. Essentially,

Taylor Models can be used in the same spirit as interval arithmetic, but the most fundamental drawbacks of intervals are alleviated significantly by the use of Taylor Models:

1. the dependency problem can not occur in Taylor Model problems by design, as the multiple occurence of identical monomials in the code list for a function is immediately accounted for in the Taylor polynomial of said function.

2. wrapping effect: the cause for the overestimation of an interval enclosure of a set is the nonlinear distortion of said set, the bulk of which is represented by the high-order polynomial part of the Taylor Model.

3. dimensionality curse: if over a certain domain a function is to be enclosed up to a fineness $0 < \delta < 1$ by a set of interval boxes $\{Ij\}_{j=1}^{N}$ of maximal width δ, then the number of boxes required scales as

$$N \backsim \left(\frac{1}{\delta}\right)^{v}$$

with the dimensionality v of the problem.

In contrast, a Taylor Model enclosure of the function up to the same accuracy can often be achieved with a single Taylor Model. The amount of memory storage a Taylor Model of a given expansion order N and dimensionality v requires is mostly given by the number of monomial coefficients it needs to store. The maximal number of polynomial coefficients $M\left(N, v\right)$ is for a polynomial of order N and dimensionality v is

$$M\left(N, v\right) = \frac{(N+v)!}{N!v!},$$

which grows much slower with v than the exponential growth of the numbers of boxes.

Of course, the interval problems still persist in principle in the manipulation of the remainder bounds of the Taylor Models, but the remainder bounds are usually so small that even the overestimation effects do not come significantly into play.

We next list two applications for which Taylor Models have proven to be very successful, and which are required for some of the algorithms later in this work.

Taylor Model Verified Flows for ODEs

We consider the standard autonomous intial value problem

$$\begin{aligned} \dot{x} &= f(x), \\ x(0) &= x_0, \end{aligned} \tag{2.3}$$

where $f : \mathbb{R}^v \longrightarrow \mathbb{R}^v$ is a function, at least C^1, given as a finite code list of binary operations and intrinsic functions available in Taylor Model arithmetic (in particular, f is locally Lipschitz and uniqueness and existence of solutions to (2.3) are guaranteed).

The Picard-Lindelöf Theorem shows that the Picard iteration

$$\begin{aligned} \varphi_0 &:= x_0, \\ \varphi_{n+1}(t) &:= x_0 + \int_0^t f(\varphi_n(s))\, ds \end{aligned}$$

converges uniformly to the flow $\varphi(x,t)$ of the IVP. Based on Schauder's Fixed Point Theorem, we can design an algorithm to compute verified Taylor Model representations of the flow which is in the same spirit:

2.29 Theorem. *(Schauder) Let X be a topological vector space and $\mathcal{O} : X \longrightarrow X$ a continuous map. Let Y be a compact convex subset of X such that $\mathcal{O}(Y) \subset Y$. Then there exists a fixed point of $\mathcal{O}$ in Y.*

2.30 Algorithm. *(Taylor Model flows) Let $N \in \mathbb{N}$ be a fixed computation order. The total integration time is set to $T > 0$. Set the midpoint of the initial condition box to $X_0 \in \mathbb{R}^v$ and let $x \in [-d, d]^v$ for $d > 0$.*

1. *The first time step: Let the polynomial $P_0 := X_0 + x$ and the TM $\varphi_0 := P_0 + [0, 0]$. Let δt_1 be the integration step size for the first step.*

   (a) *The polynomial part P_0 is stored in a DA-vector, and define the DA-vector Picard operator*

   $$\Pi_{DA}(.) := P_0 + \partial_t^{-1} f(.)$$

   (refer to Appendix B for details on the antiderivation operation) and iteratively compute

   $$P_{n+1}(x, t) := \Pi_{DA}(P_n(x, t)).$$

   After N steps, a polynomial P_N invariant up to order N is obtained, i.e. $P_N =_N P_{N+1} = \Pi_{DA}(P_N)$.

   (b) *Define the Picard operator for Taylor Models*

   $$\Pi_{TM}(.) := P_0 + \partial_t^{-1} f(.)$$

   where now ∂_t^{-1} denotes the antiderivation in TM-arithmetic as per remark (2.26). Heuristically, find an interval remainder bound I_τ such that for the Taylor Model

   $$\tau(x, t) := P_N(x, t) + I_\tau$$

   we have

   $$P_N + \tilde{I} := \Pi_{TM}(\tau) \subset \tau, \tag{2.4}$$

   i.e. that

   $$\tilde{I} \subset I_\tau.$$

If this is the case, then the Schauder Theorem asserts that there exists a fixed point $\tau^\star$ such that

$$\tau^\star = \left(P^\star, I^\star\right) = \Pi_{TM}\left(\tau^\star\right),$$

and $\tau^\star$ can be reached through successive iteration of Π_{TM}.

(c) Iterate $\Pi_{TM}^k\left(\tau^\star\right)$ until $I^\star$ is sufficiently refined.

(d) Insert the timestep δt_1 into $\tau^\star$ and obtain the flow

$$\varphi_1(x) := P_{\varphi_1}(x) + I_{\varphi_1} = \tau^\star(x, \delta t_1).$$

2. *For the $(n+1)$st timestep, suppose the flow $\varphi_n(x) = P_{\varphi_n}(x) + I_{\varphi_n}$ has been computed in inetgration step n, and the step size for the $(n+1)$st step is δt_{n+1}. Then set the initial condition to $\varphi_n(x)$ and repeat from step 1.*

3. *Terminate the algorithm after K_T steps when $\sum_{k=1}^{K_T} \delta t_k = T$.*

It can now be shown [41] that $\varphi_{K_T}(x)$ indeed yields a rigorous TM-enclosure of the flow $\varphi(X_0 + x, T)$ for all initial conditions in $X_0 + [-d, d]^v$.

As a remark, the heuristics in step 1b) of the previous algorithm are educated. Since the bulk of I_τ that satisfies the inclusion (2.4) will be given by the truncation error, we simply set the initial test interval I_τ as the polynomial part of the Taylor Model

$$\Pi_{TM}\left(P_N + [0,0]^v\right).$$

The simple Algorithm 2.30 forms the basis for more sophisticated approaches using preconditioning and remainder bound manipulation techniques which offer superior control of remainder interval blow-up [7, 46, 47]. Taylor Model integrators of this type have been successfully applied to Astro- and Beam Physics problems [30, 43], and extensions of the theory allow rigorous enclosure of solutions of implicitly given ODEs or differential algebraic equations [28, 29].

Global Optimization

The global optimization problem, in its simplest form without constraints etc., can be phrased as follows:

Let $D \subset \mathbb{R}^v$, $D = [a_1, b_1] \times ... \times [a_v, b_v]$, be an interval box and let $f : D \longrightarrow \mathbb{R}$ be continuous. Find the global infimum of the function f over the domain D. Note that here D is compact, so the infimum of the range is actually assumed in D,

$$\inf_{x \in D} f(x) = \min_{x \in D} f(x).$$

Unlike gradient-based methods, which are fast but tend to fall into local minima, a global optimizer is able to find the absolute minimal value of $f(D)$ or at least a sharp upper bound for it through e.g. a Branch and Bound algorithm [34]:

2.31 Algorithm. *(Branch and Bound) Let $D \subset \mathbb{R}^v$ and f be as above. Then we can inductively define a procedure to find rigorous upper bounds for the minimum* $\min_{x \in D} f(x)$*:*

1. *Let the midpoint $m \in D$, $m_i = b_i - a_i \; \forall \, 1 \leq i \leq v$ and set the minimum upper bound $S := f(m)$.*

2. *In the first step: subdivide $B_0 := D$ along the coordinate axis of greatest width and obtain $B_{1,1}$ and $B_{1,2}$ such that $B_0 \subset B_{1,1} \cup B_{1,2}$, and the interiors $\mathring{B}_{1,1} \cap \mathring{B}_{1,2} = \emptyset$. Set $\mathcal{B}_1 := \left\{ B_{1,1}, B_{1,2} \right\}$.*

3. *In the k-th step, assume you have a collection of N_k boxes $\mathcal{B}_k = \left\{ B_{k,1}, ..., B_{k,N_k} \right\}$, $B_{k,j} \subset D \, \forall \, 1 \leq j \leq N_k$.*

   (a) *j=1: if $\max f\left(B_{k,1}\right) < S$, reset $S := \max f\left(B_{k,1}\right)$. Discard all boxes $B_{k,j} \subset \mathcal{B}_k$ which satisfy $\min\left(B_{k,j}\right) > S$. Else bisect $B_{k,1}$ along the coordinate axis of greatest width into two interval boxes $B_{k+1,1}$ and $B_{k+1,2}$ such that $B_{k,1} \subset B_{k+1,1} \cup B_{k+1,2}$ and the interiors $\mathring{B}_{k+1,1} \cap \mathring{B}_{k+1,1} = \emptyset$.*

(b) *for* $1 < j \leq N_k$*: assume that so far* $B_{k+1,1}, ..., B_{k+1,l}$ *have been created. If* $\max f\left(B_{k,j}\right) < S$*, reset* $S := \max f\left(B_{k,j}\right)$*. Discard all boxes* $B_{k,j} \subset \mathcal{B}_k$ *which satisfy* $\min\left(B_{k,j}\right) > S$*. Else bisect* $B_{k,j}$ *along the coordinate axis of greatest width into two interval boxes* $B_{k+1,l+1}$ *and* $B_{k+1,l+2}$ *such that* $B_{k,j} \subset \left(B_{k+1,l+1} \cup B_{k+1,l+2}\right)$*, and* $\mathring{B}_{k+1,l+1} \cap \mathring{B}_{k+1,l+2} = \emptyset$*.*

4. *Set* $\mathcal{B}_{k+1} = \left\{B_{k+1,1}, ..., B_{k+1,N_{k+1}}\right\}$*,* $B_{k+1,j} \subset D \, \forall \, 1 \leq j \leq N_{k+1}$ *and repeat from point (3) until either* S *is less than a prespecified threshold* $M_S > 0$*, or the volume of* $\bigcup_{j=1}^{N_{k+1}} B_{k+1,j}$ *is less than a threshold* $M_V > 0$*.*

This algorithm is straightfoward, and it is clear that it yields ever sharper interval enclosures of both the minimum $\min\limits_{x \in D} f(x)$ and the points in X where that mininum is assumed. It can also be fully verified by using interval based methods to find the range bound estimates for f over a specific box $B_{k,j}$, and numerous other approaches to implement interval-based global optimization routines have been investigated [13, 24, 25, 32, 60]. The practical issues with this algorithms are the slow convergence rate and the possibly large memory requirement for box storage, since the discarding process is slowed down by overestimation in function range bounding. For both problems, it is thus paramount to find methods that minimize overestimation in order to find sharp updates to S that allow us to quickly discard boxes.

This is a strength of Taylor Models, where in step 3 of the above algorithm we can find sharp Taylor Model enclosures for the range of the objective function f over the box $B_{k,j}$ expanded around the midpoint by simply evaluating the code list of f. Once this step is performed, sophisticated range bounding procedures for Taylor Models exist [45] which allow range bounding with minimal overestimation.

Additional benefits of the Taylor Model approach is that (nonverified, but highly accurate) information about the gradient of the f is immediately available and can guide more informed box splitting and selection procedures than the purely chrono-

logical ordering of new boxes as in algorithm (2.31), potentially accelerating the discarding process substantially.

2.5.2 Implementation of Taylor Models

Taylor Models and their arithmetic have been implemented as a data type in the programming language COSY Infinity [1, 15], which has been used to perform all computations found in later chapters.

COSY Infinity was conceived as a beam physics code designed for particle optical simulations, incorporating arbitrary order polynomial manipulation for the accurate approximation of Poincaré transfer maps of the beam line elements [14]. The efficient framework for polynomial arithmetic rests on the ideas of DA-vectors presented in Appendix B.

It is thus a natural progression to implement Taylor Models as an extension of this framework, such that the polynomial portion of a Taylor Model operation is performed within the DA-vector picture, and the remainder bound portion of the Taylor Model operation is executed in interval arithmetic (see Appendix A) for the rigorous estimation of truncation errors.

In practice, this implementation step is nontrivial, since so far in the definition of Taylor Models and their operations we have assumed exact arithmetic. However, on the computer we have to make a transition to floating point arithmetic, and it is not immediately clear how the rigorous enclosure properties of Theorems 2.24 and 2.28 translate into the floating point environment. In other words, suppose the C^r-function $f : [-1, 1] \longrightarrow \mathbb{R}$ is contained in the n-th order Taylor Model $T = (P, I)$, where $r \geq n$, i.e. the enclosure property

$$f(x) \in P(x) + I \,\forall\, x \in [-1, 1]$$

holds. Does then the floating point implementation $\tilde{T} = \left(\tilde{P}, \tilde{I}\right)$ of T satisfy the same

enclosure property

$$f(x) \in \tilde{P}(x) + \tilde{I} \,\forall\, x \in [-1, 1] \tag{2.5}$$

in exact arithmetic? It has been shown in [61] that the Taylor Model implementation in COSY Infinity indeed satisfies (2.5). An in-depth discussion of this issue is beyond the scope of this work, but in essence the verification in the floating point picture relies on outward rounding in the interval arithmetic and the absorption of a pessimistic floating point error into the remainder bound interval in every operation.

Furthermore, for computational efficiency COSY supports sparsity procedures in the polynomial operations and only keeps monomials with coefficients above a cutoff threshold comparable to the floating point accuracy. Monomial terms below this size are discarded and absorbed into the remainder bound, as well.

It is worth stressing that the Taylor Model data type in COSY Infinity, and in particular its polynomial part, only contains floating point information. This means e.g. that a Picard iteration as in Algorithm 2.30, which in exact arithmetic leaves the polynomial expansion invariant in every step except for the highest order, also will leave the floating point polynomial invariant up to the highest order when performed in floating point arithmetic.

CHAPTER 3

Verified Enclosure of Poincaré Maps

Poincaré maps [58] are a standard tool in general dynamical systems theory to study qualitative properties of continuous dynamical systems (e.g. the flow generated by an ordinary differential equation), most prominently the asymptotic stability of periodic or almost periodic orbits (see e.g. [23] [2] [62]). A Poincaré map essentially describes how points on a plane S (the Poincaré section) which is transversed by such an orbit $\mathcal{O}$ (the reference orbit) and which are sufficiently close to $\mathcal{O}$ get mapped back onto S by the flow. The two key benefits in this approach are that long-term behaviour of the the flow close to $\mathcal{O}$ can be analyzed through the derivative of the Poincaré map at the intersection point of S and $\mathcal{O}$, which is available after just one revolution of $\mathcal{O}$, and that the dimensionality of the problem has been reduced by one, since the Poincaré map is defined on S and neglects the "trivial" direction of the flow purpendicular to the surface.

We will actually consider a somewhat generalized notion of Poincaré maps, by dropping the restriction that the flow exhibit a periodic reference orbit. Assuming we are given a smooth surface in phase space, the Poincaré section S, and an initial

condition X_0 for the flow such that the orbit originating at X_0 actually transverses the section S at some crossing time T_0, then by a Poincaré map we understand a map that projects all flows originating in a neighborhood of X_0 directly to the section S.

Seeing that the Poincaré map itself is given implicitly, it seems like a logical progression to tackle the problem of computing Poincaré maps in the Differential Algebraic (DA) framework of polynomial approximations (see Appendix B), since under quite general assumptions high-order polynomial approxiations to inverse or implicitly given functions are available in an automated fashion.

Finding rigorous Taylor Model enclosures for the Poincaré map is *a priori* challenging, since the issue of verified functional inversion is very subtle. Here however, we can use the vector field of the differential equations as an additional tool to estimate trunctation errors, which leads to quite natural geometric condtions, which can be checked

The key question that will be discussed is how to project a domain box exactly to a given surface under the action of the flow. In the above setting, where a reference orbit starting at the initial condition X_0 transverses a surface S at time T_0, then for all points x in a sufficiently small region containing X_0 a unique crossing time for the surface also exists, and can be represented as a Taylor expansion in terms of small variations $(X_0 - x_0)$ around the reference crossing time T_0. We will present a method to obtain nonverified and verified polynomial representations of this crossing time and the subsequent construction of a Poincaré map.

3.1 The nonverified method

Consider a system

$$\begin{aligned} \dot{x}(t) &= f(x(t), t), \\ x(0) &= X_0 + x_0, \end{aligned} \tag{3.1}$$

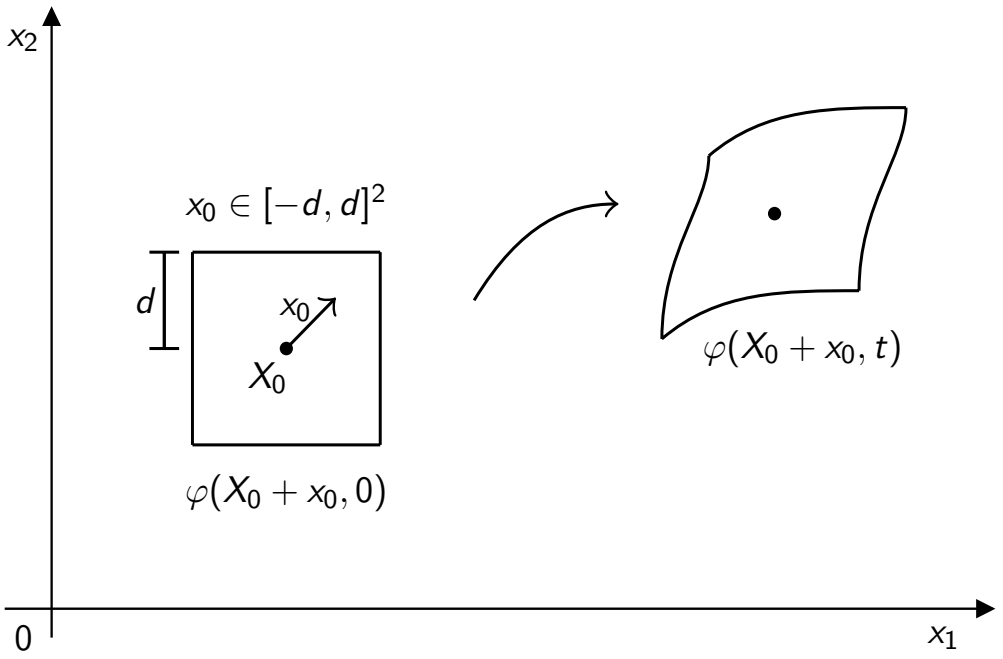

Figure 3.1. Forward propagation of the box $X_0 + [-d, d]^2$ from time 0 to time t using the DA-integration method.

where $f : \mathbb{R}^\nu \supset U^{open} \longrightarrow \mathbb{R}^\nu$, $\nu \in \mathbb{N}$, is a finite code list of binary operations and intrinsic functions available for DA-vectors. Suppose we are given a surface S which is transversed by the reference orbit (where $x_0 = 0$) at a crossing time T_0. This crossing time needs to be known to high accuracy (however, a non-verified result for T_0 is sufficient) and we assume that it is known. Typically the computation of T_0 can be formed as a scalar constraint satisfaction problem and can be determined using a high-order Runge-Kutta integrator.

We assume that a DA-integration as in Appendix B of the domain box $X_0 + D$, where $D := [-d_1, d_1] \times ... \times [-d_\nu, d_\nu]$, has been performed until the time T_0 (cf. Figure 3.1). In the last integration step, the time dependence has been retained, and we have a polynomial expansion $\varphi(x_0, t)$ of the flow.

We want to consider as large a class of surfaces as Poincaré sections as possible. A suitable assumption is that locally around the point $\varphi(0, T_0)$ the Poincaré section

$S \subset \mathbb{R}$ is given implicitly in terms of a function $\sigma : \mathbb{R}^\nu \longrightarrow \mathbb{R}$ as

$$S := \{x \in \mathbb{R}^\nu : \sigma(x) = 0\}.$$

Since the function σ also needs to be expressed in terms of binary opertions and elementary functions available in the computer environment for DA-arithmetic, it is necessarily smooth, and hence also the surface S. This contains most surfaces which are of practical interest, in particular the most common case where S is an affine plane of the form $S := \{x \in \mathbb{R}^\nu : x_1 = c\}$ where the first component x_1 of the vector x is set to the fixed value $c \in \mathbb{R}$; here $\sigma(x) = x_1 - c$.

The other condition which needs to be met by S is that the flow is transverse to it for all possible initial conditions $x_0 \in D$, i.e. that

$$0 \neq \langle \nabla\sigma(\varphi(x_0, t)), f(\varphi(x_0, t), t)\rangle \forall x_0 \in D.$$

Without this assumption a Poincaré map cannot be defined meaningfully, since for its definition the existence of a uniquely defined crossing time for each initial condition is required. However, for our method this question can be neglected. In the 'pathological' case that the vectorfield is in the tangent space of the surface at any point, the functional inversion step described in the following will fail.

The interesting question is how the object $\{\varphi(x_0, t) : x_0 \in D\}$ can be projected to S by insertion of a suitable crossing time. For every possible initial condition, we wish to derive an expression of the crossing time $t_c(x_0)$ at which the trajectory originating at the said initial value traverses the section S, and then reinsert this time $t_c(x_0)$ back into the DA vector $\varphi(x_0, t)$ describing the flow. This yields a polynomial $\varphi(x_0, t_c(x_0))$ only depending on the initial conditions x_0 which projects these values almost exactly onto the Poincaré section, up to accuracy restrictions depending on the approximation order. The information about this crossing time is contained in the flow and the geometry of S in an implicit way, hence we need to use suitable tools for functional inversion in the DA context as has been described above. The

function $\varphi(x_0, t)$ as such cannot be invertible, since the dimensionality of its domain and range do not even agree. Instead, we will introduce an auxiliary function ψ which is substantially easier to handle and yields all relevant results. For $\psi(x, t)$ to be invertible in the first place we need ψ to map into $\mathbb{R}^{\nu+1}$.

This motivates the following construction: Define a function $\psi : \mathbb{R}^{\nu+1} \longrightarrow \mathbb{R}^{\nu+1}$ by

$$\begin{aligned} \psi_k(x_0, t) &:= x_{0,k} \forall k \in \{1, ..., \nu\} \\ \psi_{\nu+1}(x_0, t) &:= \sigma(\varphi(x_0, t)) \end{aligned} \tag{3.2}$$

where the indices k denote components of the respective vectors. To get an idea how the construction of ψ comes about, we remark that a functional inversion step is expected because of the implicit occurrence of the $t_c(x_0)$ in the problem, and hence ψ needs to map between spaces of equal dimension. Furthermore $t_c(x_0)$ depends on the variables x_0 and is determined by the constraint condition

$$\sigma(\varphi(x_0, t_c(x_0))) = 0. \tag{3.3}$$

Because of the last statement $t_c(x_0)$ satisfies

$$\psi(x_0, t_c(x_0)) = (x_0, 0)$$

and assuming that ψ is invertible we can evaluate

$$\psi^{-1}(x_0, 0) = \psi^{-1}(\psi(x_0, t_c(x_0))) = (x_0, t_c(x_0))^T$$

and immediately extract the DA-vector representation of $t_c(x_0)$ in terms of the x_0 in the last component. In this case the invertibility of ψ at the point $(x_0, t_c(x_0))$ is actually guaranteed by the condition of transversality. This proves the next statement:

3.1 Theorem. *Suppose for the system (3.1) and a surface S given by a smooth function $\sigma : \mathbb{R}^\nu \longrightarrow \mathbb{R}$ as $S := \{x \in \mathbb{R}^\nu : \sigma(x) = 0\}$, the crossing time T_0 of*

the reference orbit is known. Assume that (3.1) has been integrated until T_0 *and let* $\varphi(x_0, t)$ *be the local flow. Then the function* ψ *defined as in (3.2) is invertible, and the function*

$$t_c(x_0) := \psi_{\nu+1}^{-1}(x_0, 0) \tag{3.4}$$

projects the flow directly onto the surface S*, i.e.* $\varphi(x_0, t_c(x_0))$ *satisfies (3.3) for all* $x_0 \in D$*.*

Performing the inversion of ψ *to* ψ^{-1} *as in section (2.3) and the evaluation (3.4) in DA-arithmetic yields a DA-vector that contains the Taylor expansion coefficients of* $t_c(x_0)$ *up to the desired order.*

Now the DA-vector representation of the Poincaré map $\mathcal{P}(x_0)$ is simply constructed by inserting $t_c(x_0)$ into the flow:

$$\mathcal{P}(x_0) := \varphi(x_0, t_c(x_0)).$$

In figure 2 it is illustrated how $\mathcal{P}(x_0)$ projects the original transported box $\{\varphi(x_0, t) : x_0 \in D\}$ almost exactly onto the surface S.

3.1.1 Summary of the nonverified algorithm

1. For the system (3.1) and a given surface S, find the crossing time T_0 of the reference orbit, i.e. $\varphi(X_0, T_0) \in S$

2. Integrate (3.1) until the time T_0, perform one extra integration step in which the time dependence is preserved. This yields a time-dependent flow $\varphi(x_0, t)$.

3. Expand the parametrization $\sigma(x)$ of S around the point $\varphi(0, T_0)$

4. Set up and invert the auxiliary function ψ using DA functional inversion to obtain a DA-vector represenation of ψ^{-1}.

5. Evaluate $t_c(x_0) := \psi^{-1}(x_0, 0)$.

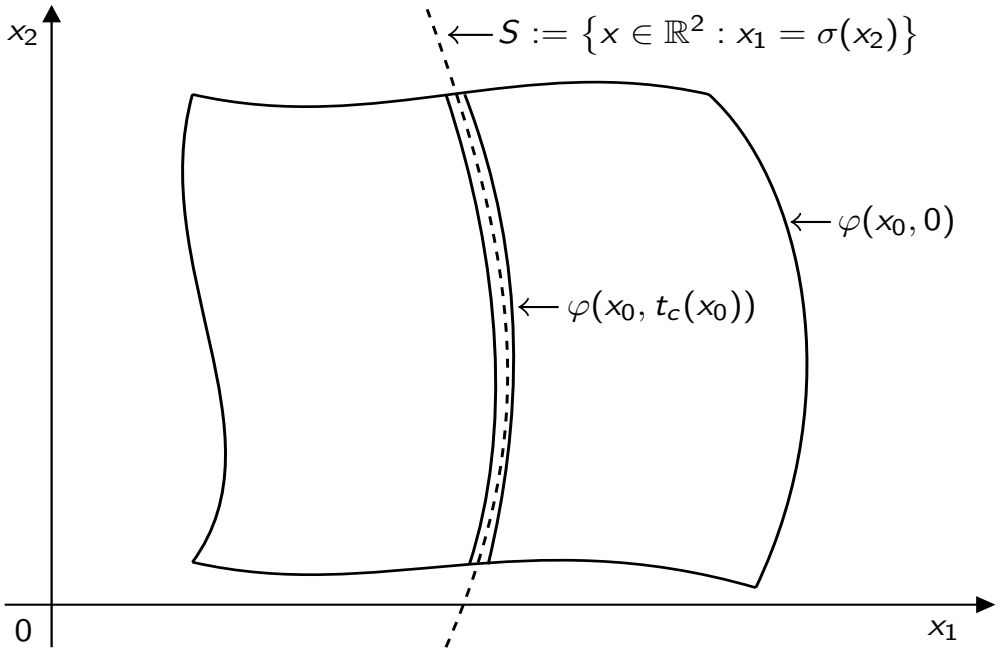

Figure 3.2. Projection of $\{\varphi(x_0, t) : x_o \in D\}$ onto the surface S by insertion of the crossing time $t_c(x_0)$.

6. Evaluate $\mathcal{P}(x_0) := \varphi(x_0, t_c(x_0))$.

3.2 Verification

In the same way that Taylor Models offer a somewhat natural extension to DA-methods to a verified setting, one can ask whether it is possible to modify the previously described algorithm to obtain verified interval bounds for the truncation error of the polynomial representation of both the crossing time $t_c(x_0)$ as well as the Poincaré map $\mathcal{P}(x_0)$ itself. We will see that indeed this is possible. Again the objective will be to compute a TM for the crossing time to be inserted into the TM for the local flow in order to construct a TM-representation of the Poincaré map.

3.2.1 Specification of the surface parameterization

We now assume that for a given reference initial condition X_0 the crossing time T_0 at a surface S is well-known. Let S be parametrized as

$$S := \{x \in \mathbb{R}^v : x_1 = g(x_2, ..., x_v)\}; \tag{3.5}$$

comparing this to section 3.2, we see that in this case $\sigma(x) = x_1 - g(x_2, ..., x_v)$. For simplicity we will write $x_1 = g(x)$, but indeed g does not have any x_1-dependence; the x_1-component of a point x on S is uniquely specified by its last $v-1$ components. We demand that $g : \mathbb{R}^v \longrightarrow \mathbb{R}$ is a function comprised of a finite code list of binary operations and instrinsic functions which are available in Taylor Model arithmetic, which entails smoothness for g and hence also for S just like in section 3.1 . We will denote the TM-representation of g also by $g(x) + I_g$, it should be clear from the context whether the parametrization g or the DA-part of its Taylor Model is meant.

3.2.2 Interval enclosure of feasible crossing times

Assume that a TM-based verified integration of the system (3.1) has been performed until the time T_0, and the final coordinates are given by a TM-flow of the form $\varphi(x_0, T_0) + I_\varphi$. This means that the trajectory $\varphi(0, T_0)$ originating at the midpoint X_0 exactly coincides with the surface S, i.e. $\varphi_1(0, T_0) = g(\varphi(0, T_0))$. Also note that there is no time-dependence in $\varphi(x_0, T_0) + I_\varphi$ anymore after the time T_0 has been inserted into the flow.

Just like in the nonverified method, we need an extra integration step in which we keep the full local time dependence in the flow $\varphi(x_0, t)$. This is obtained by the same verified TM-integration procedure with initial conditions $x(0) = (\varphi(x_0, T_0) + I_\varphi)$, except the insertion of the time step is not carried out.

However, the time domain of the extra interation step explicitly enters the calculation of the remainder bound. So it is mandatory to get a good guess about a time

interval $[-\tilde{t}, \tilde{t}]$, where $\tilde{t} > 0$, such that all true crossing times $t_c^\star(x_0)$ of all trajectories originating in the box $X_0 + D$ are contained in the time interval $T_0 + [-\tilde{t}, \tilde{t}]$.

To obtain this estimate, we first take the DA-part $\varphi(x_0, T_0)$ of the verified solution at time T_0 and use it as the initial condition for one extra nonverified integration step in DA-arithmetic (as in section 2.1). This yields a DA-representation of the local time-dependent flow, which we can use, together with the DA-part $g(x)$ of the surface parametrization, to compute a polynomial of the local crossing time $t_c(x_0)$ as described in the previous section. This polynomial, albeit not verified, already represents the functional dependency of the true crossing time $t_c^\star(x_0)$ on x_0 to a high degree, and so a range bound of $t_c(x_0)$ over all $x_0 \in D$ will yield an interval enclosure $[t_l, t_u]$, with $t_l < 0 < t_u$, which is a very good estimate of the range of $t_c^\star(x_0)$ around T_0 . Inflating the interval bounds (say by p per cent, where p is typically around 10 to 20) and taking the bigger modulus, we see by setting

$$\tilde{t} := (1 + \frac{p}{100}) \cdot \max\{|t_l|, t_u\} \tag{3.6}$$

that the time interval $T_0 + [-\tilde{t}, \tilde{t}]$ has very good chances to satisfy the crossing time enclosure stated above. We can actually verify that $T_0 + [-\tilde{t}, \tilde{t}]$ constitutes a rigorous interval bound of $t_c^\star(x_0) \,\forall\, x_0 \in D$ by a somewhat involved but straightforward argument that $g(\varphi(x_0, T_0 - \tilde{t})) < 0 \,\forall\, x_0 \in D$ and $g(\varphi(x_0, T_0 + \tilde{t})) > 0 \,\forall\, x_0 \in D$ or vice versa.

3.2.3 TM-enclosure of the Poincaré map

Now we are able to integrate the system

$$\begin{aligned} \dot{x}(t) &= f(x(t), t), \\ x(0) &= \varphi(x_0, T_0) + I_\varphi \end{aligned} \tag{3.7}$$

in TM-arithmetic as in section 2.5.1 with full local time dependence of the time domain $[-\tilde{t}, \tilde{t}]$. Again, for simplicity we will just call the resulting flow $\varphi(x_0, t) + I_\varphi$,

though the interval bound I_φ has changed.

Observe that the set $B := \{\varphi(x_0,t) + I_\varphi : (x_0,t) \in D \times [-\tilde{t},\tilde{t}]\}$ contains all trajectories satisfying (3.7) over the time interval $[-\tilde{t},\tilde{t}]$. Thus we are able to obtain an interval bound I_g for the TM of g by expanding g in TM-arithmetic over a $\tilde{B}$, where $\tilde{B}$ is an interval vector which contains B. $\tilde{B}$ can be obtained, e.g. by range bounding $\varphi(x_0,t)+I_\varphi$ over all $(x_0,t) \in D \times [-\tilde{t},\tilde{t}]$. Note that in typical applications the curvature scale of the surface S is several orders of magnitude bigger than the scale of the transported box B (or $\tilde{B}$ respectively), and hence the range of g over $\tilde{B}$ is very small, typically smaller than the remainder bounds I_φ. In fact, in the case where g is a polynomial of order less than or equal to the computation order in the TM-arithmetic, g will have a zero remainder bound, up to small floating point errors.

We proceed by first obtaining the polynomial part of the TM-representation of the crossing time, $t_c(x_0)$. We extract the polynomial $\varphi(x_0,t)$ from the TM-solution of the local flow, and use the DA-part $g(x)$ of the parameterization of S to compute a nonverified DA-representation for the polynomial part $t_c(x_0)$ of the crossing time exactly as described in section 3.1 .

We are allowed to insert any Taylor Model with a range in $T_0+[-\tilde{t},\tilde{t}]$ into the time dependence of the flow-TM $\varphi(x_0,t)+I_\varphi$ in an attempt to project the flow onto the surface S. In particular, we are allowed to insert our best educated guess for a TM which approximates the true crossing time $t_c^\star(x_0)$, namely the DA-approximation $t_c(x_0)$ outfitted with a zero remainder bound. Note that the TM $t_c(x_0) + [0,0]$ approximates $t_c^\star(x_0)$, but does not necessarily *contain* $t_c^\star(x_0)$ for all $x_0 \in D$, or any $x_0 \in D$ for that matter. We will actually be able to find a rigorous interval bound for $t_c^\star(x_0)$ later.

Insertion of $t_c(x_0)+[0,0]$ into $\varphi(x_0,t)+I_\varphi$ yields a Taylor Model which describes a curvilinear rectangle that 'hugs' the surface S narrowly, i.e. the displacement of the set $\varphi(x_0, t_c(x_0)+[0,0])+I_\varphi$ in the transverse x_1-direction from the surface is almost

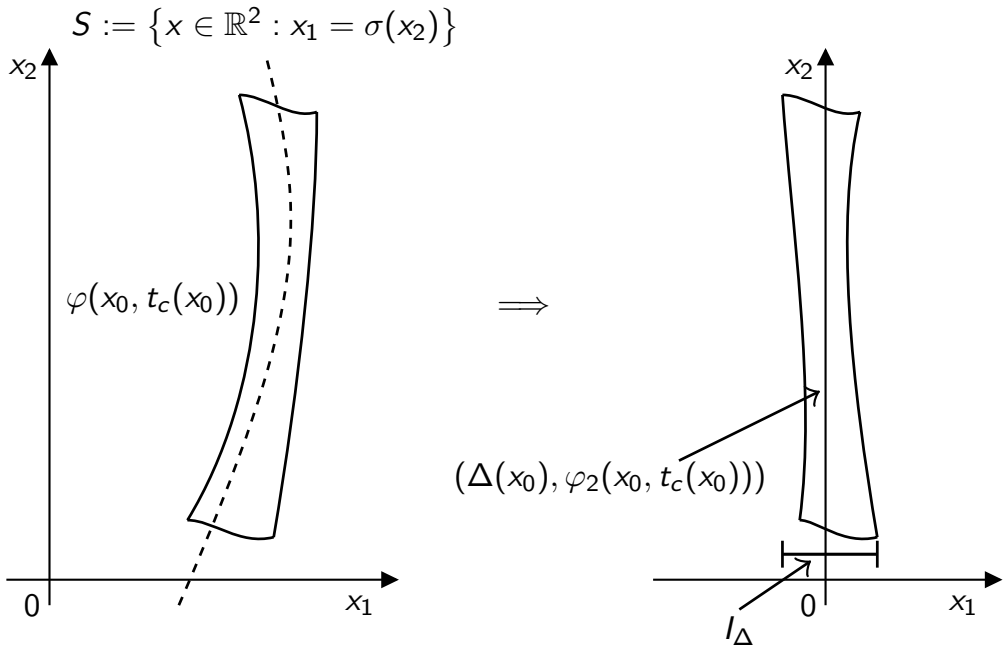

Figure 3.3. Calculation of maximal displacement of $\varphi(x_0, t_c(x_0))$ with respect to S.

zero. However, we cannot expect the inclusion

$$\{g(\varphi(x_0, t_c(x_0) + [0,0])) + I_g : x_0 \in D\} \subset \{\varphi(x_0, t_c(x_0) + [0,0]) + I_\varphi : x_0 \in D\}.$$

To obtain a TM-enclosure $\mathcal{P}_1(x_0) + I_{\mathcal{P}_1}$ of the first component of the true Poincaré map $\mathcal{P}^\star(x_0)$, we first introduce the Taylor Model

$$\Delta(x_0) := (\varphi_1(x_0, t_c(x_0) + [0,0]) + I_{\varphi_1}) - (g(\varphi(x_0, t_c(x_0) + [0,0])) + I_g). \quad (3.8)$$

$\Delta(x_0)$ is a measure of the displacement parallel to the first coordinate axis of $\varphi_1(x_0, t_c(x_0) + [0,0])$ relative to the surface (cf. Figure 3.3), so range bounding $\Delta(x_0)$ over all $x_0 \in D$ yields an interval bound I_Δ, which is very narrow, basically the order of magnitude of the remainder bound I_{φ_1} of the original TM-flow. Thus we have already found a TM-enclosure of the first component of the Poincaré map by setting

$$\mathcal{P}_1(x_0) + I_{\mathcal{P}_1} := \varphi_1(x_0, t_c(x_0) + [0,0]) + I_\Delta. \quad (3.9)$$

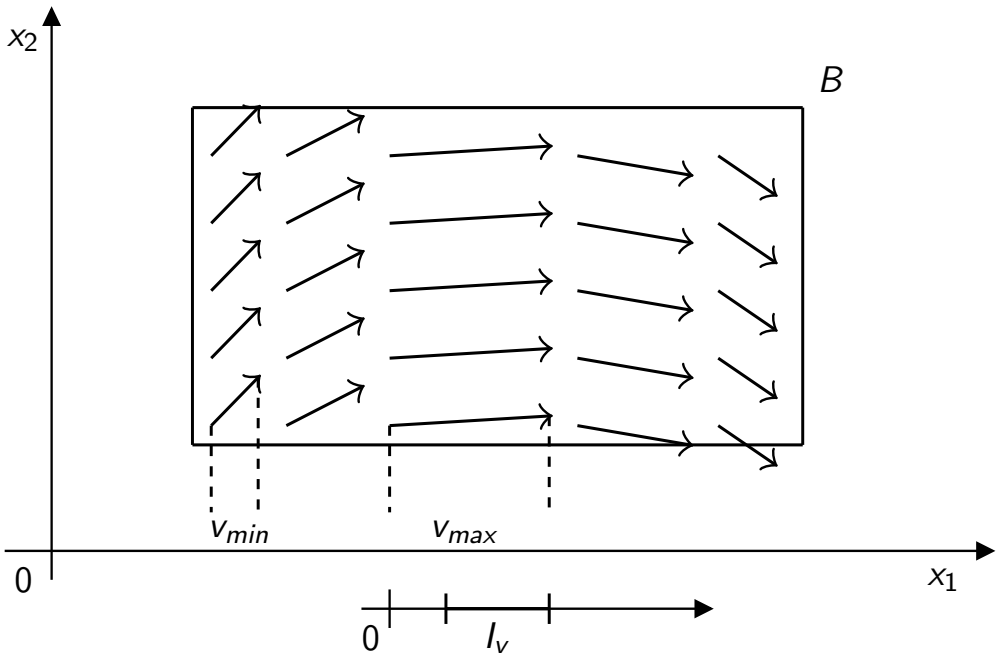

Figure 3.4. Range bound of the vector field f_1 and f_2 over the box B.

We are now able to also find the remaining, 'tangential' components $\mathcal{P}_2(x_0) + I_{\mathcal{P}_2}, ..., \mathcal{P}_\nu(x_0) + I_{\mathcal{P}_\nu}$ of the TM-enclosure of $\mathcal{P}^\star(x_0)$. In order to outfit the TMs $\varphi_j(x_0, t_c(x_0) + [0,0])$, $j \in \{2, ..., \nu\}$ with suitable remainder bounds $I_{\mathcal{P}_j}$, we need to make use of the vectorfield of the system (3.7) and make 'velocity'-type arguments. We first observe that an interval bound $I_{vel,\perp}$ of the velocity in x_1-direction, i.e. the function f_1, over the entire set B can be found by simply range bounding the TM $f_1(\varphi(x_0,t),t) \forall (x_0,t) \in D \times [-\tilde{t}, \tilde{t}]$ as in figure 3.4.

Note that except in pathological cases $I_{vel,\perp}$ does not contain zero and its upper and lower bounds are typically of similar size since the vectorfield $f(x,t)$ does not vary significantly over the the set B. If we consider the interval

$$I_{t_c} := \frac{I_\Delta}{I_{vel,\perp}} \tag{3.10}$$

we see that I_t is very narrow due to the smallness of I_Δ and that it contains the largest possible time duration that it can take the flow to traverse the surface in x_1-direction.

Bounding the tangential velocities, i.e. the TMs $f_j(\varphi(x_0,t),t)\,\forall\,(x_0,t)\in D\times[-\tilde{t},\tilde{t}]$ for $j\in\{2,...,\nu\}$, we get interval bounds $I_{vel,j,\|}\forall j$ and can define the intervals

$$I_{j,\|}:=I_t\cdot I_{vel,j,\|}\forall\, j\in\{2,...,\nu\},\tag{3.11}$$

which allow the rigorous bounding of the tangential components of the Poincaré map by

$$\mathcal{P}_j(x_0)+I_{\mathcal{P}_j}:=\varphi_j(x_0,t_c(x_0)+[0,0])+(I_{\varphi_j}\cup I_{j,\|})\,\forall\, j\in\{2,...,\nu\}.\tag{3.12}$$

We can summarize the construction of a validated TM-enclosure of the Poincaré map in the following theorem:

3.2 Theorem. *Suppose that for the system (3.1), with $x_0\in D$, and a surface S as given in (3.5) the crossing time T_0 of the true reference trajectory $\varphi^\star(X_0,t)$ is known approximately, and that a TM-integration has been performed until T_0. Suppose further that a time interval $T_0+[-\tilde{t},\tilde{t}]$ that encloses all true crossing times has been constructed as in (3.6) and that a verified time-dependent TM-representation of the flow of (3.7) has been obtained over $D\times(T_0+[-\tilde{t},\tilde{t}])$ as in section 2.2.*

Then, a TM $\mathcal{P}(x_0)+I_{\mathcal{P}}$ constructed as in (3.9) and (3.12) using the interval estimates (3.8), (3.10) and (3.11) has the property that for the true Poincaré map $\mathcal{P}^\star(x_0)$ we have the enclosure

$$\mathcal{P}^\star(x_0)\in\mathcal{P}(x_0)+I_{\mathcal{P}}\,\forall\, x_0\in D.$$

We conclude the discussion by remarking that there is an alternative route to obtaining a suitable TM-representation $\mathcal{P}(x_0)+I_{\mathcal{P}}$ of $\mathcal{P}^\star(x_0)$, namely by simply finding a sharp remainder bound I_{t_c} for the crossing time $t_c(x_0)$ such that the true crossing time $t_c^\star(x_0)$, for $x_0\in D$, is enclosed by the TM $t_c(x_0)+I_{t_c}\forall x_0\in D$. We indeed have already found such an interval enclosure for the crossing time, namely the interval I_t as computed in (3.10). Insertion of this TM $t_c(x_0)+I_t$ into the time-dependence of the flow $\varphi(x_0,t)+I_\varphi$ yields a TM for the Poincaré map as well, but we expect the aforementioned construction to have slightly sharper bounds for $\mathcal{P}^\star(x_0)$.

3.2.4 Summary of the verified algorithm

1. For the system (3.1) and a given surface S, find the crossing time T_0 of the reference orbit, i.e. $\varphi(X_0, T_0) \in S$

2. Integrate (3.1) in TM-arithmetic until the time T_0 and obtain a verified flow $\varphi(x_0, T_0) + I_t$

3. Expand the parametrization $g(x) + I_g$ of S around the point $\varphi(0, T_0)$

4. Extract the polynomial part $\varphi(x_0, T_0)$, perform one extra integration step in DA-arithmetic with full local time-dependence

5. Compute a DA-approximation $t_c(x_0)$ of the crossing time like in section 2.3

6. Perform a range bound $[t_l, t_u]$ of $t_c(x_0)$ over $x_0 \in D$, construct the time domain $T_0 + [-\tilde{t}, \tilde{t}]$ as in (3.10)

7. Perform a TM-integration of the system (3.7) over the time domain $T_0 + [-\tilde{t}, \tilde{t}]$, keep local time dependence. This yields a verified time-dependent flow $\varphi(x_0, t) + I_\varphi$. Extract the remainder interval of the code list evaluation $g(\varphi(x_0, t) + I_\varphi)$ as a remainder interval I_g for the TM-representation of g.

8. Extract the polynomial part $\varphi(x_0, t)$, together with $g(x_0)$ perform the nonvalidated computation of the crossing time $t_c(x_0)$ like in section 2.3

9. Find interval bound I_Δ for the displacement (3.8) over the set D

10. Find interval bound $I_{vel,\perp}$ of the vector field component $f_1(x, t)$

11. Find interval bound I_{t_c}as in (3.10)

12. Find interval bounds $I_{vel,j,\parallel}$ of the tangential vector field components $f_j(x, t)$ as in (3.11)

13. Construct the TM-enclosure $\mathcal{P}(x_0) + I_{\mathcal{P}}$ of the true Poincaré map $\mathcal{P}_{true}(x_0)$ as in (3.9) and (3.12)

3.3 Numerical Example: the Volterra-Lotka equations

We consider the Volterra-Lotka equations

$$\begin{aligned} \dot{x}_1 &= 2x_1(1 - x_2) \\ \dot{x}_2 &= -x_2(1 - x_1) \end{aligned} \tag{3.13}$$

with the initial conditions $(x_1(0), x_2(0)) = (1, 3)$. These initial conditions leads to a periodic trajectory with a period of $T_0 \approx 5.488138468035$. For testing purposes it is furthermore beneficial that actually all trajectories in the first quadrant are periodic, and the closed orbits are the level sets of the function

$$f(x_1, x_2) = x_1 x_2^2 e^{-x_1 - 2x_2},$$

as shown in figure 3.5. This means that f stays constant along a single trajectory.

The Poincaré section onto which we want to project is $S := \{(x_1, x_2) : x_1 = 1\}$, i.e. $g(x) = x_1 - 1$ exactly and we may assume that $I_g = [0, 0]$. Note that all nonconstant trajectories traversing this surface do so horizontally, since the x_2-component of the vectorfield vanishes on S. Furthermore, one can easily show that at the points $(1, x_2) \in S$ the maximal x_2-value of the corresponding orbit is assumed. We consider a domain box $X_0 + [-d, d]^2$, where $X_0 := (x_1(0), x_2(0)) = (1, 3)$ and $d := 10^{-3}$. We perform a $16th$ order verified TM-integration over the time interval $[0, T_0]$ using the arbitrary-order code COSY Infinity [1, 15], which fully supports verified operation using interval and Taylor Model data types. We will not review steps 1-6 in the verified algorithm, since for the most parts they need to be repeated in the later

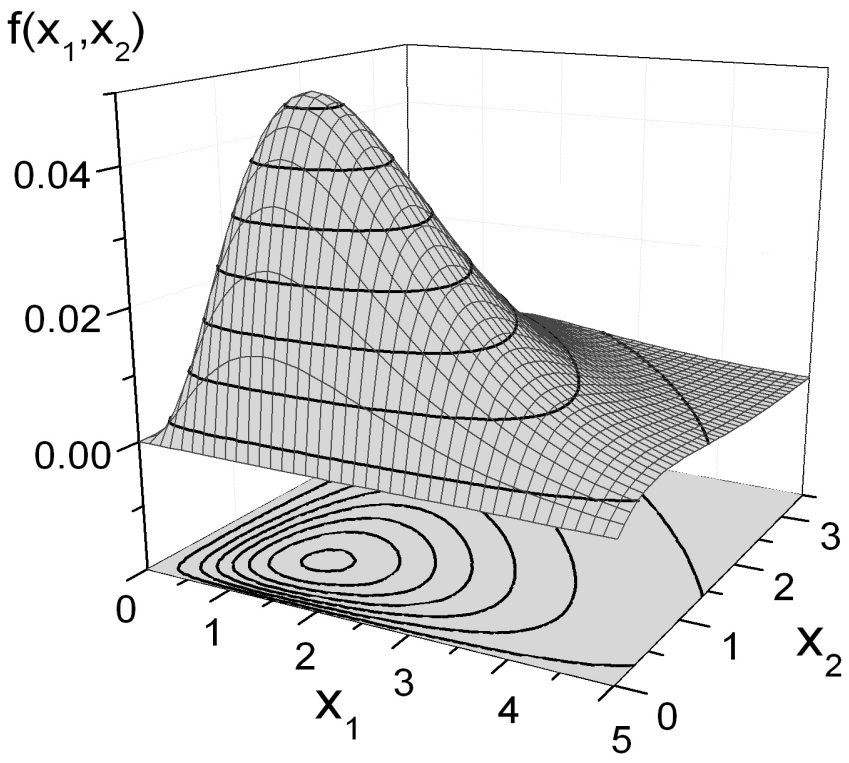

Figure 3.5. Periodic orbits of the Volterra-Lotka system plotted as level sets of $f(x_1, x_2) = x_1 x_2^2 e^{-x_1 - 2x_2}$.

steps, and just state the fact that we obtained an interval enclosure of all crossing times for trajectories originating in $X_0 + [-d, d]^2$ as $T_0 + [-\tilde{t}, \tilde{t}]$, where

$$\tilde{t} = 0.3488916233200980.$$

Using the TM-integration scheme from section 2.2, we obtained time-dependent TMs $\varphi(x_0, t) + I_\varphi$ for the flow over the time-domain $T_0 + [-\tilde{t}, \tilde{t}]$. The $\varphi_1(x_0, t) + I_{\varphi_1}$-component is

TM VARIABLE:		NO=16	NV=3		
I	COEFFICIENT	ORDER	EXPONENTS		
1	1.000000000416704	0	0	0	0
2	0.1000000000363324E-02	1	1	0	0
3	0.3187097194452020E-02	1	0	1	0
4	-.1584341969869541	1	0	0	1
5	0.1195161448703009E-05	2	2	0	0
6	0.3187097199172751E-05	2	1	1	0
7	0.6983455150714117E-05	2	0	2	0
8	-.1584341969567188E-03	2	1	0	1
9	-.5841622829368688E-03	2	0	1	1
10	0.1255069738025934E-01	2	0	0	0
...					
264	-.2772494477873786E-19	16	1	0	15
265	-.1205045114232825E-18	16	0	1	15
266	0.2745362100462193E-18	16	0	0	16

REMAINDER BOUND INTERVAL:

[-.2812625244546855E-009,0.2827141034585959E-009]

and the $\varphi_2(x_0, t) + I_{\varphi_2}$-component is

TM VARIABLE:		NO=16	NV=3		
I	COEFFICIENT	ORDER	EXPONENTS		
1	2.999999999998760	0	0	0	0
2	-.2749150733449834E-12	1	1	0	0
3	0.9999999991337136E-03	1	0	1	0
4	0.4951517601531404E-10	1	0	0	1
5	-.8889349260011417E-15	2	2	0	0
6	-.2390322899443805E-05	2	1	1	0
7	-.3809095702117611E-05	2	0	2	0
8	0.1188256477338971E-03	2	1	0	1
9	0.3787088884005587E-03	2	0	1	1
10	-.9413023036667367E-02	2	0	0	0
...					
254	0.3499033280718983E-17	15	0	0	15
255	0.6881983195065229E-19	16	0	1	15
256	-.1623038355645917E-18	16	0	0	16

REMAINDER BOUND INTERVAL:
[-.1509589656350207E-009,0.1465844505110771E-009]

The exponent notation refers to the expansion in terms of $x_{0,1}$, $x_{0,2}$ and t. Note here that for internal purposes supporting the verified computation COSY Infinity rescales all variables to the domain $[-1, 1]$. Indeed, the coefficient 3 in the expansion of the flow in x_2-direction should be the identity in $x_{0,2}$, which is the case taking into account the rescaling (recall the domain size for the $x_{0,j}$ is $[-10^{-3}, 10^{-3}]$ for $j = 1, 2$).

Extracting the DA-part of $\varphi(x_0, t) + I_\varphi$, we can set up the auxiliary function ψ as in step 8 and invert it using DA-methods. This yields the DA-part $t_c(x_0)$ of the crossing time:

TM VARIABLE:		NO=16	NV=3		
I	COEFFICIENT	ORDER	EXPONENTS		
1	0.2630142082556787E-08	0	0	0	0
2	0.6311768667250960E-02	1	1	0	0
3	0.2011622020280193E-01	1	0	1	0
4	0.4387698247913437E-05	2	2	0	0
5	-.3155884300401868E-05	2	1	1	0
6	0.1963668821309683E-05	2	0	2	0
7	-.3714103288167166E-08	2	0	2	0
8	0.1793429553434871E-08	2	0	2	0
9	0.1577940909990520E-08	2	0	2	0
10	-.4277865429354660E-09	2	0	2	0
...					
27	0.6212283471025129E-18	7	5	2	0
28	-.2159517257712372E-18	7	4	3	0
29	0.1677381555981327E-18	7	2	5	0

We next perform step 9 by outfitting this polynomial part of the crossing time with a zero remainder bound and inserting it into $\varphi(x_0, t) + I_\varphi$, and subsequently we construct the TM $\Delta(x_0)$ from (3.8)

TM VARIABLE:		NO=16	NV=3		
I	COEFFICIENT	ORDER	EXPONENTS		
1	0.1738810083033253E-18	1	0	1	0

REMAINDER BOUND INTERVAL:
[-.2812625477812596E-009,0.2827141267851699E-009]

which can be range bounded by

$$I_\Delta = [-.2812625479551414E-009, 0.2827141269590517E-009].$$

Next we can find remainder bounds for the transverse and tangential velocity as in

steps 10 and 12, by inserting $\varphi(x_0,t)+I_\varphi$ into (3.13), which leads to the range bounds

$$I_{vel,\perp} = [-4.683179956640803, -3.383171090471566]$$
$$I_{vel,2,\parallel} = [-.4478418602052703, 0.5274061209170990].$$

Then, according to step 11 we can use I_Δ and $I_{vel,\perp}$ to compute

$$I_{t_c} = [-.8356483293301176E-010, 0.8313577422888692E-010].$$

This allows us to estimate the remainder bounds I_Δ and

$$I_{2,\parallel} = I_{t_c} \cdot I_{vel,2,\parallel} = [-.4407260438228519E-010, 0.4384631619549699E-010]$$

for the TM-representation of the Poincaré map and finally complete step 13 by computing, according to (3.9) and (3.12), the TM-representation $\mathcal{P}_1(x_0) + I_{\mathcal{P}_1}$:

```
TM VARIABLE:                    NO=16  NV=3
I  COEFFICIENT                  ORDER  EXPONENTS
1  1.000000000000000              0     0     0     0
2  0.1738810083033253E-18         1     0     1     0
REMAINDER BOUND INTERVAL:
[-.2812636815047402E-009,0.2827152370081946E-009]
```

and for $\mathcal{P}_2(x_0) + I_{\mathcal{P}_2}$:

TM VARIABLE:		NO=16	NV=3		
I	COEFFICIENT	ORDER	EXPONENTS		
1	2.999999999998760	0	0	0	0
2	0.3761326318189197E-13	1	1	0	0
3	0.1000000000129772E-02	1	0	1	0
4	0.3749999994446287E-06	2	2	0	0
5	-.3783981671657100E-14	2	1	1	0
6	-.5693365190215309E-14	2	0	2	0
...					
25	-.3816772356026731E-19	7	5	2	0
26	0.7400323546967589E-19	7	4	3	0
27	-.4375766016780720E-19	7	2	5	0

REMAINDER BOUND INTERVAL:
[-.1509623028476050E-009,0.1509623028476049E-009]

The two Taylor Models constitute an enclosure of the true Poincaré map $\mathcal{P}^\star(x_0)$ for all $x_0 \in D$. It is indeed more intuitive to analyze the result as a function mapping the initial conditions $X_0 + x_0$ from the surface S back to S, which can be performed by simply setting $x_{0,1} = 0$. Note that the result is still verified, since we are allowed to insert any Taylor Model with a range in $[-1, 1]^3$ into $\mathcal{P}(x_0) + I_{\mathcal{P}}$.

Performing the restriction $x_{0,1} = 0$ yields for $\mathcal{P}_1(x_0) + I_{\mathcal{P}_1}$ the same as above (no $x_{0,1}$-dependence), and for $\mathcal{P}_2(x_0) + I_{\mathcal{P}_2}$:

TM VARIABLE:		NO=16	NV=3		
I	COEFFICIENT	ORDER	EXPONENTS		
1	2.999999999998760	0	0	0	0
2	0.1000000000129772E-02	1	0	1	0
3	-.5693365190215309E-14	2	0	2	0
4	0.1311936146646892E-15	3	0	3	0
5	-.1609031863045520E-17	4	0	4	0
6	0.9437249062120226E-19	5	0	5	0

REMAINDER BOUND INTERVAL:
[-.1509623028476050E-009,0.1509623028476049E-009]

We see that the first component is exactly 1 up to small floating point errors, which means that $\mathcal{P}(x_0) + I_{\mathcal{P}}$ indeed projects onto S. The second component offers an illuminating validation of our argument: Since all orbits of the Volterra-Lotka-system are periodic, the Poincaré map acting only on the surface S necessarily needs to be the identity map, a characteristic which is nicely reproduced here. The constant part of $\mathcal{P}_2(x_0) + I_{\mathcal{P}_2}$ is three, i.e. the same as the initial condition, and the identity map in the vertical shift is represented by the coefficient number 2, the linear identity in $x_{0,2}$ (recall the rescaling from $x_{0,2} \in [-10^{-3}, 10^{-3}]$ to $[-1, 1]$).

3.4 Summary and Outlook

The Differential Algebraic framework is a natural tool to address implicitly posed problems like the computation of Poincaré maps due to the availability of automatic and efficient functional inversion tools. We presented an algorithm which generates a polynomial approximation of the crossing time for orbits in the neighborhood of a reference orbit which transverses a given surface.

Starting with the nonverified polynomial expansion of the crossing time, a rigorous Taylor Model enclosure of the true crossing time can be obtained by applying velocity-type arguments using the vector field in the vicinity of the Poincaré section. Once a valid crossing time enclosure is obtained, inserting this into the Taylor Model flow yields a verified Taylor Model enclosure of the true Poincaré map.

It is a logical progression to combine the techniques for rigorous Poincaré maps presented in this chapter and the methods for invariant manifolds and related phenomena in the plane in the subsequent chapters. One can think of the Lorenz or Roessler systems, continuous three-dimensional systems, which could be restricted to a suitably chosen surface via the Poincaré map algorithm, and subsequently the restricted dynamics on the surface could be analyzed through their invariant manifold

tangle.

Lastly, we note that the construction of the crossing time as in (3.2) can be posed as a constraint satisfaction problem, and similar techniques have been applied in constrained optimization problems to model feasible sets with dramatically reduced search volume.

CHAPTER 4

Verified Representations of Invariant Manifolds

The study of stable and unstable manifolds is naturally a very rich topic, given the significance of the invariant manifold structure for the dynamical properties of a dynamical system, ranging from questions as diverse as the determination of topological invariants and hyperbolicity to applications in the description of long-term behavior of physical systems, e.g. in the three-body problem or particle optics.

Of particular interest in the present work is the study of the invariant manifold tangle with respect to the existence and the properties of the homo- and heteroclinic intersections contained in it, and the resulting implication of horseshoe dynamics [63] or similar hyperbolic phenomena. In this case, the manifold structure can be arguably complicated and it has long been a challenge to develop quality numerical tools to investigate them.

In the following we develop an approach to find Taylor Model enclosures of the local invariant manifolds for planar diffeomorphisms around a hyperbolic fixed point (in this case the existence of local invariant manifolds as injectively immersed curves is guaranteed by the Invariant Manifold Theorem 2.7. As the global manifolds are

generated as images (or preimages) of the local unstable (or stable) manifolds, likewise Taylor Model enclosures of the global manifold structure are iteratively generated by mapping the Taylor Model representations of the local manifolds in TM-arithmetic.

The technique consists of two steps: initially, a polynomial approximation of the local invariant manifolds is obtained, via various techniques as presented in section (4.1).

In the second step, these polynomials are extended to Taylor Model enclosures of the true local manifolds by heuristically outfitting them with remainder intervals bounding the truncation error. The algorithm confirms the validity of the C^0-estimates in a self-verified enclosure check.

After the TM-enclosures for the local manifolds have been constructed, we compute sharp verified TM-enclosures of significant pieces of the global manifold tangles. Subsequently we compute rigorous interval enclosures for homoclinic points in the tangle, and give numerical examples that support the accuracy claims.

4.1 High-order approximation of the local manifold

The first step to obtaining rigorous Taylor Model enclosures of local invariant manifolds is the construction of nonverified, yet highly accurate polynomial approximations. We present three DA-based approaches which can be used to generate the polynomial expansions in the neighborhood of the fixed point. All three techniques are somewhat similiar in spirit, essentially based on normal form arguments, but with different intuitions and realms of applicability.

4.1.1 Normal form transformation

Let $f : \mathbb{R}^\nu \supseteq D \longrightarrow \mathbb{R}^\nu$ be a C^r-map on an open set D with a fixed point $p \in D$ such that there is a hyperbolic splitting $T_p\mathbb{R}^\nu = \mathbb{R}^\nu = E_p^u \oplus E_p^s$ at p. For simplicity, we also assume p to be at the origin, which can be achieved through a suitable affine transformation. Suppose now that there exists a normal form transformation $\mathcal{N} : \mathbb{R}^\nu \longrightarrow \mathbb{R}^\nu$ that fully linearizes f around p, i.e.

$$\left(\mathcal{N}^{-1} \circ f \circ \mathcal{N}\right)(x) = Df\,(p) \cdot x = L\,(x)\,.$$

in the neighborhood of p. A prerequisite for this is that the eigenvalues satisfy the nonresonance conditions

$$\lambda_j - \lambda_1^{k1} \cdot ... \cdot \lambda_\nu^{k\nu} \neq 0 \,\forall\, 1 \leq j \leq \nu \text{ and } k_1, ..., k_\nu \in \mathbb{N}. \tag{4.1}$$

We now have a way of representing the local stable and unstable manifolds of f at the origin through those of L. Consider the unstable manifold $W^u\,(p)$, and let E^u be the unstable eigenspace of the linearized map L:

$$\begin{aligned} W^u\,(p) &= \{x \in \mathbb{R}^\nu : f^k(x) \underset{k\to-\infty}{\longrightarrow} 0\} = \{x \in \mathbb{R}^\nu : \left(\mathcal{N} \circ L \circ \mathcal{N}^{-1}\right)^k (x) \underset{k\to-\infty}{\longrightarrow} 0\} \\ &= \{x \in \mathbb{R}^\nu : \left(\mathcal{N} \circ L^k \circ \mathcal{N}^{-1}\right)(x) \underset{k\to-\infty}{\longrightarrow} 0\} = \{x \in \mathbb{R}^\nu : L^k(\mathcal{N}^{-1}(x)) \underset{k\to-\infty}{\longrightarrow} 0\} \\ &= \{x \in \mathbb{R}^\nu : \mathcal{N}^{-1}(x) \in E^u\} \end{aligned}$$

We are thus able to approximate the local unstable manifold $W^u\,(p)$ of f as

$$W^u\,(p) = \mathcal{N}(E^u).$$

The technique works likewise for the stable manifold $W^s\,(p)$ as the image of E^s under $\mathcal{N}$. For the fully linearized map, the eigenspaces are hypersurfaces parametrized by coordinate axes at the fixed point.

In the case where W^u or W^s are just curves, E^u or E^s correspond to the coordinate axes and we have e.g. $W^u = \mathcal{N}\left(\left\{(0,...,0,x_i,0,...,0)^T : x_i \in \mathbb{R}\right\}\right)$ for some index $1 \leq i \leq \nu$.

While the nonresonance condition (4.1) is merely necessary, but not sufficient for the convergence of the NFT construction, it guarantees that we may perform the construction in DA-arithmetic, as presented in section B.5 of Appendix B. In the case of nonconvergence, the thus obtained polynomial approximations of the invariant manifolds would possibly fail the automated validation tests in the verification steps presented in the following section.

To this end it is important to note that for a finite computation order N in the DA-framework, where $N < r$, condition (4.1) only needs to be satisfied for multiindices $|\mathbf{k}| = k_1 + ... + k_\nu \leq N$. Assume now a DA-vector representation $[\mathcal{N}]$ of the normal form transformation has been obtained as in section B.5 . Suppose the unstable eigenspace is spanned by the coordinate axes unit vectors, say

$$E^u := span\left\{\hat{e}_1, ..., \hat{e}_M\right\},$$

for some $M \in \mathbb{N}$. Then the natural parametrization of E^u in DA-arithmetic is

$$\left[E^u\right] = \left(\left[x_1\right], ..., \left[x_M\right], \left[0\right], ..., \left[0\right]\right) \in {}_N D_\nu^\nu$$

and locally we can get a polynomial approximation for a parametrization of $W^u_{loc}(p)$ as

$$[W_p^{loc}] = [\mathcal{N}] \circ \left[E^u\right] \in {}_N D_\nu^\nu.$$

4.1.2 Hubbard's method

In the special case of a planar analytic (so in particular smooth) map Hubbard's method [31] provides an approach that can be implemented in a straightforward fashion.

4.1 Theorem. *(Hubbard) Let $f : \mathbb{C}^2 \longrightarrow \mathbb{C}^2$ be a complex analytic diffeomorphism with a hyperbolic saddle point at p. Let λ_u and λ_s be the unstable and stable eigenvalues of $\mathcal{D}f(p)$ with corresponding eigenvectors v_u and v_s. For $t \in \mathbb{C}$, define the test curves*

$$\begin{aligned} \gamma_n^u(t) &:= f^n(p + \frac{t}{\lambda_u^n} v_u), \\ \gamma_n^s(t) &:= f^{-n}(p + t\lambda_s^n v_s). \end{aligned} \tag{4.2}$$

Then the sequences $\{\gamma_n^u\}_{n\geq 1}$ and $\{\gamma_n^s\}_{n\geq 1}$ converge uniformly on compact sets to limit functions γ^u and γ^s, and the following properties hold:

1. *$f(\gamma^u(t)) = \gamma^u(\lambda_u t)$ and $f(\gamma^s(t)) = \gamma^s(\lambda_s t)$ for all $t \in \mathbb{C}$*
2. *The maps γ^u and γ^s are injective immersions.*
3. *The images of γ^u and γ^s coincide with the unstable and stable manifolds, respectively, of f containing p.*

Since typically fixed points and eigenvalues can be determined well, the functions in (4.2) can be constructed to the desired order with high accuracy.

For a finite computation order N, straightforward application of DA-arithmetic yields the curves

$$\begin{aligned} \left[\gamma_N^u(t)\right] &:= f^N\left(p + \left[\lambda_u^{-N}\, t\, v_u\right]\right), \\ \left[\gamma_N^s(t)\right] &:= f^{-N}\left(p + \left[\lambda_s^{N}\, t\, v_s\right]\right), \end{aligned}$$

as local DA-vector representations, and taking the real part if necessary. Here we may actually relax the assumption that f be complex analytic and just demand that f is C^r for some $r \geq N + 1$.

4.1.3 Polynomial parametrization from functional equation

Another technique for the explicit construction of polynomial approximations of invariant manifolds can be obtained from the fact that the manifold parametrizations can be chosen in such a way that they obey an eigenvalue scaling law, described below in (4.3). In the plane one can relatively simply derive the coefficients of the polynomial expansions of the manifolds. These techniques are standard and are covered in great detail in [9, 10, 16, 17, 35, 67].

In the following let again $f : \mathbb{R}^2 \supseteq D \longrightarrow \mathbb{R}^2$ denote a planar analytic diffeomorphism with a hyperbolic saddle point $p \in D$, here assumed to be at the origin. We further assume that the eigenvector corresponding to the unstable eigenvalue λ_u with $|\lambda_u| > 1$ coincides with the x_1-axis, and the eigenvector of the stable eigenvalue λ_s satisfying $|\lambda_s| < 1$ with the x_2-axis. Let the eigenvalues satisfy the nonresonance condition (4.1).

Let f_n denote the Taylor expansion of f around $(0, 0)$ to order $n \leq k$, and let $f =_n g$ for two sufficiently differentiable functions f and g denote agreement of their Taylor expansions around $(0, 0)$ up to order n (for more detail refer to Appendix B, esp. Def. B.1 and following).

The following outlines the construction of a polynomial curve $\gamma^u = (\gamma_1^u, \gamma_2^u)$ parametrizing the unstable manifold, again an analogous algorithm can be performed for the stable manifold. We seek a curve $\gamma^u : \mathbb{R} \longrightarrow \mathbb{R}^2$ such that

$$f(\gamma^u(t)) = \gamma^u(\lambda_u t), \tag{4.3}$$

a scaling property of the unstable manifold which stems directly from the Invariant Manifold Theorem (2.7). We make the polynomial Ansatz

$$\gamma_1^{u,n}(t) = t + \sum_{i=2}^{n} \alpha_i\, t^i = \gamma_1^{u,n-1}(t) + \alpha_n\, t^n,$$
$$\gamma_2^{u,n}(t) = 0 + \sum_{i=2}^{n} \beta_i\, t^i = \gamma_2^{u,n-1}(t) + \beta_n\, t^n,$$

and see that in fact $\dot{\gamma}^{u,n}(0,0) = (1,0)^T$ is tangent to the x_1-axis at the origin for every $n \in \mathbb{N}$. Rewriting the diffeomorphism we obtain

$$f_1(x_1, x_2) = \lambda_u x_1 + \tilde{f}_1(x_1, x_2),$$
$$f_2(x_1, x_2) = \lambda_s x_2 + \tilde{f}_2(x_1, x_2),$$

where $\tilde{f} = \left(\tilde{f}_1, \tilde{f}_2\right)$ denotes the nonlinear part of f. Note in particular that $\tilde{f}$ can be written as a power series expansion because of the analyticity of f. By inserting the above expressions into the condition (4.3) we obtain

$$\lambda_u\, t + \lambda_u \sum_{i=2}^{n} \alpha_i\, t^i + \tilde{f}_1\left(\gamma_1^{u,n}(t), \gamma_2^{u,n}(t)\right) = \lambda_u\, t + \sum_{i=2}^{n} \lambda_u^i\, \alpha_i\, t^i, \tag{4.4}$$
$$\lambda_s \sum_{i=2}^{n} \beta_i\, t^i + \tilde{f}_2\left(\gamma_1^{u,n}(t), \gamma_2^{u,n}(t)\right) = \sum_{i=2}^{n} \lambda_u^i\, \beta_i\, t^i.$$

For the determination of α_n, β_n we are interested in the terms of (4.4) of exact order n in t, or in other words the part of (4.4) which is homogeneous of order n in t. To this end we observe that the part of $\tilde{f}\left(\gamma_1^{u,n}(t), \gamma_2^{u,n}(t)\right)$ which is homogeneous of order n in t is identical to the part homogeneous of order n in t of $\tilde{f}\left(\gamma_1^{u,n-1}(t), \gamma_2^{u,n-1}(t)\right)$. Indeed this is the case since $\tilde{f}$ is a power series expansion of order 2 and greater, and so the n-th order terms of $\gamma^{u,n}$ do not contribute to the terms of $\tilde{f}\left(\gamma_1^{u,n}(t), \gamma_2^{u,n}(t)\right)$ homogeneous of order n.

Inserting this into the equations (4.4) and rearranging terms we obtain

$$(\lambda_u - \lambda_u^n) \cdot \alpha_n \, t^n = \sum_{i=2}^{n-1} \lambda_u^i \, \alpha_i \, t^i - \tilde{f}_1 \left(\gamma_1^{u,n-1}(t), \gamma_2^{u,n-1}(t) \right),$$
$$(\lambda_s - \lambda_u^n) \cdot \beta_n \, t^n = \sum_{i=2}^{n-1} \left(\lambda_u^i - \lambda_s \right) \beta_i \, t^i - \tilde{f}_2 \left(\gamma_1^{u,n-1}(t), \gamma_2^{u,n-1}(t) \right),$$

and hence, because $(\lambda_\sigma - \lambda_u^n) \neq 0 \, \forall \, n \in \mathbb{N}$, $\sigma = u, s$ due to the nonresonance,

$$\alpha_n = \frac{S_1^{(n)}}{(\lambda_u - \lambda_u^n)}, \quad \beta_n = \frac{S_2^{(n)}}{(\lambda_s - \lambda_u^n)}, \tag{4.5}$$

where $S_1^{(n)}$ and $S_2^{(n)}$ denote the sum of the coefficients of terms of exact order n in $\tilde{f}_1 \left(\gamma_1^{u,n-1}(t), \gamma_2^{u,n-1}(t) \right)$ and $\tilde{f}_2 \left(\gamma_1^{u,n-1}(t), \gamma_2^{u,n-1}(t) \right)$. The construction (4.5) is fully explicit and inductive, since computation of α_n and β_n only requires knowledge of the α_i, β_i for $1 \leq i \leq n-1$.

Making the transition to DA-arithmetic is again straightforward here. Again we may relax our assumption that f is analytic and just demand that f is C^r for some $r \geq N+1$, where N is the desired expansion order of the DA-vector-computation. Additionally, the nonresonance condition (4.1) only needs to hold up to order N as well. We get

$$\left[\gamma_1^{u,n} \right] = \left[\gamma_1^{u,n-1} \right] + \left[\alpha_n t^n \right],$$
$$\left[\gamma_2^{u,n} \right] = \left[\gamma_2^{u,n-1} \right] + \left[\beta_n t^n \right],$$

where

$$[\alpha_n t^n] = \frac{1}{(\lambda_u - \lambda_u^n)} \left[S_1^{(n)} \, t^n \right], \quad [\beta_n t^n] = \frac{1}{(\lambda_u - \lambda_u^n)} \left[S_2^{(n)} \, t^n \right],$$

and

$$\left[S_i^{(n)} \, t^n \right] := \left[\tilde{f}_i \left(\gamma_1^{u,n-1}(t), \gamma_2^{u,n-1}(t) \right) \right]_N - \left[\tilde{f}_i \left(\gamma_1^{u,n-1}(t), \gamma_2^{u,n-1}(t) \right) \right]_{N-1}$$

for $i = 1, 2$ is homogeneous of order n in t.

4.2 Verified enclosure of the local manifold

4.2.1 Construction of verified local invariant curve enclosures

In the previous section techniques to find a nonverified polynomial approximation for the unstable curve near a fixed point were introduced. In the following we describe how such a polynomial approximation can be extended to a two-dimensional Taylor Model 'tube' that rigorously encloses the true invariant manifold.

Again, throughout this section let $f : \mathbb{R}^2 \supset D \longrightarrow \mathbb{R}^2$ be $\mathcal{C}^r$ with a hyperbolic fixed point at the origin, and such that the dominating eigenvector with eigenvalue λ_u with $|\lambda_u| > 1$ coincides with the x_1-axis, and the minor one with eigenvalue λ_s ($|\lambda_s| < 1$) with the x_2-axis. For simplicity we will also assume that in fact $\lambda_u > 1$, else consider the squared map.

We first introduce the notion of slopes:

4.2 Definition. *A differentiable curve $\gamma \subset \mathbb{R}^2$ parametrized as $\gamma(t) = (\gamma_1(t), \gamma_2(t))$, with $t \in [-1, 1]$, such that $|\dot{\gamma}_1(t)| \neq 0 \, \forall \, t$ is called regular. For regular curves, we define the slope s_γ as*

$$s_\gamma(t) = \frac{\dot{\gamma}_2(t)}{\dot{\gamma}_1(t)}.$$

4.3 Remark. *We can find simple transformation laws how the slope of a curve changes under iteration by a map $f \in C^2(\mathbb{R}^2)$. For a regular initial curve γ_i, we denote the tranformed curve $\gamma_f := f(\gamma_i)$ and observe that*

$$\dot{\gamma}_f(t) := Df(\gamma_i(t)) \cdot \dot{\gamma}_i(t)$$

or componentwise

$$\dot{\gamma}_{f,k}(t) = \partial_1 f_k(\gamma_i(t)) \cdot \dot{\gamma}_{i,1}(t) + \partial_2 f_k(\gamma_i(t)) \cdot \dot{\gamma}_{i,2}(t) \quad \textit{for } k = 1, 2$$

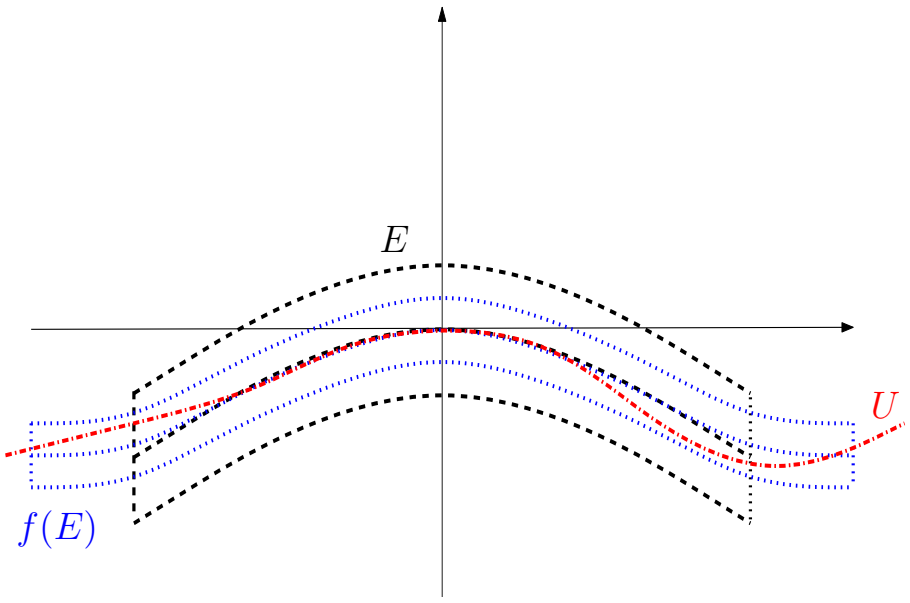

Figure 4.1. A parametrized rectangle E (black, dashed), and its image (blue, dotted). In the situation of Theorem 4.4, the true unstable manifold U (red, dash-dotted) is narrowly bound in its transverse direction by both E and $f(E)$.

and thus we obtain the new slope

$$\begin{aligned} s_{\gamma_f}(t) &= \frac{\partial_1 f_2(\gamma_i(t)) \cdot \dot{\gamma}_{i,1}(t) + \partial_2 f_2(\gamma_i(t)) \cdot \dot{\gamma}_{i,2}(t)}{\partial_1 f_1(\gamma_i(t)) \cdot \dot{\gamma}_{i,1}(t) + \partial_2 f_1(\gamma_i(t)) \cdot \dot{\gamma}_{i,2}(t)} \\ &= \frac{\partial_1 f_2(\gamma_i(t)) + \partial_2 f_2(\gamma_i(t)) \cdot s_{\gamma_i}(t)}{\partial_1 f_1(\gamma_i(t)) + \partial_2 f_1(\gamma_i(t)) \cdot s_{\gamma_i}(t)}. \end{aligned} \tag{4.6}$$

Let E be a parametrized curvilinear rectangle, i.e. the image of the unit square under an injective polynomial $P : [-1,1]^2 \longrightarrow \mathbb{R}^2$. We denote the left and right boundaries $\partial_l E$ and $\partial_r E$ of E by $\partial_l E = P(\{-1\}\times[-1,1])$ and $\partial_r E = P(\{1\}\times[-1,1])$, and call $\partial_v E := \partial_l E \cup \partial_r E$ the vertical boundary of E.

Likewise we introduce the horizontal boundary $\partial_h E := P([-1,1] \times (\{-1\} \cup \{1\}))$ of E. To visualize these notions an example for such a parametrized rectangle is depicted in Figure 4.1. We are now able to formulate conditions under which such a set can enclose the unstable curve in the vicinity of the origin:

4.4 Theorem. *Let E and P be as above such that E contains the hyperbolic fixed point at the origin. If*

$$f(E) \cap \partial_h E = \emptyset, \tag{4.7}$$

then the unstable manifold is disjoint from $\partial_h E$. If furthermore there exists $M > 1$ and $S > 0$ such that

$$|\partial_1 f_2(x) - \partial_2 f_2(x) \cdot s| < S \ \forall\ |s| \leq S, \tag{4.8}$$

$$|\partial_1 f_1(x) - \partial_2 f_1(x) \cdot s| > M \forall\ |s| \leq S, \tag{4.9}$$

then the unstable manifold is disjoint from $\partial_h E$ and leaves E through both $\partial_l E$ and $\partial_r E$.

Proof. First suppose that the unstable manifold intersects $\partial_h E$, then there exists a first such point, say p, such that the entire manifold arc A from the origin to p lies inside E. Consider the preimage $\tilde{p} := f^{-1}(p)$. Since this lies in the interior of A, we have $\tilde{p} \in E$. But then $p = f(\tilde{p}) \in f(E)$, which is in contradiction to assumption (4.7) above.

To prove the second claim, consider the open cone

$$C_S := \left\{ v = (v_1, v_2) \in \mathbb{R}^2 : v_2 = \sigma v_1 \text{ where } |\sigma| < S \right\},$$

see also Figure 4.2.

We first note that the image of any regular curve in $C_S \cap E$ which has slope less than S again has slope less than S, by virtue of the slope transformation law (4.6) and the conditions (4.8,4.9). In particular, this also entails that $(f(C_S) \cap E) \subset (C_S \cap E)$.

Let now x be an element in the connected component of $U \cap E$ containing the fixed point. Then $x \in C_S$, because the entire manifold segment between the origin and x has slope less than S. For if not, then there would be a point $\tilde{x}$ on that segment such that $s_U|_{\tilde{x}} \geq S$. At the origin $s_U(0) = 0$, so because of continuity of s_U we

have that for a positive $\varepsilon < S$ there exists a neighborhood $B(\varepsilon)$ of the origin in C_S such that $s_U|_\zeta < \varepsilon < S \,\forall\, \zeta \in B(\varepsilon)$. But $\tilde{x}$ is an element of the unstable manifold, so $\exists\, k(\varepsilon) \in \mathbb{N}$ such that $f^{-k(\varepsilon)}(\tilde{x}) \in B(\varepsilon)$, and hence $s_U|_{f^{-k(\varepsilon)}(\tilde{x})} < \varepsilon < S$. Since as stated above, slopes of less than S get transformed to slopes less than S under iteration, we most also have $s_U|_{\tilde{x}} < S$, in contradiction to our earlier choice.

So since $x \in C_S$, we may write $x_2 = \sigma x_1$ for some $|\sigma| < S$. Consider the parametrized line $G(t) := (x_1, x_2)^T \cdot t$, then we have that $G(0) = 0$, $G(1) = x$ and hence by the Mean Value Theorem for some $\xi \in [0, 1]$:

$$\begin{aligned} f_1(x) &= f_1(G(1)) = D\left(f_1(G(\xi))\right) \\ &= \langle \nabla f_1(G(\xi)), (x_1, x_2)^T \rangle \\ &= \partial_1 f_1(G(\xi)) \cdot x_1 + \partial_2 f_1(G(\xi)) \cdot x_2 \\ &= (\partial_1 f_1(G(\xi)) + \partial_2 f_1(G(\xi)) \cdot \sigma) \cdot x_1 \,, \end{aligned}$$

and thus

$$|f_1(x)| = |\partial_1 f_1(G(\xi)) + \partial_2 f_1(G(\xi)) \cdot \sigma| \cdot |x_1\,| > M \cdot |x_1|$$

by assumption (4.9). So the x_1-component of the image of any point x on the connected component of $U \cap E$ containing the origin has its modulus inflated by at least $M > 1$, and consequently the unstable manifold must leave E. Since U cannot leave through the horizontal boundary, it must leave through $\partial_l E$ and $\partial_r E$. Note that a horseshoe-shape of U such that it leaves E through only one of its vertical boundaries cannot happen, since in this case the slope of U would be unbounded in $C_S \cap E$. $\square$

Let now $\gamma_0 : [-1, 1] \longrightarrow \mathbb{R}^2$ be a polynomial curve approximating the unstable manifold near the origin, $\gamma_0(0) = (0, 0)$, and assume that γ_0 is regular, a natural condition which can easily be checked rigorously. We will now use γ_0 as the basis to construct a curvilinear rectangle as in the preceding theorem, and then employ Taylor Model arithmetic to rigorously check the assumptions in guaranteeing the valid unstable curve enclosure.

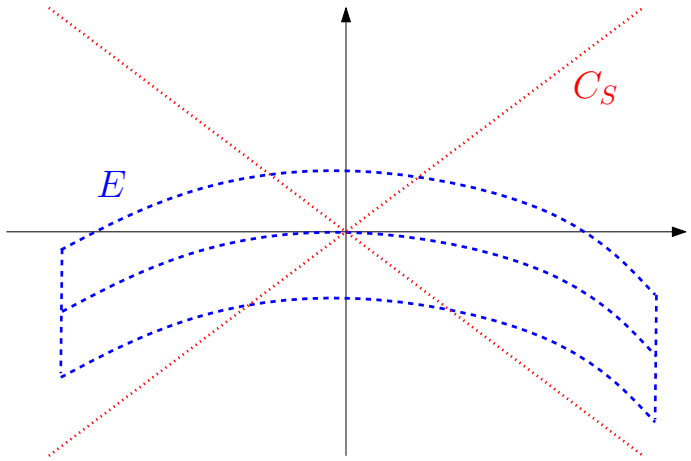

Figure 4.2. The parametrized rectangle E (blue, dashed), and the cone C_S (red, dotted) with an opening slope S such that $(f(C_S) \cap E) \subset (C_S \cap E)$.

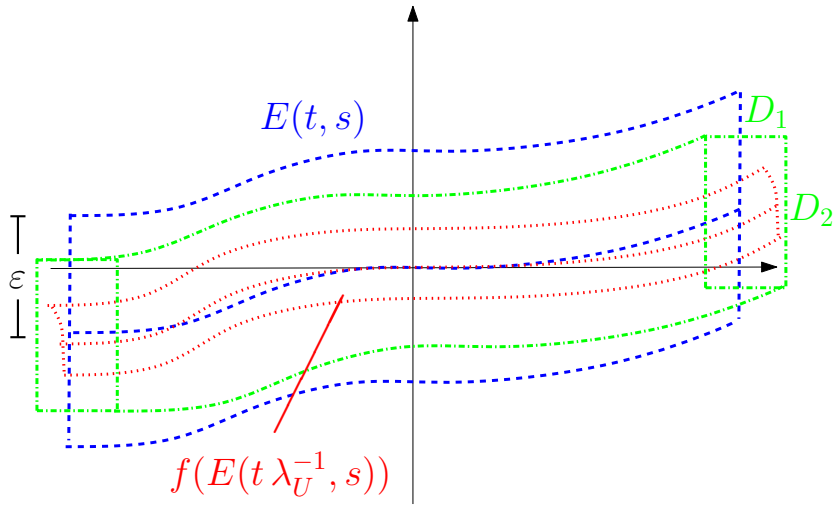

Figure 4.3. The parametrized rectangle E (blue, dashed) is constructed around its center curve γ_0. The difference between γ_0 and the rescaled iterate $f(E)$ (red, dotted) can be bounded by the interval box $D = (D_1, D_2)$ (green, dash-dotted) such that $f(E) \subset \gamma_0 + D$.

4.5 Lemma. *Let $\varepsilon > 0$, define the polynomial $P : [-1,1]^2 \longrightarrow \mathbb{R}^2$ as*

$$P(t,s) := \begin{pmatrix} \gamma_{0,1}(t) \\ \gamma_{0,2}(t) + \varepsilon \cdot s \end{pmatrix}, \tag{4.10}$$

and let $I_s, D_1, D_2 \subset \mathbb{R}$ be closed intervals (cf. Fig(4.3)) such that for the slope of γ_0 we have

$$s\gamma_0(t) \in I_s \, \forall \, t \in [-1,1] \tag{4.11}$$

and furthermore

$$f_i\left(P\left(\frac{t}{\lambda_u}, s\right)\right) - \gamma_0(t) \in D_i \;\forall\; (t,s) \in [-1,1]^2. \tag{4.12}$$

Consider the parametrized rectangle $E := P\left([-1,1^2]\right)$. If there exists a positive $K < \varepsilon$ such that

$$I_s \cdot D_1 + D_2 \subset [-K, K] \;, \tag{4.13}$$

then $f(E) \cap \partial_h E = \emptyset$ and condition (4.7) is satisfied.

4.6 Remark. *The intuition behind the lemma is the following: if a polynomial curve γ_0 approximates the true local unstable manifold U well, then by thickening it slightly by a width ε, which in practice will be very small (10^{-12} and smaller), we obtain a thin parametrized rectangle P which has a chance to rigorously contain U. P mirrors the functional equation $f(U(t)) = U(\lambda_u t)$ of the true local manifold $U = U(t)$, i.e.*

$$f(P(t,s)) \approx \gamma_0(\lambda_u t),$$

up to some small contributions of size less than ε, and the difference bounds D_i in (4.12) can be very sharp.

Proof. First note that E is indeed an embedded rectangle, since P is bijective and smooth. Further note that the set $\gamma_0([-1,1]) + (D_1, D_2)^T$ contains the connected component of the unstable manifold in E containing the fixed point. Now suppose

$f(E) \cap \partial_h E \neq \emptyset$, then pick a point p in that intersection, and assume without loss of generality that $p \in \partial_u E$. Then by (4.12) we know $p = \gamma_0(t_0) + \delta$ for some $t_0 \in [-1,1]$ and $\delta_i \in D_i$ for $i = 1,2$.

There exists a curve segment $C \subset \partial_u E$ connecting p and $\zeta := \Big(\gamma_{0,1}(t_0), \gamma_{0,2}(t_0) + \varepsilon\Big)$. By the Mean Value Theorem we have a point $q = \Big(\gamma_{0,1}(t_2), \gamma_{0,2}(t_2) + \varepsilon\Big) \in C$, with $t_2 \in (\min\{t_0, t_1\}, \max\{t_0, t_1\})$, such that with the slope σ_q of the boundary $\partial_u E$ at q we have

$$\zeta_2 - p_2 = \varepsilon - \delta_2 = \sigma_q \cdot (\zeta_1 - p_1) = \sigma_q \cdot \delta_1.$$

Since $\partial_u E$ is γ_0 shifted vertically by ε, we simply have $\sigma_q = s_{\gamma_0}(t_2)$ and hence

$$\sigma_q \cdot \delta_1 + \delta_2 = s_{\gamma_0}(t_2) \cdot \delta_1 + \delta_2 = \varepsilon,$$

in contradiction to (4.13). □

With the last result we are now ready to verify the conditions in Thm. 4.4 using Taylor Model methods:

4.7 Corollary. *Let ε, γ_0 and P as in Lemma 4.5, and consider the Taylor Models*

$$\begin{aligned} T(t,s) &:= P(t,s) + \begin{pmatrix}[0,0]\\ [0,0]\end{pmatrix} = \begin{pmatrix}\gamma_{0,1}(t)\\ \gamma_{0,2}(t) + \varepsilon \cdot s\end{pmatrix} + \begin{pmatrix}[0,0]\\ [0,0]\end{pmatrix}, \\ \dot{\Gamma}_i(t) &:= \dot{\gamma}_{0,i}(t) + [0,0] \quad \textit{for } i = 1,2. \end{aligned}$$

Let $I_s^*, D_1^*, D_2^* \subset \mathbb{R}$ be interval range bounds such that

$$\begin{aligned} \frac{\dot{\Gamma}_2([-1,1])}{\dot{\Gamma}_1([-1,1])} &\subset I_s^*, \\ f_i\left(T\left(\frac{[-1,1]}{\lambda_u}, [-1,1]\right)\right) - \gamma_0([-1,1]) &\subset D_i^* \textit{ for } i = 1,2. \end{aligned}$$

If

$$\max\left\{\left|\min\left(I_s^* \cdot D_1^* + D_2^*\right)\right|, \max\left(I_s^* \cdot D_1^* + D_2^*\right)\right\} < \varepsilon$$

then $f(E) \cap \partial_h E = \emptyset$.

Proof. First note that $T(t,s)$ and $\dot{\Gamma}_i(t)$ are exact Taylor Model representations of the parametrized rectangle E and the curve derivatives $\dot{\gamma}_{0,i}$ for $i = 1, 2$, as the test curve γ_0 is constructed as a finite order polynomial. The rest follows directly from applying Lemma 4.5 using Taylor Model arithmetic. □

4.8 Proposition. *In the setting of Thm. 4.4, let again*

$$T(t,s) := P(t,s) + \begin{pmatrix}[0,0]\\ [0,0]\end{pmatrix} = \begin{pmatrix}\gamma_{0,1}(t)\\ \gamma_{0,2}(t) + \varepsilon \cdot s\end{pmatrix} + \begin{pmatrix}[0,0]\\ [0,0]\end{pmatrix},$$

be a Taylor Model representation of the set E. Assume that there are $S > 0$ and $M > 1$ such that there are interval range bounds on the derivatives over T given by

$$\max\left(\left|\partial_1 f_2\left(T\left([-1,1]^2\right)\right)\right| - \left|\partial_2 f_2\left(T\left([-1,1]^2\right)\right)\cdot[-S,S]\right|\right) < S,$$
$$\min\left(\left|\partial_1 f_1\left(T\left([-1,1]^2\right)\right)\right| - \left|\partial_2 f_1\left(T\left([-1,1]^2\right)\right)\cdot[-S,S]\right|\right) > M.$$

Then the conditions (4.8,4.9) hold.

Proof. Straightforward application of Taylor Model arithmetic on (4.8,4.9). □

4.9 Remark. *Finding a suitable slope bound S is not hard in practice. Due to the hyperbolic structure in the vicinity of the fixed point the derivative $\partial_1 f_1$ typically is large, and $\partial_2 f_2$ typically is small in absolute value, so that the relations (4.8,4.9) may hold true even for large test values $S > 1$. A good first candidate for S could be constructed as $\max_{t\in[-1,1]} \left|s_{\gamma_0}(t)\right|$ and subsequent inflation by some factor greater than one.*

Summing up this section, given an approximate test polynomial γ_0 and a thickening $\varepsilon > 0$ such that the Taylor Model interval range bounds in Corollary 4.7 and Proposition 4.8 are satisfied, then the true unstable curve leaves the thin parametrized rectangle constructed as in (4.10) through its vertical, and not its horizontal boundary.

4.2.2 Example: the Hénon map

As an example for the constructions we have developed so far we consider the Hénon map

$$H_{a,b}(x_1, x_2) := \left(1 + x_2 - a\, x_1^2, b x_1\right) \ . \tag{4.14}$$

Depending on the parameter choices for a and b, the map exhibits a wide range of dynamics (e.g., since $\det(DH) = -b$ everywhere, the parameter b determines volume-preservation etc.). The standard parameter values proposed by Hénon originally are $a = 1.4$ and $b = 0.3$. In this situation, H exhibits seemingly hyperbolic dynamics and a strange attractor. There are two hyperbolic saddle points p_1 and p_2, and we consider the manifold structure near $p_1 \approx (0.631354477089, 0.1894063431265)$.

Subsequently we reexpand the Hénon map around p_1 and shift it to the origin to obtain an origin-preserving version of H around p_1:

$$\begin{aligned}\tilde{H}_{a,b}(t_1, t_2) &:= H_{a,b}(p_{1,1} + t_1\,,\, p_{1,2} + t_2) - (p_{1,1}\,,\, p_{1,2}) \\ &= (-2\, a\, p_{1,1}\, t_1 + t_2 - a\, t^2, b\, t_1)\end{aligned}$$

For convenience, we will switch to diagonal coordinates at p_1, the construction of which can still be performed analytically in dependence on the parameters a and b. The Jacobian of $\tilde{H}_{a,b}$ is

$$D\tilde{H}_{a,b}(t_1, t_2) = \begin{pmatrix} -2\, a\, p_{1,1} - 2\, a\, t_1 & 1 \\ b & 0 \end{pmatrix}$$

and evaluated at the origin, this yields the eigenvalues

$$\lambda_{1,2} = a\, p_{1,1} \mp \sqrt{\left(a\, p_{1,1}\right)^2 + b} \Longrightarrow \lambda_1 \approx -1.92\,,\ \lambda_2 \approx 0.155$$

with corresponding normalized eigenvectors

$$\mathbf{e}_i = \left(\frac{\lambda_i}{b}\eta_i\,,\, \eta_i\right)^T \ , i = 1, 2,$$

where $\eta_i := \left(\left(\frac{\lambda_i}{b}\right)^2 + 1\right)^{-\frac{1}{2}}$. With these, we can set up the transformation matrices

$$M_{a,b} := \begin{pmatrix} \mathbf{e}_1 & \mathbf{e}_2 \end{pmatrix} = \begin{pmatrix} \frac{\lambda_1}{b}\eta_1 & \frac{\lambda_2}{b}\eta_2 \\ \eta_1 & \eta_2 \end{pmatrix} =: \left[M_{i,j}\right]_{i,j=1,2}$$

and the inverse

$$M_{a,b}^{-1} = \frac{b}{(\lambda_1 - \lambda_2)\ \eta_1\,\eta_2} \begin{pmatrix} \eta_2 & -\frac{\lambda_2}{b}\eta_2 \\ -\eta_1 & \frac{\lambda_1}{b}\eta_1 \end{pmatrix} =: \left[M_{i,j}^{-1}\right]_{i,j=1,2}$$

which will provide that $M_{a,b}^{-1} \circ \tilde{H}_{a,b} \circ M_{a,b}$ has diagonal linear part. We can perform the compositions explicitly as

$$\left(\tilde{H}_{a,b} \circ M_{a,b}\right)(t_1, t_2) = \begin{pmatrix} K_1\, t_1^2 \ +\ K_2\, t_1 \ +\ K_3\, t_1\, t_2 \ +\ K_4\, t_2 + \ K_5\, t_2^2 \\ K_6\, t_1 \ +\ K_7\, t_2 \end{pmatrix},$$

where

$$\begin{aligned} K_1 &:= -a\, M_{11}^2 & K_5 &:= -a\, M_{12}^2 \\ K_2 &:= -2\, a\, p_{1,1}\, M_{11} + M_{21} & K_6 &:= b\, M_{11} \\ K_3 &:= -2\, a\, M_{11} M_{12} & K_7 &:= b\, M_{12} \\ K_4 &:= -2\, a\, p_{1,1}\, M_{12} \ +\ M_{22} \end{aligned}$$

and subsequently

$$\left(M_{a,b}^{-1} \circ \left(\tilde{H}_{a,b} \circ M_{a,b}\right)\right)(t_1, t_2) = \begin{pmatrix} \lambda_1 & 0 \\ 0 & \lambda_2 \end{pmatrix} \cdot \begin{pmatrix} t_1 \\ t_2 \end{pmatrix} + \begin{pmatrix} J_1\, t_1^2 \ +\ J_2\, t_1\, t_2 \ +\ J_3\, t_2^2 \\ J_4\, t_1^2 \ +\ J_5\, t_1 t_2 \ +\ J_6\, t_2^2 \end{pmatrix} \tag{4.15}$$

where

$$\begin{aligned} J_1 &:= M_{11}^{-1}\, K_1 & J_4 &:= M_{21}^{-1}\, K_1 \\ J_2 &:= M_{11}^{-1}\, K_3 & J_5 &:= M_{21}^{-1}\, K_3 \\ J_3 &:= M_{11}^{-1}\, K_5 & J_6 &:= M_{21}^{-1}\, K_5 \end{aligned} .$$

For convenience, we again denote the transformed map $\left(M_{a,b}^{-1} \circ \tilde{H}_{a,b} \circ M_{a,b}\right)$ by $\tilde{H}_{a,b}$. Note that the linear part of $\tilde{H}_{a,b}$ is now diagonal, due to the first order

normal form transformation, and furthermore that all coefficients J_i are still analytic expressions solely in terms of a and b. For the cone type argument we consider the Jacobian of the transformed map

$$D\tilde{H}_{a,b}(t_1,t_2) = \begin{pmatrix} 2\,J_1\,t_1 + \lambda_1 + J_3\,t_2 & J_3\,t_3 + 2\,J_4\,t_2 \\ 2\,J_5\,t_1 + J_6\,t_2 & J_6\,t_1 + \lambda_2 + 2\,J_8\,t_2 \end{pmatrix}$$

Evaluating the formula (4.15) with our parameters yields the approximate linearly diagonalized Hénon map in the new coordinates as

$$\tilde{H}_{a,b}(t_1,t_2) \approx \begin{pmatrix} -1.92 & 0 \\ 0 & 0.16 \end{pmatrix} \cdot \begin{pmatrix} t_1 \\ t_2 \end{pmatrix} + \begin{pmatrix} -1.28\,t_1^2 + 1.19\,t_1\,t_2 - 0.29\,t_2^2 \\ 0.22t_1^2 + 0.21\,t_1t_2 - 0.05\,t_2^2 \end{pmatrix}.$$

We performed a 20th order computation as outlined in section 4.2 for TM-enclosures for the local stable and unstable manifolds over parameters $(t,s) \in [-0.2,0.2]^2$. Linearly transforming back into the natural coordinate system, we obtain Taylor Model enclosures T_u and T_s for pieces of the local unstable and stable manifolds of finite length as depicted in Figure **??**.

In the following we list the actual Taylor Models for manifold enclosures. Note that per the construction in Corollary 4.7 and Proposition 4.8, they are outfitted with a zero-width remainder bound, however due to the implementation of rigorous outward rounding in COSY Infinity [15], the depicted remainder bound has a width just above the machine accuracy threshold.

The Taylor Models for $T_{u,1}$ is:

TM VARIABLE:		NO=20	NV=2	
I	COEFFICIENT	ORDER	EXPONENTS	
1	0.6313544770895047	0	0	0
2	-.1976115511989409	1	1	0
3	-.1014764915954764E-01	2	2	0
4	0.1057527102942118E-02	3	3	0
5	0.2855780728643021E-04	4	4	0
6	-.1866238471492046E-05	5	5	0

...

REMAINDER BOUND INTERVAL:

[-.6012505080026924E-291,0.6012505080026924E-291]

We see $T_{u,1}$ is centered at the fixed point, has a dominant linear part and only dependence on the longitudinal parameter t.

For the vertical component $T_{u,2}$:

TM VARIABLE:		NO=20	NV=2	
I	COEFFICIENT	ORDER	EXPONENTS	
1	0.1894063431268514	0	0	0
2	0.3081679465402512E-01	1	1	0
3	0.3200000000000000E-14	1	0	1
4	-.8226109067472505E-03	2	2	0
5	-.4456299883934181E-04	3	3	0
6	0.6255494451670481E-06	4	4	0

...

REMAINDER BOUND INTERVAL:

[-.6012505080026924E-291,0.6012505080026924E-291]

Again $T_{u,2}$ has no s-dependence except for the linear term $0.32 \cdot 10^{-14} \cdot s$ according to the choice in Eq.(4.10). So in this case the accuracy with which T_u encloses $W^u_{loc}(p)$ is $\varepsilon = 0.32 \cdot 10^{-14}$.

Analogously we have the component $T_{s,1}$:

TM VARIABLE:		NO=20	NV=2	
I	COEFFICIENT	ORDER	EXPONENTS	
1	0.6313544770895047	0	0	0
2	0.1024000000000000E-12	1	1	0
3	-.9224555310786783E-01	1	0	1
4	0.1129853346959211E-02	2	0	2
5	-.3773693602439372E-05	3	0	3
6	0.5463903367657585E-08	4	0	4
...				

REMAINDER BOUND INTERVAL:
[-.6012505080026924E-291,0.6012505080026924E-291]

This time $T_{s,1}$ has no t-dependence except in the linear term, analogous to $T_{u,2}$, except in $\hat{e}_1$-direction.The obtained enclosure accuracy is $\varepsilon = 0.1024 \cdot 10^{-12}$, significantly worse than in the unstable case. This is likely a consequence of the much stronger expansion of the inverse Hénon map near p than the map itself.

Lastly, the component $T_{s,2}$:

TM VARIABLE:		NO=20	NV=2	
I	COEFFICIENT	ORDER	EXPONENTS	
1	0.1894063431268514	0	0	0
2	-.1774563550054591	1	0	1
3	0.1393776240096155E-01	2	0	2
4	-.2985124704889843E-03	3	0	3
5	0.2771556369100959E-05	4	0	4
6	-.1335693482088341E-07	5	0	5
...				

REMAINDER BOUND INTERVAL:
[-.6012505080026924E-291,0.6012505080026924E-291]

4.3 Global manifold tangles

In the previous section we have demonstrated how the local invariant manifolds near a hyperbolic fixed point can be enclosed sharply using Taylor Model approximations.

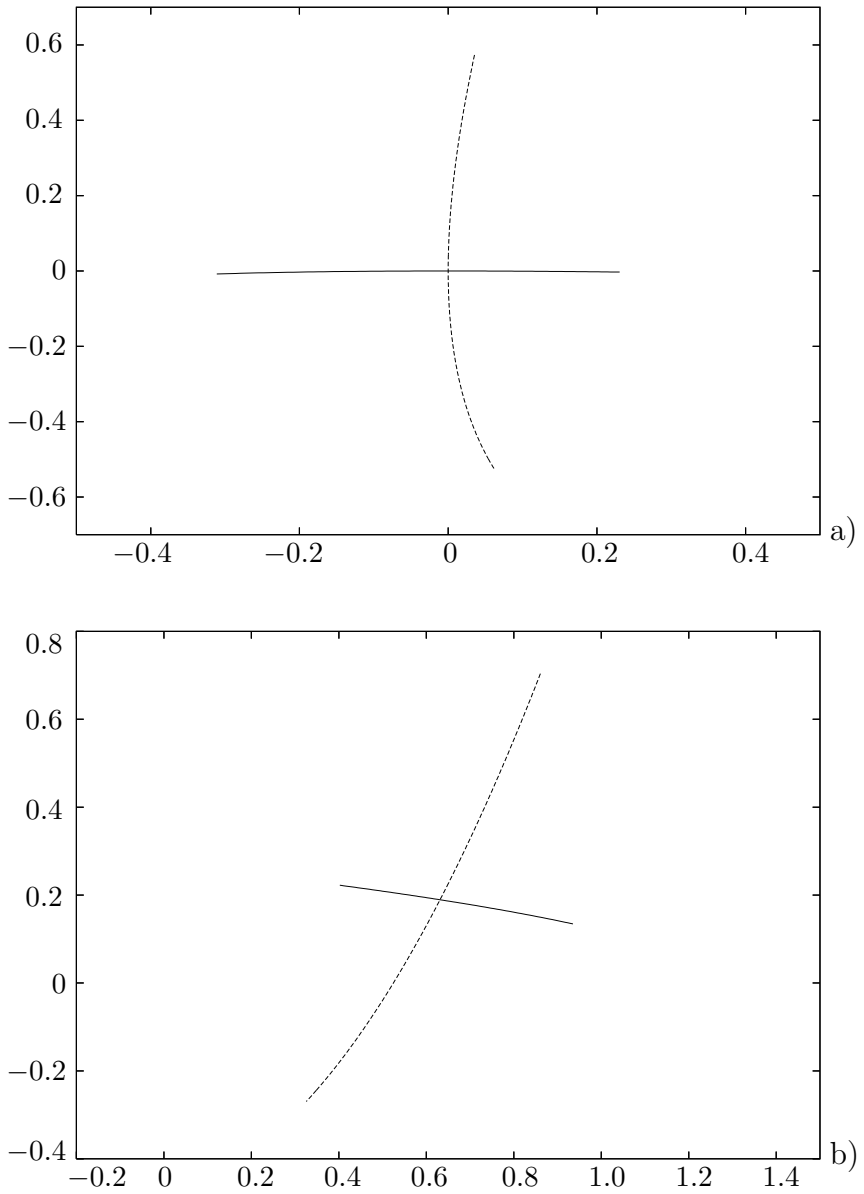

Figure 4.4. In **a**) the enclosures of the local unstable (solid) and stable (dashed) manifold near the origin are plotted. In **b**) we see the local manifold enclosures T_u and T_s from section 4.2.1 around the fixed point $p_0 \approx (-.63, 0.18)$ and retransformed into the original coordinate system.

We can now proceed to generate significant pieces of the global manifold structure simply by iteration. Iterating the Taylor Model enclosures of the unstable manifold through the map f or the stable manifold enclosures through the inverse f^{-1} in Taylor Model arithmetic will yield valid Taylor Model enclosures of successively larger global manifold pieces.

In practice, this approach requires a bisection and reparametrization of the Taylor Model enclosures of the manifolds, even though the initial basic premise is retained in spirit. The fundamental problem is the blow-up of the remainder bound size under iteration, which is caused by two main factors.

1. If the map f (or its inverse) is volume-expanding and the unstable (or stable) manifold is repelling, then the Taylor Model enclosure of said manifold must also expand, by the inclusion property. In this case actually not only the remainder bound increases in size, but the polynomial part as well.

2. The remainder bound grows disproportionally if the truncation error between the true manifold and the polynomial part of the Taylor model enclosure becomes large. This is the case when the manifold parametrization can only unsatisfactorily be modeled by a polynomial of finite order, for instance when the true manifold grows exponentially in length under iteration, or if it makes sharp turns. Thus, the truncation error is primarily scaling with the longitudinally parametrizing variable of the Taylor model.

The first issue can not be controlled through any sophisticated manipulation of the TM manifold enclosure, since the expansion is an intrinsic property of the map. The only way to obtain sharp estimates even for higher iterates is to increase the computation order and to employ high-precision or arbitrary-precision arithmetic, so that the initial Taylor Model enclosure of the local invariant manifold is sharper to begin with.

The second problem, however, can be remedied. The solution to keeping the truncation error size in check is to rescale and locally reexpand the polynomial approximation:

4.10 Algorithm. *Let $T = P_T(t,s) + I_T$ be a Taylor Model enclosure containing a piece of unstable manifold, and parametrized longitudinally by the variable t . Let $\delta > 0$ be the desired threshold of the C^0-approximation of the unstable manifold by the TM-enclosures, i.e. the maximal size of the remainder bounds. Let $M \in \mathbb{N}$ be the maximal number of bisection steps (typically $M < 10$). To generate TM-enclosures of new pieces of unstable manifold, execute the following algorithm:*

1. *Compute $f(T) =: P_{f(T)} + I_{f(T)}$ in Taylor Model arithmetic. If $\left|I_{f(T)}\right| \leq \delta$, the iteration is successful.*
2. *If $\left|I_{f(T)}\right| > \delta$, split and reparametrize the TM T as $T_1 := P_T\left(-\frac{1}{2} + \frac{t}{2}\right) + I_T$ and $T_2 := P_T\left(\frac{1}{2} + \frac{t}{2}\right) + I_T$, with $t \in [-1,1]$.*
3. *Compute $f(T_1) =: P_{f(T_1)}(t,s) + I_{f(T_1)}$ and $f(T_2) =: P_{f(T_2)}(t,s) + I_{f(T_2)}$. If $\left|I_{f(T_1)}\right| \leq \delta$ and $\left|I_{f(T2)}\right| \leq \delta$, the iteration is successful.*
4. *If $\left|I_{f(T_1)}\right| > \delta$ or $\left|I_{f(T_2)}\right| > \delta$, repeat iteration from step 2.*
5. *If after M subdivisions not all remainder bounds are of width less than δ, either stop iteration or increase δ.*

The algorithm can be performed analogously for the stable manifold enclosures with the inverse map.

This algorithm generates an ordered list of local Taylor Model enclosures $\{T_1, ..., T_K\}$, the union of which still contains the true manifold $f(U) \subset \bigcup_{j=1}^{K} T_j$, instead of one big Taylor Model which fails to sharply enclose the manifold iterate.

While this particular algorithm only factors in the remainder bound size of the iterated manifold enclosures as the benchmark of where and how to bisect and reexpand the Taylor Model pieces, more sophisticated bisection methods can be implemented that take into account information like length, length growth or curvature.

We infer that under repeated iteration this algorithm inductively computes an ordered list of $K(n)$ Taylor Models $\left\{T_j\right\}_{j=1}^{K(n)}$ such that for the n-th iterate we have

$$f^n\left(W^u_{loc}(p)\right) \subset \bigcup_{j=1}^{K(n)} T_j.$$

4.3.1 Discarding manifold pieces

In this section we discuss a criterion which allows us to discard large subsets of the global manifold tangle in certain special cases, easing the computational workload and memory requirement substantially.

In the following let $f : \mathbb{R}^v \supseteq D \longrightarrow D$, where D is open, be a C^r-diffeomorphism. We first introduce the notion of an attractor:

4.11 Definition. *(Attractor) An attractor for f is a compact set $A \subset \mathbb{R}^v$ that has an open neighborhood $V \subseteq \mathbb{R}^v$ such that $f^K(V) \subset V$ for some $K \in \mathbb{N}$ and $A = \bigcap_{k\in\mathbb{N}} f^k(V)$.*

The set $B_A := \bigcup_{k\in\mathbb{N}} f^{-k}(V)$ is called the basin of A.

It is clear that A is invariant under f and that all orbits starting in B_A converge to A.

Consider now the case where f is volume-decreasing, i.e. the determinant $\|\det(Df(x))\| < 1 \,\forall\, x \in D$. In this case, the unstable manifolds may be bounded (in particular they may be contained in an attractor), but in turn this means that the inverse map is expanding and the stable manifolds can be unbounded. An example for this phenomenon is the Hénon map $H_{a,b}$ with standard parameters $a = 1.4$ and

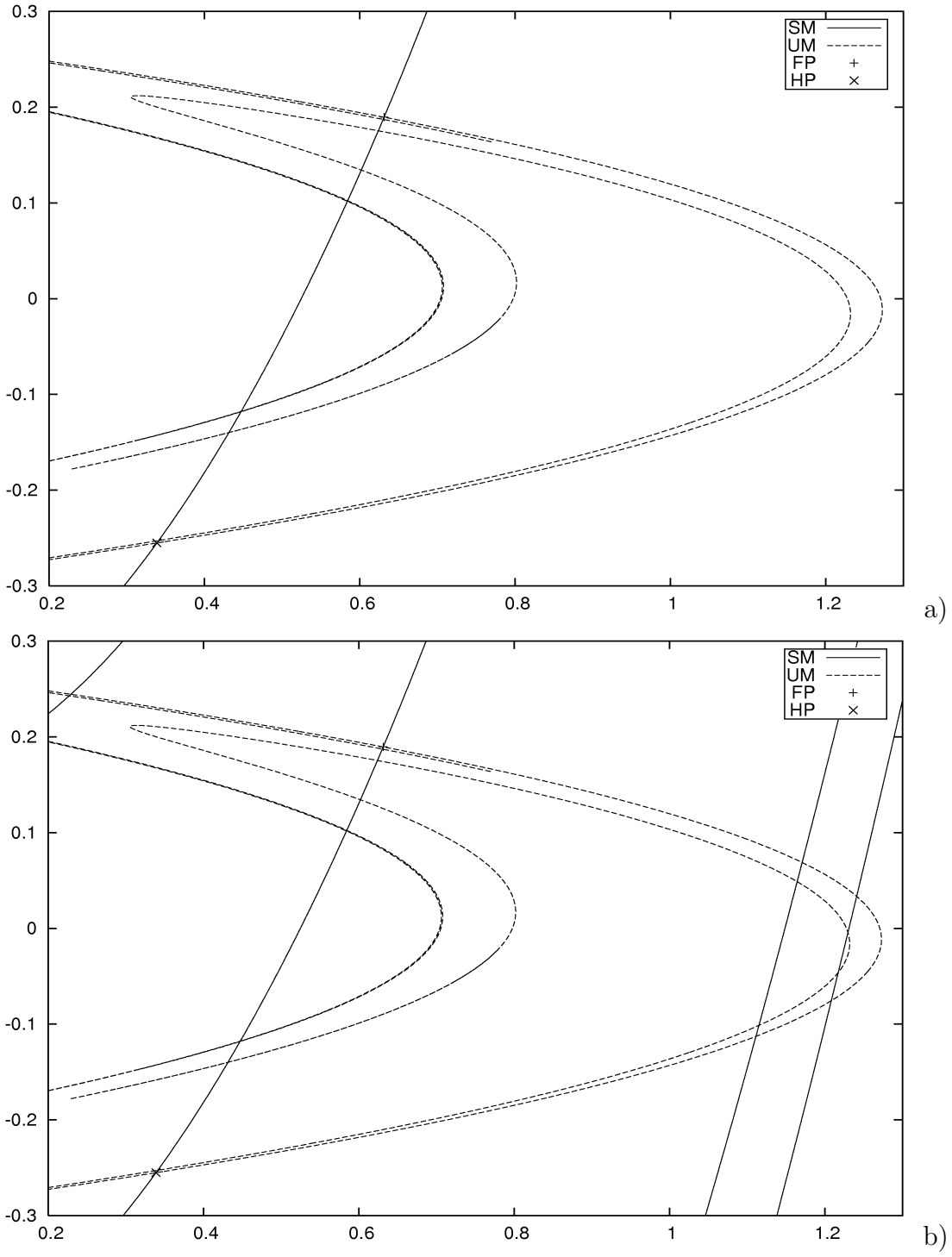

Figure 4.5. (**a** a local stable manifold segment (solid) of the Hénon map $H_{a,b}$ for $a = 1.4$, $b = 0.3$, together with the unstable manifold (dashed). The actual Taylor Model enclosures are several orders of magnitude below printer resolution in size. In (**b**) the 3rd preimage of the stable segment is shown.

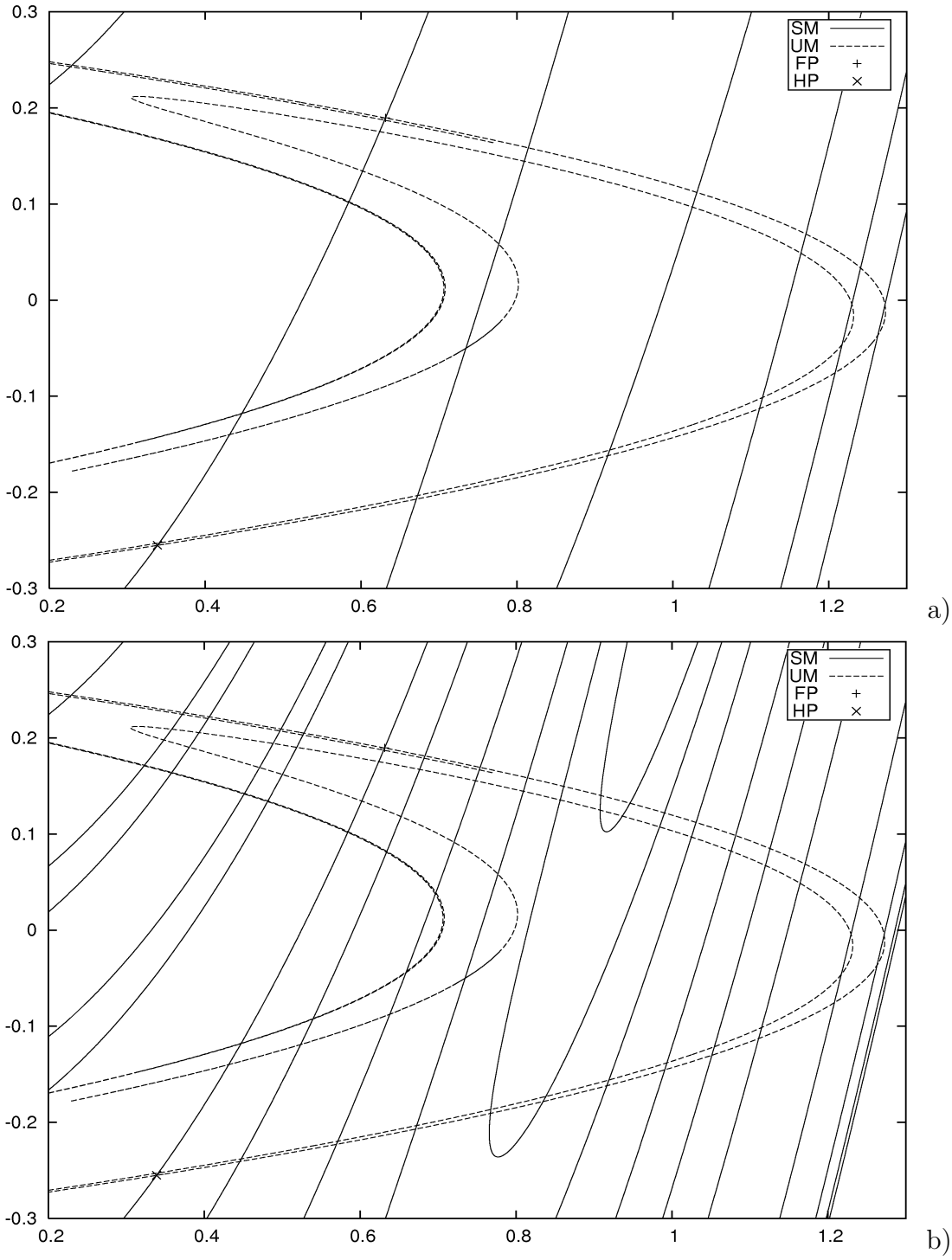

Figure 4.6. 4th (**a**) and 6th (**b**) preimages of the local stable manifold segment (solid), together with the unstable manifold (dashed).

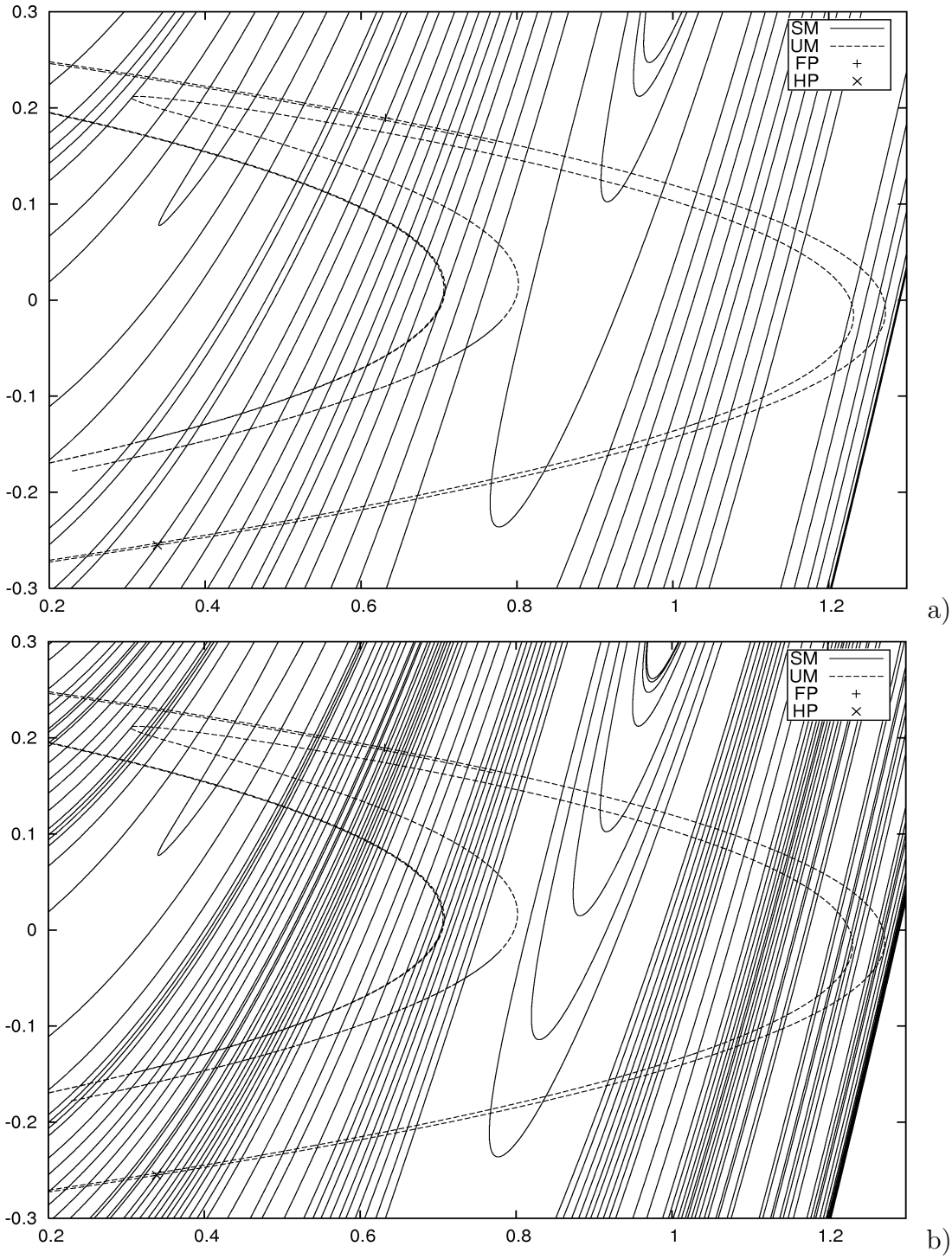

Figure 4.7. 8th (**a**) and 10th (**b**) preimages of the local stable manifold segment (solid), together with the unstable manifold (dashed).

$b = 0.3$, in which the determinant of the Jacobian $\left\|\det\left(DH_{a,b}\right)\right\| = b < 1$ everywhere. Here, numerical experimentation suggests that the unstable manifold of both fixed points is bounded and contained in an attractor with an unbounded basin. The stable manifold is contained within the basin, but extends very far, loosely speaking 'to near-infinity' (the Lipschitz constant of $H_{a,b}$ is unbounded) , before returning to the attractor to form homo-/heteroclinic intersections and running off again. From a practical point of view, in particular with respect to a verified Taylor Model enclosure of the stable manifold, this behavior is disheartening, as there is little chance to sharply bound truncation errors of polynomial approximations for curves which exhibit accelerating length-growth.

However, in the volume-decreasing case we may be able to determine a trapping region in the neighborhood of an attractor:

4.12 Definition. *(Trapping region) A trapping region is a nonempty compact subset $E \subseteq D$ such that $f(E) \subset E$.*

A trapping region E always contains a fixed point by Schauder's Theorem (2.29), and in particular contains the global unstable manifold $W^u(p)$ for any hyperbolic fixed point $p \in E$. If we are interested in the homoclinic intersections of $W^s(p) \cap W^u(p)$, and we iteratively generate $W^s(p)$ as $f^{-n}\left(W^s_{loc}(p)\right)\ n \overrightarrow{\to} \infty\ W^s(p)$, we indeed only need to iterate stable manifold segments which are contained in E:

4.13 Proposition. *Let f, D, E as above, let $p \in E$ be a hyperbolic fixed point, and let $x \in W^s(p)$. If $f^{-k_0}(x) \notin E$ for some $k_0 \geq 0$, then also $f^{-k}(x) \notin E \,\forall\, k > k_0$.*

Proof. If there were any $k > k_0$ such that $f^{-k}(x) \in E$, then also every image of $f^{-k}(x)$ is contained in E, in particular $f^{k-k_0}\left(f^{-k}(x)\right) = f^{-k_0}(x) \in E$, a contradiction. □

In practice this means that in order to generate branches of the stable manifold for the purpose of studying the homoclinic tangle, we may discard any stable manifold

branch which gets mapped outside the trapping region, or in particular outside any superset of a trapping region.

In the case of the Hénon map $H_{a,b}$, a set of three parallelepipeds E_1-E_3 (cf. Figure 4.8**a**) was identified by K. Makino which could be shown to contain its fifth Hénon iterate (cf. Figures 4.8**b** and 4.9). We will not denote the exact specifications of the parallelepipeds here, but instead state the following result which has been verified using Taylor Model iteration:

4.14 Proposition. *The sets E_1-E_3 satisfy*

$$H_{a,b}^5 (E_1 \cup E_2 \cup E_3) \subset (E_1 \cup E_2 \cup E_3) ,$$

and hence the set

$$E := \bigcup_{i=0}^{4} H_{a,b}^i (E_1 \cup E_2 \cup E_3)$$

is a trapping region for $H_{a,b}$.

It can be shown that the set E is contained within the interval box $I_D := [-1.5, 1.5] \times [-0.5, 0.5]$, and in the generation of the stable manifolds from Figures 4.5-4.7 one is allowed to discard and not further propagate all Taylor Model pieces getting mapped outside I_D. We note that this discarding criterion is still somewhat crude, and a more sophisticated test to discard stable manifold segments outside the region of interest can be formulated: Since the set E consist essentially of the parallelepipeds E_1-E_3, it can be bounded sharply by a superset consisting of slightly inflated parallelepipeds which capture the structure of E more finely than I_D. The rigorous test which segments of a Taylor Model curve lie outside a parallelepiped is however only marginally more difficult than the same test for an interval box.

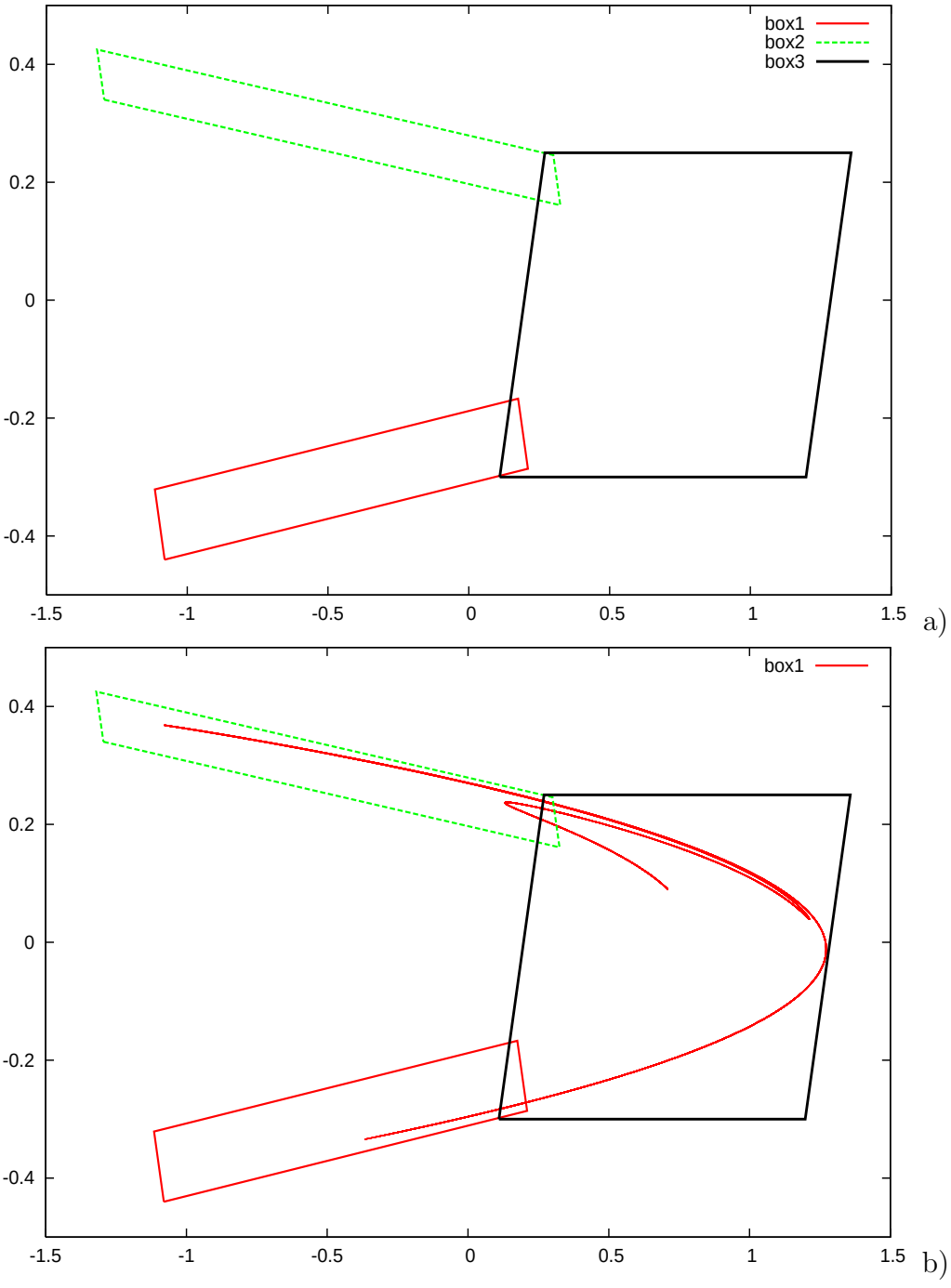

Figure 4.8. **a**) The parallelepipeds E_1 (red), E_2 (green, dashed) and E_3 (black, bold) contain the Hénon attractor and form the basis for a trapping region. **b**) The fifth iterate $H^5_{a,b}(E_1)$ (red) is contained in $(E_1 \cup E_2 \cup E_3)$. (Pictures courtesy of K. Makino)

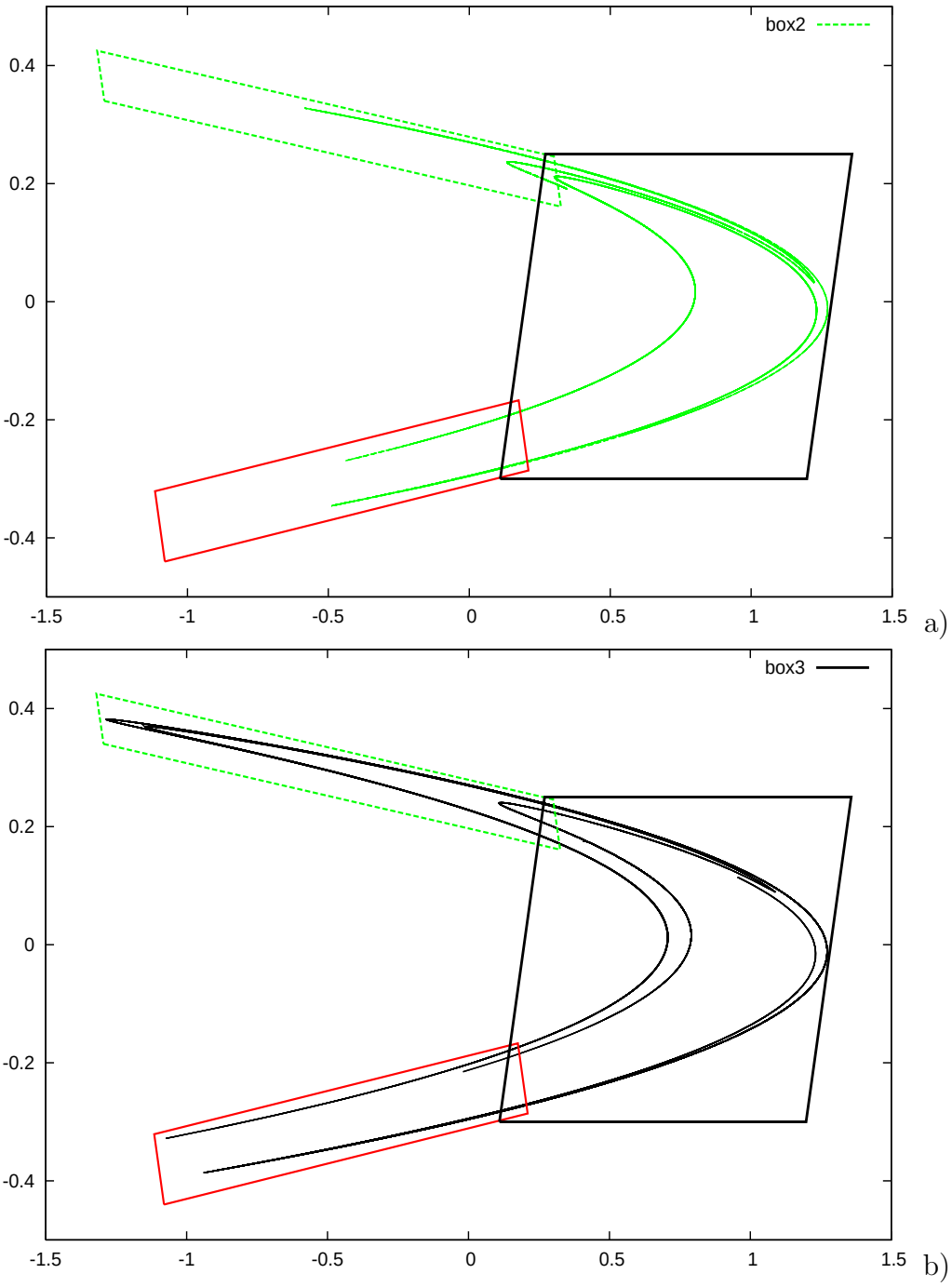

Figure 4.9. **a**) The fifth iterate $H^5_{a,b}(E_2)$ (green, dashed) is contained in $(E_1 \cup E_2 \cup E_3)$. **b**) The fifth iterate $H^5_{a,b}(E_3)$ (black, bold) is contained in $(E_1 \cup E_2 \cup E_3)$. (Pictures courtesy of K. Makino)

4.4 Computation of homoclinic point enclosures

In the preceding sections we have presented a technique to get verified TM-enclosures of the invariant manifolds near a hyperbolic fixed point p, as well as a propagation scheme which yields an ordered list of TMs which rigorously enclose finite forward (inverse) images of the unstable (stable) manifold pieces at p, up to a finite number of iterates.

In the following we will describe a simple way of computing sharp interval bounds of the homoclinic intersection points of these parts of the invariant manifolds of p, with the added advantage that the compuation can be automated in a straightforward fashion. In other words, we are confident that this technique is suitable to compute all intersection points of particularly long pieces of the invariant manifolds of p. Naturally, the approach can readily be extended to compute heteroclinic intersection points of two stable and unstable manifold pieces belonging to two different hyperbolic fixed points, but for brevity we will only consider homoclinic intersections of the manifold tangle of a single fixed point p.

The knowledge about homoclinic points is of course valuable in itself, since there are numerous deep questions in the study of hyperbolic and chaotic dynamics directly related to their existence, abundance and mapping properties. But for the purpose of this presentation, the added benefit is that the quality of a numerical approximation of a homoclinic point can readily be checked through various quantitative techniques, which will give us good tests to assess the accuracy of the TM-manifold-enclosures that are used to compute the homoclinic points in the first place.

4.4.1 Verification of existence of homoclinic points

Assume we are given TM-enclosures of two pieces of the planar unstable and stable manifold which are known to intersect. Let these TMs be parametrized as $T_1(t, s) =$

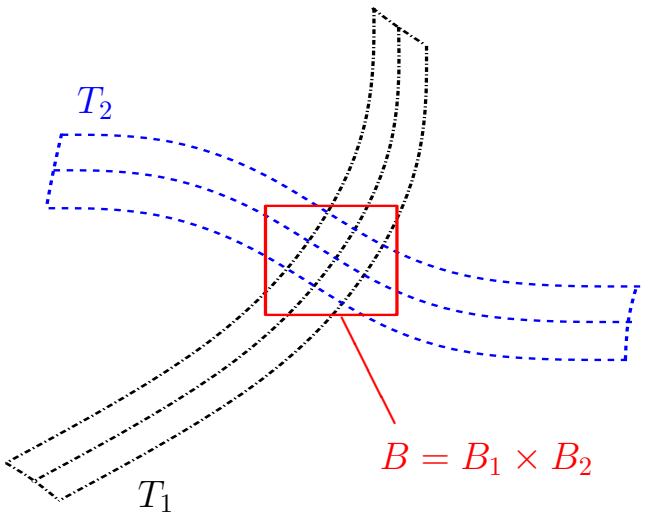

Figure 4.10. Transverse crossing of two Taylor Models T_1 (dash-dotted) and T_2 (dashed). Their intersection can be enclosed into an interval box B (red, solid) which contains the homoclinic intersection of the true manifold pieces contained in T_1 and T_2.

$P_1(t,s) + I_1$ and $T_2(t,s) = P_2(t,s) + I_2$, with t and s as longitudinal parameters respectively, where $(t,s) \in [-1,1]^2$.

We note that as representations of two-dimensional sets, P_1 and P_2 overlap over a range of parameters, as depicted in Figure 4.10. However, as the Taylor Models enclosing the manifold pieces are very thin (transverse width is several orders of magnitudes smaller than length), as a first step we may assume there is a single point (t_0, s_0) at which $P_1(t_0, s_0) \approx P_2(t_0, s_0)$. There are straightforward ways how (s_0, t_0) can be determined sharply, for example as a two-dimensional global optimization problem minimizing the distance between T_1 and T_2, or a suitable Newton-type iteration once one is near the intersection point of the polynomial parts. Note that (t_0, s_0) need not be known rigorously.

Let us furthermore assume that T_1 and T_2 have been reexpanded around (t_0, s_0), so that their intersection point is close to the origin, and that we have performed a linear transformation on T_1 and T_2 with their inverse linear parts, which means that

T_1 and T_2 are tangent to the x_1- and x_2-axes at the origin, respectively.
For easy of notation we also assume orientation such that

$$T_{1,1}(-1, s_0) < T_{1,1}(t_0, s_0) < T_{1,1}(1, s_0),$$
$$T_{2,2}(t_0, -1) < T_{2,2}(t_0, s_0) < T_{2,2}(t_0, 1),$$

but the following algorithm can easily be generalized to arbitrary orientations. We use $T_{i,j}$ for the j-th component of the TM T_i, i.e. $T_{i,j} = P_{i,j}(t, s) + I_{i,j}$.

4.15 Algorithm. *First check that*

$$\left(\max\left(T_{1,1}\left(\{-1\} \times [-1,1]\right)\right) < \min\left(T_{2,1}\left([-1,1]^2\right)\right)\right)$$
$$\wedge \left(\max\left(T_{2,1}\left([-1,1]^2\right)\right) < \min\left(T_{1,1}\left(\{1\} \times [-1,1]\right)\right)\right)$$

and that

$$\left(\max\left(T_{2,2}\left([-1,1] \times \{-1\}\right)\right) < \min\left(T_{1,2}\left([-1,1]^2\right)\right)\right)$$
$$\wedge \left(\max\left(T_{1,2}\left([-1,1]^2\right)\right) < \min\left(T_{2,2}\left([-1,1] \times \{1\}\right)\right)\right)$$

Then the intersection contains a homoclinic point h. Furthermore, we can sharpen the interval enclosure of h by iterating the following algorithm:

1. *Compute the range bound in x_1-direction $T_{2,1}\left([-1,1]^2\right)$.*

2. *If there are $-1 < \theta_l < \theta_u < 1$ such that*

$$\left(\max\left(T_{1,1}\left([-1,\theta_l] \times [-1,1]\right)\right) < \min\left(T_{2,1}\left([-1,1]^2\right)\right)\right)$$
$$\wedge \left(\max\left(T_{2,1}\left([-1,1]^2\right)\right) < \min\left(T_{1,1}\left([\theta_u,1] \times [-1,1]\right)\right)\right)$$

   reexpand T_1 around $t_1 \longrightarrow \frac{\theta_u - \theta_l}{2} + \frac{\theta_u - \theta_l}{4} t_1$.

3. *Repeat from step 1, but switch the indices 1 and 2 in both the TMs T_1, T_2 and their components, and the variables t and s.*

4. *Stop the algorithm if step 2 cannot be performed successfully or if the widths of* $T_{1,1}\left([-1,1]^2\right)$ *and* $T_{2,2}\left([-1,1]^2\right)$ *undercut the desired accuracy threshold.*

It is of note that the heuristic determination of $\theta_{l,u}$ in step 2 can be done somewhat 'optimally' if we use the map inversion tools which are available in DA-arithmetic. The values

$$\theta_l \approx P_{1,1}^{-1}\left(\min(T_{2,1}([-1,1])^2), 0\right)$$
$$\theta_u \approx P_{1,1}^{-1}\left(\max(T_{2,1}([-1,1])^2), 0\right)$$

are a good initial guess for $\theta_{l,u}$, possibly after a slight inflation by 10 percent or so.

To give an example for the performance of the last algorithm we return to the Hénon map. It is not immediately clear what it means to rigorously enclose homoclinic points in this case, as these are dense in the unstable manifold and hence any interval enclosure with nonempty intersection with the unstable manifold contains homoclinic points. However, we can enclose specific homoclinic points, as follows:
In the global manifold tangle constructed in the previous section we see that successive iteration of the TM-enclosures of the local stable and unstable manifolds at the fixed point p_1 through the map $H_{a,b}$ or the inverse $H_{a,b}^{-1}$ seems to generate the 'first' (in the sense of arclength) homoclinic intersection point of the iterated TM-enclosures, which we call q_1, at about $(0.33, -0.25)$. Applying the above sharpening algorithm, we are able to assert existence of such a point in a quite sharp interval box enclosure of width $\approx 10^{-12}$:

4.16 Theorem. *In the standard Hénon map (4.14), the transverse homoclinic intersection* q_1 *of* W^u *and* W^s *of the hyperbolic fixed point* $p_1 \approx (0.63, 0.18)$ *is contained within the interval box*

$$([0.338852549387, 0.33885254939], [-0.255112629783, -0.2551126297832]) \ . \quad (4.16)$$

4.4.2 Numerical tests

The rigorous homoclinic point enclosures from the last section serve as an excellent litmus test for the claimed accuracy of the manifold enclosure themselves, and various *a posteriori* tests to check the quality of the homoclinic point enclosure can be performed to support the sharpness of the interval enclosure. Unfortunately, no analytic formula for the coordinates of the true homoclinic point of the Hénon map near $(0.35, -0.25)$ exist, so we have to resort to some nonverified, but quantitative numerical experiments to corroborate the statement 4.16.

In the following we assume that p is a hyperbolic fixed point of a planar diffeomorphism $f : \mathbb{R}^2 \longrightarrow \mathbb{R}^2$ with eigenvalues $0 < |\lambda_1| < 1 < |\lambda_2|$ of $Df_p(0)$, h_t is a true homoclinic point in $W_p^s \cap W_p^u$, and h_c is a computed numerical approximation of h_t. It is clear that there are completely analogous method to estimate the displacement of h_c from the unstable manifold by correspondingly using f^{-1} instead of f.

Theorem 4.16 must hold true by virtue of every step in algorithm 4.15 having been performed in Taylor Model arithmetic. However, there are nonverified numerical techniques that can substantiate the claim of the theorem in an intuitive manner. Define the midpoint of the homoclinic point enclosure (4.16) as

$$h_c := (0.3388525493875, -0.25511262978315)\,, \tag{4.17}$$

and let h_t be a the true homoclinic point q_1 contained in (4.16).

Number of forward iterates near fixed point as a measure

The first very simple and straightforward method to measure the quality of h_c is the number of forward iterates that stay within a neighborhood of p. Since h_c is close to h_t, the images $f^k(h_c)$ first converge to p_1 along the stable manifold and, once near p_1, get pulled away from p_1 again along W_p^u with a factor of $\approx |\lambda_1|$ in every iteration for the distance to W_p^s . If we consider the maximal number K of iterations such

that the forward iterates $f^k(h_c)$ do not leave a ball $B_\delta(p)$ for $k \leq K$ (where δ is reasonably small, say $\delta \approx 0.1$), then we know that the original displacement of h_c from W_p^s, or from h_t respectively, can be approximately be expressed as

$$d(h_c, h_t) \approx dist(h_c, W_p^s) \approx \frac{\delta}{|\lambda_1|^K}. \tag{4.18}$$

In the example above with $f = H_{a,b}$, $|\lambda_1| \approx 1.92$ and $\delta = 0.1$, we get $K = 40$, i.e.

$$d(h_c, h_t) \approx 0.1/(1.92)^{40} \approx 0.4655 \cdot 10^{-13} \tag{4.19}$$

which is compatible with the claimed sharpness of the enclosure from Theorem 4.16.

Monitoring of distance to stable manifold under forward iteration

The second method is very much similar in spirit to the first one, but with a more accurate numerical result for the original displacement of h_c from W_p^s, and hence h_t. The reason why the first method only gives a rough estimate about $d(h_c, h_t)$ is that the expansion of the distance of $f^k(h_c)$ to the stable manifold only goes with a factor of $|\lambda_1|$ in the higher iterates where $k \approx K$, i.e. where $f^k(h_c)$ is near p. For the lower iterates with small k, while there still is expansion of $dist(f^k(h_c), W_p^s)$ in principle due to the hyperbolic structure of the system near W_p^s, that expansion factor need not be $|\lambda_1|$, which when combined as in eq.(4.18) can produce errors in the range of one order of magnitude.

The approach for a more plausible estimate of $d(h_c, h_t)$ is to monitor the contraction of $dist(f^k(h_c), W_p^s)$ for every iterate $0 \leq k \leq K$, and keep track of all shrinking factors. In the following we outline the algorithm:

1. Let $\gamma(t)$ be the polynomial part of the TM-enclosure of W_p^s between h_t and p. Define $h_0 := h_c$.

2. For $0 \leq n \leq K - 1$: Let $h_n := f(h_{n-1})$. Compute the perpendicular unit vector u_n from h_n to γ by minimizing the scalar product $|\langle \dot{\gamma}(t), \gamma(t) - h_n \rangle|$ over

the parameter t at t_n. Set $u_n := \gamma(t_n) - h_n \cdot (|\gamma(t_n) - h_n|)^{-1}$. Evaluate the Jacobian $Df(h_n)$ and compute the length growth factor $k_n := |Df(h_n) \cdot u_n|$.

3. Approximate $d(h_c, h_t) \approx dist(h_K, W_p^s) \cdot \left(\prod_{n=0}^{K-1} k_n \right)^{-1}$.

In our present case with h_c as in (4.17), $h_t = q_1$ and $K = 40$we obtain a numerical value

$$d(h_c, h_t) \approx 0.897 \cdot 10^{-13}$$

which is again in agreement with the previous rigorous claim.

Mapping to different sides of the stable manifold

Considering the computed point h_c and the tangent direction of the stable manifold near h_c, we can construct another point $\tilde{h}_c$ that has been translated perpendicularly to the manifold tangent from h_c by a small (positive or negative) length l roughly of the size of the expected displacement $dist(h_c, W_p^s)$. If indeed the points h_c and $\tilde{h}_c$ lie on different sides of the manifold, then so will all their forward iterates. In other words, once the points $f^k(h_c)$ and $f^k(\tilde{h}_c)$ get near p, their images slowly drift away from each other to follow different branches of the unstable manifold under subsequent iteration, which can be observed by simply printing the iterates of both points to the screen. If this diverging behavior of $f^k(h_c)$ and $f^k(\tilde{h}_c)$ persists, the true set W_p^s has to be within $|l|$ of h_c.

Returning to the claimed homoclinic point interval enclosure in Theorem 4.16, its top left and right cornerpoints were mapped successively by the squared Hénon map $H_{a,b}^2$ (to avoid confusing switching of sides of the iterates) as depicted in Figure 4.11**a**. Likewise, Figure 4.11**b** shows the iterates by $H_{a,b}^{-2}$ of the right top and bottom cornerpoints of the interval box. In both cases we see that the iterates follow different branches of the unstable and stable manifold near the fixed point, respectively, which is again compatible with the claim of Theorem 4.16.

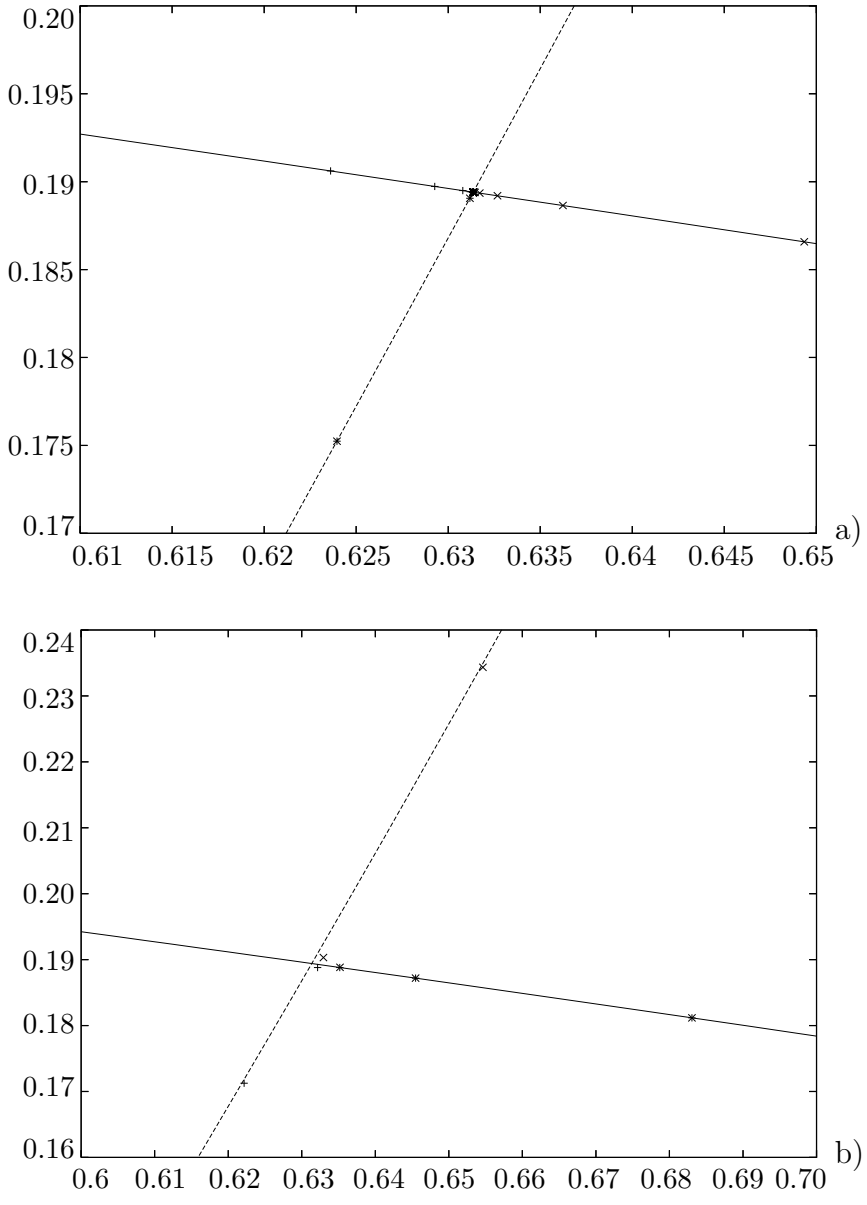

Figure 4.11. In **a)** the first 20 iterates of H^2 of the left (plus) and right (x) top cornerpoints of the claimed homoclinic point interval enclosure form Thm. (4.16) are plotted, in **b)** the first 10 iterates of H^{-2} of the top (plus) and bottom (x) right cornerpoint of the same interval box enclosure are plotted. The unstable manifold is drawn solid, the stable manifold dashed.

4.5 Summary and Outlook

Normal form type methods offer expansions of local parametrizations of invariant manifolds in the neighborhood of a hyperbolic saddle point in the plane. The operations involved are suitable to be performed using sophisticated polynomial manipulations offered in DA-arithmetic.

Thus, highly accurate polynomial approximations to the local invariant manifolds are obtained. The question about the truncation error can be answered automatically, as in the Taylor Model validation step a heuristic C^0-error bound can be proven to be self-contained.

This enables us to compute Taylor Model enclosures of the true invariant manifolds over a length proportional to 0.1, with an error estimate of 10^{-12} and smaller.

The global manifold tangle is obtained through repeated iteration in Taylor Model arithmetic of the initial local piece. To control blow-up of remainder bounds, the iterating scheme splits and reexpands Taylor Model enclosure pieces if necessary, and we obtain a finite list of Taylor Model pieces ordered along the arclength of the true manifold. It is evident that high-precision arithmetic is required to extend the iteration scheme to higher iterates before TM-pieces become so large that meaningful manipulation is not feasible anymore.

Based on verified global optimization, rigorous bounds for all homoclinic intersections of a finite manifold tangle can be obtained. Typically existence of homoclinic points within the enclosure balls can be guaranteed.

CHAPTER 5

Construction of Symbolic Dynamics and Entropy Estimates

In this chapter we develop an approach to obtain rigorous lower bounds for the topological entropy of planar diffeomorphisms. The technique is based on finding symbolic dynamics exhibited by the original map and performing entropy calculations on the simplified finite system. This is achieved by defining regions in phase space, so-called generalized curvilinear rectangles, and considering how they overlap under mapping, which allows to draw conclusions about the existence of real orbits of the diffeomorphism within those rectangle sequences (see e.g. [8] for related work on this approach).

In light of the last chapter, where part of the global manifold tangle has been sharply enclosed in Taylor Models, as well as verification of existence and ordering of homoclinic points within that tangle, we then introduce procedures to fully automate the rectangle construction mentioned above. Rectangles are bound by segments of stable and unstable manifold, with homoclinic points at their corners, which allows to construct and analyze rectangle sequences on a large scale and thus yields rigorous lower entropy estimates which are very close to the numerically suggested true entropy

values.

5.1 Some basic topological tools

Before we proceed with the presentation of the algorithm, we first review some fundamental results from algebraic topology, in particular in two dimensions, which will prove to be useful in establishing the algorithm rigorously. We first cite Brouwer's fixed point theorem [18]:

5.1 Theorem. *(Brouwer) Every continuous function from the closed unit ball in* $\mathbb{R}^n$ *into itself has a fixed point.*

Using Brouwer's theorem we can prove a seemingly simple fact about the existence of an intersection of two horizontally and vertically, respectively, oriented curves in a rectangle. We follow [40] in the presentation;

5.2 Lemma. *Let* $\gamma_h(s) = \left(\gamma_{h,1}(s), \gamma_{h,2}(s)\right)$ *and* $\gamma_v(t) = \left(\gamma_{v,1}(t), \gamma_{v,2}(t)\right)$*, with* $s,t \in [-1,1]$*, be two continuous curves in the rectangle* $[a,b] \times [c,d] \subset \mathbb{R}^2$*, with* $a,b,c,d \in \mathbb{R}$*, such that* $\gamma_{h,1}(-1) = a$*,* $\gamma_{h,1}(1) = b$*,* $\gamma_{v,2}(-1) = c$ *and* $\gamma_{v,2}(1) = d$*. Then there exists* $(s_0,t_0) \in [-1,1]^2$ *such that* $\gamma_h(s_0) = \gamma_v(t_0)$*.*

Proof. In the following we consider the max norm $||x||_\infty := \max\{|x_1|, |x_2|\}$ on $\mathbb{R}^2$. Note that with this norm the set $[-1,1]^2$ is actually the closed unit ball. Suppose now that no intersection of γ_h and γ_v exists, then $||\gamma_h(s) - \gamma_v(t)|| \neq 0 \,\forall\, (s,t) \in [-1,1]^2$, and we may define the map

$$f(s,t) := \left(\frac{\gamma_{v,1}(t) - \gamma_{h,1}(s)}{||\gamma_h(s) - \gamma_v(t)||_\infty}, \frac{\gamma_{h,2}(s) - \gamma_{v,2}(t)}{||\gamma_h(s) - \gamma_v(t)||_\infty} \right) .$$

We see that f maps $[-1,1]^2$ into itself, or more precisely, into the boundary of $[-1,1]^2$, and thus must have a fixed point by Theorem 5.1, say at (σ,τ), i.e. $f(\sigma,\tau) = (\sigma,\tau)$. Then $||(\sigma,\tau)|| = 1$ must hold and thus either $|\sigma| = 1$ or $|\tau| = 1$. Suppose now that

$\sigma = -1$, then also $f_1(-1,\tau) = -1$, but this cannot be the case as $f_1(-1,\tau) \geq 0$ by definition. The remaining three cases of $|\sigma| = 1$ or $|\tau| = 1$ lead to similar contradictions. □

It is interesting to note that the previous lemma can be used (see [40]) to prove the Jordan Curve Theorem (JCT) in a relatively simple fashion.

5.3 Theorem. *(Jordan Curve Theorem) Given a Jordan curve $J \subset \mathbb{R}^2$, the complement $\mathbb{R}^2 \backslash J$ consists of two mutually disjoint nonempty components, each with J as its boundary. Exactly one of them is bounded (also called interior of J), the other unbounded (called the exterior of J). Furthermore, both components are path-connected and open.*

In the situation of the theorem, we can write $\mathbb{R}^2 \backslash J = B \cup U$, where B and U are the bounded and unbounded components, respectively. It is then easy to see that $B = \mathring{B}$ und $U = \mathring{U}$. The JCT can be extended to higher dimensions, but we only consider the planar case in this work. In this situation, there actually holds a stronger result, the Jordan-Schoenflies Theorem:

5.4 Theorem. *(Jordan-Schoenflies) assume a Jordan curve $J \subset \mathbb{R}^2$ with a corresponding homeomorphism $h : S^1 \longrightarrow \mathbb{R}^2$ such that $J = h\left(S^1\right)$. Then h can be extended to the entire plane, i.e. there is a homeomorphism $\tilde{h} : \mathbb{R}^2 \longrightarrow \mathbb{R}^2$ such that $\tilde{h}|_{S^1} = h$.*

A consequence of the last theorem is that for a planar Jordan curve, the closure of its bounded component (according to the JCT) is the homeomorphic image of the unit disk in $\mathbb{R}^2$.

5.2 Rectangles and their overlapping

The construction of symbolic dynamics in a dynamical system is possible by picking suitably chosen subsets of phase space and checking how they overlap under iteration. The subsets that we consider are generalized, curvilinear 'rectangles'.

5.5 Definition. *Let $\gamma : [a,b] \longrightarrow \mathbb{R}^v$ be an injective homeomorphic curve. Let p_1, p_2 be points in the same connected component of γ.*
Then by $\wp_\gamma(p_1,p_2)$ we denote the subarc of γ which has p_1 and p_2 as its endpoints, and is oriented from p_1 to p_2.

5.6 Definition. *(Rectangles) A set $R \subset \mathbb{R}^2$ is called a 'rectangle' if R is the homeomorphic image of the unit square, i.e. $R = h\left([-1,1]^2\right)$ for some homeomorphism $h : [-1,1]^2 \longrightarrow \mathbb{R}^2$. Accordingly, we define the top, bottom, left and right edges of R with the following notation:*

1. *$tR := h([-1,1] \times \{1\})$, the top edge,*
2. *$bR := h([-1,1] \times \{-1\})$, the bottom edge,*
3. *$lR := h(\{-1\} \times [-1,1])$, the left edge,*
4. *$rR := h(\{1\} \times [-1,1])$, the right edge.*

In light of the Jordan-Schoenflies Theorem it becomes clear that the 'rectangles' we consider are in a general sense simply Jordan curves together with their bounded component, but the rectangle picture has two main advantages: it simplifies some technicalities in the proofs and allows an easy transition, both practically and intuitively, into the computational implementation of the algorithm later.

Note that the edges are parametrized curves, e.g. as $tR = tR(s) = h((s,1))$ and likewise with the other edges. We customarily identify the point sets tR etc., and their parametrizations, this shall not lead to any confusions. Note furthermore

that the homeomorphic (in particular, we will consider diffeomorphisms later) image of a rectangle is again a rectangle with preserved top, bottom, left and right edge classifications. For the finding of symbolic dynamics, we have to consider the way in which images of rectangles overlap and introduce the following notion:

5.7 Definition. *(Markov crossing) Assume two rectangles R_1 and R_2 are given. We say that R_1 Markov-crosses R_2, in symbols $R_1 \sharp R_2$, iff the following hold:*

1. $tR_2 \cap \mathring{R}_1 = \emptyset$, *where* $\mathring{R}_1$ *denotes the interior of* R_1,
2. $bR_2 \cap \mathring{R}_1 = \emptyset$,
3. $lR_1 \cap \mathring{R}_2 = \emptyset$,
4. $rR_1 \cap \mathring{R}_2 = \emptyset$,
5. *The intersections* $tR_1 \cap lR_2$, $tR_1 \cap rR_2$, $bR_1 \cap lR_2$ *and* $bR_1 \cap rR_2$ *consist of a single point each, called* x_{tl}, x_{tr}, x_{bl} *and* x_{br} *respectively,*
6. *The interior* B *of the Jordan curve* $J := \wp_{tR_1}(x_{tl}x_{tr}) \cup \wp_{rR_2}(x_{tr}x_{br}) \cup \wp_{bR_1}(x_{br}x_{bl}) \cup \wp_{lR_2}(x_{bl}x_{tl})$ *is fully contained in* $R_1 \cap R_2$.

An intuitive idea of Markov crossings can be gained form Figure 5.1. It is clear that Def. 5.7 can directly be extended to allow multiple Markov-crossings as in the bottom right picture in Figure 5.1.

The fact that in point (6) the stated set J is a Jordan curve is easy to prove. Furthermore, by the Jordan-Schoenflies f the union $B \cup J$ is actually a rectangle in the sense of Def. 5.6 which is contained in $R_1 \cap R_2$, with the top, bottom, left and right edges of $B \cup J$ contained in tR_1, bR_1, lR_2 and rR_2 , respectively.

Intuitively, a Markov crossing of R_1 and R_2 is an overlap of the rectangles such that R_1 is thinner than R_2 in the 'vertical' direction and stretches fully across R_2 in the 'horizontal' direction. We now introduce the notion of a chain of rectangles, Markov-crossing each other under iteration:

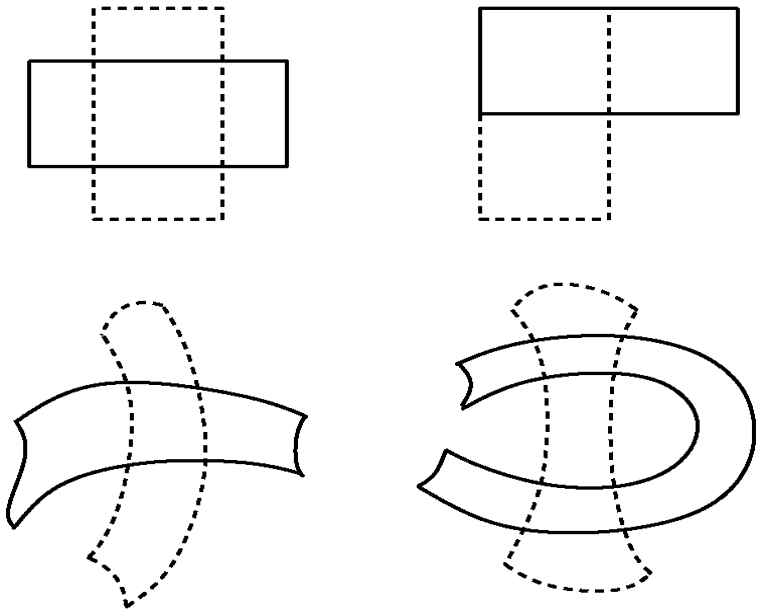

Figure 5.1. Typical types of Markov crossings $R_1 \sharp R_2$ between two rectangles R_1 (solid) and R_2 (dashed).

5.8 Definition. *(Rectangle N-chains) For a homeomorphism $f : \mathbb{R}^2 \supset D \longrightarrow \mathbb{R}^2$, and some $N \in \mathbb{N}_0$, assume we are given an ordered sequence of rectangles $\mathcal{R} = \{R_n\}_{n=0}^{N-1}$, such that $R_n \subset D$ and $f(R_n) \sharp R_{n+1} \, \forall \, 0 \leq n \leq N-1$. Then we call $\mathcal{R}$ a rectangle N-chain for f. If $N = \infty$, we say $\mathcal{R}$ is a global rectangle chain.*

Two rectangle N-chains $\mathcal{R}^{(1)}$ and $\mathcal{R}^{(2)}$ are equal iff $R_i^{(1)} = R_i^{(2)} \forall \, 0 \leq i \leq N-1$.

5.9 Definition. *(h/v-transverse curves) For a given rectangle R, an injective curve $\gamma : [a, b] \longrightarrow R$ connecting lR and rR is called an h-transverse curve. If γ connects tR and bR, we call it a v-transverse curve.*

It follows directly from Lemma 5.2 that two curves, one being an h-transverse and the other being a v-transverse curve for the same rectangle, must intersect.

5.10 Lemma. *Suppose two rectangles R_1 and R_2 are given such that $R_1 \sharp R_2$, and there is an h-transverse curve $\gamma_1 \subset R_1$. Then γ_1 contains a subarc $\gamma_2 \subset R_2$ that is an h-transverse curve for R_2.*

Proof. We prove the statement in several steps, and use the same notation as in Def. 5.7:

1. For a Jordan curve J, a path γ connecting two points $\chi \in B$ and $\xi \in U$ in the interior and exterior of J must intersect J. For if not, $\gamma \subset \mathbb{R}^2 \backslash J = (B \cup U)$, and since B and U are path-connected, then also their union $B \cup U$ must be path-connected, and thus connected. But then by definition, $B \cup U$ cannot be the union of two nonempty, disjoint open sets, which it is according to the JCT.

2. The segments $\wp_{lR_2}(x_{bl}x_{tl})$ and $\wp_{rR_2}(x_{tr}x_{br})$ are v-transverse curves for R_1. We will show this for the segment $\wp_{lR_2}(x_{bl}x_{tl})$, the proof then works analogously for $\wp_{rR_2}(x_{tr}x_{br})$. It is obvious that $\wp_{lR_2}(x_{bl}x_{tl})$ connects tR_1 and bR_1, hence we only need to show that in fact $\wp_{lR_2}(x_{bl}x_{tl}) \subset R_1$. Suppose this is not the case, then there is a point $\eta \in \wp_{lR_2}(x_{bl}x_{tl})$ such that $\eta \notin R_1$. As R_1 is compact, we can find $\varepsilon > 0$ such that the ball $B_\varepsilon(\eta) \cap R_1 = \emptyset$. Since η is furthermore on the boundary of the rectangle $B \cup J$, there exists a point $\xi \in B_\varepsilon(\eta) \cap B$, i.e. $\xi \notin R_1$ and $\xi \in B$. This is a contradiction to $B \subset R_1$.

3. The h-transverse curve γ_1 in R_1 crosses both segments $\wp_{lR_2}(x_{bl}x_{tl})$ and $\wp_{rR_2}(x_{tr}x_{br})$. This is an immediate consequence from Lemma 5.2 and the previous claim.

4. γ_1 contains a subarc $\gamma_2 \subset R_2$ that is an h-transverse curve for R_2. Without loss of generality, assume that $\gamma_1 : [-1,1] \longrightarrow R_1$ such that $\gamma_1(-1) \in lR_1$ and $\gamma_1(1) \in rR_1$, and that γ_1 intersects $\wp_{lR_2}(x_{bl}x_{tl})$ before it intersects $\wp_{rR_2}(x_{tr}x_{br})$. Consider the nonempty (by (3)) set I_l of intersection points of γ_1 and $\wp_{lR_2}(x_{bl}x_{tl})$ in the sense of the parametrization of γ_1, i.e. $I_l = \left\{t \in (-1,1) : \gamma_1(t) \in \wp_{lR_2}(x_{bl}x_{tl})\right\}$. Let $t_l := \sup I_l$, then $t_l > -1$ and $\gamma_1(t_l) \in \wp_{lR_2}(x_{bl}x_{tl})$ by continuity of γ_1. Likewise consider now the set $I_r = \left\{t \in (t_l,1) : \gamma_1(t) \in \wp_{rR_2}(x_{tr}x_{br})\right\}$.

We show that $I_r \neq \emptyset$. First note that the set $R_1 \setminus (R_1 \cap R_2)$ has exactly one connected component that contains the curve segment $\wp_{\gamma_1}(\gamma_1(-1)\,\gamma_1(t_l))$, call that set R_1^*. Then define the rectangle $\tilde{R} := R_1 \setminus R_1^*$, and note that the curve segment $\wp_{\gamma_1}(\gamma_1(t_l)\,\gamma_1(1))$ is an h-transverse curve for $\tilde{R}$. Also, $\wp_{rR_2}(x_{tr}x_{br})$ is a v-transverse curve for $\tilde{R}$ and thus by Lemma 5.2 $\wp_{\gamma_1}(\gamma_1(t_l)\,\gamma_1(1)) \cap \wp_{rR_2}(x_{tr}x_{br}) \neq \emptyset$, hence there $\exists\, \tilde{t} \in (t_l, 1)$ such that $\gamma_1(\tilde{t}) \in \wp_{rR_2}(x_{tr}x_{br})$. Let now $t_r := \inf I_r$, then $t_r > t_l$ and $\gamma_1(t_r) \in \wp_{rR_2}(x_{tr}x_{br})$, again by continuity of γ_1. Now set $\gamma_2 := \gamma_1|_{[t_l,t_r]}$, then $\gamma_2 \subset \gamma_1$ and γ_2 connects $\wp_{lR_2}(x_{bl}x_{tl}) \subset lR_2$, and $\wp_{rR_2}(x_{tr}x_{br}) \subset rR_2$ and thus is an h-transverse curve for R_2.

□

The last lemma will provide us with a means of counting orbits:

5.11 Theorem. *For a homeomorphism $f : \mathbb{R}^2 \supset D \longrightarrow \mathbb{R}^2$, let $\mathcal{R} = \{R_n\}_{n=0}^{N-1}$ be a rectangle N-chain. Then there is an N-orbit in $\mathcal{R}$, i.e. there exists a point $x_0 \in R_0$ such that $f^n(x_0) \in R_n\ \forall 0 \leq n \leq N-1$. A global orbit exists if $\mathcal{R}$ is a global rectangle chain, i.e. if $N = \infty$.*

Proof. Let γ_0 be an h-transverse curve for R_0. Then $f(\gamma_0)$ is an h-transverse curve for $f(R_0)$, and by the last lemma contains a subarc γ_1 which is an h-transverse curve for R_1. Inductively, we get a sequence of curves $\{\gamma_n\}_{n\in\mathbb{N}_0}$ such that $f^{-1}(\gamma_{n+1}) \subset \gamma_n$, and each γ_n is an h-transverse curve for R_n. This yields that $f^{-(n+1)}(\gamma_{n+1}) \subset f^{-n}(\gamma_n) \subset \gamma_0$. Since all preimages $f^{-n}(\gamma_n)$ are closed, we get a nested sequence of closed sets and thus the intersection $\bigcap_{n\in\mathbb{N}_0} f^{-n}(\gamma_n) \neq \emptyset$. So pick a point x_0 in that intersection, and it is obvious that $x_0 \in \gamma_0 \subset R_0$ and $f^n(x_0) \in \gamma_n \subset R_n$, and thus satisfies the desired properties. □

5.3 Entropy estimates

Given the results form the previous section, we can now make the transition from rectangle crossings under iteration by a diffeomorphism to entropy estimates for that same map:

5.12 Theorem. *(Entropy from orbit counting) For a homeomorphism* $f : \mathbb{R}^2 \supset D \longrightarrow \mathbb{R}^2$*, let* $\{R_1, ..., R_v\}$ *be a set of mutually disjoint rectangles, and let* $A \in \mathbb{N}^{v \times v}$ *be a matrix with integer entries such that* $A_{i,j} = 1$ *iff* $f(Rj) \sharp R_i$ *and 0 else. Then we have for the topological entropy of* f

$$h(f) \geq \log(sp(A)),$$

where $sp(A)$ *is the spectral radius of* A*.*

Proof. 1. First note that, since all rectangles are mutually disjoint and by definition compact, $\exists\, \varepsilon_0 > 0$ smaller than the minimal distance between the rectangles, i.e.

$$dist\left(R_i, R_j\right) > \varepsilon_0 \,\forall\, 1 \leq i, j \leq v.$$

Since the entropy $h(f) := \lim\limits_{\varepsilon \to 0} \limsup\limits_{n \to \infty} \frac{1}{n} \log(r(n, \varepsilon, f))$ is growing monotonously as $\varepsilon \to 0$, for this finite ε_0 we then get

$$h(f) \geq \limsup_{n \to \infty} \frac{1}{n} \log(r(n, \varepsilon_0, f)).$$

2. We now inductively define the sequence of state vectors

$$r^{(0)} := (1, ..., 1)^T,$$
$$r^{(n)} := A^n r^{(0)}.$$

For any integer vector $w \in \mathbb{N}^v$, let

$$||w||_1 = \sum_{i=1}^{v} |w_i|$$

denote its 1-norm. We claim that $r_i^{(n)} \in \mathbb{N}$ gives a lower bound for the number of mutually distinct rectangle $(n+1)$-chains with elements in $\{R_1, ..., R_v\}$ the last element of which is R_i. Obviously, this is true for $n = 0$, since $r_i^{(0)} = 1 \,\forall\, 1 \leq i \leq v$ and there is exactly one rectangle 1-chain $\{R_i\}$ with R_i as the last element, and trivially $f^0(R_i) \sharp R_i \,\forall\, 1 \leq i \leq v$.

Now for the step $n \to n+1$, consider a nonzero entry $r_j^{(n)}$, then there are $r_j^{(n)}$ rectangle n-chains ending in R_j, and pick one, say $\mathcal{R} := \left\{R_{i_k}\right\}_{k=0}^{n-1}$. If $A_{i,j} \neq 0$, $f\left(R_{i_{n-1}}\right) = f\left(R_j\right) \sharp R_i$, and the set $\mathcal{R} \cup \{R_i\}$ is an $(n+1)$-chain ending in R_i. Since $\mathcal{R}$ is distinct from all other n-chains (both ending and not ending in R_j), then also $\mathcal{R} \cup \{R_i\}$ is distinct from all other $(n+1)$-chains ending in R_i. Thus, summing up we have that the total number of mutually distinct $(n+1)$-chains ending in R_i must be greater or equal to

$$\sum_{j=1}^{v} A_{i,j} r_j^{(n)} = r_i^{(n+1)},$$

which proves the claim. But moreover we have shown that the total number of all mutually distinct $(n+1)$-chains for f with elements in $\mathcal{R}$ is bounded below by

$$\sum_{i=1}^{v} r_i^{(n+1)} = \left|\left|r^{(n+1)}\right|\right|_1.$$

3. We claim that

$$r(n, \varepsilon_0, f) \geq \left|\left|r^{(n-1)}\right|\right|_1 \tag{5.1}$$

and additionally, $r_i^{(n-1)}$ gives a lower bound for the number of n-orbits starting in $\bigcup_{j=1}^{v} R_j$ and ending in R_i. This is true since by step (2), there are exactly $r_i^{(n-1)}$ rectangle n-chains ending in R_i, and by Theorem 5.11 each contains at least one n-orbit starting in $\bigcup_{j=1}^{v} R_j$. Since by (1) all rectangles are separated by at least ε_0, then also these $r_i^{(n-1)}$ n-orbits must be ε_0-separated. Summation over all $r_i^{(n-1)}$ yields (5.1).

4. We can express $\left|\left|r^{(n)}\right|\right|_1$ via the matrix norm of A :

$$\begin{aligned}\left|\left|r^{(n)}\right|\right|_1 &= \sum_{i=1}^{v} r_i^{(n)} = \sum_{i,j=1}^{v} \left(A^n\right)_{i,j} r_j^{(0)} \\ &= \sum_{i,j=1}^{v} \left|\left(A^n\right)_{i,j}\right| \geq \max_{1\leq i\leq v} \left(\sum_{j=1}^{v} \left|\left(A^n\right)_{i,j}\right|\right) = \left|\left|A^n\right|\right|_\infty ,\end{aligned}$$

where $||A^n||_\infty$ denotes the row-sum-norm of A^n. It is a standard result (see [59]) that for any real square matrix M and any matrix norm $||.||$ for M, we have

$$\sqrt[n]{||M^n||} \underset{n\to\infty}{\longrightarrow} sp\left(M\right),$$

and so we have the estimate

$$\begin{aligned}h\left(f\right) &\geq \limsup_{n\to\infty} \frac{1}{n} \log\left(r\left(n,\varepsilon_0,f\right)\right) \geq \limsup_{n\to\infty} \frac{1}{n} \log\left(\left|\left|r^{(n)}\right|\right|_1\right) \\ &\geq \limsup_{n\to\infty} \log\left(\sqrt[n]{||A^n||_\infty}\right) = \log\left(sp\left(A\right)\right) \ .\end{aligned}$$

□

As an alternative approach, we can obtain entropy estimates from the length growth of curves. The benefit of this technique is that the rectangles under consideration here may share boundaries, which will prove to be of fundamental importance in our later algorithms where we construct rectangles that are bounded by invariant manifolds. The cost is a restriction to smooth maps and rectangles with piecewise smooth boundaries.

We start by stating canonical results about smooth extensions of functions [36]:

5.13 Lemma. *(Extension lemma) Let M be a closed subset of a smooth manifold. If $f : M \longrightarrow \mathbb{R}^v$ is smooth, then for every open neighborhood V of M there exists a smooth function $f_V : V \longrightarrow \mathbb{R}^v$ such that $f_V|_M = f$.*

The proof of this statement is based on the existence of so-called bump functions, i.e. smooth functions with a compact support. A typical example β for a bump

function on $\mathbb{R}$ is given by

$$\beta(x) := \begin{cases} e^{-\frac{1}{1-x^2}} & \text{for } |x| < 1 \\ 0 & \text{else} \end{cases} .$$

These bump functions can be 'tailored' to the choices of V and M and the smoothing of f outside M is performed using a convolution with a suitably chosen bump function. In particular we have the following results about curve connection in the plane as a corollary:

5.14 Corollary. *(Smooth connection of curves) Let $\gamma_i : \mathbb{R} \longrightarrow \mathbb{R}^2$ for $i = 1, 2$ be smooth immersed curves (not necessarily injective). Let $a < b < c < d \in \mathbb{R}$ and consider the restricted curves $\gamma_1|_{[a,b]}$ and $\gamma_2|_{[c,d]}$. Note that all one-sided derivatives of γ_i exist at the endpoints and $\dot{\gamma}_i \neq 0$ there. Then there exists a smooth curve $c_{1,2} : (b, c) \longrightarrow \mathbb{R}^2$ such that the concatenated curve $\left(\gamma_1 \,\&\, c_{1,2} \,\&\, \gamma_2\right) : [a_1, b_2] \longrightarrow \mathbb{R}^2$ given by*

$$\left(\gamma_1 \,\&\, c_{1,2} \,\&\, \gamma_2\right)(t) := \begin{cases} \gamma_1(t) & \text{if } t \in [a, b] \\ c_{1,2}(t) & \text{if } t \in (b, c) \\ \gamma_2(t) & \text{if } t \in [c, d] \end{cases}$$

is again smooth and an immersed curve. In particular note that $c_{1,2}$ is of finite length since the first derivatives are bounded on the compact set $\overline{(b, c)}$.

We can now prove the entropy estimates stemming from curve length growth:

5.15 Theorem. *(Entropy from curve length growth) For a $\mathcal{C}^\infty$-diffeomorphism $f : \mathbb{R}^2 \supset M \longrightarrow D$, where M is compact, let $\{R_1, ..., R_v\}$ be a set of rectangles in M with mutually disjoint interior such that the boundary segments tR_i, bR_i, lR_i and rR_i are smooth for every $1 \leq i \leq v$. Let $A \in \mathbb{N}^{v \times v}$ be a matrix with integer entries such that $A_{i,j} = 1$ iff $f\left(R_j\right) \pitchfork R_i$ and 0 else. Then we have for the topological entropy of f*

$$h(f) \geq \log\left(sp(A)\right).$$

Proof. 1. By Theorem 2.13 we know that

$$\begin{aligned} h(f) &= \sup_{C^\infty\text{-curves } \gamma\subset M} G(\gamma, f) \\ &= \sup_{C^\infty\text{-curves } \gamma\subset M} \limsup_{n\to\infty} \frac{1}{n} \log \left| f^n \circ \gamma \right|. \end{aligned}$$

where $|.|$ denotes the arclength of a C^1-curve. So for a choice of a fixed C^∞-curve $\gamma_0 \subset M$, we have that

$$h(f) \geq \limsup_{n\to\infty} \frac{1}{n} \log \left| f^n \circ \gamma_0 \right|. \tag{5.2}$$

2. For a rectangle R_i and any associated C^∞ h-transverse curve $\gamma_h(R_i)$, we have

$$\inf_{\gamma_h(R_i)\subset R_i} (|\gamma_h(R_i)|) > 0.$$

3. For a rectangle R_i there exists $\varepsilon(R_i) > 0$ such that and , we have

$$|\gamma_h(R_i)| > \varepsilon(R_i).$$

for any associated C^∞ h-transverse curve $\gamma_h(R_i) \subset R_i$. For if not, then for continuity reasons $lR_i \cap rR_i \neq \emptyset$, which contradicts Def. 5.6. Then define

$$l_0 := \min\{\varepsilon(R_i) : 1 \leq i \leq v\} > 0,$$

so l_0 is the positive minimal length of any h-transverse curve for any rectangle in $\{R_1, ..., R_v\}$.

For every $R_i \in \{R_1, ..., R_v\}$, select now a C^∞ h-transverse curve $\gamma_{h,i}$ (these exist for every R_i, in particular the boundaries tR_i and bR_i are smooth h-transverse curves for R_i), and connect their endpoints with C^∞ curves $c_{j,j+1} \subset M$, $1 \leq j \leq v-1$, according to corollary (5.14) such that the concatenated curve γ_0 defined as

$$\gamma_0 := \gamma_{h,1} \,\&\, c_{1,2} \,\&\, \gamma_{h,2} \,\&\, c_{2,3} \,\&...\&\, c_{v-1,v} \,\&\, \gamma_{h,v}$$

is an immersed (not necessarily injective) C^∞-curve in M. Let

$$K_n := \sum_{j=1}^{v-1} \left| f^n \circ c_{j,j+1} \right| \geq 0 \, \forall \, n \in \mathbb{N}_0.$$

4. We claim that

$$\left| f^n \circ \gamma_0 \right| \geq \left|\left| A^n \right|\right|_\infty \, l_0 + K_n.$$

We already know from steps (2) and (4) in Thm. 5.12 that $||A^n||_\infty$ gives a lower bound for the number of mutually distinct rectangle $(n+1)$-chains. From Lemma 5.10 we know that every $(n+1)$-chain ends in a rectangle which has a subarc of $f^n \circ \gamma_0$ as an h-transverse curve, which has a minimal length of l_0. This proves the statement.

5. Combining the last claim with (5.2) yields the estimate

$$\begin{aligned} h\left(f\right) &\geq \limsup_{n\to\infty} \frac{1}{n} \log \left| f^n \circ \gamma_0 \right| \geq \limsup_{n\to\infty} \log \sqrt[n]{||A^n|| \; l_0 + K_n} \\ &\geq \limsup_{n\to\infty} \log \left(\sqrt[n]{||A^n||} \cdot \sqrt[n]{l_0} \right) \\ &= \log\left(sp\left(A\right)\right). \end{aligned}$$

□

In light of the last two theorems, it becomes apparent that we found 'symbolic dynamics' exhibited by f, i.e. we found a subshift of finite type which satisfies the same entropy estimates as would a topological factor of f according to Thm. 2.12. Here the rectangles $\{R_1, ..., R_v\}$ form an alphabet α of $v+1$ symbols, and a subshift of finite type Σ_A^+ is given by the incidence matrix A determined by the Markov crossing properties of the R_i under iteration by f, combined with the shift map on Σ_A^+.

5.4 Construction of rectangle chains

While the theorems from the last section ascertain entropy estimates for homeomorphisms and diffeomorphisms through a collection of rectangles and their incidence

matrix under mapping, for a given problem it is neither clear how to best select a set of rectangles nor how to rigorously prove their iterative Markov crossings.

To this end we now wish to combine the theoretical framework developed so far in this chapter with the Taylor Model based techniques for the representation of manifold tangles, which was presented in chapter 4. The fundamental idea is to define suitable rectangles as sets bounded by segments of invariant manifolds, with homoclinic points as their cornerpoints. Knowledge about the mapping properties of the homoclinic points together with the invariance of the unstable and stable manifold pieces will allow us to rigorously determine Markov crossings under iteration of the thus defined rectangles.

The arguments are designed in such a way that they can be established with Taylor Model arithmetic.

All definitions of sets or maps hold throughout this section.

5.4.1 Choice of manifold tangle

Let p be a hyperbolic saddle point of the C^r-diffeomorphism $f : \mathbb{R}^2 \longrightarrow \mathbb{R}^2$, and let λ_u be the unstable eigenvalue, assumed without loss of generality to have positive real part (else consider the squared map f^2). Let $W^u_{loc}(p)$ be a connected component of the local unstable manifold around p containing p. Define the subarc $W^u_K(p)$ as $W^u_K(p) := f^K\left(W^u_{loc}(p)\right)$ for some finite iterate K. Observe that $\mathcal{U} \subset f(\mathcal{U})$.

Let $\mathcal{S} := \{S_1, ..., S_M\}$ be an arclength-ordered finite collection of compact stable subarcs $S_i \subset W^s(p)$ for $1 \leq i \leq M$ with mutually disjoint nonempty interiors. By arclength-ordered we mean the following: Choose a fixed parametrization $W^s(p) := \gamma_s(t)$ for $t \in \mathbb{R}$. Then for any two points $p_1 \in S_i$ and $p_2 \in S_{i+1}$, $p_1 \neq p_2$, there exist $t_1 < t_2$ such that $p_1 = \gamma_s(t_1)$ and $p_2 = \gamma_s(t_2)$. If $p_3 \in \wp_{W^s(p)}(p_1, p_2)$, then $p_3 = \gamma_s(t_3)$ for some $t_1 < t_3 < t_2$.

Let $\mathcal{U} := \{U_1, ..., U_L\}$ be likewise an arclength-ordered finite collection of compact

unstable subarcs $U_i \subset W_K^u$, for $1 \leq i \leq L$, with mutually disjoint nonempty interiors.

For the rectangle construction, we now consider the manifold tangle $\mathcal{T} \subset \mathbb{R}^2$ given by

$$\mathcal{T} := (\mathcal{S} \cup f(\mathcal{S})) \cup (\mathcal{U} \cup f(\mathcal{U}))$$

where we demand that both $(\mathcal{S} \cup f(\mathcal{S}))$ and $(\mathcal{U} \cup f(\mathcal{U}))$ can be fully ordered.

In fact, we will make the assumption that $f(\mathcal{S}) \subset \mathcal{S}$ and $\mathcal{U} \subset f(\mathcal{U})$. In this case,

$$\mathcal{T} = \mathcal{S} \cup f(\mathcal{U})$$

and the orderings of $(\mathcal{S} \cup f(\mathcal{S}))$ and $(\mathcal{U} \cup f(\mathcal{U}))$ are inherited from $\mathcal{S}$ and $f(\mathcal{U})$.

5.4.2 Interval box enclosures of homoclinic points

If $\mathcal{U} \cap \mathcal{S} \neq \emptyset$, then let

$$\mathcal{B} := \{B(i, n_i) : 1 \leq i \leq N\} \tag{5.3}$$

be a collection of mutually disjoint closed balls $B(i, n_i) \subset \mathbb{R}^2$ with nonempty interior, which contains all homoclinic intersections of $\mathcal{S} \cap \mathcal{U}$, that is

$$(\mathcal{S} \cap \mathcal{U}) \subset \bigcup_{i=1}^{N} B(i, n_i).$$

We assume that every $B(i, n_i)$ gets crossed by the manifolds according to section 4.4 in such a way that existence of at least one homoclinic point of $\mathcal{S} \cap \mathcal{U}$ is guaranteed in each $B(i, n_i)$. We may assume that the homoclinic point is in the interior $\mathring{B}(i, n_i)$. Furthermore, for the box $B(i, n_i)$ the indices i and n_i denote the ordering of the boxes along the stable and unstable manifold respectively. More precisely: analogous to the previous step, choose fixed parametrizations $W^s(p) = \gamma_s(v)$ and $W^u(p) = \gamma_u(w)$ for $v, w \in \mathbb{R}$. For two points $p_1 \in B(i, n_i)$ and $p_2 \in B\left(i+1, n_{i+1}\right)$, there exist $v_1, v_2, w_1, w_2 \in \mathbb{R}$ such that $p_k = \gamma_s(v_k) = \gamma_u(w_k)$ for $k = 1, 2$. Then $v_1 < v_2$, and furthermore $w_1 \lesseqgtr w_2$ iff $n_i \lesseqgtr n_{i+1}$.

5.16 Remark. *In (5.3) and in the rest of the algorithm for the rectangle mappings we only consider closed balls. This choice is purely for notational ease in the argument. In fact, we only need the balls to be C^r-diffeomorphic images of the unit ball in $\mathbb{R}^2$, which is beneficial for sharpness of the homoclinic point enclosure in practice. The argument works unchanged for this relaxed requirement.*

5.4.3 Determination of homoclinic ball enclosure mappings

Consider now $f(\mathcal{U}) \cap \mathcal{S}$ (which is nonempty because $\mathcal{S} \cap \mathcal{U} \subset (\mathcal{S} \cap f(\mathcal{U}))$ and $\mathcal{S} \cap \mathcal{U} \neq \emptyset$). Then choose a collection of closed balls with mutually disjoint nonempty interior

$$\tilde{\mathcal{B}} := \left\{ \tilde{B}\left(j, n_j\right) : 1 \leq j \leq \tilde{N} \right\}$$

such that again

$$(\mathcal{S} \cap f(\mathcal{U})) \subset \bigcup_{j=1}^{\tilde{N}} \tilde{B}\left(j, n_j\right),$$

with the ordering of $\tilde{B}\left(j, n_j\right)$ as the j-th stable and n_j-th unstable box, and which satisfies $\mathcal{B} \subset \tilde{\mathcal{B}}$. This choice of $\tilde{\mathcal{B}}$ is clearly allowed, one simply sets

$$\tilde{B}\left(j_i, n_{j_i}\right) := B(i, n_i) \text{ for } 1 \leq i \leq N$$

and then selects interval box enclosure $\tilde{B}\left(j, n_j\right)$ for $j \in \left\{1, ..., \tilde{N}\right\} \setminus \{j_1, ..., j_N\}$ which contain the newly created homoclinic intersections in $(f(\mathcal{U}) \setminus \mathcal{U}) \cap \mathcal{S}$. Note that then $N \leq \tilde{N}$.

5.17 Definition. *(Parent/child balls) Let $B_1, B_2 \subset \mathbb{R}^2$ be two closed balls with nonempty interior. If there exist $x_1 \in B_1$ and $x_2 \in B_2$ such that $f(x_1) = x_2$, we call B_1 a parent ball of B_2, and B_2 a child ball of B_1.*

The following is clearly true:

5.18 Proposition. *Every ball $\tilde{B}(k, n_k) \in \mathcal{B} \subset \tilde{\mathcal{B}}$ is a parent ball for some $\tilde{B}\left(j_k, n_{j_k}\right) \in \tilde{\mathcal{B}}$.*

We now make the additional assumption that for every parent ball $\tilde{B}(k, n_k) \in \mathcal{B}$ exists a $j_k \in \left\{1, ..., \tilde{N}\right\}$ such that

$$\tilde{B}(k, n_k) \subset f^{-1}\left(\tilde{B}\left(j_k, n_{j_k}\right)\right),$$

and $f^{-1}\left(\tilde{B}\left(j_k, n_{j_k}\right)\right)$ is disjoint from all other balls $\tilde{B}\left(j, n_j\right)$ where $j \in \left\{1, ..., \tilde{N}\right\} \setminus \{k\}$.
This obviously also means

$$f\left(\tilde{B}(k, n_k)\right) \subset \tilde{B}\left(j_k, n_{j_k}\right),$$
$$f\left(\tilde{B}(k, n_k)\right) \cap \tilde{B}\left(j, n_j\right) = \emptyset \, \forall \, j \in \left\{1, ..., \tilde{N}\right\} \setminus \{j_k\}$$

so in particular, for every parent ball there is a unique child ball into which the parent ball maps. In other words, within the collection $\tilde{\mathcal{B}}$ we have mutually disjoint parent-child-pairs, and additional balls which are neither a parent nor a child ball.

5.4.4 Orientation of manifolds at homoclinic point enclosures

We first introduce a convenience definition:

5.19 Definition. *Let $B \subset \mathbb{R}^2$ be a closed ball with nonempty interior. Let $\gamma : [a, b] \longrightarrow \mathbb{R}^2$ be a curve which both enters and leaves B, i.e. there are $t_1 < t_2 < t_3$ in $[a, b]$ such that $\gamma(t_2) \in \mathring{B}$ and $\gamma(t_1), \gamma(t_3) \notin B$. Then we define*

$$t_{in}(\gamma, B) := \inf\{t \in [a, b] : \gamma(t) \in \partial B\},$$
$$t_{out}(\gamma, B) := \sup\{t \in [a, b] : \gamma(t) \in \partial B\}.$$

as the entrance and exit parameters for γ, and accordingly

$$q_{in}(\gamma, B) := \gamma(t_{in}(\gamma, B)),$$
$$q_{out}(\gamma, B) := \gamma(t_{out}(\gamma, B)),$$

as the entrance and exit points of γ in B.

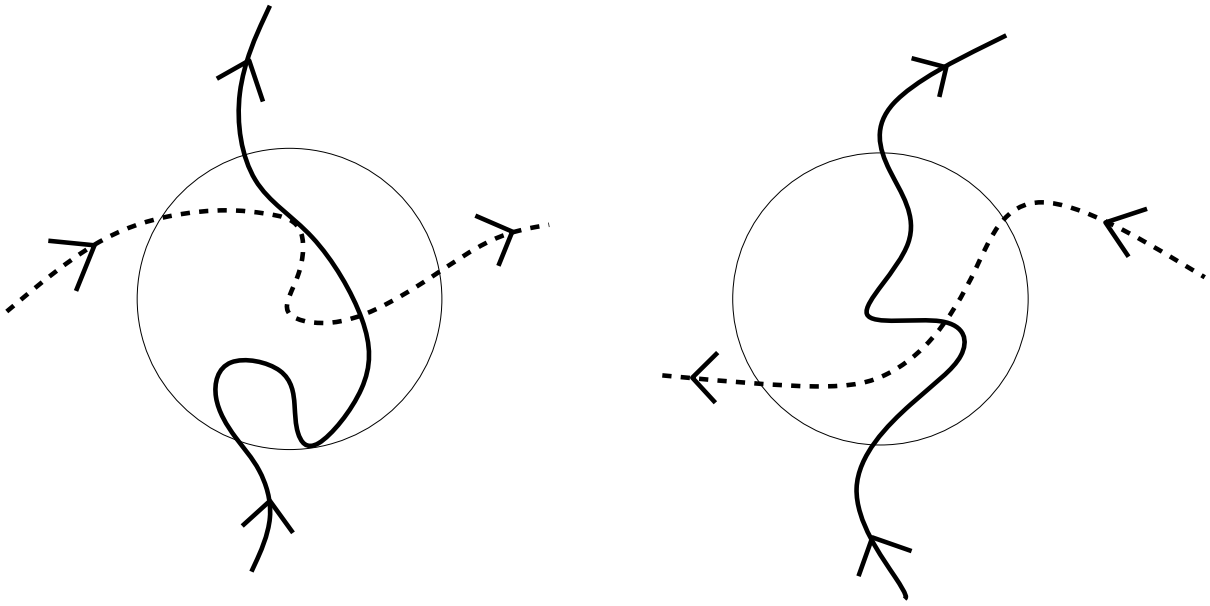

Figure 5.2. Left-handed (orientation $\mathsf{o} = -1$) and right-handed ($\mathsf{o} = 1$) crossing of stable (solid) and unstable (dashed) manifold over a homoclinic ball enclosure.

For continuity reasons in particular $q_{in}(\gamma, B) \in \partial B$ and $q_{out}(\gamma, B) \in \partial B$.

Now consider $\tilde{B}(i, n_i) \in \tilde{\mathcal{B}}$. Since $\tilde{B}(i, n_i)$ is guaranteed to contain a homoclinic point, in particular both $W^u(p)$ and $W^s(p)$ have to enter as well as leave $\tilde{B}(i, n_i)$, and we assumed that the entry/exit points of $W^u(p)$ and $W^s(p)$ on the boundary $\partial\tilde{B}(i, n_i)$ alternate and are mutually nonequal (i.e. no homoclinic points on the boundary $\partial\tilde{B}(i, n_i)$). We can now meaningfully define the orientation, or handedness, of the manifold crossing for $\tilde{B}(i, n_i)$:

5.20 Definition. *(Crossing orientation) Let $\tilde{B}(i, n_i) \in \tilde{\mathcal{B}}$, and for simplicity write $\tilde{B} = \tilde{B}(i, n_i)$. Then we define the crossing orientation $\mathsf{o}(i)$ of $\tilde{B}$ as*

1. *$\mathsf{o}(i) := 1$ if starting at $q_{in}\left(W^s(p), \tilde{B}\right)$ and going counterclockwise (positive) on $\partial\tilde{B}$, the next manifold crossing point is $q_{in}\left(W^u(p), \tilde{B}\right)$.*
2. *$\mathsf{o}(i) := -1$ else, i.e. if the next manifold crossing point is $q_{out}\left(W^u(p), \tilde{B}\right)$.*

A superset $E \subset \mathbb{R}^2$ of $\tilde{B}$ is said to have crossing direction $\mathsf{o}(i)$ if there are no further homoclinic intersections of $W^s(p)$ and $W^u(p)$ in $E \backslash \tilde{B}$.

Also see Figure 5.2 for a visualization.

5.21 Remark. *Intuitively, one can think of these definitions as taking the cross product of the tangent vectors to $W^u(p)$ and $W^s(p)$ in $\tilde{B}(i, n_i)$, with $\mathsf{o}(i, n_i)$ indicating whether the manifold crossing is right-handed ($\mathsf{o}(i) = 1$) or left-handed ($\mathsf{o}(i) = -1$). In the more general setting, this intuition does not hold fully, since we can have multiple manifold crossings or homoclinic tangencies within $\tilde{B}(i, n_i)$, hence this at first glance more involved and cumbersome definition of the crossing orientation.*

In fact, in the definition of manifold rectangles below, we are not interested in the crossing orientation at the homoclinic cornerpoints, but in the manifold orientation outside the cornerpoint ball enclosures.

5.4.5 Selection of rectangle cornerpoints and connector curves

We first introduce the notion of connector curves:

5.22 Proposition. *Let $\tilde{B}(i, n_i) \in \tilde{\mathcal{B}}$, again write $\tilde{B} = \tilde{B}(i, n_i)$, with an associated crossing direction $\mathsf{o}(i)$. Let the manifolds $W^\sigma(p)$ for $\sigma = u, s$ be C^∞ and parametrized as $\gamma^\sigma : \mathbb{R} \longrightarrow \mathbb{R}^2$, with the entrance and exit points $q_{in}\left(W^\sigma(p), \tilde{B}\right)$ and $q_{out}\left(W^\sigma(p), \tilde{B}\right)$ on $\partial\tilde{B}(i, n_i)$ mutually nonequal and alternating. For simplicity, write*

$$t^\sigma_{in} := t_{in}\left(W^\sigma(p), \tilde{B}\right), \quad t^\sigma_{out} := t_{out}\left(W^\sigma(p), \tilde{B}\right),$$
$$q^\sigma_{in} := q_{in}\left(W^\sigma(p), \tilde{B}\right), \quad q^\sigma_{out} := q_{out}\left(W^\sigma(p), \tilde{B}\right).$$

Then there exist injectively immersed C^∞-curves $\zeta_\sigma(i) : \left[t^\sigma_{in}, t^\sigma_{out}\right] \longrightarrow \tilde{B}$, for $\sigma = u, s$, such that

1. *ζ_σ connects $q^\sigma_{in} = \zeta_\sigma\left(t^\sigma_{in}\right)$ and $q^\sigma_{out} = \zeta_\sigma\left(t^\sigma_{out}\right)$ for $\sigma = u, s$.*

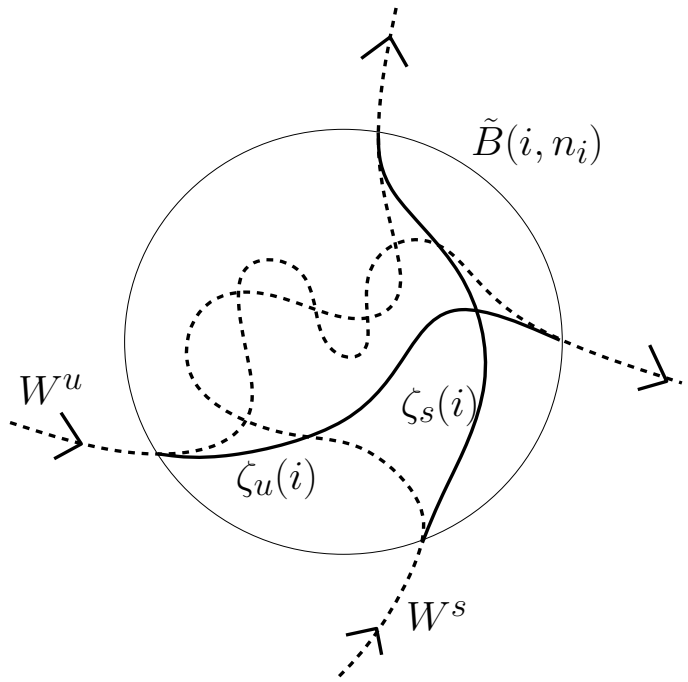

Figure 5.3. Homoclinic ball enclosure $\tilde{B}(i, n_i)$ with stable and unstable manifolds W^s and W^u (dashed). The connector curves $\zeta_s(i)$ and $\zeta_s(i)$ (solid) intersect transversely.

2. *The connection preserves the C^∞-differentiability, i.e. the concatenated curve $\xi_\sigma : \mathbb{R} \longrightarrow \mathbb{R}^2$ given by*

$$\xi_\sigma(t) := \begin{cases} \gamma^\sigma(t) & \text{if } t \in \left(-\infty, t^\sigma_{in}\right) \\ \left(\zeta_\sigma(i)\right)(t) & \text{if } t \in \left[t^\sigma_{in}, t^\sigma_{out}\right] \\ \gamma^\sigma(t) & \text{if } t \in \left(t^\sigma_{out}, \infty\right) \end{cases}$$

is again an immersed C^∞-curve for $\sigma = u, s$.

3. *The curves $\zeta_u(i)$ and $\zeta_s(i)$ intersect transversely in exactly one point $\mathsf{h}(i, n_i)$ in the interior of $\tilde{B}$, such that the orientation of their tangent vectors at $\mathsf{h}(i, n_i)$ corresponds to the crossing orientation $\mathsf{o}(i)$:*

$$\left(\dot{\zeta}_s|_{\mathsf{h}(i,n_i)} \times \dot{\zeta}_u|_{\mathsf{h}(i,n_i)}\right) \lessgtr 0 \Longleftrightarrow \mathsf{o}(i) \lessgtr 0.$$

The statement follows immediately from Proposition 5.14, also see Figure 5.3. In this situation we call the curves $\zeta_s(i)$ and $\zeta_u(i)$ the stable and unstable connector

curves for $\tilde{B}(i, n_i)$, and $\mathsf{h}(i, n_i)$ the i-th cornerpoint, for reasons that will become clear soon.

5.23 Proposition. *Let $\tilde{B}(i, n_i), \tilde{B}\left(j, n_j\right) \in \tilde{\mathcal{B}}$, and for simplicity write $B = \tilde{B}(i, n_i)$ and $\tilde{B} = \tilde{B}\left(j, n_j\right)$. Suppose now that $B \subset f^{-1}\left(\tilde{B}\right)$, and that the manifold crossing directions $\mathsf{o}(i)$ for B and for $f^{-1}\left(\tilde{B}\right)$ are equal. Let furthermore $\zeta_u(i), \zeta_s(i)$ and $\mathsf{h}(i, n_i)$ be chosen for B according to the previous proposition. Then there exist connector curves $\zeta_u(j)$ and $\zeta_s(j)$ for $\tilde{B}\left(j, n_j\right)$ such that*

$$f(\zeta_\sigma(i)) \subset \zeta_\sigma(j), \ \sigma = u, s.$$

In particular, this means that $\mathsf{h}\left(j, n_j\right) = f(\mathsf{h}(i, n_i))$.

Proof. For ease of hand we write

$$\begin{array}{ll} t_{in}^\sigma := t_{in}\left(W^\sigma(p), B\right), & t_{out}^\sigma := t_{out}\left(W^\sigma(p), B\right), \\ q_{in}^\sigma := q_{in}\left(W^\sigma(p), B\right), & q_{out}^\sigma := q_{out}\left(W^\sigma(p), B\right), \\ \tilde{q}_{in}^\sigma := q_{in}\left(W^\sigma(p), \tilde{B}\right), & \tilde{q}_{out}^\sigma := q_{out}\left(W^\sigma(p), \tilde{B}\right), \end{array}$$

Let finally the manifolds $W^\sigma(p)$ be C^∞ and parametrized as $\gamma^\sigma : \mathbb{R} \longrightarrow \mathbb{R}^2$, and $\theta_{in}^\sigma, \theta_{out}^\sigma \in \mathbb{R}$ such that

$$\gamma^\sigma\left(\theta_{in}^\sigma\right) = f^{-1}\left(\tilde{q}_{in}^\sigma\right) \text{ and } \gamma^\sigma\left(\theta_{out}^\sigma\right) = f^{-1}\left(\tilde{q}_{out}^\sigma\right)$$

for $\sigma = u, s$. Then there exist curves

$$\begin{aligned} \eta_\sigma^{in} &: \left[\theta_{in}^\sigma, t_{in}^\sigma\right] \longrightarrow f^{-1}\left(\tilde{B}\right), \\ \eta_\sigma^{out} &: \left[t_{out}^\sigma, \theta_{out}^\sigma\right] \longrightarrow f^{-1}\left(\tilde{B}\right), \end{aligned} \tag{5.4}$$

for $\sigma = u, s$ such that

1. η_σ^{in} connects $f^{-1}\left(\tilde{q}_{in}^\sigma\right) = \eta_\sigma^{in}\left(\theta_{in}^\sigma\right)$ and $q_{in}^\sigma = \eta_\sigma^{in}\left(t_{in}^\sigma\right)$ for $\sigma = u, s$.

2. η_σ^{out} connects $q_{out}^\sigma = \eta_\sigma^{out}\left(t_{out}^\sigma\right)$ and $f^{-1}\left(\tilde{q}_{out}^\sigma\right) = \eta_\sigma^{out}\left(\theta_{out}^\sigma\right)$ for $\sigma = u, s$.

3. The concatenated curve $\mu_\sigma : \left[\theta^\sigma_{in}, \theta^\sigma_{out}\right] \longrightarrow f^{-1}\left(\tilde{B}\right)$ given by

$$\mu_\sigma(t) := \begin{cases} \eta^{in}_\sigma(t) & \text{if } t \in \left[\theta^\sigma_{in}, t^\sigma_{in}\right] \\ \left(\zeta_\sigma(i)\right)(t) & \text{if } t \in \left(t^\sigma_{in}, t^\sigma_{out}\right) \\ \eta^{out}_\sigma(t) & \text{if } t \in \left[t^\sigma_{out}, \theta^\sigma_{out}\right] \end{cases}$$

is an injectively immersed C^∞-curve for $\sigma = u, s$.

4. The concatenated curve $\xi_\sigma : \mathbb{R} \longrightarrow \mathbb{R}^2$ given by

$$\xi_\sigma(t) := \begin{cases} \gamma^\sigma(t) & \text{if } t \in \left(-\infty, \theta^\sigma_{in}\right) \\ \mu_\sigma(t) & \text{if } t \in \left[\theta^\sigma_{in}, \theta^\sigma_{out}\right] \\ \gamma^\sigma(t) & \text{if } t \in \left(\theta^\sigma_{out}, \infty\right) \end{cases}$$

is an injectively immersed C^∞-curve for $\sigma = u, s$.

5. The curves μ_u and μ_s do not intersect in $f^{-1}\left(\tilde{B}\right) \setminus B$, i.e. they only have a single transverse intersection point $\mathsf{h}(i)$ inherited from B.

Once such curves $\eta^{in}_\sigma, \eta^{out}_\sigma$ as in Figure 5.4 and subsequently μ_σ have been constructed for $\sigma = u, s$, define curves $\zeta_\sigma(j)$ in $\tilde{B}$ as

$$\zeta_\sigma(j) := f(\mu_\sigma).$$

Then the $\zeta_\sigma(j)$ are connector curves for $\tilde{B} = \tilde{B}\left(j, n_j\right)$ which intersect transversely in the point $\mathsf{h}\left(j, n_j\right) := f\left(\mathsf{h}\left(i, n_i\right)\right)$ with the same orientation as $\mathsf{o}(j)$. □

This proposition enables us to select rectangle cornerpoints and connector curves which merge smoothly into the invariant manifolds outside a child ball $\tilde{B}\left(j, n_j\right) \in \tilde{\mathcal{B}}$ if the same are known for the parent ball.

Based on the last two results, we can now proceed to assign such connector curves and rectangle cornerpoints to every homoclinic enclosure ball in $\tilde{\mathcal{B}}$. For convenience we define rosaries:

5.24 Definition. *(Rosary) A rosary is a finite set of L balls $\rho := \left\{\tilde{B}\left(i_j, n_{i_j}\right)\right\}_{j=0}^{L}$ such that*

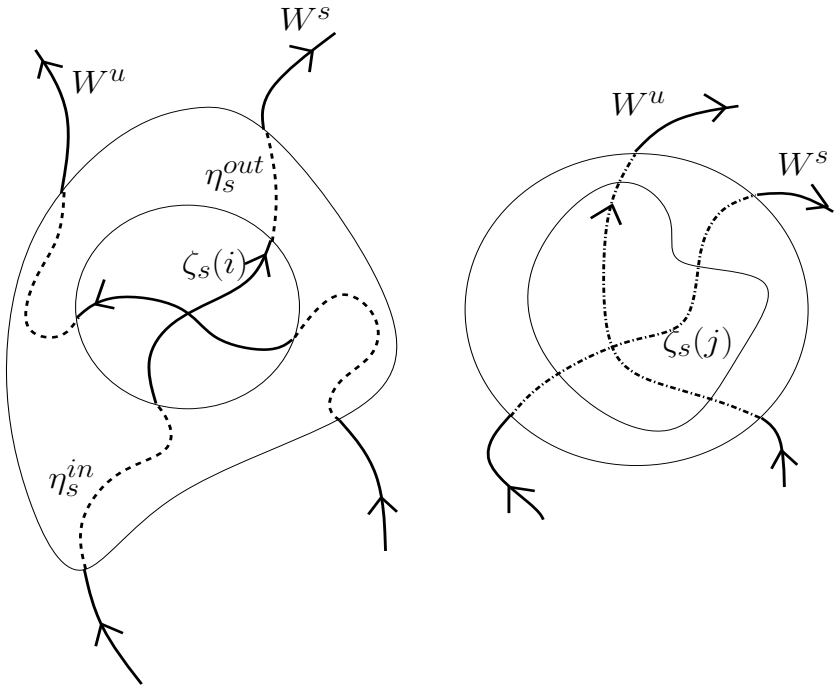

Figure 5.4. $\tilde{B}(i, n_i)$ contained in $f^{-1}(\tilde{B}(j, n_j))$ (left). $\zeta_s(j)$ (dashdotted) for $\tilde{B}(j, n_j)$ (right) is the image of the concatenated curves η_s^{in}, $\zeta_s(i)$ and η^{out}.

1. *Unless* $\tilde{B}\left(i_0, n_{i_0}\right)$ *or* $\tilde{B}\left(i_L, n_{i_L}\right)$ *contain the fixed point, then* $\tilde{B}\left(i_j, n_{i_j}\right) \subset f^{-k}\left(\tilde{B}\left(i_{j+k}, n_{i_{j+k}}\right)\right)$ *for* $1 \leq j \leq L$ *and* $1 \leq k \leq L - j$,
2. $f^{-1}\left(\tilde{B}\left(i_0, n_{i_0}\right)\right)$ *and* $f\left(\tilde{B}\left(i_L, n_{i_L}\right)\right)$ *are disjoint from all elements of* $\tilde{\mathcal{B}}$.

In other words, a rosary defines a sequence of L balls in $\tilde{\mathcal{B}}$ such that the j-th ball is mapped fully into the subsequent balls in the rosary, no ball maps into the first ball, and the last ball maps outside $\tilde{\mathcal{B}}$. A rosary with only a single element contains a ball $\tilde{B}\left(i_1, n_{i_1}\right)$ which is neither a parent nor a child ball.

5.25 Lemma. *The set* $\tilde{\mathcal{B}}$ *consist of finitely many mutually disjoint rosaries* $\rho_1, ..., \rho_K$, *i.e.*

$$\tilde{\mathcal{B}} = \bigcup_{k=1}^{K} \rho_k$$

such that no last elements of any ρ_k maps into another rosary, i.e.

$$f\left(\tilde{B}\left(i_{L(k)}, n_{i_{L(k)}}\right)\right) \cap \tilde{\mathcal{B}} \backslash \left\{\tilde{B}\left(i_{L(k)}, n_{i_{L(k)}}\right)\right\} = \emptyset,$$

where $L(k)$ is the number of elements in ρ_k.

Proof. We select the ρ_k inductively:

1. $k = 1$: It is clear that the fixed point p of the manifold tangle is contained in some element of $\tilde{\mathcal{B}}$, say $p \in \tilde{B}\left(i_1, n_{i_1}\right)$. Then by the mapping assumption (5.4.3), $f\left(\tilde{B}\left(i_1, n_{i_1}\right)\right) \cap \tilde{B}\left(j, n_j\right) = \emptyset \, \forall \, j \neq i_1$, and hence $\rho_1 := \left\{\tilde{B}\left(i_1, n_{i_1}\right)\right\}$ is a rosary.

2. $k \longrightarrow k+1$: Let ρ_1 through ρ_k be chosen, and let

$$\mathfrak{B}_k := \left\{\tilde{B}\left(\alpha, n_\alpha\right) : 1 \leq \alpha \leq N(k)\right\} := \tilde{\mathcal{B}} \backslash \left(\bigcup_{j=1}^{k} \rho_j\right).$$

   be the set of elements in $\tilde{\mathcal{B}}$ not yet contained in the rosaries chosen so far. Since the images of all elements in $\bigcup_{j=1}^{k} \rho_j$ are disjoint from elements in $\mathfrak{B}_k$, there must be a ball $\tilde{B}(\alpha_0, n_{\alpha_0})$ such that

$$f^{-1}\left(\tilde{B}(\alpha_0, n_{\alpha_0})\right) \cap \left(\tilde{\mathcal{B}} \backslash \left\{\tilde{B}(\alpha_0, n_{\alpha_0})\right\}\right) = \emptyset.$$

   Per the mapping property (5.4.3), select a sequence $\{\mathsf{B}_i\}_{i \geq 0}$ of balls in $\mathfrak{B}_k$ such that $\mathsf{B}_0 = \tilde{B}(\alpha_0, n_{\alpha_0})$ and $f\left(\mathsf{B}_i\right) \subset \mathsf{B}_{i+1}$. Any such sequence $\{\mathsf{B}_i\}_{i \geq 0}$ has to be finite, for if it were infinite, then we would have

$$f^{\tilde{n}}\left(\mathsf{B}_{\tilde{\imath}}\right) \subset \mathsf{B}_{\tilde{\imath}} \tag{5.5}$$

   for some $\tilde{n} \in \mathbb{N}$, $1 \leq \tilde{\imath} \leq N(k)$. But due to the locally hyperbolic manifold structure persisting in all balls $\tilde{B}(i, j_i) \in \tilde{\mathcal{B}}$, the invariance (5.5) can not occur. Hence there must exist a finite $L \in \mathbb{N}$, $1 \leq L \leq N(k)$, such that $f\left(\mathsf{B}_L\right)$ maps outside $\tilde{\mathcal{B}} \backslash \left(\bigcup_{j=1}^{k} \rho_j \cup \{\mathsf{B}_i\}_{i=1}^{L}\right)$. This makes $\{\mathsf{B}_i\}_{i=1}^{L}$ the longest rosary in $\mathfrak{B}_k$ starting with $\tilde{B}(\alpha_0, n_{\alpha_0})$, and we call this rosary ρ_{k+1}.

This procedure obviously is exhaustive and assigns every element of $\tilde{\mathcal{B}}$ to a rosary. Disjointness of the rosaries is clear by construction. $\square$

By Propositions 5.22 and 5.23 we know that we can construct cornerpoints and connector curves for every parent and child ball in $\tilde{\mathcal{B}}$. We now want to select $\mathsf{h}(i, n_i)$, $\zeta_u(i)$ and $\zeta_s(i)$ for every $\tilde{B}(i, n_i) \in \tilde{\mathcal{B}}$, but do so contingent on the rosary that contains $\tilde{B}(i, n_i)$:

5.26 Algorithm. *(Cornerpoint and connector curve selection) Let* $\tilde{\mathcal{B}} = \bigcup_{k=1}^{K} \rho_k$, *and assume that for two rosaries* $\rho_{k_1} = \left\{\tilde{B}\left(i_j, n_{i_j}\right)\right\}_{j=0}^{L_{k_1}}$ *and* $\rho_{k_2} = \left\{\tilde{B}\left(l_m, n_{l_m}\right)\right\}_{m=0}^{L_{k_2}}$ *(k_1 may equal k_2) and any two elements* $\tilde{B}\left(i_j, n_{i_j}\right) \in \rho_{k_1}$ *and* $\tilde{B}\left(l_m, n_{l_m}\right) \in \rho_{k_2}$, *we have the disjointness condition*

$$f^{-t}\left(\tilde{B}\left(i_j, n_{i_j}\right)\right) \cap f^{-s}\left(\tilde{B}\left(l_m, n_{l_m}\right)\right) = \emptyset \,\forall\, 0 \le t \le j,\ 0 \le s \le m, \tag{5.6}$$

except where $s = 0$, $l_m = i_{j-t}$ *for a given* i_j, t.

Assume further that for any rosary $\rho_k = \left\{\tilde{B}\left(i_j, n_{i_j}\right)\right\}_{j=0}^{L_k}$ *we have that the crossing orientation of* $f^{-1}\left(\tilde{B}\left(i_{j+1}, n_{i_{j+1}}\right)\right)$ *(in the sense of Def.5.20) equals* $\mathsf{o}\left(i_j\right)$.

We choose cornerpoints and connector curves for elements of ρ_k *inductively:*

1. *Consider the rosary* ρ_1, *and let* $j = 0$: *For* $\tilde{B}\left(i_0, n_{i_0}\right)$, *choose a cornerpoint* $\mathsf{h}\left(i_0, n_{i_0}\right)$ *and connector curves* $\zeta_u(i_0)$ *and* $\zeta_s(i_0)$ *as in Prop. 5.22.*

2. $j \longrightarrow j+1$: *Let* $\mathsf{h}\left(i_j, n_{i_j}\right)$, $\zeta_u\left(i_j\right)$ *and* $\zeta_s\left(i_j\right)$ *be constructed for* $\tilde{B}\left(i_j, n_{i_j}\right)$. *By definition,*

$$f^{-j}\left(\tilde{B}\left(i_j, n_{i_j}\right)\right) \subset f^{-(j+1)}\left(\tilde{B}\left(i_{j+1}, n_{i_{j+1}}\right)\right).$$

So proceed as in Prop. 5.23 and for $\sigma = u, s$ *construct mutually disjoint curves* η_{in}^{σ} *which connect* $f^{-(j+1)}\left(q_{in}\left(W^{\sigma}(p), \tilde{B}\left(i_{j+1}, n_{i_{j+1}}\right)\right)\right)$ *to* $f^{-j}\left(q_{in}\left(W^{\sigma}(p), \tilde{B}\left(i_j, n_{i_j}\right)\right)\right)$ *and* η_{out}^{σ}

which connect $f^{-j}\left(q_{out}\left(W^{\sigma}\left(p\right),\tilde{B}\left(i_j,n_{i_j}\right)\right)\right)$ *to* $f^{-(j+1)}\left(q_{out}\left(W^{\sigma}\left(p\right),\tilde{B}\left(i_{j+1},n_{i_{j+1}}\right)\right)\right)$.

Map the concatenated curve $\xi_\sigma := \eta_{in}^{\sigma}\&f^{-j}\left(\zeta_\sigma\left(i_j\right)\right)\&\eta_{out}^{\sigma}$ *to obtain*

$$\zeta_\sigma\left(i_{j+1}\right) := f^{j+1}\left(\xi_\sigma\right).$$

Since furthermore $\mathsf{h}\left(i_0,n_{i_0}\right) = f^{-j}\left(\mathsf{h}\left(i_j,n_{i_j}\right)\right)$ *is the only intersection of the curves* ξ_u *and* ξ_s *in* $f^{-(j+1)}\left(\tilde{B}\left(i_{j+1},n_{i_{j+1}}\right)\right)$, *also we set*

$$\mathsf{h}\left(i_{j+1},n_{i_{j+1}}\right) := f\left(\mathsf{h}\left(i_j,n_{i_j}\right)\right) = f^{j+1}\left(\mathsf{h}\left(i_0,n_{i_0}\right)\right)$$

as the unique transverse intersection of $\zeta_u\left(i_{j+1}\right)$ *and* $\zeta_s\left(i_{j+1}\right)$ *in* $\tilde{B}\left(i_{j+1},n_{i_{j+1}}\right)$.

Stop the induction when $j = L_k$.

3. *Repeat steps 1 and 2 over all rosaries* ρ_k *for* $k = 2,...,K$.

5.27 Remark. *The disjointness condition (5.6) is a natural one. If we did not have ball enclosures of the homoclinic points, but the actual homoclinic points, this condition would always be given. So for continuity reasons, by having sufficiently small ball enclosures of the homoclinic points, we are still be able to satisfy (5.6). In practice, however, due to the hyperbolic nature of the map in the neighborhood of homoclinic points, this disjointness demand for the homoclinic ball mappings is quite hard to satisfy and is the primary reason for a breakdown of the Taylor Model verification of the the rectangle chain construction described in this section.*

Obviously the above algorithm exhaustively assigns a unique rectangle cornerpoint to every ball in $\tilde{\mathcal{B}}$ by finding mapping sequences, and we can define the set of cornerpoints as

$$\mathcal{H}_{\tilde{\mathcal{B}}} := \left\{\mathsf{h}\left(i,n_i\right) \in \mathbb{R}^2 : 1 \le i \le \tilde{N}\right\}.$$

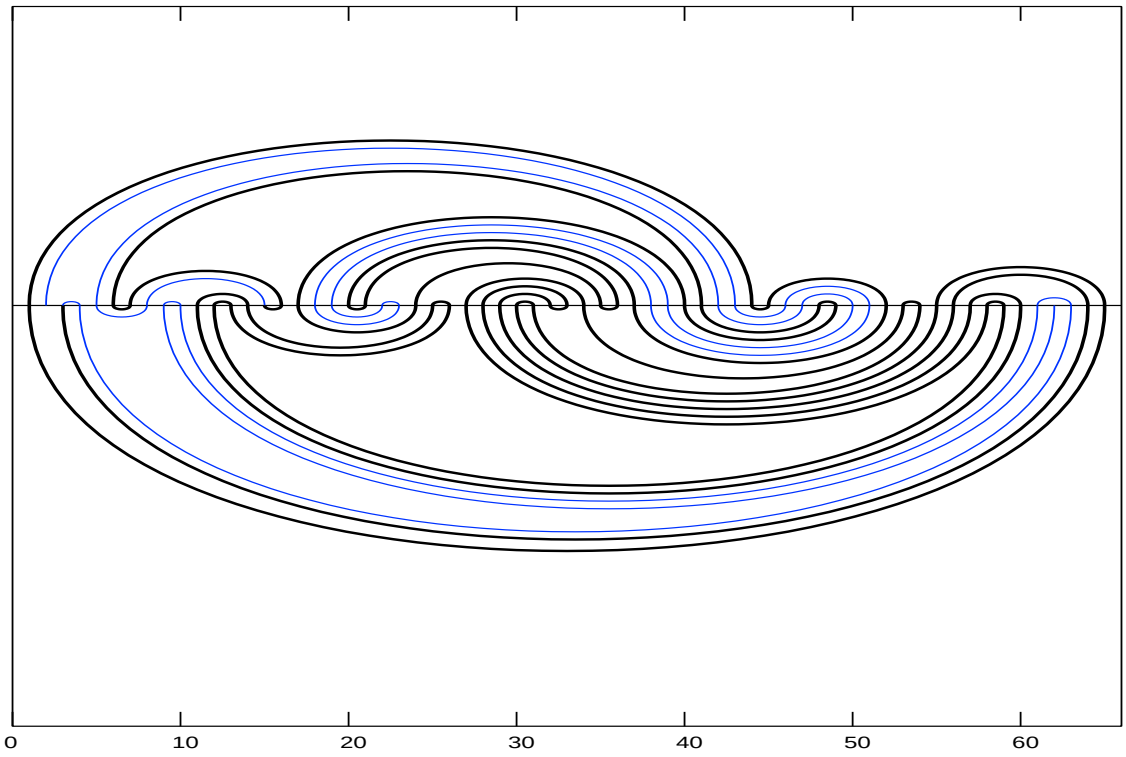

Figure 5.5. A manifold tangle with 65 transverse cornerpoints, ordered along the stable manifold $\mathcal{S}$ (horizontal axis), and the unstable segments $\mathcal{U}$ (black) and $f(\mathcal{U})$ (blue).

It is also clear that the following mapping property holds: If $\tilde{B}\left(i,n_i\right),\tilde{B}\left(j,n_j\right)\in\tilde{\mathcal{B}}$ such that $\tilde{B}\left(i,n_i\right)$ is a parent ball for $\tilde{B}\left(j,n_j\right)$, then for the associated cornerpoints and connector curves we have

$$f\left(\mathsf{h}\left(i,n_i\right)\right)=\mathsf{h}\left(j,n_j\right),$$

$$f\left(\zeta_\sigma\left(i\right)\right)\subset\zeta_\sigma\left(j\right)\text{ for }\sigma=u,s.$$

5.4.6 Definition of rectangles

5.28 Remark. *At this point, we have 'untangled' the manifold tangle $\mathcal{T}$ from section 5.4.1 . For every ball in $\tilde{B}\left(i,n_i\right)\in\tilde{\mathcal{B}}$, a unique point $\mathsf{h}\left(i,n_i\right)$ is selected at which*

the 'patched' manifolds intersect transversely with the same orientation $\mathsf{o}(i)$ *as is assigned to* $\tilde{B}(i, n_i)$ *as in section 3.4.4 . By 'patched' manifolds we mean the curves obtained from taking the invariant manifolds outside the balls in* $\tilde{\mathcal{B}}$ *and connecting them with the respective connector curves inside the balls.*

The ordering of all points $\mathsf{h}(i, n_i)$ *along the patched manifold as given by the indices* i *and* n_i *is still valid. This information is sufficient to draw the manifold tangle* $\mathcal{T}$ *as in Figure 5.5.*

It is important to note that we have thus made a transition from the problem of finding rectangle chains for f *in the plane, to describing the construction in a completely discrete framework.*

Consider a subset $\mathcal{H}_{\mathcal{B}}$ of $\mathcal{H}_{\tilde{\mathcal{B}}}$ given as

$$\begin{aligned}\mathcal{H}_{\mathcal{B}} &:= \left\{\mathsf{h}(i, n_i) \in \mathbb{R}^2 : \mathsf{h}(i, n_i) \text{ is the cornerpoint in } \tilde{B}(i, n_i) \in \mathcal{B} \cap \tilde{\mathcal{B}}\right\}, \\ &=: \{\mathsf{h}(\alpha, m_\alpha) : 1 \leq \alpha \leq N\}.\end{aligned}$$

where the indices (α, m_a) correspond to the stable and unstable ordering (i, n_i) restricted to the intersections in $\mathcal{S} \cap \mathcal{U}$. So $\mathcal{H}_{\mathcal{B}}$ contains the cornerpoints selected for the closed balls in $\mathcal{S} \cap \mathcal{U}$. In particular, by design all balls in $\mathcal{B} \cap \tilde{\mathcal{B}}$ are parent balls, so we have that

$$f(\mathsf{h}(\alpha, m_\alpha)) \in \mathcal{H}_{\tilde{\mathcal{B}}} \, \forall \, 1 \leq \alpha \leq N.$$

In other words, if we define rectangles with cornerpoints in $\mathcal{H}_{\mathcal{B}}$, their images will again be rectangles with cornerpoints in $\mathcal{H}_{\tilde{\mathcal{B}}}$. We now proceed with the rectangle construction with an eye to the untangled manifold picture in remark (5.28). Specifically, we will use the manifold orientation at the intersection points to define rectangles 'above' and 'below' the stable axis to ensure disjointness of rectangle interiors.

5.29 Algorithm. *(Cornerpoint loop)*

1. *Construction 'above' the stable axis: Let* $\alpha = 1$ *and consider* $\mathsf{h}(\alpha, m_\alpha) \in \mathcal{H}_{\tilde{\mathcal{B}}}$.

(a) *Select the next cornerpoint in the unstable direction as* $\mathsf{h}\left(\beta, m_\beta\right)$*, where* $m_\beta = m_\alpha + \mathsf{o}(\alpha)$*, i.e.* $\mathsf{h}\left(\beta, m_\beta\right)$ *is the next (or previous) cornerpoint along the unstable arc above the stable axis if the crossing is positive (or negative). See also Figure 5.6 for visualization.*

(b) *Select the previous cornerpoint* $\mathsf{h}\left(\gamma, m_\gamma\right)$ *in the stable direction, i.e.* $\gamma = \beta - 1$.

(c) *Select the next cornerpoint in the unstable direction as* $\mathsf{h}(\delta, m_\delta)$*, where* $m_\delta = m_\alpha + \mathsf{o}(\alpha)$.

(d) *If* $\delta = \alpha + 1$*, record the ordered sequence of cornerpoint indices* $c_\alpha := \{\alpha, \beta, \gamma, \delta\}$*. Let* $\alpha \longrightarrow \alpha + 1$ *and repeat from step 1.*

(e) *Stop when* $\alpha = N$.

2. *Construction 'below' the stable axis is analogous to above: Let* $\alpha = 1$ *and consider* $\mathsf{h}(\alpha, m_\alpha) \in \mathcal{H}_{\tilde{\mathcal{B}}}$.

(a) *Select the next cornerpoint in the unstable direction as* $\mathsf{h}\left(\beta, m_\beta\right)$*, where* $m_\beta = m_\alpha + \mathsf{o}(\alpha)$*, i.e.* $\mathsf{h}\left(\beta, m_\beta\right)$ *is the next (or previous) cornerpoint along the unstable arc above the stable axis if the crossing is positive (or negative).*

(b) *Select the previous cornerpoint* $\mathsf{h}\left(\gamma, m_\gamma\right)$ *in the stable direction, i.e.* $\gamma = \beta - 1$.

(c) *Select the next cornerpoint in the unstable direction as* $\mathsf{h}(\delta, m_\delta)$*, where* $m_\delta = m_\alpha + \mathsf{o}(\alpha)$.

(d) *If* $\delta = \alpha + 1$*, record the ordered sequence of cornerpoint indices* $c_\alpha := \{\alpha, \beta, \gamma, \delta\}$*. Let* $\alpha \longrightarrow \alpha + 1$ *and repeat from step 1.*

(e) *Stop when* $\alpha = N$.

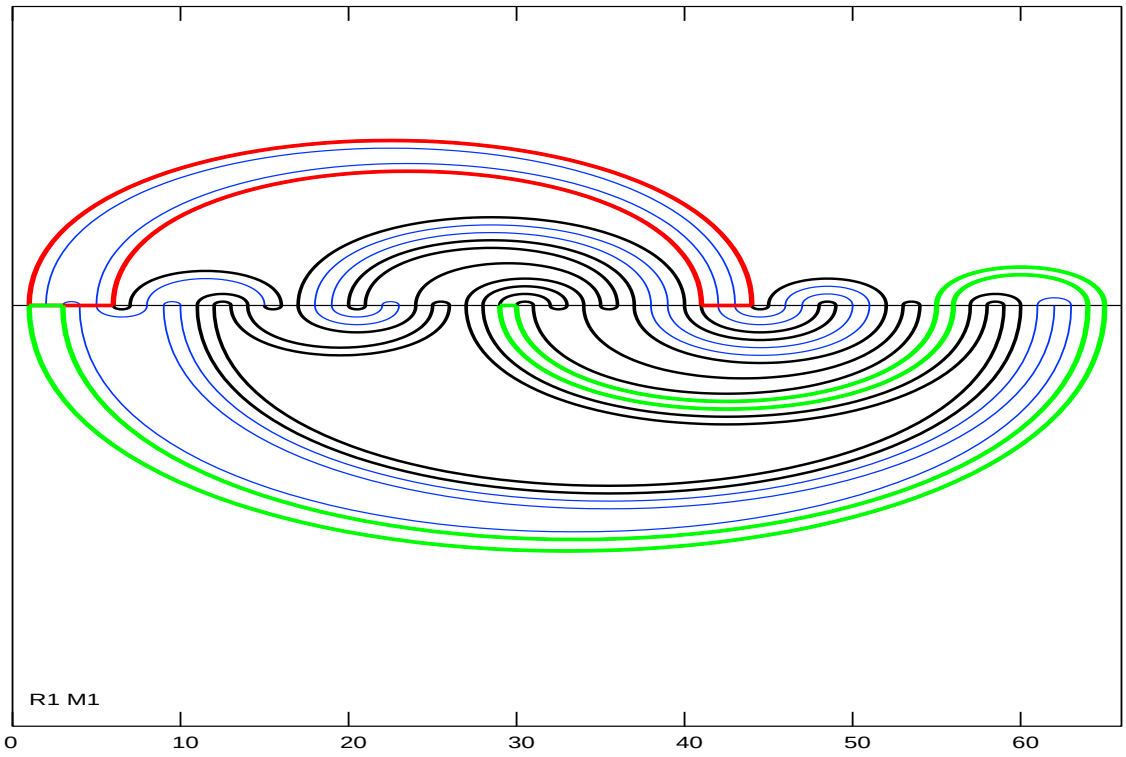

Figure 5.6. A rectangle $R(\alpha,\beta,\gamma,\delta) = R(1,44,41,6)$ (red) as constructed in section 5.4.6 . Also shown is the mapped rectangle $f(R(1,44,41,6))$ (green).

Identify all index sequences that are cyclic permutations of each other, i.e. if $c_\alpha := \{\alpha,\beta,\gamma,\delta\}$ *and* $c_{\tilde{\alpha}} := \left\{\tilde{\alpha},\tilde{\beta},\tilde{\gamma},\tilde{\delta}\right\} = \{\gamma,\delta,\alpha\,\beta\}$*, then discard* $c_{\tilde{\alpha}}$*.*

We now have a collection of M cornerpoint index sequences $\left\{c_{\alpha_i}\right\}_{i=1}^{M}$ such that for each index sequence $c_\alpha := \{\alpha,\beta,\gamma,\delta\}$ the cornerpoints $\mathsf{h}\left(\alpha,m_\alpha\right), \mathsf{h}\left(\beta,m_\beta\right), \mathsf{h}\left(\gamma,m_\gamma\right), \mathsf{h}\left(\delta,m_\delta\right)$ are adjacent to each other in the stable and unstable directions of $\mathcal{S}\cap\mathcal{U}$ as per algorithm steps 1 and 2, and form a closed loop

$$\mathsf{h}\left(\alpha,m_\alpha\right) \longrightarrow \mathsf{h}\left(\beta,m_\beta\right) \longrightarrow \mathsf{h}\left(\gamma,m_\gamma\right) \longrightarrow \mathsf{h}\left(\delta,m_\delta\right) \longrightarrow \mathsf{h}\left(\alpha,m_\alpha\right).$$

We now use these cornerpoint sequences to define rectangles, with special care about the choice of curves connecting them so that invariance under mapping is guaranteed:

Consider an index sequence $c_\alpha := \{\alpha, \beta, \gamma, \delta\}$, and select the cornerpoints $\mathsf{h}(\alpha, m_\alpha)$ and $\mathsf{h}\left(\beta, m_\beta\right)$. They are contained in balls $\tilde{B}(\alpha, n_\alpha)$ and $\tilde{B}\left(\beta, n_\beta\right)$ which are directly adjacent to each other in the unstable manifold of $\mathcal{S} \cap \mathcal{U}$. Furthermore they are contained in rosaries $\rho_{k_1}, \rho_{k_2} \subset \tilde{\mathcal{B}}$ as

$$\tilde{B}(\alpha, n_\alpha) = \tilde{B}\left(i_{j_0}, n_{i_{j_0}}\right) \in \rho_{k_1} = \left\{\tilde{B}\left(i_j, n_{i_j}\right)\right\}_{j=1}^{N(k_1)},$$
$$\tilde{B}\left(\beta, n_\beta\right) = \tilde{B}\left(l_{m_0}, n_{l_{m_0}}\right) \in \rho_{k_2} = \left\{\tilde{B}\left(l_m, n_{l_m}\right)\right\}_{m=1}^{N(k_2)}.$$

The balls $\tilde{B}\left(i_{N(k_1)}, n_{i_{N(k_1)}}\right)$ and $\tilde{B}\left(l_{N(k_2)}, n_{l_{N(k_2)}}\right)$ are the last elements of their respective rosaries, and have associated unstable connector curves $\zeta_u\left(i_{N(k_1)}\right)$ and $\zeta_u\left(l_{N(k_2)}\right)$. The preimages

$$f^{-\left(N(k_1)-i_{j_0}\right)}\left(\zeta_u\left(i_{N(k_1)}\right)\right),$$
$$f^{-\left(N(k_2)-l_{m_0}\right)}\left(\zeta_u\left(l_{N(k_2)}\right)\right),$$

are disjoint, contain $\mathsf{h}(\alpha, m_\alpha)$ and $\mathsf{h}\left(\beta, m_\beta\right)$ and are connected C^r by exactly one subarc of the unstable manifold $W^u(p)$. Define the curve $tR(\alpha, \beta, \gamma, \delta)$ as the curve concatenated from $f^{-\left(N(k_1)-i_{j_0}\right)}\left(\zeta_u\left(i_{N(k_1)}\right)\right)$, $W^u(p)$ and $f^{-\left(N(k_2)-l_{m_0}\right)}\left(\zeta_u\left(l_{N(k_2)}\right)\right)$ and having $\mathsf{h}(\alpha, m_\alpha)$ and $\mathsf{h}\left(\beta, m_\beta\right)$ as its endpoints.

Analogously, connect $\mathsf{h}\left(\beta, m_\beta\right), \mathsf{h}\left(\gamma, m_\gamma\right)$ and $\mathsf{h}(\delta, m_\delta), \mathsf{h}(\alpha, m_\alpha)$ with 'stable' curves $rR(\alpha, \beta, \gamma, \delta)$ and $lR(\alpha, \beta, \gamma, \delta)$, and connect $\mathsf{h}\left(\gamma, m_\gamma\right), \mathsf{h}(\delta, m_\delta)$ with an 'unstable' curve $bR(\alpha, \beta, \gamma, \delta)$.

This construction leads to the following result:

5.30 Lemma. *For the index sequence* $c_\alpha := \{\alpha, \beta, \gamma, \delta\}$, *let* $\mathsf{h}(\alpha, m_\alpha), \mathsf{h}\left(\beta, m_\beta\right), \mathsf{h}\left(\gamma, m_\gamma\right), \mathsf{h}(\delta, m_\delta)$ *and* $tR(\alpha, \beta, \gamma, \delta)$, $rR(\alpha, \beta, \gamma, \delta)$,

$bR(\alpha,\beta,\gamma,\delta)$ and $lR(\alpha,\beta,\gamma,\delta)$ be given as above. Then the concatenated curve

$$\begin{aligned} J := & \, tR(\alpha,\beta,\gamma,\delta) \\ & \cup rR(\alpha,\beta,\gamma,\delta) \\ & \cup bR(\alpha,\beta,\gamma,\delta) \\ & \cup lR(\alpha,\beta,\gamma,\delta) \end{aligned}$$

is a Jordan curve and J together with its interior forms a retangle with piecewise C^r boundaries and with cornerpoints

$$\begin{aligned} x_{tl} &= \mathsf{h}(\alpha, m_\alpha), \quad x_{tr} = \mathsf{h}\left(\beta, m_\beta\right), \\ x_{br} &= \mathsf{h}\left(\gamma, m_\gamma\right), \quad x_{bl} = \mathsf{h}(\delta, m_\delta). \end{aligned}$$

This rectangle is naturally denoted $R(\alpha,\beta,\gamma,\delta)$.

Repeating the rectangle construction over all index sequences yields the set of suitable rectangles:

5.31 Lemma. *For all index sequences $\left\{c_{\alpha_i}\right\}_{i=1}^{M}$ stemming from the rosaries $\rho_1, ..., \rho_K$ containing $\tilde{\mathcal{B}}$, we can construct M rectangles $R(\alpha,\beta,\gamma,\delta)$ with piecewise C^r boundaries. All M rectangles have disjoint interior.*

The disjointness follows directly from the construction, since two rectangles can share at most one boundary. We also observe the following:

5.32 Proposition. *If $R(\alpha,\beta,\gamma,\delta)$ is a rectangle, then its image $f(R(\alpha,\beta,\gamma,\delta))$ is again a rectangle with*

$$\begin{aligned} & f(\mathsf{h}(\alpha, m_\alpha)), \quad f\left(\mathsf{h}\left(\beta, m_\beta\right)\right), \\ & f\left(\mathsf{h}\left(\gamma, m_\gamma\right)\right), \quad f(\mathsf{h}(\delta, m_\delta)), \end{aligned}$$

as its top left, top right, bottom right and bottom left cornerpoints, and

$$\begin{aligned} & f(tR(\alpha,\beta,\gamma,\delta)), \quad f(rR(\alpha,\beta,\gamma,\delta)), \\ & f(bR(\alpha,\beta,\gamma,\delta)), \quad f(lR(\alpha,\beta,\gamma,\delta)), \end{aligned}$$

as its top, right, bottom and left boundaries.

This is illustrated in Figure 5.6.

5.4.7 Mapping of rectangles

The rather involved construction of rectangle boundaries yields this fundamental and important mapping property:

5.33 Theorem. *(Invariance of rectangles under mapping) Let* $R(\alpha,\beta,\gamma,\delta)$ *and* $R\left(\tilde{\alpha},\tilde{\beta},\tilde{\gamma},\tilde{\delta}\right)$ *be two rectangles constructed as in the previous section. If the cornerpoints of* $R(\alpha,\beta,\gamma,\delta)$ *map into those of* $R\left(\tilde{\alpha},\tilde{\beta},\tilde{\gamma},\tilde{\delta}\right)$*, then*

$$f\left(R\left(\alpha,\beta,\gamma,\delta\right)\right)=R\left(\tilde{\alpha},\tilde{\beta},\tilde{\gamma},\tilde{\delta}\right).$$

However, typically the rectangles do not map into each other, but due to the hyperbolic nature of the map across each other instead, i.e. they form Markov crossings under iteration. This observation is the content of the next mapping theorem.

Let $R_1=R_1\left(\alpha,\beta,\gamma,\delta\right)$ be a rectangle given by the top left, top right, bottom right and bottom left cornerpoints $x_{tl}=\mathsf{h}\left(\alpha,n_\alpha\right),x_{tr}=\mathsf{h}\left(\beta,n_\beta\right),x_{br}=\mathsf{h}\left(\gamma,n_\gamma\right)$ and $x_{bl}=\mathsf{h}\left(\delta,n_\delta\right)$. Consider the mappings

$$\begin{aligned}\mathsf{h}\left(a,n_a\right)&:=f\left(x_{tl}\right)=f\left(\mathsf{h}\left(\alpha,n_\alpha\right)\right)\\ \mathsf{h}\left(b,n_b\right)&:=f\left(x_{tr}\right)=f\left(\mathsf{h}\left(\beta,n_\beta\right)\right)\\ \mathsf{h}\left(c,n_c\right)&:=f\left(x_{br}\right)=f\left(\mathsf{h}\left(\gamma,n_\gamma\right)\right)\\ \mathsf{h}\left(d,n_d\right)&:=f\left(x_{bl}\right)=f\left(\mathsf{h}\left(\delta,n_\delta\right)\right).\end{aligned}$$

Then these are the cornerpoints for the rectangle $f\left(R_1\right)$.

Let now a second rectangle $R_2=R_2\left(\varepsilon,\zeta,\eta,\theta\right)$ be given with the top left, top right, bottom right and bottom left cornerpoints $x_{tl}=\mathsf{h}\left(\varepsilon,n_\varepsilon\right),x_{tr}=\mathsf{h}\left(\zeta,n_\zeta\right),x_{br}=\mathsf{h}\left(\eta,n_\eta\right)$ and $x_{bl}=\mathsf{h}\left(\theta,n_\theta\right)$.

5.34 Theorem. *(Rectangle Markov crossing) Let the rectangles* R_1 *and* R_2 *have cornerpoints as above, and let their boundary segments be oriented as in Figure 5.7. There is a Markov crossing* $f\left(R_1\right)\sharp R_2$ *if there exist homoclinic points*

$\mathsf{h}(i,n_i)$, $\mathsf{h}\left(j,n_j\right)$, $\mathsf{h}(k,n_k)$ *and* $\mathsf{h}(l,n_l)$ *such that the following hold:*

$$\begin{array}{llll} i) & a \le i < j \le b & ii) & c \le k < l \le d \\ iii) & n_\zeta \le n_j < n_k \le n_\eta & iv) & n_\theta \le n_l < n_i \le n_\varepsilon \ . \end{array} \tag{5.7}$$

If R_1 or R_2 have other orientations of their boundary segments, then analogous statements to Thm. 5.7 hold with altered orderings.

Proof. The proof follows directly from Figure 5.7. We concatenate the unstable arc $\wp_{W^u(p)}\left(\mathsf{h}(i,n_i)\ \mathsf{h}\left(j,n_j\right)\right)$, the stable arc $\wp_{W^s(p)}\left(\mathsf{h}\left(j,n_j\right)\ \mathsf{h}(k,n_k)\right)$, the unstable arc $\wp_{W^u(p)}\left(\mathsf{h}(k,n_l)\ \mathsf{h}(l,n_l)\right)$ and the stable arc$\wp_{W^s(p)}\left(\mathsf{h}(l,n_l)\ \mathsf{h}(i,n_i)\right)$. Then the concatenated curve

$$\begin{aligned} J := & \wp_{W^u(p)}\left(\mathsf{h}(i,n_i)\ \mathsf{h}\left(j,n_j\right)\right) \\ & \cup \wp_{W^s(p)}\left(\mathsf{h}\left(j,n_j\right)\ \mathsf{h}(k,n_k)\right) \\ & \cup \wp_{W^u(p)}\left(\mathsf{h}(k,n_l)\ \mathsf{h}(l,n_l)\right) \\ & \cup \wp_{W^s(p)}\left(\mathsf{h}(l,n_l)\ \mathsf{h}(i,n_i)\right) \end{aligned}$$

is a Jordan curve, the interior of which is contained in both rectangles $f(R_1)$ and R_2, and thus we have a Markov crossing. □

5.4.8 Entropy estimates

The entire rectangle chain construction of Section 5.4 culminates in the following theorem, a direct consequence of Thm. 5.15:

5.35 Theorem. *Let $f : \mathbb{R}^2 \supset M \longrightarrow M$, where M is compact, be a smooth diffeomorphism with a homoclinic saddle point p. Starting from p, generate the manifold tangle $\mathcal{T}$ as in section 5.4.1 and proceed to obtain homoclinic ball enclosures $\tilde{\mathcal{B}}$ with the ordering information (as in section 5.4.2), mapping information (as in section 5.4.4) and manifold crossing orientation (as in section 5.4.3) of elements $\tilde{\mathcal{B}}$.*

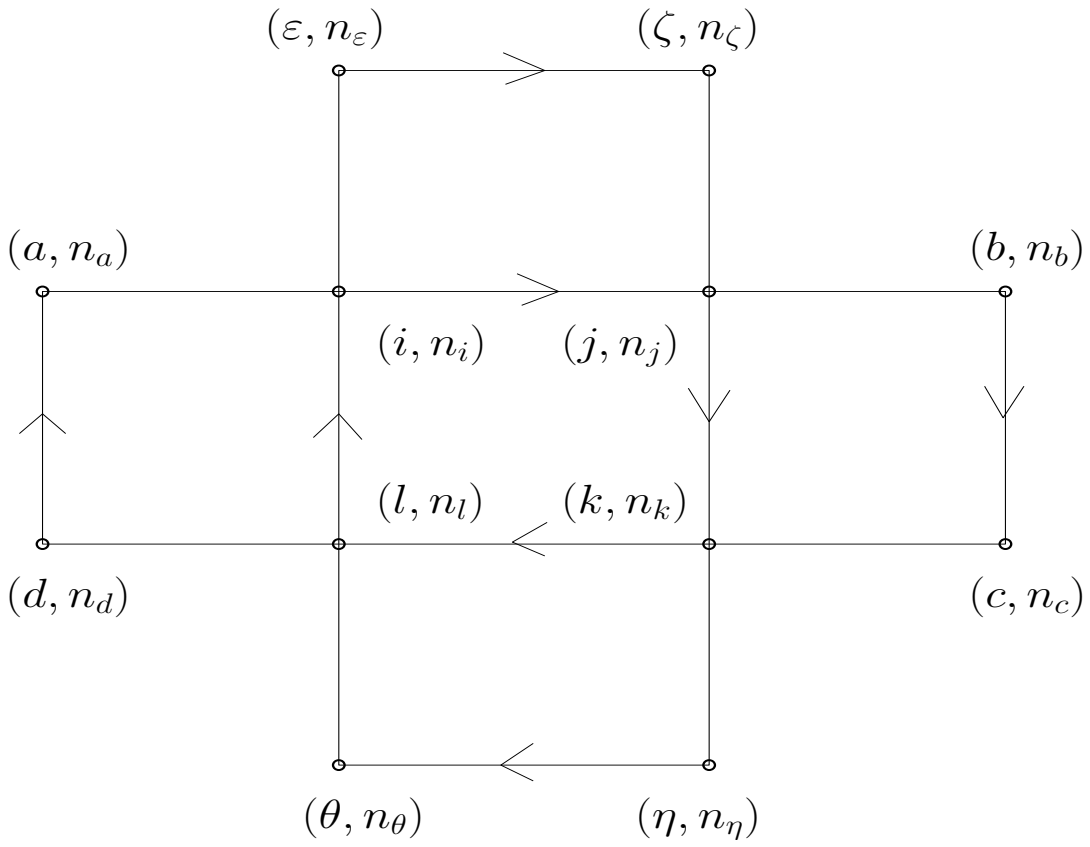

Figure 5.7. The determination of the Markov-crossing of $f(R(\alpha, \beta, \gamma, \delta)) = R(a, b, c, d)$ and $R(\varepsilon, \zeta, \eta, \theta)$ amounts to a simple check on the cornerpoint ordering in the manifold tangle.

This data permits the automatic construction of rectangles and rectangle crossings such that for an incidence matrix A obtained from the Markov crossings in Thm. 5.34 we have

$$h(f) \geq sp(A).$$

5.5 Taylor Model verification of rectangle chain construction

In the previous section an algorithm to construct topological rectangles using the invariant manifold tangle, and to determine their Markov crossings, has been presented. In the following we now rigorously verify this construction, i.e. we introduce Taylor Model based algorithms that can check the assumptions that were made for the construction in section 5.4. Conceptually, this will prove to be not difficult, since the construction in section 5.4 was developed with an eye on the implementation in the Taylor Model framework.

5.5.1 Manifold tangle

Let p be a hyperbolic saddle point of the C^r-diffeomorphism $f : \mathbb{R}^2 \longrightarrow \mathbb{R}^2$, and let λ_u be the unstable eigenvalue, assumed without loss of generality to have positive real part (else consider the squared map f^2).

According to the construction in section 4.4 we are able to find ordered sequences of Taylor Models that form a C^0-enclosure of the invariant manifolds. Starting with verified Taylor Model enclosures $T_{s,u}$ of the local invariant manifolds $W^{s,u}_{loc}(p)$, we simply iterate in Taylor Model arithmetic to obtain

$$f^{Ku}\left(W^u_{loc}(p)\right) \subset f^{Ku}(T_u) \quad \text{and} \quad f^{-Ks}\left(W^s_{loc}(p)\right) \subset f^{-Ks}(T_s).$$

for some iterates $K_u, K_s \in \mathbb{N}_0$. The fundamental assumption which needs to be

satisfied is $\mathcal{U} \subset f(\mathcal{U})$ and $f(\mathcal{S}) \subset \mathcal{S}$. The simplest choice of tangle that guarantees this property is to choose $\mathcal{S} := \{S_1\}$ and $\mathcal{U} := \{U_1\}$ where

$$U_1 := f^{-Ks}\left(W^s_{loc}(p)\right) \quad \text{and} \quad S_1 := f^{Ku}\left(W^u_{loc}(p)\right), \tag{5.8}$$

in which case the desired containments are immediately satisfied.

Selecting the entire manifold iterates as in (5.8) for the manifold tangle is not necessarily desirable, e.g. for high iterates K_u, K_s the manifolds accumulate so densely upon themselves that the Taylor Model enclosures $f^{Ku}(T_u)$ and $f^{-Ks}(T_s)$ cannot resolve them anymore, and one may wish to select only a finite collection of subarcs of the entire manifold iterates.

We note that there is a technique to suitably pick a finite collection $\mathcal{U}^\star \subset \mathcal{U}$ of unstable subarcs for the tangle selection and still have $\mathcal{U}^\star \cup f(\mathcal{U}^\star)$ fully ordered:

Let $\mathcal{U}^\star := \left\{U^\star_1, ..., U^\star_{L^\star}\right\}$ be an ordered collection of compact unstable subarcs with mutually disjoint interiors. For a subarc $U^\star_i \in \mathcal{U}^\star$, let $b_l(i)$ and $b_u(i)$ denote the lower and upper endpoints of $U^\star_i$ in the orientation of $W^u(p)$. Then $\mathcal{U}^\star \cup f(\mathcal{U}^\star)$ can be ordered if the following two conditions hold:

1. $f(b_l(k)) \geq b_u(k)\ \forall\, 1 \leq k \leq L^\star$.

2. $f(b_u(k)) \leq b_l(k+1)\ \forall\, 1 \leq k \leq (L^\star - 1)$

where $\leq$ and $\geq$ denote ordering in the orientation of $W^u(p)$.

5.5.2 Interval box enclosures of homoclinic points, ordering and crossing orientation

In section 4.4 we presented an algorithm to find set enclosures of homoclinic intersections of a stable and unstable manifold piece contained in intersecting Taylor Models. Immediately we can extend this algorithm to enclose all homoclinic intersections of

entire lists of TMs $\left\{T_{u,i}\right\}_{i=1}^{J_u}$ and $\left\{T_{s,j}\right\}_{j=1}^{J_s}$. The algorithm is simply performed $J_u \cdot J_s$ times.

Candidate parameter enclosures for intersections of two Taylor Models $T_{u,i}$ and $T_{s,j}$ are found by a verified global optimization scheme. Since the lists $\left\{T_{u,i}\right\}_{i=1}^{J_u}$ and $\left\{T_{s,j}\right\}_{j=1}^{J_s}$ are ordered along the arclength of the manifold they contain, and every $T_{u,i}$ and $T_{s,j}$ is parametrized longitudinally on $[-1,1]$, the candidate parameter enclosures for the intersections can easily be ordered.

Existence of a homoclinic intersection points as in section 5.4.2 and following is being proved via Algorithm 4.15. Since Algorithm 4.15 checks the existence of entry and exit points and determines the correponding boundary segment of the interval enclosure, the manifold crossing orientation is obtained immediately as well.

5.5.3 Homoclinic interval box enclosure mappings

The containment conditions (5.4.3) and (5.6) are required for the determination of mapping properties and rosaries. Performing the mappings of an interval box enclosure $\tilde{B} \in \tilde{\mathcal{B}}$ in Taylor Model or interval arithmetic yields verified outer estimates of their ranges and containment can be rigorously checked. Techniques for the efficient range bounding for specific cases Taylor Model are available [45, 48].

Finding sharp range estimates of $f\left(\tilde{B}\right)$ and $f^{-1}\left(\tilde{B}\right)$ in light of the inavoidable accumulation of homoclinic interval box enclosures for higher iterates of the manifold is the biggest challenge.

5.6 Results: Entropy of the Hénon map

As an example of the entropy construction in the last section we again consider the Hénon map

$$H_{a,b}(x,y) := \left(1 + y - ax^2, bx\right)$$

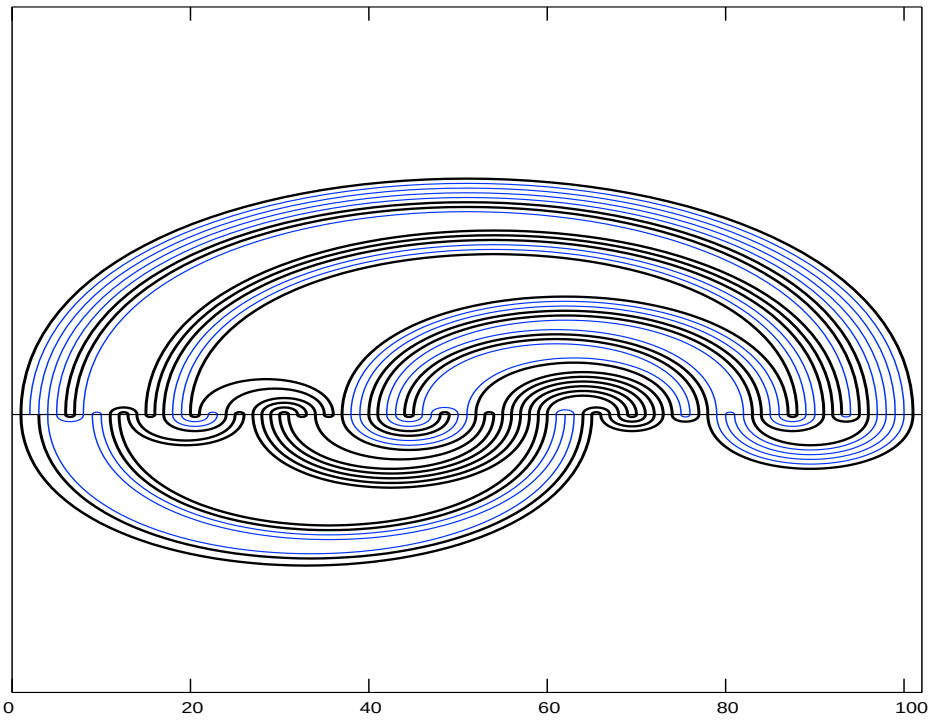

a)

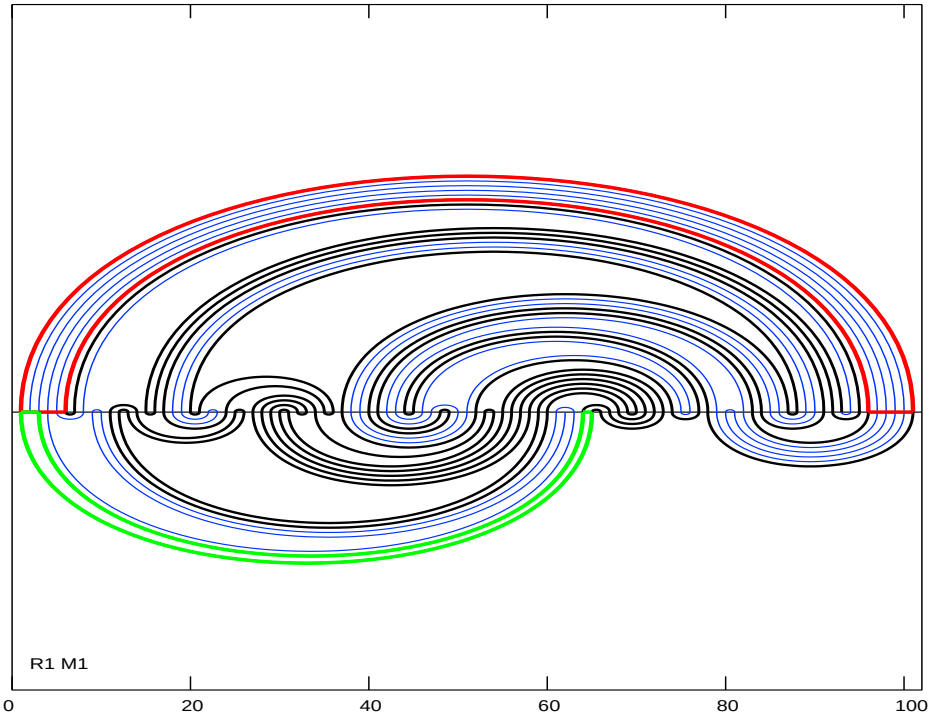

b)

Figure 5.8. **a**) Rectangle R_{12} (blue) and its 7th image (red). **b**) Rectangle R_1 (red) and its image (green).

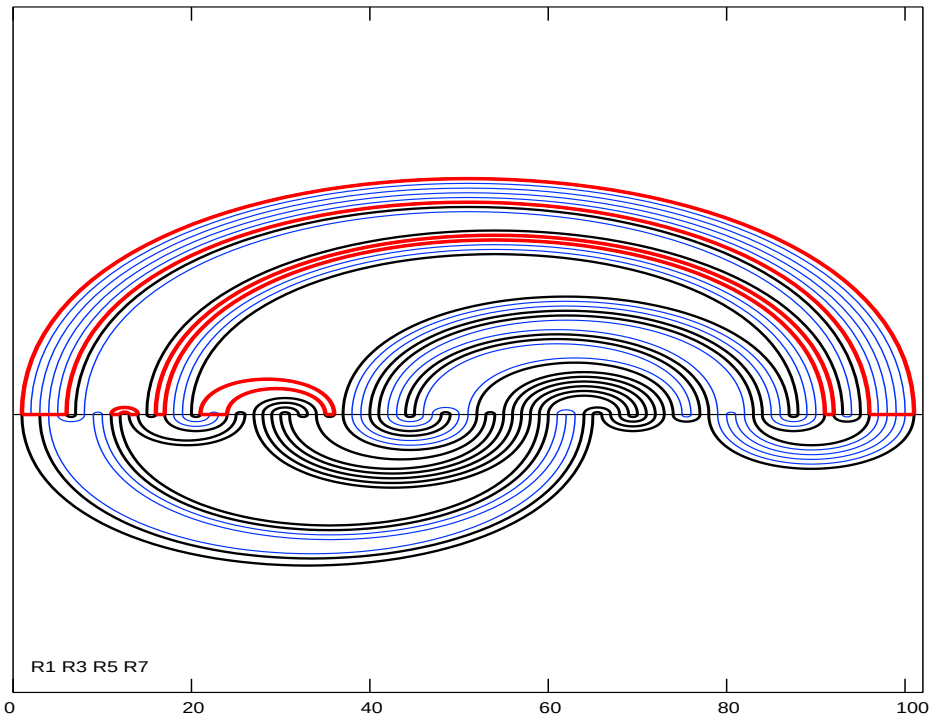

a)

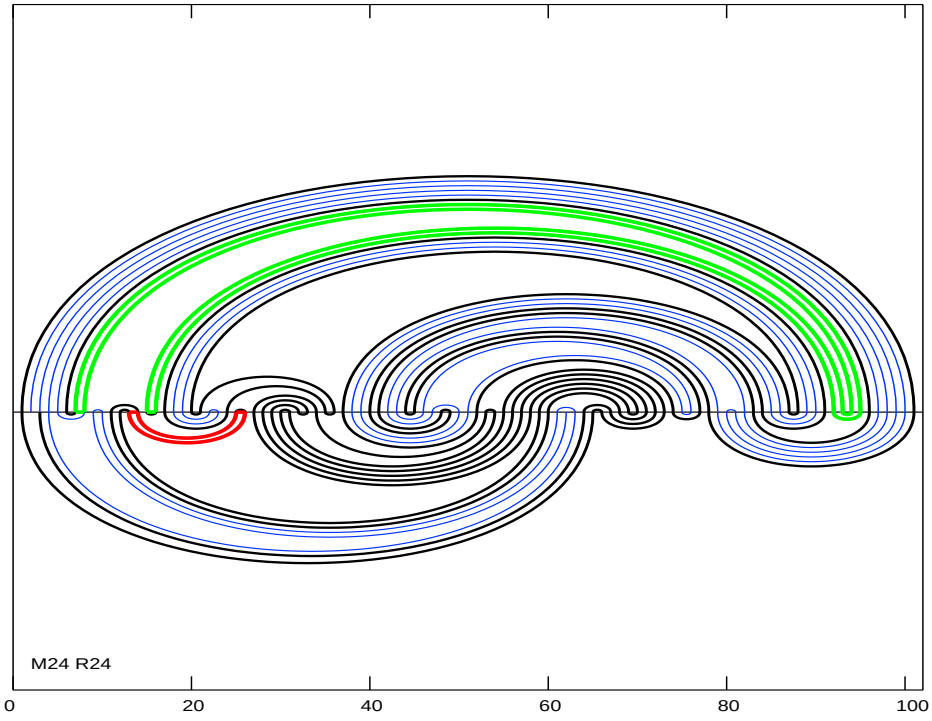

b)

Figure 5.9. **a**) Rectangles R_1, R_3, R_5, and R_7 (red). **b**) Rectangle R_{24} (red) and its image (green).

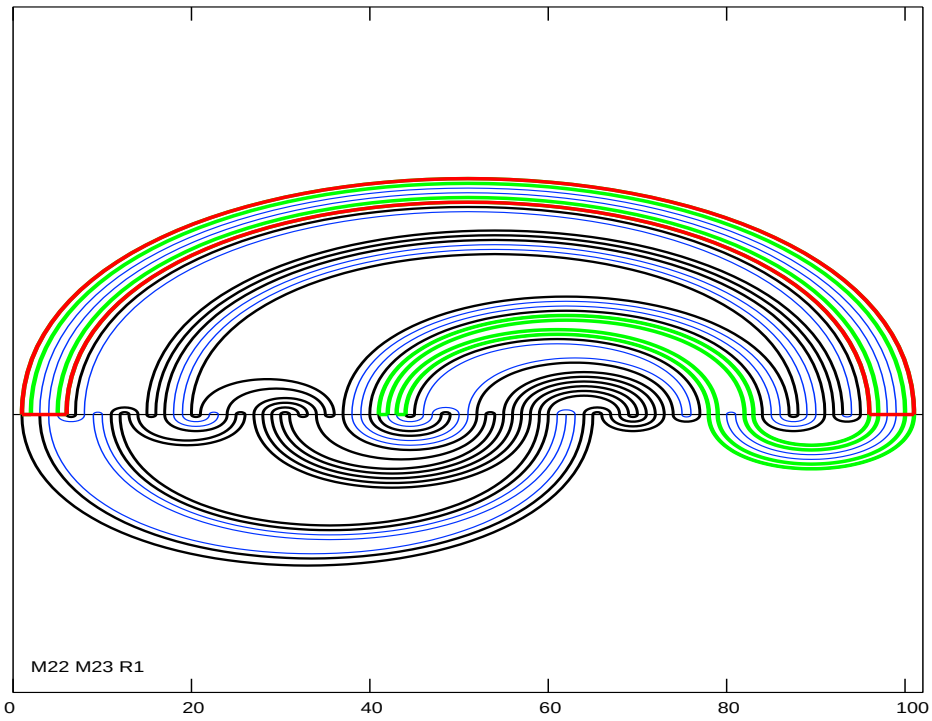

a)

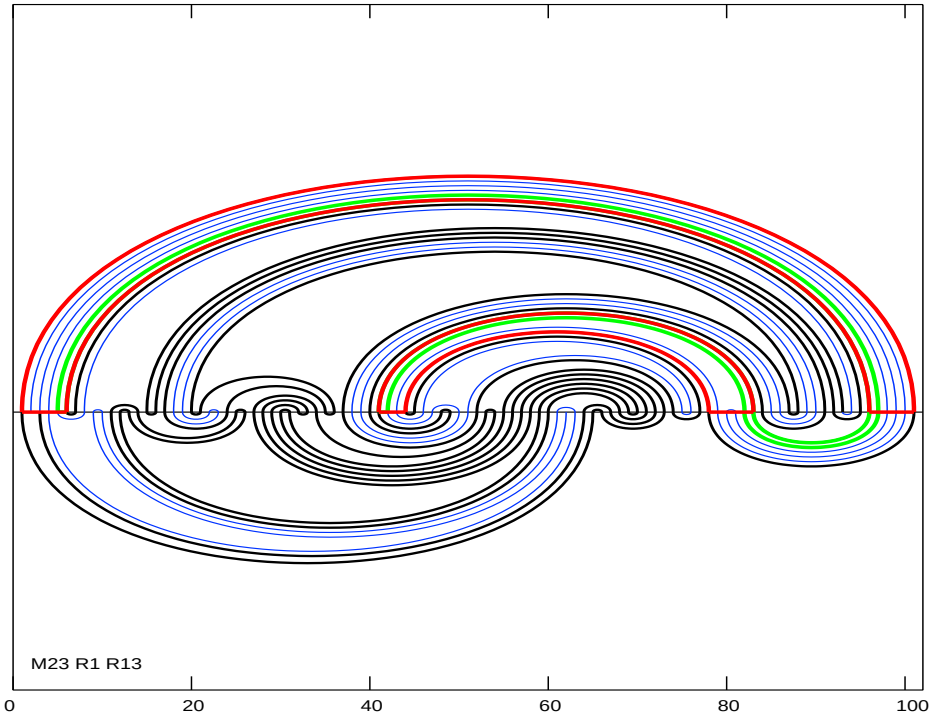

b)

Figure 5.10. **a**) The mapped rectangles R_{22} and R_{23} (green) both cross R_1 (red). **b**) The mapped rectangle R_{23} (green) crosses both rectangles R_1 and R_{13} (red).

with the standard parameters of $a = 1.4$, $b = 0.3$. This map has been a subject of detailed study before and nonverified numerical approximations of its topological entropy have been calculated using various approaches, e.g. via periodic orbit counting [19,20] or from curve length growth algorithms [57]. Numerical experiments suggests that

$$h\left(H_{a,b}\right) \approx 0.464. \tag{5.9}$$

Work has been done using concepts similar to Markov-crossings in interval arithmetic for rigorous bounds [21,22], but without employing the invariant manifold structure. The largest lower entropy bound obtained with such interval methods as of the time of this writing is

$$h\left(H_{a,b}\right) \geq 0.430.$$

In comparison, the construction in section 5.4 has been implemented using Taylor Model arithmetic in COSY Infinity [1,15]. Coding for the determination of the homoclinic ball data (ordering, orientation, mapping) from section 5.4.1 through 5.4.4 was implemented by the author, the construction of rectangles and their Markov-crossings was performed by the COSY program *dyn2.fox* due to K. Makino. *dyn2.fox* also created Figures 5.5, 5.6 and 5.8-5.10.

Data sets with interesting results ranged from sample sizes of about 100 homoclinic ball enclosures to over 700, with the corresponding number of rectangle (# R) and Markov crossings (# MC) as listed in the following table:

n	# HP	# R	# MC	$h\left(H_{a,b}\right) \geq$
7	101	37	43	0.3466
8	161	66	94	0.4132
9	267	119	185	0.4132
10	437	218	346	0.4283
11	707	381	603	0.4417

(5.10)

The best lower entropy estimate obtained so far from this automatic procedure is

thus

$$h\left(H_{a,b}\right) \geq 0.4417 \ .$$

5.7 Verification of preselected tangles

The preceding sections have been concerned with the fully automatic verified construction of symbolic dynamics through the knowledge of the ordering and mapping properties of homoclinic points within a homoclinic tangle. While this method is designed to fully rely on computational power, one could argue that it disregards the experience and intuition of the user to a certain degree. That is to say, the method tries to get 'good' symbolic dynamics, i.e. subshifts as topological factors that retain a majority of the original dynamics, by a brute-force approach in which the sheer number of homoclinic points and the rectangles constructed from the data is maximized, thus coding the dynamics more finely.

The approach of the experienced researcher is typically a different one: he has an educated idea about which rectangles (and their associated homoclinic cornerpoints) are essential to retaining the interesting dynamics in a subshift on the selected symbol space, and which ones might be redundant. For example, near-tangencies between the stable and unstable manifold which form a very thin bigon (a set with a boundary consisting of exactly one subsegment each of the stable and unstable manifold) contribute significantly to entropy estimations, because they expand disproportionally under iteration and lead to many entries in the incidence matrix. Naturally, the number of homoclinic points that a researcher is able to consider for these constructions is very small, maybe in the few dozens, compared to the computational effort required in the automatic methods described above, which need hundreds or thousands of homoclinic points to code the dynamics well. This suggests that it is worthwhile to try to verify a manually selected homoclinic tangle with Taylor Model

methods, i.e. prove that a selected set of rectangles, cornered by homoclinic points, indeed satisfies the mapping properties suggested by numerical experimentation.
In the following, we analyze a homoclinic tangle suggested by Newhouse in [56]. The authors consider the Hénon map with standard parameter values $a = 1.4$ and $b = 0.3$ and are able to find a rigorous lower entropy bound which is within 10^{-3} of the numerically suggested true entropy value for this map.

5.7.1 Determination of trellis

Newhouse proposed a trellis constructed around the hyperbolic saddle

$$p_0 \approx (0.6313544770895048, 0.1894063431268514)$$

and the transverse homoclinic point

$$q_1 \approx (0.3388525493895907, -0.2551125297830196)$$

(the existence of which has been confirmed already in chapter 4). There are subarcs $S_1 \subset W^s(p_0)$ and $U_1 \subset W^u(p_0)$ connecting p_0 and q_1 which form a bigon D. The intersection $H^2(U_1) \cap D$ contains a second unstable arc U_2 which lies in the interior of D and forms a bigon with a subarc of S_1. These manifold pieces together with stable subarcs S_2-S_{13}, which were generated as $S_i \subset H^{-k_i}(S_1) \cap D$ for some k_i-th preimage of S_1, form the trellis which defines a set of 13 rectangles $\{R_1, ..., R_{13}\}$ with mutually disjoint interiors as shown in picture (5.11).

All rectangles R_i are have top and bottom boundaries in $W^u(p_0)$ and left and right boundaries in $W^s(p_0)$. The rectangles R_1-R_6 and R_8-R_{10} are of full height in D, whereas R_7 has its upper unstable boundary in U_2 and R_{11}-R_{13} have their lower unstable boundaries in U_2. Clearly, the bigon $D \supset \bigcup_{i=1}^{13} R_i$, and we want to consider return maps from D back into itself, and how iterates $H^{m_i}(R_i)$ Markov-cross other rectangles R_j:

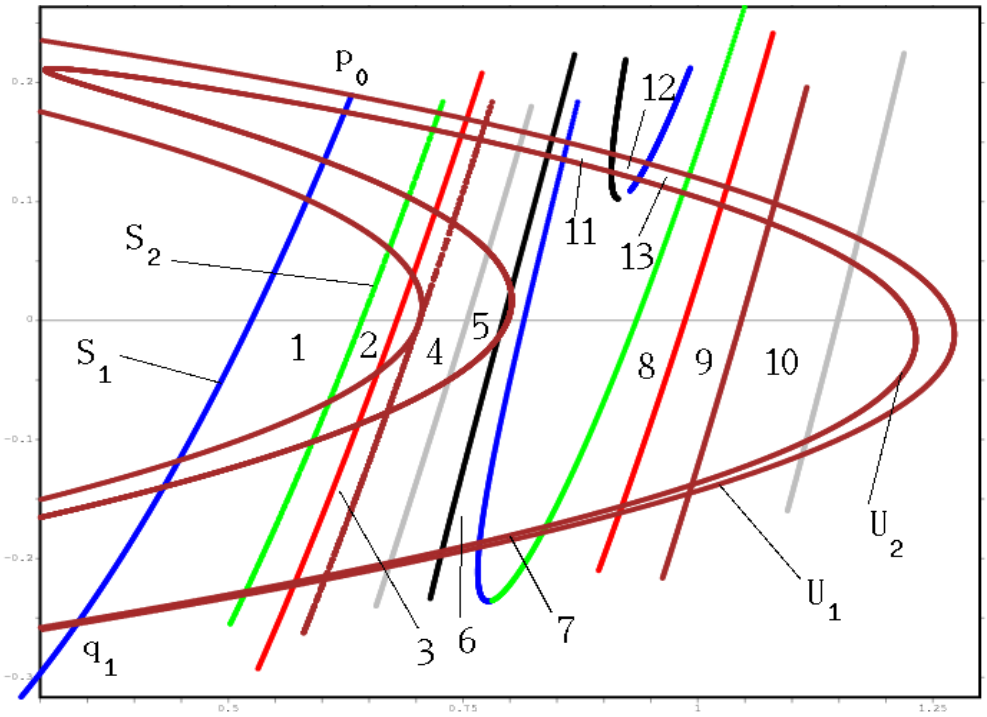

Figure 5.11. Thirteen rectangles are contained in the trellis formed by stable manifold segments S_1-S_{10} and unstable segments U_1 and U_2. Picture from [56].

5.36 Proposition. *(Newhouse) The rectangles R_1-R_{13} satisfy the following mapping properties:*

1. $H^2(R_1)$ *crosses* $R_1, R_2, R_3, R_4, R_5, R_6, R_{11}$ *and* R_{12}.
2. $H^2(R_2)$ *crosses* R_{13} *and* R_8.
3. $H^2(R_3)$ *crosses* R_9.
4. $H^2(R_4)$ *crosses* R_{10}.
5. $H^5(R_5)$ *crosses* R_1, R_2 *and* R_3*; the crossing of* R_3 *is a double crossing.*
6. $H^5(R_6)$ *crosses* R_1 *and* R_2.
7. $H^6(R_7)$ *crosses* R_1*; the crossing is a double crossing.*
8. $H^5(R_8)$ *crosses* R_1, R_2 *and* R_3*; all crossings are double crossings.*
9. $H^2(R_9)$ *crosses* R_9 *and* R_{10}.
10. $H^2(R_{10})$ *crosses* $R_1, R_2, R_3, R_4, R_5, R_6, R_7$ *and* R_8.
11. $H^6(R_{11})$ *crosses* R_1, R_2, R_3, R_4 *and* R_5*; all crossings are double crossings.*
12. $H^7(R_{12})$ *crosses* R_1, R_2 *and* R_3*; all crossings are double crossings.*
13. $H^6(R_{12})$ *crosses* R_1, R_2, R_3, R_4 *and* R_5*; all crossings are double crossings.*

This proposition is seemingly true as suggested by nonverified numerical experimentation, but that these intersection do in fact occur as claimed will be shown later using verified Taylor Model manifold enclosures.

5.37 Definition. *(Return vector) For $x \in D$, let $\tilde{r} : D \longrightarrow \mathbb{N}_+$ denote the first return iterate such that $H^{\tilde{r}(x)}(x) \in D$. It turns out that $\tilde{r}(x) \geq 2 \,\forall\, x \in D$ and that*

$\tilde{r}$ is constant on R_i. We can thus define the return vector r for the set of rectangles $\{R_1, ..., R_{13}\}$ as

$$r \in \mathbb{N}_+^{13} \ , \ r_i := \tilde{r}\left(x_i\right) \ \textit{for some } x_i \in R_i.$$

According to Proposition 5.36, the return vector r is apparently given by

$$r = (2, 2, 2, 2, 5, 5, 6, 5, 2, 2, 6, 7, 6) \ .$$

The matrix $A \in \mathbb{N}^{13\times 13}$ is defined as $A_{ij} = k$ iff $H^{r_i}\left(R_i\right)$ Markov-crosses R_j exactly k times. From the claim we can see that

$$A = \begin{pmatrix}
1 & 1 & 1 & 1 & 1 & 1 & 0 & 0 & 0 & 0 & 1 & 1 & 0 \\
0 & 0 & 0 & 0 & 0 & 0 & 0 & 1 & 0 & 0 & 0 & 0 & 1 \\
0 & 0 & 0 & 0 & 0 & 0 & 0 & 0 & 1 & 0 & 0 & 0 & 0 \\
0 & 0 & 0 & 0 & 0 & 0 & 0 & 0 & 0 & 1 & 0 & 0 & 0 \\
1 & 1 & 2 & 0 & 0 & 0 & 0 & 0 & 0 & 0 & 0 & 0 & 0 \\
1 & 1 & 0 & 0 & 0 & 0 & 0 & 0 & 0 & 0 & 0 & 0 & 0 \\
2 & 0 & 0 & 0 & 0 & 0 & 0 & 0 & 0 & 0 & 0 & 0 & 0 \\
2 & 2 & 2 & 0 & 0 & 0 & 0 & 0 & 0 & 0 & 0 & 0 & 0 \\
0 & 0 & 0 & 0 & 0 & 0 & 0 & 0 & 1 & 1 & 0 & 0 & 0 \\
1 & 1 & 1 & 1 & 1 & 1 & 1 & 1 & 0 & 0 & 0 & 0 & 0 \\
2 & 2 & 2 & 2 & 2 & 0 & 0 & 0 & 0 & 0 & 0 & 0 & 0 \\
2 & 2 & 2 & 0 & 0 & 0 & 0 & 0 & 0 & 0 & 0 & 0 & 0 \\
2 & 2 & 2 & 2 & 2 & 0 & 0 & 0 & 0 & 0 & 0 & 0 & 0
\end{pmatrix}$$

The jargon is to call A an incidence matrix for the trellis composed of the rectangles R_1-R_{13}. Strictly speaking, A is not an incidence matrix according to Def. 2.15, as the encoded crossing properties under iteration are based on higher iterates of H. However, there is a standard and straightforward procedure to transform A into a form compatible with our notion of incidence matrices: consider the i-th row of A which denotes the Markov crossings of $H^{r_i}\left(R_i\right)$ with R_j. We construct a tower by adding new rectangles $R_{i,1} := H^1\left(R_i\right), R_{i,2} := H^2\left(R_i\right), ..., R_{i,r_i-1} := H^{r_i-1}\left(R_i\right)$, and insert them as additional rows and columns between rows/colums i and $i+1$. Trivially, by definition $H\left(R_{i,j}\right)$ Markov crosses $R_{i,j+1}$ only, leading to additional rows in the expanded matrix A as $A_{(i,j),k} = \delta_{k,j+1}$. We call this incidence matrix on this expanded rectangle set $\tilde{A}$.

$\tilde{A}$ is an $\mathbb{N}^{52\times 52}$-incidence matrix in the sense of Def. 2.15. We do not state $\tilde{A}$ here for obvious formatting reasons. According to Thm. 2.17, the logarithm of the spectral radius of $\tilde{A}$ yields a lower bound on the entropy of the Hénon map H. There are standard techniques available for the determination of verified lower bounds of the spectral radius of real-valued matrices, and we were able to determine the following entropy bound:

5.38 Theorem. *The topological entropy $h(H)$ of the standard Hénon map $H = H_{a,b}$ with $a = 1.4$ and $b = 0.3$ satisfies the estimate*

$$h(H) \geq 0.46469 \ .$$

This theorem obviously requires Proposition 5.36 to hold, which we will prove in the next section. It is quite remarkable that this rigorous lower bound which relies on only 13 symbols is so close to the numerically suggested true value of the topological entropy of the Hénon map with standard parameters.

5.7.2 Verification of mapping pictures

Let $S_1 \subset W^s(p_0)$ be the segment of the stable manifold connecting the fixed point p_0 to the homoclinic point q_1 and consider the 11th preimage $S := H^{-11}(S_1)$. We first determine subarcs S_2 through S_{13} of S as shown in Figure 5.11 (in the figure the arcs S_1-S_{13} actually extend slightly above and below the domain D, we crop them such that their ends lie in $U_1 \cup U_2$).

The approximate position of the homoclinic intersections of the arcs S_1-s_{13} with the unstable segment $U_1 \cup U_2$ as shown in Figure 5.11 is sufficient to determine the number n_i of backward iterates of $H^{-n_i}(S_1)$ at which each of the exact arcs S_i, $1 \leq i \leq 13$, are first generated. With one exception, the respective iterates are much

smaller than 11, leading to easy identification of the corresponding pieces.

$$\begin{array}{lllll} S_1:0 & S_2:8 & S_3:6 & S_4:8 & \\ S_5:4 & S_6:11 & S_7:5 & S_8:5 & \\ S_9:4 & S_{10}:6 & S_{11}:2 & S_{12}:6 & S_{13}:6 \end{array}$$

Figures 5.12-5.17 justify the last statement. The figures contain the approximate boundary points of the rectangles R_i from Figure 5.11, and rigorous Taylor Model enclosures of the manifold pieces U_1, U_2 and the respective preimages of S_1. The curvilinear rectangles R_1 through R_{13} are defined analogously to Figure 5.11, each formed by two stable and two unstable arcs, but with the rigorously determined true manifold segments:

5.39 Proposition. *Let $n_l(i)$ and $n_r(i)$ be the numbers of the inverse iterate of S_1 at which the left and right stable boundaries of rectangle R_i are first generated, as shown in Figures 5.12-5.17. We see that the following table holds:*

Rectangle	n_l	n_r	*Rectangle*	n_l	n_r
R_1	0	8	R_8	5	4
R_2	8	6	R_9	4	6
R_3	6	8	R_{10}	6	3
R_4	8	4	R_{11}	5	6
R_5	4	11	R_{12}	6	6
R_6	11	5	R_{13}	6	5
R_7	5	5			

With these definitions, we can now prove the following rectangle crossing under iteration:

5.40 Theorem. *The rectangle mappings claimed in Prop. 5.36 occur in the given trellis.*

Proof. The proof is based on the fact that the pictures (5.12-5.17) are verified, i.e. that the rigorously computed error bounds for all manifold pieces are below printer resolution. More precisely, the plotted curves are contained in Taylor Models with error bounds of size less than 10^{-12} for the unstable arcs U_1 and U_2, and between

10^{-12}-10^{-5} for the iterates of the stable arcs S_1-S_{13}. Together with the information of iterates first generating the S_i we can show that the mapping properties in suggested in the pictures are in fact true.

First consider R_1. We observe that the upper unstable boundary of R_1 is contained in U_1 and extends between the stable subarcs S_1 and S_2. Then its second iterate must be contained in $H^2(U_1) \cap D = U_1 \cup U_2$, and per the picture one can identify that it is again contained in the upper portion of U_1. It extends between $H^2(S_1)$ and $H^2(S_2)$, and since according to Prop.5.39 $n_l(R_1) = 0$ and $n_r(R_1) = 8$, we have $n_l\left(H^2(R_1)\right) = 0$ and $n_r\left(H^2(R_1)\right) = 6$, and we can identify that the mapped rectangle $H^2(R_1)$ is bounded on the left by S_1 and on the right by S_{13}. For the remaining lower unstable boundary of $H^2(R_1)$ we know that it is again contained in $U_1 \cup U_2$, and inspection of the picture shows that it is a subarc of U_2 again extending between the stable segments S_1 and S_{13}. With this information it is now clear that indeed the second iterate $H^2(R_1)$ stretches Markov across $R_1, R_2, R_3, R_4, R_5, R_6, R_{11}$ and R_{12}. This proves claim 1.

Next we analyze the crossing properties of $H^5(R_8)$. For its left and right stable boundaries we have $n_l(R_5) = 5$ and $n_r(R_5) = 4$. Hence for the stable boundaries of the fifth iterate we have $n_l\left(H^5(R_5)\right) = 0$ and $n_r\left(H^5(R_5)\right) = 0$, and we can thus infer that both stable boundaries of $H^5(R_8)$ must be subarcs in S_1. Furthermore, from Figure 5.21**b** and the magnification Figure 5.22**a** it is clear that both upper and lower unstable boundaries of $H^5(R_8)$ extend fully to the right of R_3, and thus we have that $H^5(R_8)$ Markov-crosses R_1, R_2 and R_3 twice. This establishes claim 8.

The remaining claims 2-7 and 9-13 work analogously to the two cases discussed in detail here. □

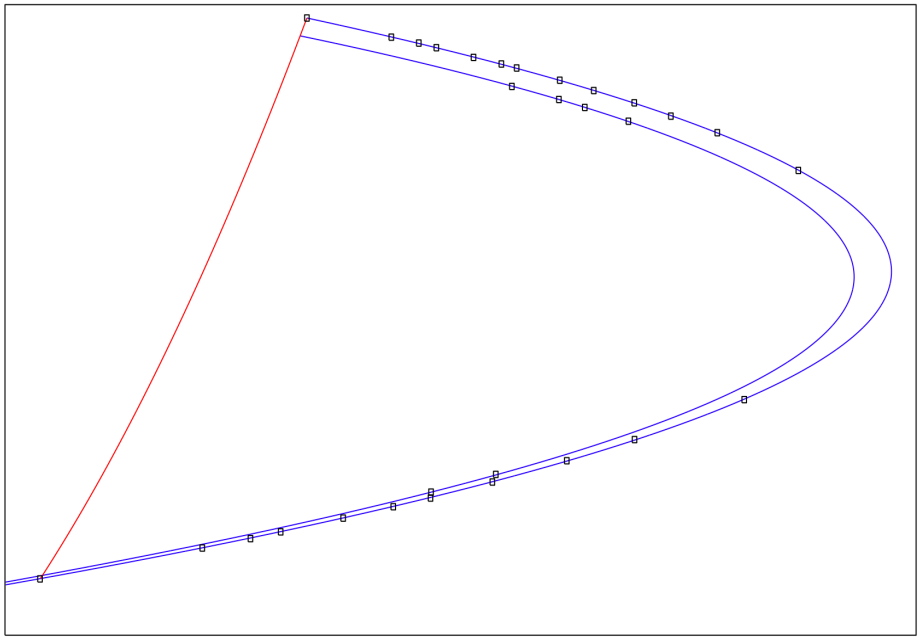

a)

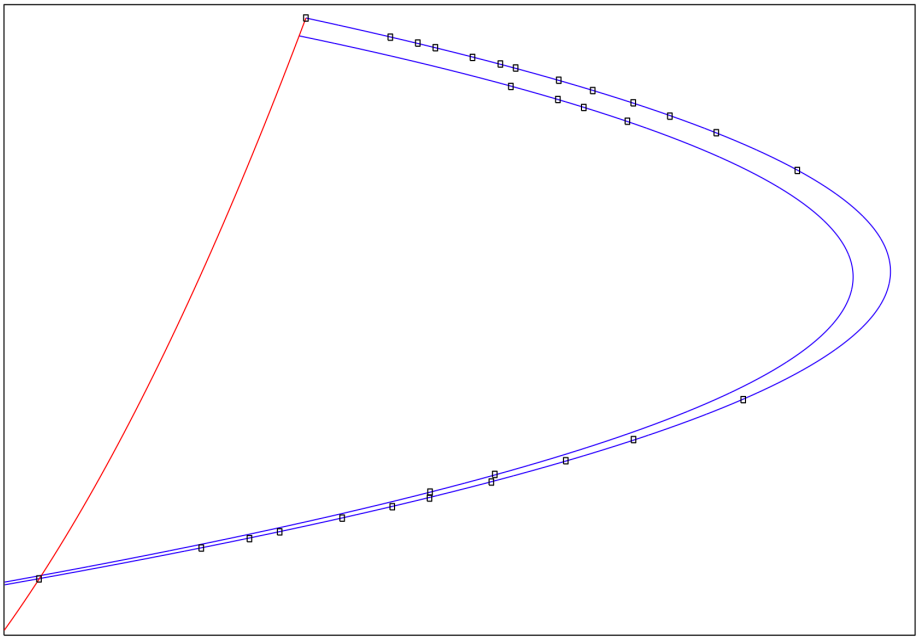

b)

Figure 5.12. **a**) The fundamental stable arc S_1 (red). Also printed are the segment of the unstable manifold (blue) and the homoclinic points (black) that are relevant for the rectangle construction. **b**) The first preimage $H^{-1}(S_1)$ (red).

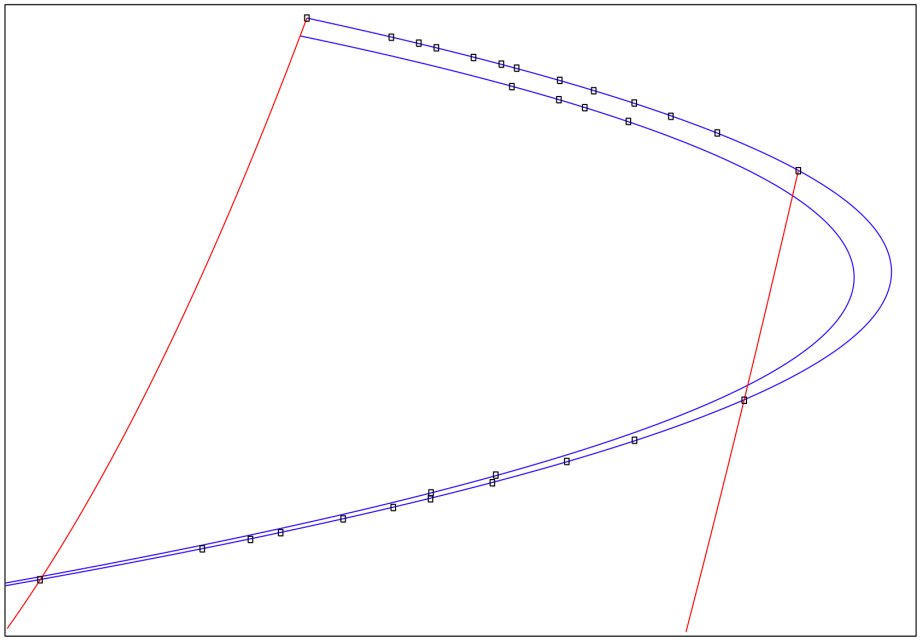

a)

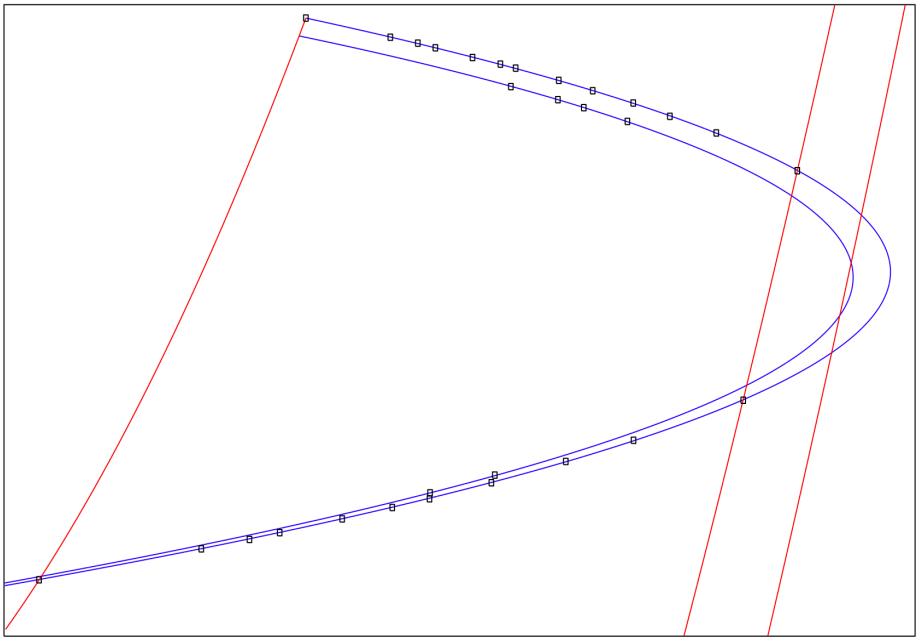

b)

Figure 5.13. **a**) The second preimage $H^{-2}(S_1)$ (red). **b**) The third preimage $H^{-3}(S_1)$ (red).

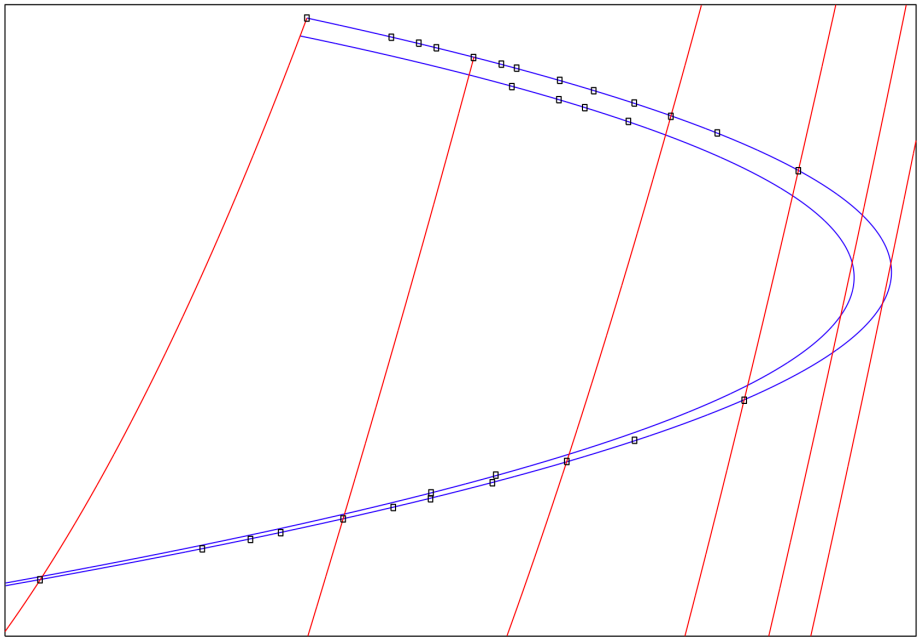

a)

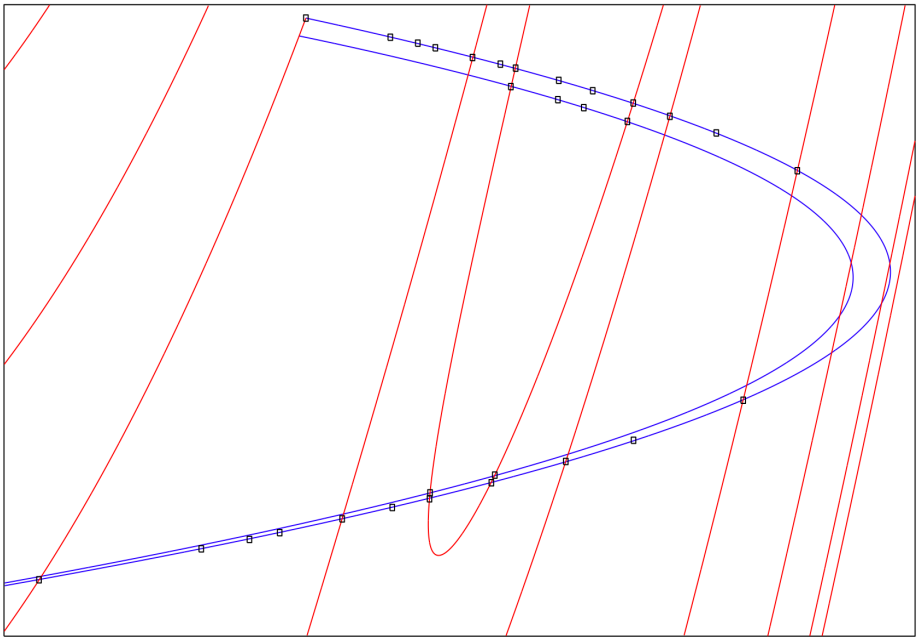

b)

Figure 5.14. **a**) The fourth preimage $H^{-4}(S_1)$ (red). **b**) The fifth preimage $H^{-5}(S_1)$ (red).

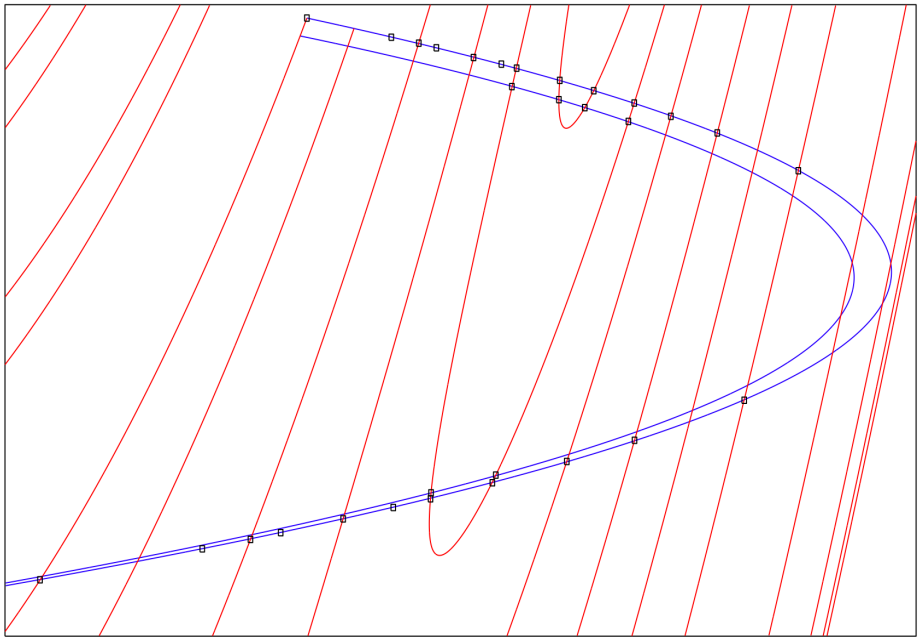

a)

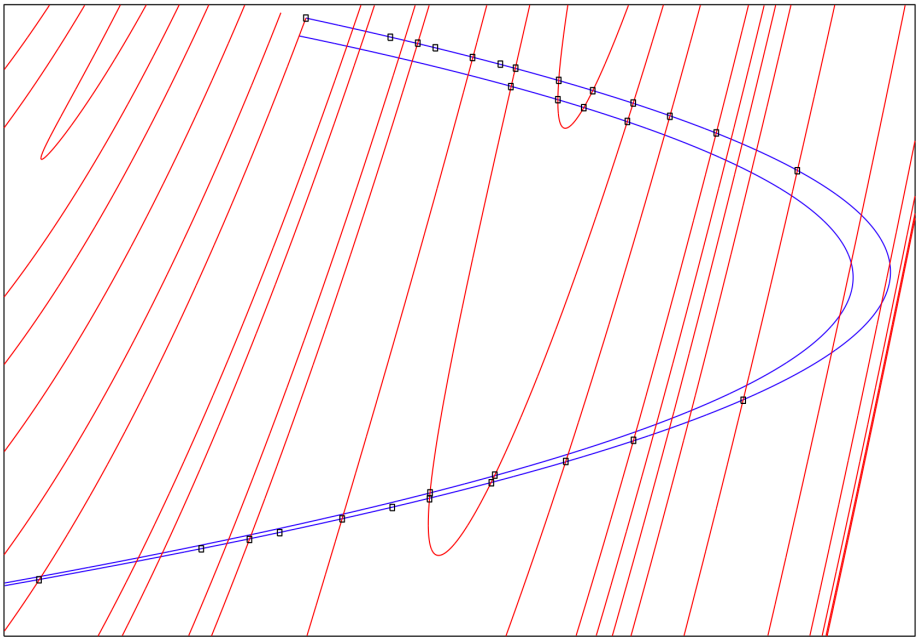

b)

Figure 5.15. **a**) The sixth preimage $H^{-6}(S_1)$ (red). **b**) The seventh preimage $H^{-7}(S_1)$ (red).

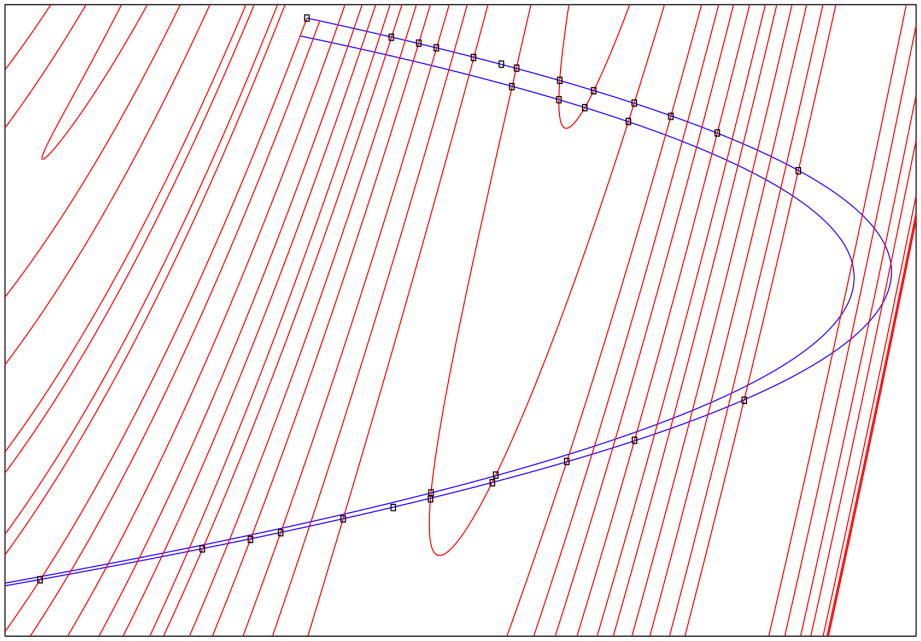

a)

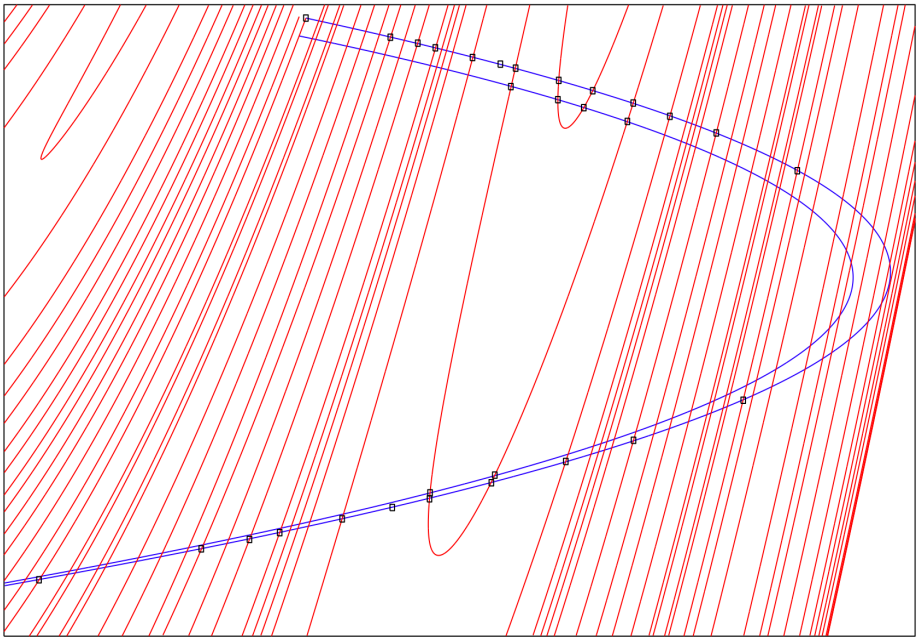

b)

Figure 5.16. **a**) The eigth preimage $H^{-8}(S_1)$ (red). **b**) The ninth preimage $H^{-9}(S_1)$ (red).

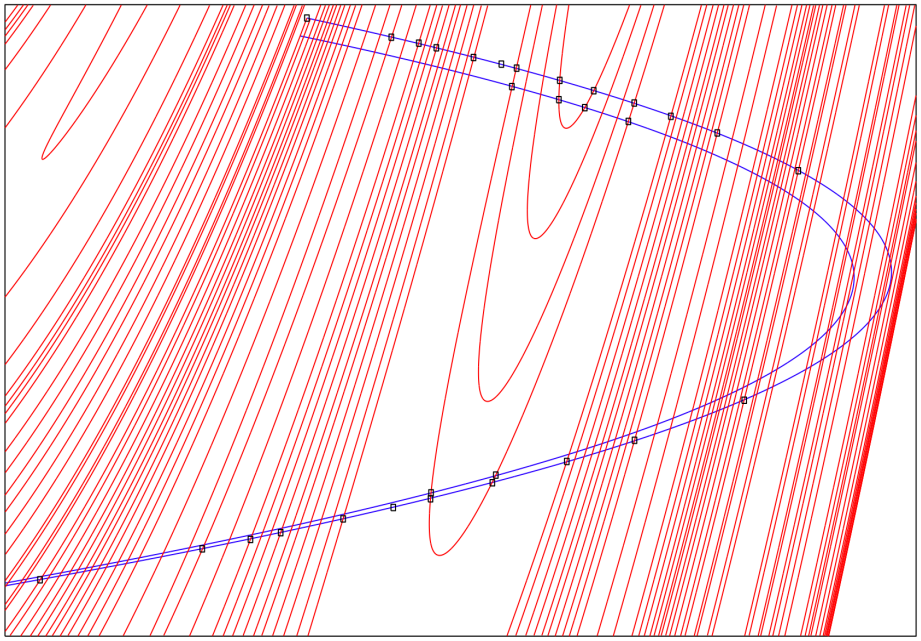

a)

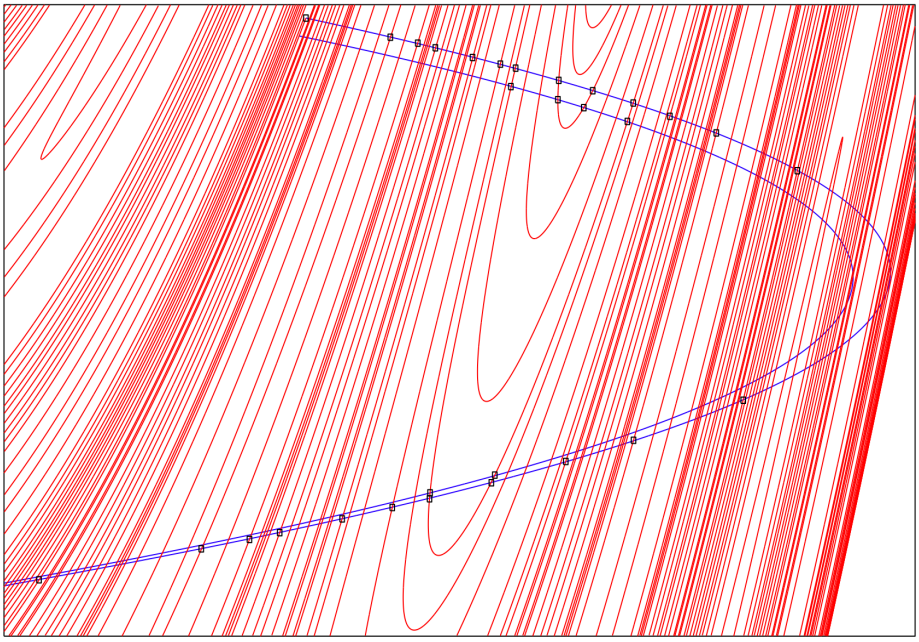

b)

Figure 5.17. **a**) The tenth preimage $H^{-10}(S_1)$ (red). **b**) The eleventh preimage $H^{-11}(S_1)$ (red).

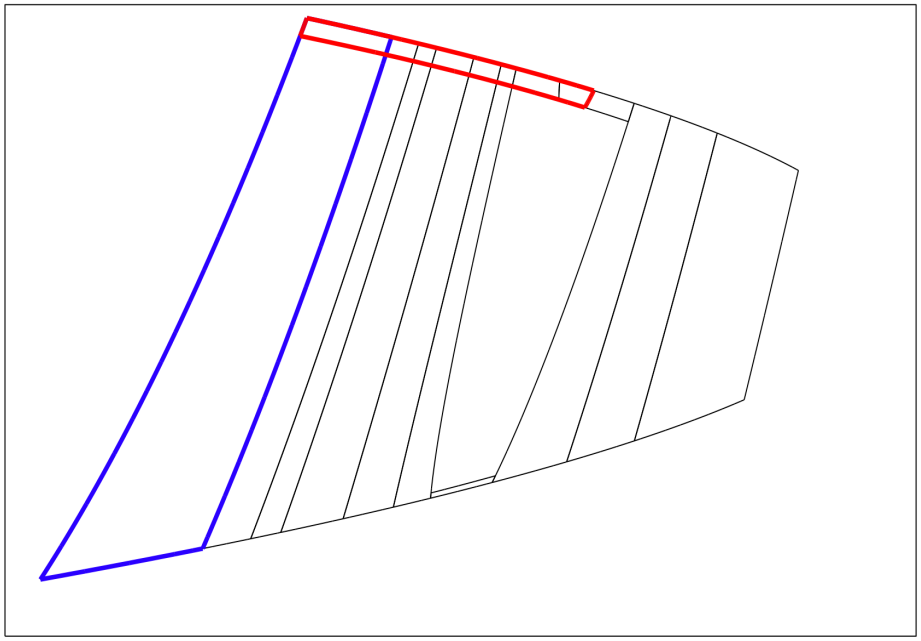

a)

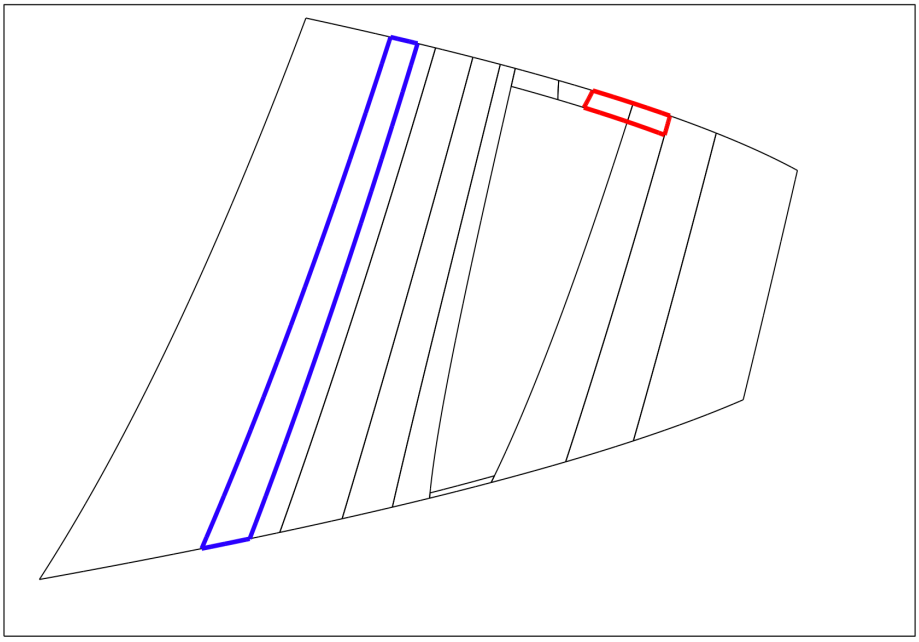

b)

Figure 5.18. **a**) Rectangle R_1 (blue) and its 2nd image (red). **b**) Rectangle R_2 (blue) and its 2nd image (red). The remaining rectangles are printed in black.

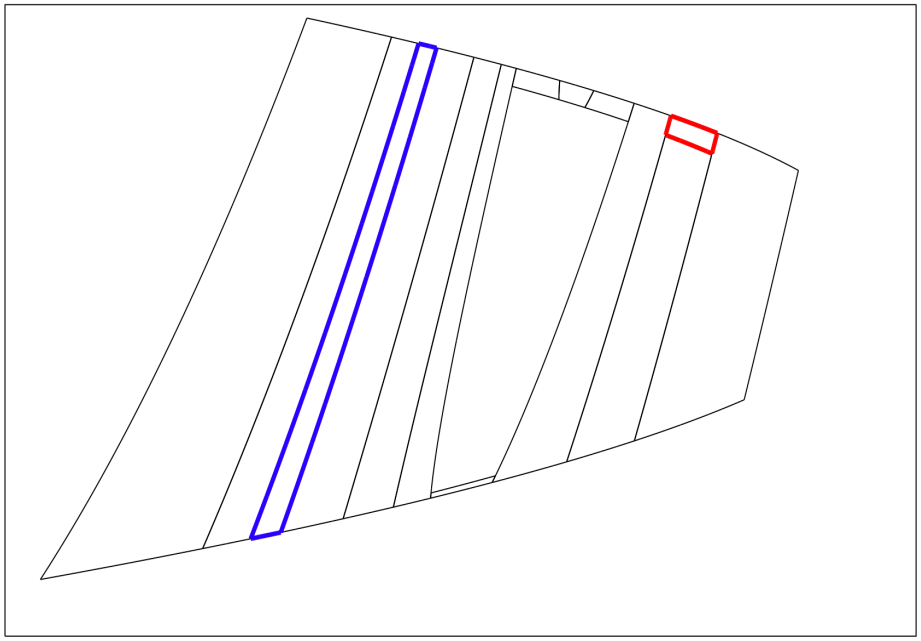

a)

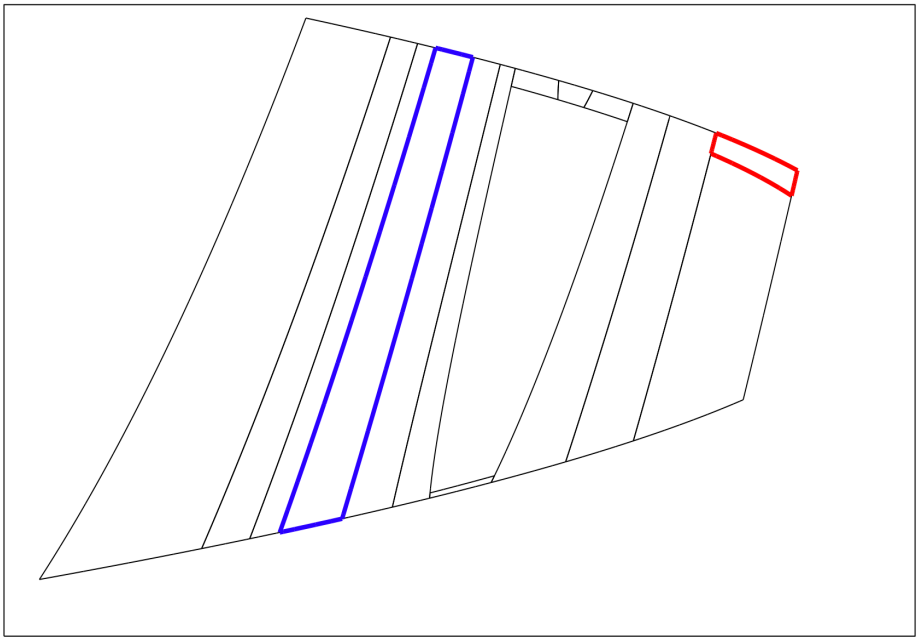

b)

Figure 5.19. **a**) Rectangle R_3 (blue) and its 2nd image (red). **b**) Rectangle R_4 (blue) and its 2nd image (red).

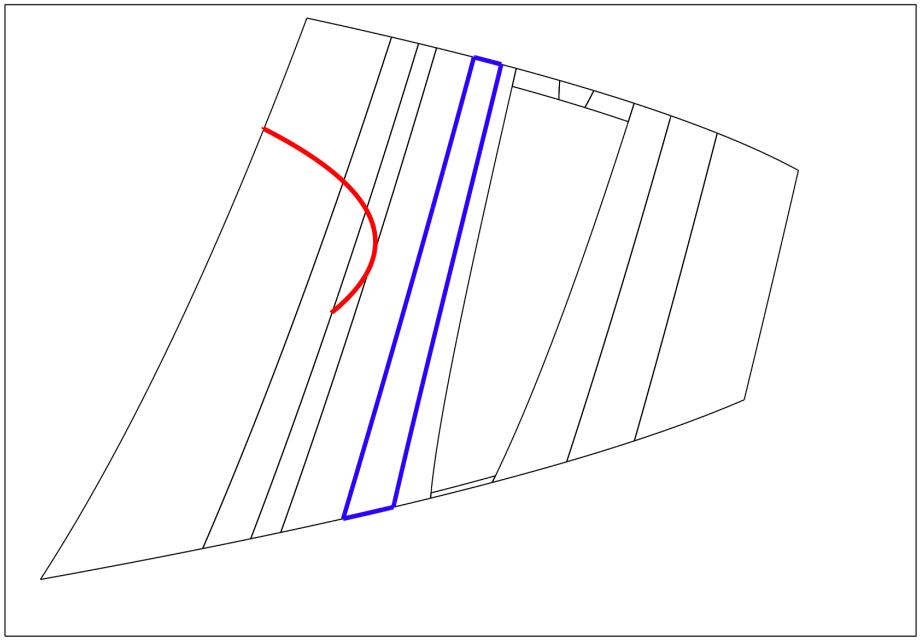

a)

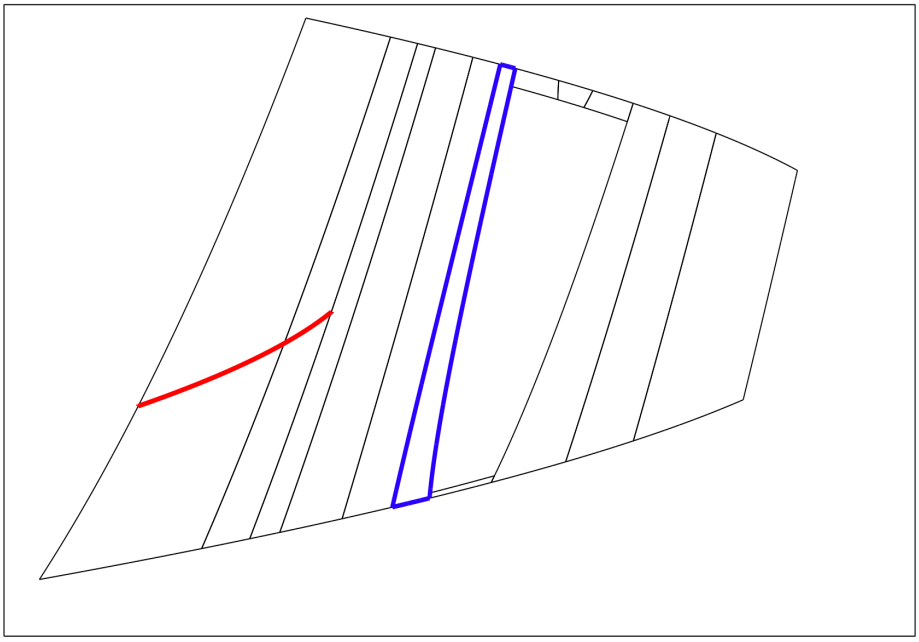

b)

Figure 5.20. **a**) Rectangle R_5 (blue) and its 5th image (red). **b**) Rectangle R_6 (blue) and its 5th image (red).

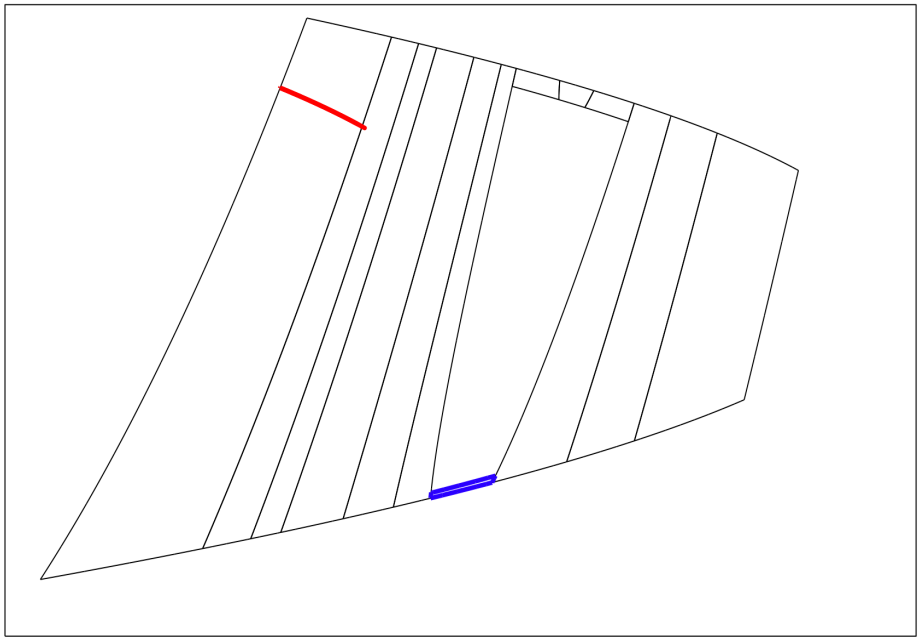

a)

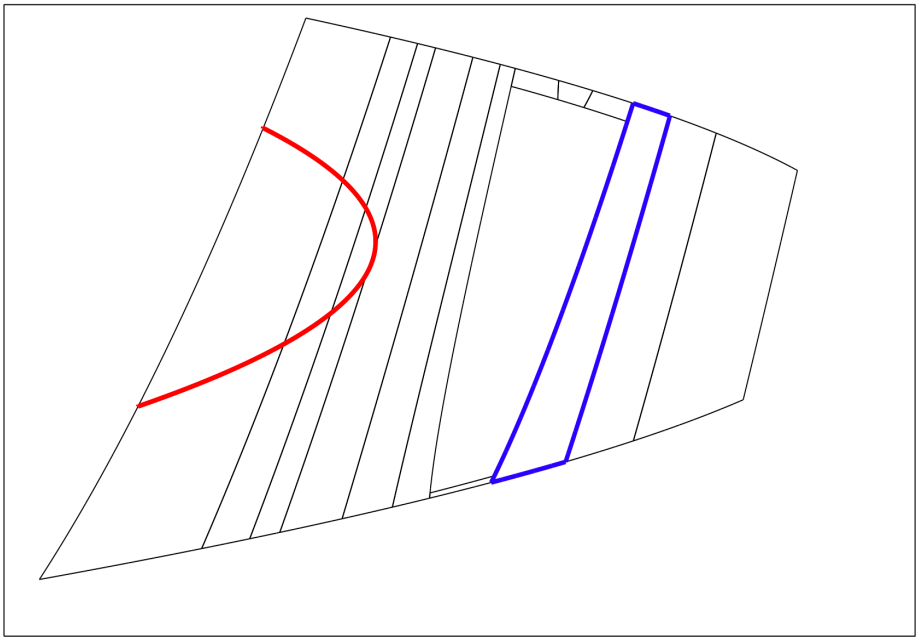

b)

Figure 5.21. **a**) Rectangle R_7 (blue) and its 6th image (red). **b**) Rectangle R_8 (blue) and its 5th image (red).

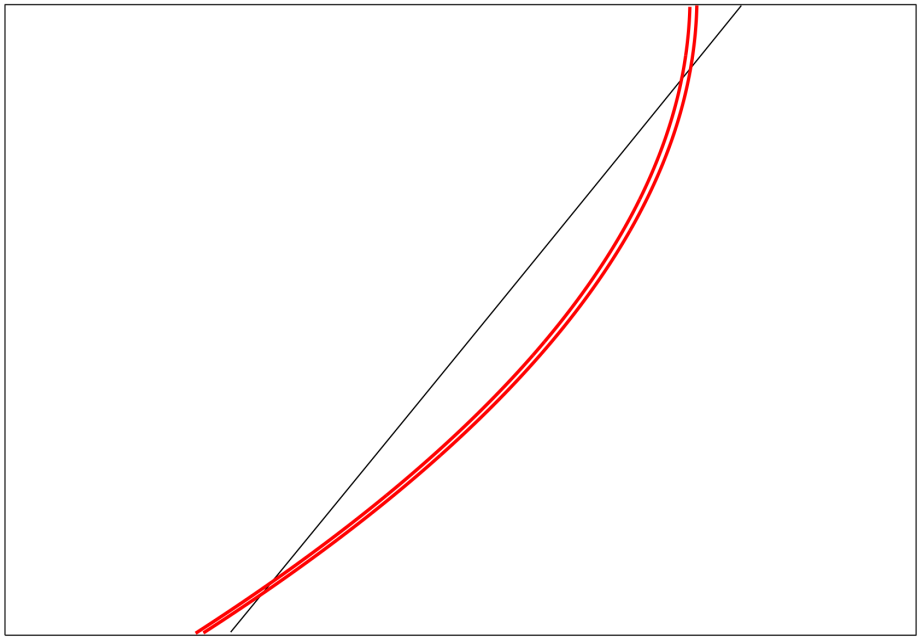

a)

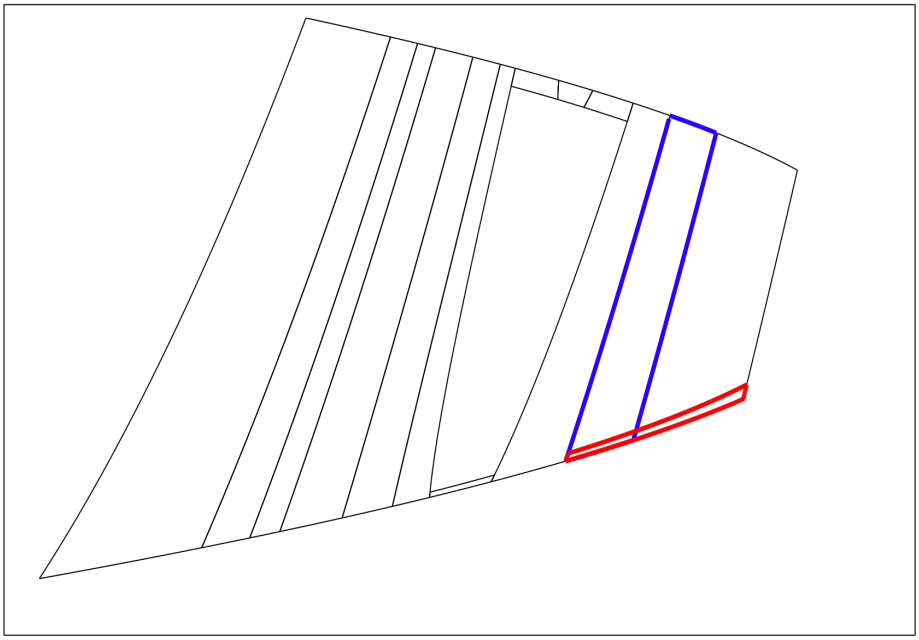

b)

Figure 5.22. **a**) A magnified view of the 5th image of rectangle R_5 (red). We see that $H^5(R_5)$ maps fully across the right boundary S_4 of R_4. **b**) Rectangle R_9 (blue) and its 2nd image (red).

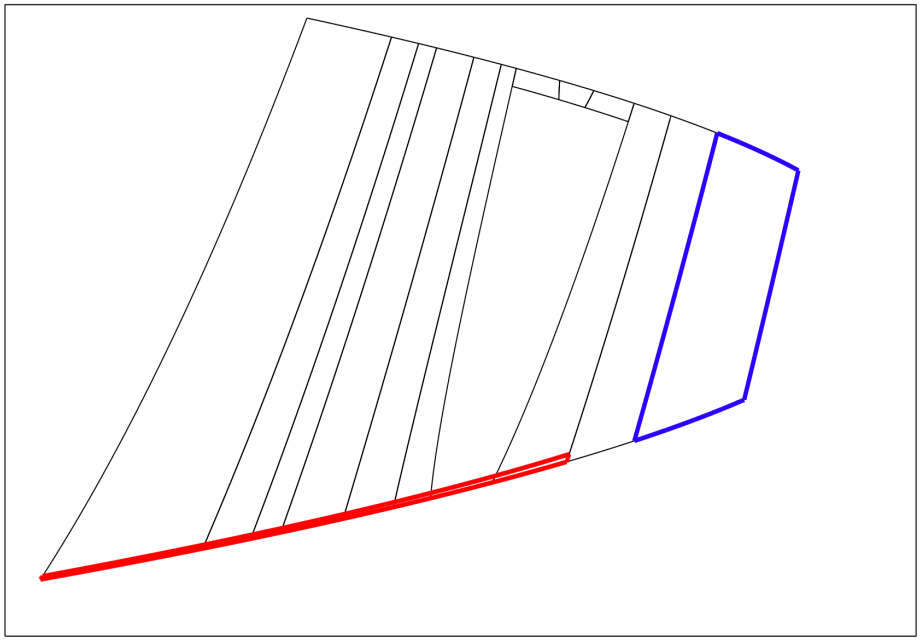

a)

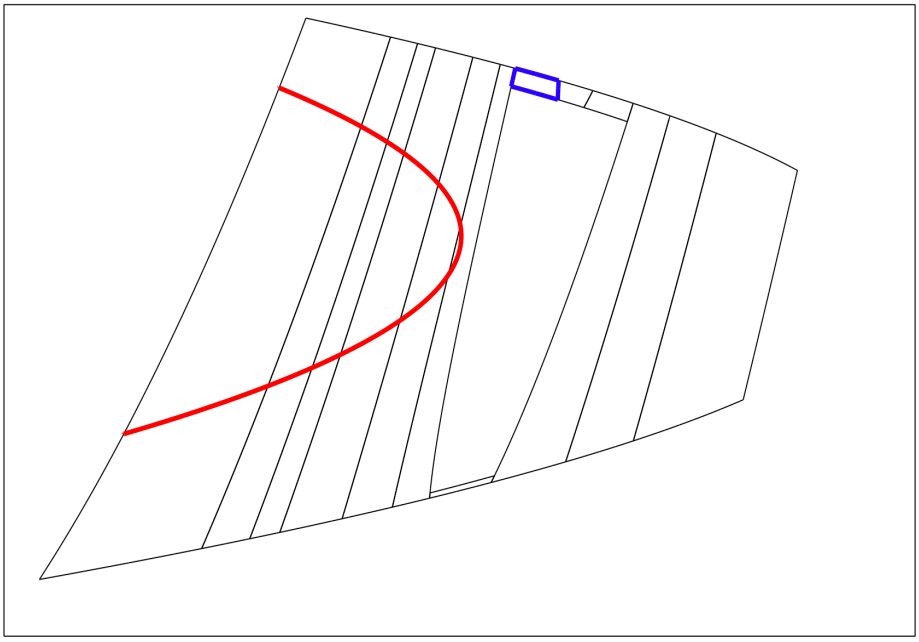

b)

Figure 5.23. **a**) Rectangle R_{10} (blue) and its 2nd image (red). **b**) Rectangle R_{11} (blue) and its 6th image (red).

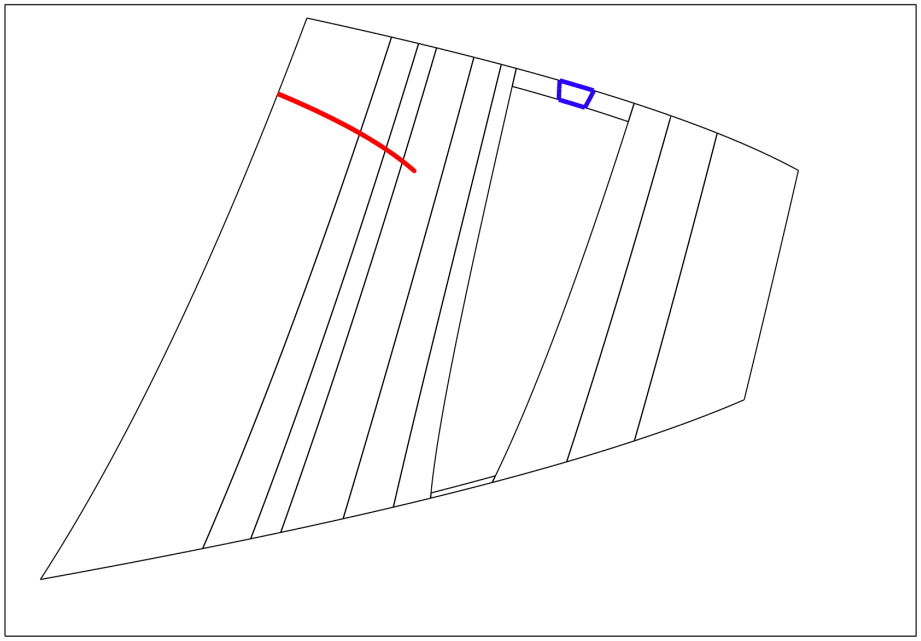

a)

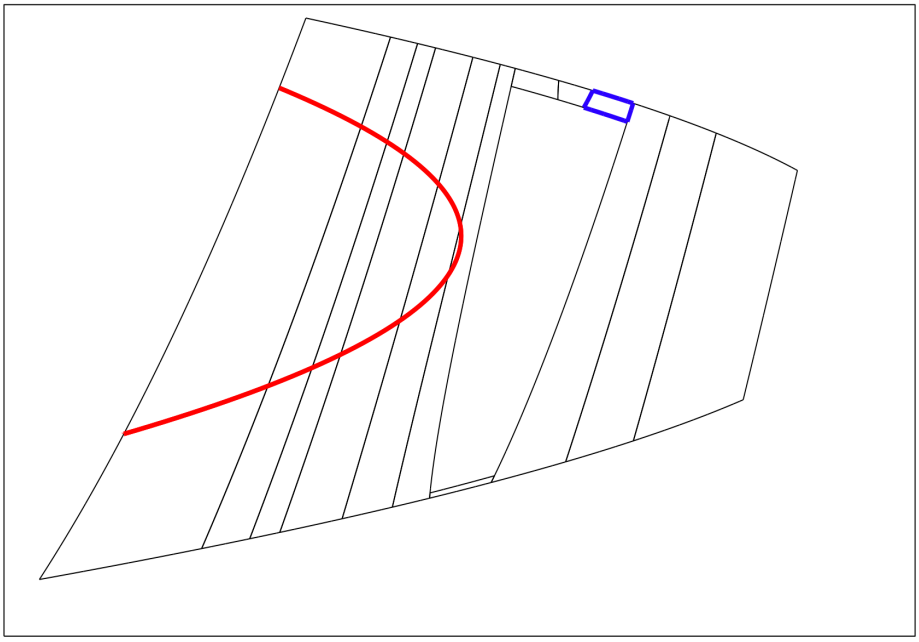

b)

Figure 5.24. **a**) Rectangle R_{12} (blue) and its 7th image (red). **b**) Rectangle R_{13} (blue) and its 6th image (red).

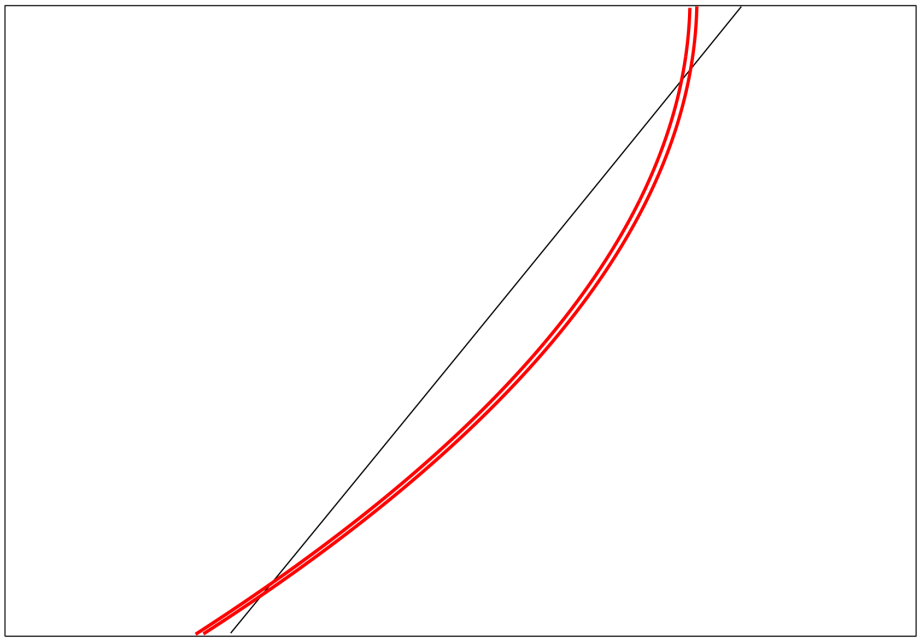

Figure 5.25. A magnified view of the 6th image of rectangle R_{13} (red). We see that $H^6(R_{13})$ maps fully across the right boundary S_6 of R_5.

5.8 Summary and Outlook

We presented a method to compute lower bounds for the topological entropy of planar diffeomorphisms by selecting generalized rectangles and checking their Markov-crossings under iterations. In the case of a smooth diffeomorphism, only disjointness of the rectangle interiors is required, thus allowing invariant manifolds to be used as the rectangle boundaries.

Having C^0-enclosures of the invariant manifolds given by an arclength-ordered set of Taylor Models enables us to find a set of closed balls rigorously containing all homoclinic points of a finite manifold tangle. The ordering of the balls along both the stable and unstable manifold in the tangle, together with their mapping properties and orientation of the manifold crossing is sufficient information to prove the existence of rectangles with well-defined mapping and Markov-crossing properties, the boundaries of which are contained in the original Taylor Model C^0-enclosures of

the invariant manifolds.

The entire algorithm can be fully automated and all assumptions that enter the rigorous rectangle construction are suitable to be checked using Taylor Model methods.

The largest lower bound for the entropy of the standard Hénon map thus computed is

$$h\left(H_{a,b}\right) \geq 0.4417,$$

obtained from a data set of 707 homoclinic points. The estimates can be improved by accounting for hexagons, octagons etc. in the manifold tangle which have boundaries alternating in the stable and unstable manifold. Such sets can be converted to rectangles through the incorporation of bigons, i.e. sets that have exactly one stable and one unstable arc as their boundary.

Conversions of this type increase the number of rectangles and Markov-crossings and lead to incidence matrices with larger spectral radii. In the following table we can see how the number of rectangles (# R), the number of Markov crossings (# MC), and the entropy estimates ($h\left(H_{a,b}\right) \geq$) change if rectangle conversion of higher n-gons is performed.

n	# R	# MC	$h\left(H_{a,b}\right) \geq$	# R with conv.	# MC with conv.	$h\left(H_{a,b}\right) \geq$
7	37	43	0.3466	47	62	0.3738
8	66	94	0.4132	77	110	0.4309
9	119	185	0.4132	130	205	0.4403
10	218	346	0.4283	229	366	0.4499
11	381	603	0.4417	392	621	0.4536

The data suggests an improved lower bound

$$h\left(H_{a,b}\right) \geq 0.4536.$$

The n-gon conversion will be treated in detail in forthcoming publications.

Recent work shows that there are more sophisticated ways to check Markov-crossings than the method in sections (5.4.6) and (5.4.7). Using the same data for ordering, mapping and orientation of the homoclinic balls as produced the above estimates, P. Collins [11,12] suggested an algorithm that claims a rigorous lower entropy bound of

$$h\left(H_{a,b}\right) \geq 0.4571.$$

An investigation to which degree these methods can be implemented in the verified computational framework seems worthwile.

Future modifications of the method should include updates in the computational framework, such as the implementation of high-precision Taylor Model arithmetic, which should increase the size of the manifold tangle and the number of homoclinic enclosure balls that can be rigorously shown to satisfy condition (5.6), the foremost criterion where the verification using Taylor Models can fail. Lastly, Taylor Model enclosures of invariant manifolds were used to produce verified pictures, accurate to below printer resolution, which rigorously establish a rectangle construction suggested by S. Newhouse [56]. Using 52 rectangles, the lower entropy bound stemming from the incidence matrix is

$$h\left(H_{a,b}\right) \geq 0.46469,$$

which to the best knowledge of the authors is the largest lower bound that has been established for the Hénon map with the standard parameter values so far, and which agrees to within 10^{-3} with the entropy value (5.9) suggested through nonverified numerical experiments.

APPENDICES

APPENDIX A

Interval Arithmetic

A.1 Definitions

The concept of interval arithmetic as introduced by Moore [49, 50] is one of the earliest frameworks to offer numerical computations with automated self-contained error estimates. Instead of performing operations on real numbers (which may or may not be accurately known or even representable), one performs operations on intervals known to contain the respective numbers , where the interval operations are compatible with the original number operations, i.e. for any operation $\circledast$ (summation, subtraction, multiplication or division) and any two closed intervals $I_1, I_2 \subset \mathbb{R}$, we must satisfy

$$a \in I_1, b \in I_2 \Longrightarrow a \circledast b \in I_1 \circledast I_2, \tag{A.1}$$

where we again identify the symbols for number and interval operations for convenience.

A.1 Definition. *(Interval operations) Let* $I_1 = [a_1, b_1], I_2 = [a_2, b_2] \subset \mathbb{R}$ *be closed*

real intervals. Then we define

$$
\begin{aligned}
I_1 + I_2 &:= [a_1 + a_2, b_1 + b_2] \ , \\
I_1 - I_2 &:= [a_1 - b_2, b_1 - a_2] \ , \\
I_1 \cdot I_2 &:= [\min\{a_1a_2, a_1b_2, b_1a_2, b_1b_2\}, \max\{a_1a_2, a_1b_2, b_1a_2, b_1b_2\}] \ , \\
I_1/I_2 &:= I_1 \cdot I_2^{-1}, \textit{ where } I_2^{-1} := [1/b_2, 1/a_2] \textit{ provided } 0 \notin I_2 \ .
\end{aligned}
$$

It is easy to check that indeed the operations from definition (A.1) satisfy the condition (A.1). Moreover, it is important to note that the above operations can be implemented in a computer environment with proper outward rounding of the resulting imtervals to satisfy the inclusion property (A.1) in a fully rigorous way, even accounting for round-off errors.

Analogous to the binary operations also elementary functions can be extended to intervals. For a function $f : \mathbb{R} \supset D \longrightarrow \mathbb{R}$ and a closed interval $I \subset D$, the interval equivalent function (again abusing notation) has to satisfy

$$a \in I \Longrightarrow f(a) \in f(I) \ .$$

For detailed discussions on the implementation of such interval extensions of mathematical functions we refer to [27].

The availablity of general classes of functions for interval arguments has led to a wide range of applications for interval arithmetic in self-contained error analysis, from root-finding (interval Newton methods) and global optimization (Branch-and-Bound algorithms) to verified interval inclusion of ODE-flows [37, 38]. Tucker used interval ODE integrators to prove the existence of the geometric model for the Lorenz-attractor [64].

A.2 Fundamental problems of interval arithmetic

The goal of interval algorithms is of course to keep the resulting interval enclosures of the mathematical solutions as narrow as possible. However, in a general setting in practice all applications mentioned above suffer from significant overestimation, i.e. a blow-up of the interval enclosures after frequent evaluation of code lists in interval arithmetic. The major causes of this problem are unfortunately rooted in the very definition of interval operations themselves, which can lead to overly pessimistic interval widths in the right hand side of condition (A.1).

A.2.1 Dependency problem

To illustrate the dependency problem [42],we consider a classic simple example. Let $f : [-1, 1] \longrightarrow \mathbb{R}$ given as $f(x) := x - x$. Clearly f is just the zero function, and its range over the entire domain $[-1, 1]$ is simply $\{0\}$, but when we evaluate the expression in interval arithmetic we obtain

$$x - x \in [-1, 1] - [-1, 1] = [-2, 2] \ ,$$

which is a true statement, but obviously the estimation is both impractically coarse and fails to reflect the mathematical reality. This is precisely the dependency problem, the artificial blowup in the interval evaluation of a function if that function is given as a code list that requires many individual interval evaluations, e.g. in a Horner scheme or an inductively defined function.

A.2.2 Wrapping effect

The second cause for overestimation is the so called wrapping effect [3, 39, 51, 52], based on the fact that interval arithmetic provides interval range bounds along the coordinate axes. Consider planar functions $f_1, f_2 : [-1, 1]^2 \longrightarrow \mathbb{R}^2$ that map the

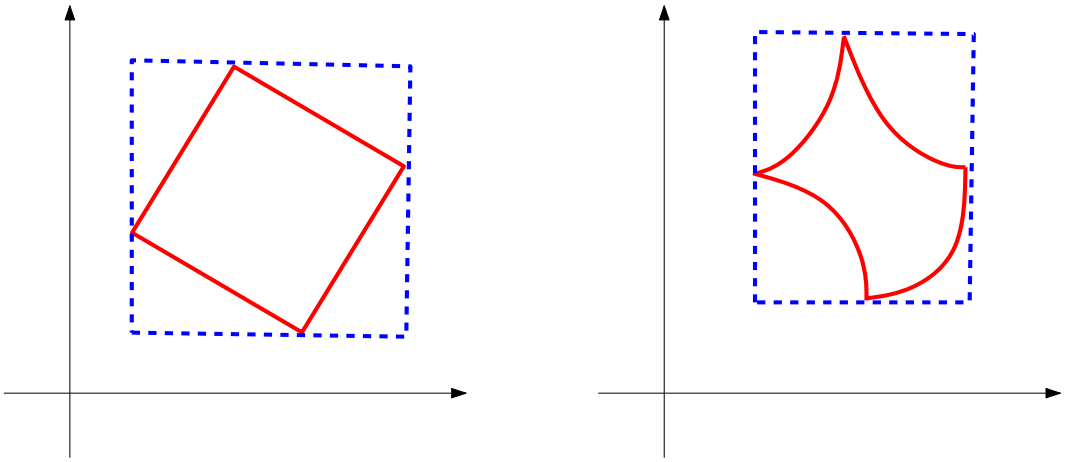

Figure A.1. Schematic depiction of the wrapping effect in the linear (left) and nonlinear (right) case. The range enclosure (blue dotted line) exhibits overestimation versus the true mapped square (red).

initial square as in Figure A.1 for an intuitive idea of the wrapping effect. In both cases the resulting interval range bounds severly overestimates the true range bounds. While in the first case, where the action of f_1 is linear, the effect can be alleviated to a certain degree by linearly transforming the coordinate system, in the nonlinear second case of f_2 the overestimation by interval arithmetic can be arbitrarily large.

A.2.3 Dimensionality curse

The dimensionality curse is jargon for the unfavorable exponential scaling of computational effort and memory requirement with the dimension of the problem in interval arithmetic. Typically, one wishes to model a set (e.g. a box of initial coordinates transported through an ODE or the set containing all zeroes of a function) as contained within a union of interval boxes of a given fineness. That is, for a collection of interval boxes $\mathcal{I} = \{I_k\}_{k=1}^{m}$ with $I_k = [a_{k,1}, b_{k,1}] \times ... \times \left[a_{k,v}, b_{k,v}\right] \subset \mathbb{R}^v$, $b_{k,l} > a_{k,l}$ $\forall\ 1 \leq k \leq m$, $1 \leq l \leq v$, let

$$\varepsilon_k := \max\left\{\left(b_{k,l} - a_{k,l}\right) : 1 \leq l \leq v\right\}.$$

Note that $\varepsilon_k > 0$. Then define the fineness of $\mathcal{I}$ as

$$\varepsilon_{\mathcal{I}} := \max\left\{\varepsilon_k : 1 \leq k \leq m\right\}.$$

Typically however, the fineness $\varepsilon_{\mathcal{I}}$ is a given quantity in the context of the problem, say the threshold accuracy with which one wants to approximate sets. Let $D \subset \mathbb{R}^v$ have full dimension v, and we want to construct a collection of intervals $\mathcal{I} = \{I_k\}_{k=1}^{card(\mathcal{I})}$ with $0 < \varepsilon_{\mathcal{I}} << 1$ such that $D \subset \bigcup_{k=1}^{card(\mathcal{I})} I_k$, then

$$card\left(\mathcal{I}\right) \backsim \left(\frac{1}{\varepsilon_{\mathcal{I}}}\right)^v,$$

an undesirable exponential scaling with the dimensionality.

APPENDIX B

The differential algebra ${}_nD_v$

B.1 Definitions

In the following, we introduce a framework that allows the efficient numerical manipulation of high-order multivariate polynomials and of Taylor polynomials in particular. Given that by its very nature Taylor Model arithmetic combines both polynomial manipulation and, for the remainder bound, interval arithmetic, the techniques presented in this section bridge the gap to the former.

Consider an open subset $G \subset \mathbb{R}^v$ containing the origin, and let the set $C^n(G, \mathbb{R})$ be the set of all real-valued n -times continuously differentiable functions on G. Then we introduce an equivalence relation on this function space as follows:

B.1 Definition. *For two functions $f, g \in C^n(G, \mathbb{R})$ we say that $f =_n g$ ('f equals g up to order n') if and only if $f(0) = g(0)$ and all partial derivatives of f and g agree at the origin up to order n.*

It is obvious that $=_n$ indeed establishes an equivalence relation on $C^n(G, \mathbb{R})$.

B.2 Definition. *On the function space $C^n(G, \mathbb{R})$, equivalence classes modulo the relation $=_m$, $m \leq n$, are called 'DA-vectors of order m'. For $f \in C^n(G, \mathbb{R})$, its DA-vector of order m is denoted by $[f]_m$.*

The collection of DA-vectors up to and including order n is called ${}_nD_v$.

The DA-vector $[f]_n$ contains all functions that agree with f at the origin up to their n-th derivative, and in particular it is easy to see the following:

B.3 Proposition. *For a function $f \in C^n(G, \mathbb{R})$, its Taylor polynomial of order n is contained in ${}_nD_v$.*

We can therefore think of the DA-vector $[f]_n$ as the n-th order Taylor polynomial. Since basic arithmetic operations on $\mathbb{R}$ carry over naturally to $C^n(G, \mathbb{R})$, we wish to establish these operations on ${}_nD_v$ as well.

B.4 Definition. *(Elementary operations) Let $f, g \in C^n(G, \mathbb{R})$ and consider their DA-vectors $[f]_n$ and $[g]_n$. Let $t \in \mathbb{R}$. We define*

$$\begin{aligned} [f]_n + [g]_n &:= [f + g]_n \,, \\ t \cdot [f]_n &:= [t \cdot f]_n \ . \end{aligned} \tag{B.1}$$

Furthermore, we can define a multiplication

$$[f]_n \cdot [g]_n := [f \cdot g]_n \ . \tag{B.2}$$

Here we take the liberty of denoting operations on $C^n(G, \mathbb{R})$ and ${}_nD_v$ with the same symbols.

In a more intuitive manner, which is beneficial when thinking of DA-vectors in the Taylor Model context, this means that knowledge of the Taylor polynomials of two functions f and g at the origin immediately yields the Taylor polynomials for the sum $f + g$ and the product $f \cdot g$. For a more detailed study of this property of DA-arithmetic we refer to [4, 6].

It is clear that with addition and scalar multiplication as in (B.1) ${}_nD_v$ becomes a vector space and with the vector multiplication (B.2) an algebra. In fact, we can

define a derivative operation that observes the product rule such that ${}_nD_v$ becomes a differential algebra.

B.5 Definition. *Let $1 \leq k \leq n$ and $[f]_n \in {}_nD_v$. Then we define the derivation ∂_k as*

$$\partial_k [f]_n := [\pi_k \cdot \partial_k f]_n \,, \tag{B.3}$$

where $\pi_k \in C^n(G, \mathbb{R})$, $\pi_k(x) := x_k$ for $x \in \mathbb{R}^v$, is the projection of the k-th component of x.

This derivation operation is thus analogous to the differentiation on $C^n(G, \mathbb{R})$, except that ∂_k had to be modified as in (B.3) as a Lie derivative in order to make ${}_nD_v$ closed under ∂_k.

B.6 Proposition. *For all $1 \leq k \leq n$ and $f, g \in C^n(G, \mathbb{R})$ we have*

$$\begin{aligned} \partial_k ([f]_n + [g]_n) &= \partial_k [f]_n + \partial_k [g]_n \ , \\ \partial_k ([f]_n \cdot [g]_n) &= \partial_k [f]_n \cdot [g]_n + [f]_n \cdot \partial_k [g]_n \ . \end{aligned}$$

The fact that the derivation operation observes a product rule indeed makes ${}_nD_v$ a differential algebra.

The extension of the ${}_nD_v$-concept from real-valued functions to vector valued functions in $C^n(G, \mathbb{R}^m)$ is straightforward:

B.7 Definition. *Let $f, g \in C^n(G, \mathbb{R}^m)$. We say that $f =_n g$ if and only if their components satisfy $f_i =_n g_i$, $1 \leq i \leq m$, in the sense of the Definition B.1.*

Analogously we see that $=_n$ defines an equivalence relation also on these vector valued functions and we can define the collection of equivalence classes ${}_nD_v^m$.

B.2 Composition on ${}_nD_v$

Consider a function $\mathcal{M} : \mathbb{R}^v \supset G \to G \subset \mathbb{R}^v$ that is n-times continuously differentiable and which satisfies $\mathcal{M}(0) = 0$, and let $g \in C^n(G, \mathbb{R})$. Then $g \circ \mathcal{M} \in C^n(G, \mathbb{R})$

and $[g \circ \mathcal{M}]_n \in {}_nD_v$. Hence we may define the composition as follows:

B.8 Definition. *Let $\mathcal{M} : G \to G$ and $g \in C^n(G, \mathbb{R})$, and consider their respective DA-vectors $[\mathcal{M}]_n \in {}_nD_v^v$ and $[g]_n \in {}_nD_v$. Then define the composition of $[\mathcal{M}]_n$ and $[g]_n$ as*

$$[g]_n \circ [\mathcal{M}]_n := [g \circ \mathcal{M}]_n \ .$$

In other words, knowledge of the Taylor polynomials for g and $\mathcal{M}$ yields the Taylor polynomial for $g \circ \mathcal{M}$, provided the constant part of $\mathcal{M}$ is compatible with the expansion point of g (the origin in this case).

From the composition of DA-vectors we immediately obtain the DA-vectors of elementary functions, if care is taken that we work on domains and ranges where the functions have the necessary smoothness. In particular, intrinsic functions available in a computer environment are of interest here.

B.9 Definition. *(Elementary Functions) Let $f \in C^n(G, \mathbb{R})$ sucht that $f(0) = 0$ and consider $[f]_n \in {}_nD_v$. The we define*

$$\begin{aligned}
\exp\left([f]_n\right) &:= [\exp(f)]_n \\
\log\left([f]_n\right) &:= [\log\left(f\right)]_n \ \textit{ where } f > 0 \textit{ on } G \\
\sin\left([f]_n\right) &:= [\sin\left(f\right)]_n \\
\cos\left([f]_n\right) &:= [\cos\left(f\right)]_n \\
\sqrt{[f]_n} &:= \left[\sqrt{f}\right]_n \ \textit{ where } f > 0 \textit{ on } G \ .
\end{aligned}$$

We see that for any function which can be written as a finite code list of elementary operations and intrinsic functions in a computer environment, we are able to obtain its Taylor expansion around the origin in an automated way by starting with the identity DA-vector $[\mathcal{I}]_n$ and then inductively evaluating the code list in DA-arithmetic.

B.3 Depth, Contractions and Fixed Point Theorems on ${}_nD_v$

B.10 Definition. *For $[f]_n \in {}_nD_v$, $[f]_n \neq 0$, define the depth $\lambda([f]_n)$ as the order of the first nonvanishing derivative of $f \in C^n(G, \mathbb{R})$ at the origin. If $[f]_n = 0$, set $\lambda([f]_n) := n + 1$.*

For vector-valued functions, $[f]_n \in {}_nD_v^m$, we set $\lambda([f]_n) := \min_{1 \leq i \leq m} \lambda([f_i]_n)$.

Intuitively, the depth of the difference of two DA-vectors is somewhat comparable to a metric, except that two DA-vectors are the more similar the *larger* the depth of their difference is. Hence we introduce the notion of a contracting operator on DA-vectors.

B.11 Definition. *Let $\mathcal{O} : M \longrightarrow {}_nD_v^m$ be an operator on $M \subset {}_nD_v^m$, and let $[f]_n, [g]_n \in M$, Then we say that $\mathcal{O}$ is contracting if and only if*

$$\lambda(\mathcal{O}([f]_n) - \mathcal{O}([g]_n)) > \lambda([f]_n - [g]_n) \ .$$

Naturally, one would hope that for this type of contractions traditional fixed-point theorems exist, and it turns out this is the case:

B.12 Theorem. *(Fixed Point Theorem) Let $M \subset {}_nD_v$ and let $\mathcal{O} : M \longrightarrow M$ be a contracting operator. Then $\mathcal{O}$ has a unique fixed point $[p_0] \in {}_nD_v$. Furthermore, starting with the identity $[\mathcal{I}]_n$, $[p_0]_n$ is assumed after finitely many iterations, namely $n + 1$,*

$$\mathcal{O}^{n+1}([\mathcal{I}]_n) = [p_0]_n \ .$$

Again for details we refer to [2].

B.13 Remark. *A particularly useful operation for the computation of flows of ODEs both in the DA-vector picture and the verified integration using Taylor Models is the antiderivation ∂_i^{-1}, essentially the integration with respect to the i-th variable.*

If for two DA-vectors $[f]_n, [g]_n \in {}_nD_v$ *we have that* $\lambda([f]_n - [g]_n) = k$*, then after integration the first nonvanishing derivative of* $f - g$ *is of order* $k+1$*, and hence*

$$\begin{aligned}
&\lambda\left(\partial_i^{-1}([f]_n) - \partial_i^{-1}([g]_n)\right) \\
=&\lambda\left(\partial_i^{-1}([f]_n - [g]_n)\right) \\
=&\lambda\left(\partial_i^{-1}([f-g]_n)\right) > \lambda([f-g]_n) = \lambda([f]_n - [g]_n)\ .
\end{aligned}$$

In other words, if the Taylor polynomial of a function f *is known up to order* n *at the origin, one can immediately obtain the Taylor polynomial of its indefinite integral w.r.t. the* i*-th variable up to the same order.*

This allows the computation of high-order expansions of ODE-flows. Assume the autonomous IVP

$$\dot{x}(t) = f(x)\ ,\ x(0) = x_0,$$

for a C^1*-function* $f : \mathbb{R}^v \to \mathbb{R}^v$*, then the local expansion of the flow* $\varphi(x,t)$ *around* x_0 *can be obtained through the Picard-iteration*

$$\begin{aligned}
[\varphi(x,t)]_0 &:= [x_0]_n\ , \\
[\varphi(x,t)]_{k+1} &:= [x_0]_n + \partial_{v+1}^{-1}\left(f\left([\varphi(x,t)]_k\right)\right)\ .
\end{aligned}$$

Since the Picard-iteration yields Taylor expansions of successively increasing orders, i.e. $[\varphi(x,t)]_{k+1} =_k [\varphi(x,t)]_k$*, this scheme converges after at most* n *steps.*

B.4 Functional inversion

The most useful advanced feature in the context of the present work is the automated functional inversion of a DA-vector. The claim states the following: assume a smooth origin-preserving function $\mathcal{M} : \mathbb{R}^v \longrightarrow \mathbb{R}^v$ that is invertible at the origin, i.e. its Jacobian $Df(0)$ is regular, and we know its Taylor polynomial up to order n stored in the DA-vector $[\mathcal{M}]_n$, then there is an algorithm to compute the Taylor polynomial

of the local inverse $\mathcal{M}^{-1}$ around the origin up to the same expansion order n in the DA-vector $\left[\mathcal{M}^{-1}\right]_n$, and furthermore $[\mathcal{M}]_n \circ \left[\mathcal{M}^{-1}\right]_n = \left[\mathcal{M}^{-1}\right]_n \circ [\mathcal{M}]_n = [\mathcal{I}]_n$:

B.14 Theorem. *(Functional DA-inversion) Let $G \subset \mathbb{R}^v$, $0 \in G$, and let $\mathcal{M} \in C^n(G, G)$ such that $\mathcal{M}(0) = 0$ and the linear part $L(x) := D\mathcal{M}(0) \cdot x$, with a regular Jacobian $D\mathcal{M}(0)$. Write $\mathcal{M} = L + \mathcal{N}$, where $\mathcal{N}$ is the purely nonlinear part of $\mathcal{M}$. Then the operator*

$$\mathcal{O}(.) := L^{-1} \circ (\mathcal{I} - \mathcal{N} \circ .)$$

is contracting on ${}_nD_v^v$ and for the identity $[\mathcal{I}]_n \in {}_nD_v^v$ we have

$$\mathcal{O}^{n+1}([\mathcal{I}]_n) = \left[\mathcal{M}^{-1}\right] .$$

Proof. First we note that the DA-vector $\left[\mathcal{M}^{-1}\right]$ is indeed a fixed point of the operator $\mathcal{O}$. For the original function $\mathcal{M}$ we have

$$\begin{aligned} & \mathcal{M} \circ \mathcal{M}^{-1} = \mathcal{I} \\ \Longleftrightarrow & L \circ \mathcal{M}^{-1} = \mathcal{I} - \mathcal{N} \circ \mathcal{M}^{-1} \\ \Longleftrightarrow & \mathcal{M}^{-1} = L^{-1} \circ \left(\mathcal{I} - \mathcal{N} \circ \mathcal{M}^{-1}\right) \end{aligned}$$

and thus

$$\left[\mathcal{M}^{-1}\right] = L^{-1} \circ \left(\mathcal{I} - \mathcal{N} \circ \left[\mathcal{M}^{-1}\right]\right) .$$

We only need to show that $\mathcal{O}$ is contracting on ${}_nD_v^v$ and have proved both existence and uniqueness of $\left[\mathcal{M}^{-1}\right]$.

Let $[f]_n, [g]_n \in {}_nD_v^v$, then

$$\begin{aligned} \mathcal{O}([f]_n) - \mathcal{O}([g]_n) &= L^{-1} \circ (\mathcal{I} - \mathcal{N} \circ [f]_n) - L^{-1} \circ (\mathcal{I} - \mathcal{N} \circ [g]_n) \\ &= L^{-1} \circ (\mathcal{N} \circ [f]_n - \mathcal{N} \circ [g]_n) \end{aligned}$$

If we assume that $\lambda([f]_n - [g]_n) = k$, then the lowest nonvanishing order of $\mathcal{O}([f]_n) - \mathcal{O}([g]_n)$ has to be at least $k + 1$, since every term in $[f]_n - [g]_n$ gets

multiplied with a nonlinear term of $\mathcal{N}$. Hence

$$\lambda\left(\mathcal{O}\left([f]_n\right) - \mathcal{O}\left([g]_n\right)\right) \geq k+1 > k = \lambda\left([f]_n - [g]_n\right) \ .$$

and

$$\lambda\left(\mathcal{O}^{n+1}\left([f]_n\right) - \mathcal{O}^{n+1}\left([g]_n\right)\right) \geq k+n+1 \geq n+1$$

and thus $\mathcal{O}^{n+1}\left([f]_n\right)$ and $\mathcal{O}^{n+1}\left([g]_n\right)$ coincide with all derivatives at the origin up to order n. □

B.5 Normal form transformations

Utilizing the functional inversion algorithm from the previous section, we can formulate an automated approach to compute normal form transformations for suitable maps. Assume we are given an origin-preserving $\mathcal{C}^r$-map $f : \mathbb{R}^v \longrightarrow \mathbb{R}^v$, where the linear part of f is diagonal, and such that the origin is a hyperbolic fixed point, i.e.

$$|\lambda_i| \neq 1 \forall\, 1 \leq i \leq v.$$

Given a fixed compuation order n, we assume that the eigenvalues are nonresonant up to that maximal order, i.e. satisfy

$$\lambda_j - \lambda_1^{k1} \cdot ... \cdot \lambda_v^{kv} \neq 0 \forall\, 1 \leq j \leq v \forall\ |\mathbf{k}| \leq n, \tag{B.4}$$

where $\mathbf{k} = (k_1, ..., k_v)$ is a multiindex of length v. Up to finite order n, this criterion can usually be easily checked once the eigenvalues are known.

The objective is to find a coordinate transformation $\mathcal{N}$ which reduces f to its linear part L in the new coordinates,

$$\mathcal{N}^{-1} \circ f \circ \mathcal{N} = L, \tag{B.5}$$

using normal forms. Assume this can be done order-by-order using near-identity transformations

$$\mathcal{T}_1 := \mathcal{I},$$
$$\mathcal{T}_i := \mathcal{I} + \mathcal{S}_i,$$

with nonlinear parts $\mathcal{S}_i$ of exact order i (i.e. homogoneous). For the inverse transformations $\mathcal{T}^{-1}$ we then have

$$\mathcal{T}_i^{-1} =_i \mathcal{I} - \mathcal{S}_i.$$

Suppose that f has been transformed such that in new coordinates it takes the form $\tilde{f} : \mathbb{R}^v \longrightarrow \mathbb{R}^v$, where $\tilde{f}$ is origin-preserving, $\mathcal{C}^r$ and up to order $i-1$ we have

$$\tilde{f} =_{i-1} L$$

and hence

$$\tilde{f} =_i L + R_i,$$

where R_i contains only terms of order i and higher. We now derive a condition for the transformations $\mathcal{T}_i$, or more specifically their nonlinear parts $\mathcal{S}_i$, such that application of $\mathcal{T}_i$ eliminates the nonlinear part R_i, i.e.

$$\mathcal{T}_i^{-1} \circ \tilde{f} \circ \mathcal{T}_i =_i L$$

Observe that up to order i we have

$$\begin{aligned}
\mathcal{T}_i^{-1} \circ \tilde{f} \circ \mathcal{T}_i &=_i (\mathcal{I} - \mathcal{S}_i) \circ (L + R_i) \circ (\mathcal{I} + \mathcal{S}_i) \\
&=_i (L + R_i) \circ (\mathcal{I} + \mathcal{S}_i) - \mathcal{S}_i \circ (L + R_i) \circ (\mathcal{I} + \mathcal{S}_i) \\
&=_i L + L \circ \mathcal{S}_i + R_i \circ (\mathcal{I} + \mathcal{S}_i) - \mathcal{S}_i \circ (L + L \circ \mathcal{S}_i + R_i \circ (\mathcal{I} + \mathcal{S}_i)) \\
&=_i L + L \circ \mathcal{S}_i + R_i - \mathcal{S}_i \circ L \\
&=_i L + R_i + [L, \mathcal{S}_i].
\end{aligned}$$

Looking at the last expression componentwise, we can choose the coefficients in $\mathcal{S}_i$ such that the commutator eliminates respective terms in R_i. Suppose that both R_i and $\mathcal{S}_i$ can be represented by their Taylor polynomial expansion, and that the j-th components in their expansions are

$$\begin{aligned} R_i^{(j)} &= \sum_{|\mathbf{k}|=i} \rho(\mathbf{k}, j) \cdot x_1^{k1} \cdot \ldots \cdot x_v^{kv}, \\ \mathcal{S}_i^{(j)} &= \sum_{|\mathbf{k}|=i} \sigma(\mathbf{k}, j) \cdot x_1^{k1} \cdot \ldots \cdot x_v^{kv}. \end{aligned} \tag{B.6}$$

Since L is diagonal we have that for the j-th component of the commutator

$$\begin{aligned} (L \circ \mathcal{S}_i - \mathcal{S}_i \circ L)^{(j)} =_i & \left(\sum_{|\mathbf{k}|=i} \lambda_j \sigma(\mathbf{k}, j) \cdot x_1^{k1} \cdot \ldots \cdot x_v^{kv} \right) \\ & - \left(\sum_{|\mathbf{k}|=j} \sigma(\mathbf{k}, j) \cdot (\lambda_1 x_1)^{k1} \cdot \ldots \cdot (\lambda_v x_v)^{kv} \right) \\ =_i & \sum_{|\mathbf{k}|=i} \left(\lambda_j - \lambda_1^{k1} \cdot \ldots \cdot \lambda_v^{kv} \right) \sigma(\mathbf{k}, j) \cdot x_1^{k1} \cdot \ldots \cdot x_v^{kv} \end{aligned}$$

and comparing with eq.(B.6) componentwise we see that the correct choice for $\sigma(\mathbf{k}, j)$ is given by

$$\sigma(\mathbf{k}, j) := -\frac{\rho(\mathbf{k}, j)}{\lambda_j - \lambda_1^{k1} \cdot \ldots \cdot \lambda_v^{kv}}.$$

Note that this choice for $\sigma(\mathbf{k}, j)$ is feasible due to the nonresonance condition (B.4).

Applying these transformations to f we can now remove the nonlinearities in f inductively. We define a sequence $\{\mathcal{U}_i\}_{i \geq 2}$ to fully linearize the original map f

$$\begin{aligned} \mathcal{U}_2 &:= f, \\ \mathcal{U}_{i+1} &:= \mathcal{T}_i^{-1} \circ \mathcal{U}_i \circ \mathcal{T}_i \end{aligned}$$

We can now set

$$\mathcal{N} := \mathcal{T}_2 \circ \ldots \circ \mathcal{T}_n, \tag{B.7}$$

$$\mathcal{N}^{-1} := \mathcal{T}_n^{-1} \circ \ldots \circ \mathcal{T}_2^{-1}, \tag{B.8}$$

to obtain a transformation $\mathcal{N}$ which satisfies eq.(B.5) up to prespecified order n. Note that this also entails that

$$L^{-1} =_n \left(\mathcal{N}^{-1} \circ f \circ \mathcal{N}\right)^{-1} = \mathcal{N} \circ f^{-1} \circ \mathcal{N}^{-1}$$

and

$$f =_n \mathcal{N} \circ L \circ \mathcal{N}^{-1},$$
$$f^{-1} =_n \mathcal{N}^{-1} \circ L^{-1} \circ \mathcal{N} .$$

The move of the aforementioned algorithm into the DA-vector realm is beneficial, since the inverse transformations $\mathcal{T}_2^{-1}, ..., \mathcal{T}_n^{-1}$ in (B.8) can be obtained as DA-vectors $\left[\mathcal{T}_2^{-1}\right]_n, ..., \left[\mathcal{T}_n^{-1}\right]_n$ in the fashion of the last paragraph once the DA-vectors $[\mathcal{T}_2]_n, ..., [\mathcal{T}_n]_n$ are defined componentwise by

$$\begin{aligned}\left[\mathcal{T}_{i,j}\right]_n &:= \left[\mathcal{I}_j\right]_n + \left[\mathcal{S}_{i,j}\right]_n \\ &= \left[x_j\right] + \sum_{|\mathbf{k}|=i} \frac{\rho(\mathbf{k}, j)}{\lambda_j - \lambda_1^{k1} \cdot ... \cdot \lambda_v^{kv}} \cdot \left[x_1^{k1} \cdot ... \cdot x_v^{kv}\right]_n .\end{aligned}$$

Finally up to finite order n the Taylor expansions for the normal form transformation $\mathcal{N}$ and its inverse $\mathcal{N}^{-1}$ are obtained in the DA-vectors

$$[\mathcal{N}]_n := [\mathcal{T}_2]_n \circ ... \circ [\mathcal{T}_n]_n ,$$
$$\left[\mathcal{N}^{-1}\right]_n := \left[\mathcal{T}_n^{-1}\right]_n \circ ... \circ \left[\mathcal{T}_2^{-1}\right]_n .$$

BIBLIOGRAPHY

[1] COSY INFINITY Version 9.0 - Manual and Introduction. `http://cosy.pa.msu.edu/manual/index.html`.

[2] D. V. Anosov and V. I. Arnold, editors. *Dynamical Systems I, Ordinary Differential Equations and Smooth Dynamical Systems*. Springer-Verlag, 1988.

[3] C. Barbarosie. Reducing the Wrapping Effect. *Computing*, 54:347–357, 1995.

[4] M. Berz. *Modern Map Methods in Particle Beam Physics*. Academic Press, San Diego, 1999. Also available at http://bt.pa.msu.edu/pub.

[5] M. Berz and G. Hoffstätter. Computation and Application of Taylor Polynomials with Interval Remainder Bounds. *Reliable Computing*, 4(1):83–97, 1998.

[6] M. Berz and K. Makino. Verified Integration of ODEs and Flows Using Differential Algebraic Methods on High-Order Taylor Models. *Reliable Computing*, 4(4):361–369, 1998.

[7] M. Berz and K. Makino. Suppression of the Wrapping Effect by Taylor Model-based Verified Integrators: Long-term Stabilization by Shrink Wrapping. *International Journal of Differential Equations and Applications*, 10:385–403, 2005.

[8] K. Burns and H. Weiss. A Geometric Criterion for Positive Topological Entropy. *Comm. Math. Phys.*, 172(1):95–118, 1995.

[9] X. Cabré, E. Fontich, and R. de la Llave. The Parametrization Method for Invariant Manifolds I: Manifolds Associated to Non-resonant Subspaces. *Indiana Univ. Math. J.*, 52:283–328, 2003.

[10] X. Cabré, E. Fontich, and Rr. de la Llave. The Parametrization Method for Invariant Manifolds II: Regularity with Respect to Parameters. *Indiana Univ. Math. J.*, 52:329–360, 2003.

[11] P. Collins. Dynamics Forced by Surface Trellises. *Contemp. Math.*, 246, 1999.

[12] P. Collins. Symbolic Dynamics from Homoclinic Tangles. *Intern. J. Bifur. Chaos*, 12(3):605–617, 2002.

[13] T. Csenes. Test Results of Interval Methods for Global Optimization. *Computer Arithmetic, Scientific Computation and Mathematical Modelling*, 12, 1991.

[14] A. J. Dragt, F. Neri, G. Rangarajan, D. R. Douglas, L. M. Healy, and R. D. Ryne. Lie Algebraic Treatment of Linear and Nonlinear Beam Dynamics. *Annual Review of Nuclear and Particle Science*, 38:455–496, 1988.

[15] M. Berz et al. The COSY INFINITY Web Page. `http://cosyinfinity.org`.

[16] J. Fornaess and E. Gavosto. Tangencies for Real and Complex Hénon Maps: An Analytic Method. *Experiment. Math.*, 8(3):253–260, 1999.

[17] B. Franceschini and C. Russo. Stable and Unstable Manifolds of the Hénon Mapping. *J. Stat. Phys.*, 25(4):757–769, 1981.

[18] D. Gale. The Game of Hex and the Brouwer Fixed-Point Theorem. *Amer. Math. Monthly*, 86(10):818–827, 1979.

[19] Z. Galias. Existence and Uniqueness of Low-Period Cycles and Estimation of Topological Entropy for the Hénon Map. In *Proc. Int. Symposium on Nonlinear Theory and its Applications, NOLTA'98*, volume 1, pages 187–190, Crans–Montana, 1998.

[20] Z. Galias. All Periodic Orbits with Period $n \leq 26$ for the Hénon Map. In *Proc. European Conference on Circuit Theory and Design, ECCTD'99*, volume 1, pages 361–364, Stresa, 1999.

[21] Z. Galias. Obtaining Rigorous Bounds for Topological Entropy for Discrete Time Dynamical Systems. In *Proc. Int. Symposium on Nonlinear Theory and its Applications, NOLTA'02*, pages 619–622, Xi'an, PRC, 2002.

[22] Z. Galias and P. Zgliczyński. Abundance of Homoclinic and Heteroclinic Orbits and Rigorous Bounds for the Topological Entropy for the Hénon map. *Nonlinearity*, 14:909–932, 2001.

[23] J. Guckenheimer and P. Holmes. *Nonlinear Oscillations, Dynamical Systems, and Bifurcations of Vector Fieds*. Springer, New York, 1983.

[24] E. Hansen and G. W. Walster. *Global Optimization using Interval Analysis*. Marcel Dekker, 2003.

[25] E. R. Hansen. *An Overview of Global Optimization Using Interval Analysis*, pages 289–307. Academic Press, New York, 1988.

[26] B. Hasselblatt and A. Katok. *Introduction to the Modern Theory of Dynamical Systems*. Encyclopedia of Mathematics and its Applications, Volume 54. Cambridge University Press, 1995.

[27] J. Hoefkens. *Verified Methods for Differential Algebraic Equations*. PhD thesis, Michigan State University, East Lansing, Michigan, USA, 2001.

[28] J. Hoefkens, M. Berz, and K. Makino. Verified High-Order Integration of DAEs and Higher-Order ODEs. In W. Kraemer and J.W. v. Gudenburg, editors, *Scientific Computing, Validated Numerics, Interval Methods*, pages 281–292, Boston, 2001. Kluwer.

[29] J. Hoefkens, M. Berz, and K. Makino. Computing Validated Solutions of Implicit Differential Equations. *Advances in Computational Mathematics*, 19:231–253, 2003.

[30] J. Hoefkens, M. Berz, K. Makino, and R. E. Moore. Verified Long-Term Propagation of Large Sets of Initial Conditions in the Integration of Asteroid Orbits. *Celestial Mechanics and Dynamical Astronomy*, submitted.

[31] J. Hubbard. Parametrizing Unstable and Very Unstable Manifolds. *Mosc. Math. J.*, 5(1):105–124, 2005.

[32] C. Jansson. A Global Optimization Method Using Interval Arithmetic. In *Computer Arithmetic and Scientific Computation, Proceedings of the SCAN 91*, Amsterdam, 1992. North–Holland, Elsevier.

[33] A. Katok. Lyapunov Exponents, Entropy and Periodic Orbits for Diffeomorphisms. *Publ. Math. IHES*, 51:137–173, 1980.

[34] R. B. Kearfott. An Interval Branch and Bound Algorithm for Bound Constrained Optimization. *J. Global Optim.*, 2:259–280, 1992.

[35] B. Krauskopf and H. Osinga. Growing 1D and Quasi-2D Unstable Manifolds of Maps. *J. Comp. Phys.*, 146:404–419, 1998.

[36] J. Lee. *Introduction to Smooth Manifolds*. Springer, New York, 2002.

[37] R. J. Lohner. AWA - Software for the Computation of Guaranteed Bounds for Solutions of Ordinary Initial Value Problems.

[38] R. J. Lohner. Computation of Guaranteed Enclosures for the Solutions of Ordinary Initial and Boundary Value Problems. In J.R. Cash and I. Gladwell, editors, *Computational Ordinary Differential Equations*, pages 425–435. Clarendon Press, Oxford, 1992.

[39] R. J. Lohner. *On the Ubiquity of the Wrapping Effect in the Computation of Error Bounds*, pages 201–217. Springer, Berlin, 2001.

[40] R. Maehara. The Jordan Curve Theorem Via the Brouwer Fixed Point Theorem. *Amer. Math. Monthly*, 91(10):641–643, 1984.

[41] K. Makino. *Rigorous Analysis of Nonlinear Motion in Particle Accelerators*. PhD thesis, Michigan State University, East Lansing, Michigan, USA, 1998. Also MSUCL-1093.

[42] K. Makino and M. Berz. Efficient Control of the Dependency Problem based on Taylor Model Methods. *Reliable Computing*, 5(1):3–12, 1999.

[43] K. Makino and M. Berz. Verified Integration for Transfer Maps. In *Sixth International Computational Accelerator Physics Conference*, 2001. http://temf34.temf.e-technik.tu-darmstadt.de/frames/proceedings_res.htm.

[44] K. Makino and M. Berz. Taylor Models and Other Validated Functional Inclusion Methods. *International Journal of Pure and Applied Mathematics*, 6,3:239–316, 2003.

[45] K. Makino and M. Berz. Range Bounding for Global Optimization with Taylor Models. *Transactions on Computers*, 4,11:1611–1618, 2005.

[46] K. Makino and M. Berz. Suppression of the Wrapping Effect by Taylor model-based Verified Integrators: Long-term Stabilization by Preconditioning. *International Journal of Differential Equations and Applications*, 10,4:253–384, 2005.

[47] K. Makino and M. Berz. Suppression of the Wrapping Effect by Taylor Model-based Verified Integrators: The Single Step. *International Journal of Pure and Applied Mathematics*, 36,2:175–187, 2006.

[48] K. Makino, M. Berz, and Y.-K. Kim. Range Bounding with Taylor Models - some Case Studies. *Transactions on Mathematics*, 3,1:137–145, 2004.

[49] R. E. Moore. *Interval Analysis*. Prentice-Hall, Englewood Cliffs, NJ, 1966.

[50] R. E. Moore. *Methods and Applications of Interval Analysis*. SIAM, 1979.

[51] N. S. Nedialkov and K. R. Jackson. A New Perspective on the Wrapping Effect in Interval Methods for IVPs for ODEs. *Proc. Scan2000, Kluwer*, 2001.

[52] A. Neumaier. The Wrapping Effect, Ellipsoid Arithmetic, Stability and Confidence Regions. *Computing Supplementum*, 9:175–190, 1993.

[53] S. Newhouse. Entropy and Volume. *Ergod. Th. and Dynam. Sys.*, 8:283–299, 1988.

[54] S. Newhouse. Continuity Properties of Entropy. *Ann. Math.*, 129:215–235, 1989.

[55] S. Newhouse. Special Topics in Applied Mathematics. Lecture notes, Michigan State University, 2006.

[56] S. Newhouse, M. Berz, J. Grote, and K. Makino. On the Estimation of Topological Entropy on Surfaces. *Contemporary Math.*, 469:243–270, 2008.

[57] S. Newhouse and T. Pignataro. On the Estimation of Topological Entropy. *J. Stat. Phys.*, 72:1331–1351, 1993.

[58] Henri Poincare. *New Methods of Celestial Mechanics*, volume 1-3. American Institute of Physics, New York, 1893/1993.

[59] A. Quarteroni, R. Sacco, and F. Saleri. *Texts in Applied Mathematics, Vol. 37: Numerical Mathematics*. Springer, 2007.

[60] H. Ratschek and J. Rokne. *New Computer Methods for Global Optimization*. Ellis Horwood Limited, Chichester, England, 1988.

[61] N. Revol, K. Makino, and M. Berz. Taylor Models and Floating-Point Arithmetic: Proof that Arithmetic Operations are Validated in COSY. *Journal of Logic and Algebraic Programming*, 64/1:135–154, 2004.

[62] C. Robinson. *Dynamical Systems*. CRC Press, Boca Raton, 1999.

[63] S. Smale. Differentiable Dynamical Systems. *Bull. Amer. Math. Soc.*, 73(10):747–817, 1967.

[64] W. Tucker. The Lorenz Attractor Exists. *C. R. Acad. Sci. Paris*, 328(1):1197–1202, 1999.

[65] Y. Yomdin. c^k-Resolution of Semialgebraic Mappings. Addendum to Volume Growth and Entropy. *Israel J. Math.*, 57(3):301–317, 1987.

[66] Y. Yomdin. Volume Growth and Entropy. *Israel J. Math.*, 57(3):253–260, 1987.

[67] Z. You, E. Kostelich, and J. Yorke. Calculating Stable and Unstable Manifolds. *Int. J. of Bifurcation and Chaos*, 1(3):1–17, 1991.